



MINISTÉRIO DA CIÊNCIA, TECNOLOGIA, INOVAÇÕES E COMUNICAÇÕES  
**INSTITUTO NACIONAL DE PESQUISAS ESPACIAIS**

sid.inpe.br/mtc-m21c/2019/11.21.08.24-TDI

**MAPPING SUCCESSIONAL FOREST STAGES AND  
TREE SPECIES IN SUBTROPICAL AREAS  
INTEGRATING UAV-BASED PHOTOGRAMMETRIC  
POINT CLOUD AND HYPERSPECTRAL DATA:  
COMPARISON OF MACHINE AND DEEP LEARNING  
ALGORITHMS**

Camile Söthe

Doctorate Thesis of the Graduate  
Course in Remote Sensing, guided  
by Drs. Claudia Maria de Almeida,  
and Marcos Benedito Schimalski,  
approved in December 18, 2019.

URL of the original document:

<http://urlib.net/8JMKD3MGP3W34R/3UED6S2>

INPE  
São José dos Campos  
2019

**PUBLISHED BY:**

Instituto Nacional de Pesquisas Espaciais - INPE  
Gabinete do Diretor (GBDIR)  
Serviço de Informação e Documentação (SESID)  
CEP 12.227-010  
São José dos Campos - SP - Brasil  
Tel.:(012) 3208-6923/7348  
E-mail: pubtc@inpe.br

**BOARD OF PUBLISHING AND PRESERVATION OF INPE  
INTELLECTUAL PRODUCTION - CEPPII (PORTARIA Nº  
176/2018/SEI-INPE):****Chairperson:**

Dra. Marley Cavalcante de Lima Moscati - Centro de Previsão de Tempo e Estudos  
Climáticos (CGCPT)

**Members:**

Dra. Carina Barros Mello - Coordenação de Laboratórios Associados (COCTE)  
Dr. Alisson Dal Lago - Coordenação-Geral de Ciências Espaciais e Atmosféricas  
(CGCEA)  
Dr. Evandro Albiach Branco - Centro de Ciência do Sistema Terrestre (COCST)  
Dr. Evandro Marconi Rocco - Coordenação-Geral de Engenharia e Tecnologia  
Espacial (CGETE)  
Dr. Hermann Johann Heinrich Kux - Coordenação-Geral de Observação da Terra  
(CGOBT)  
Dra. Ieda Del Arco Sanches - Conselho de Pós-Graduação - (CPG)  
Sílvia Castro Marcelino - Serviço de Informação e Documentação (SESID)

**DIGITAL LIBRARY:**

Dr. Gerald Jean Francis Banon  
Clayton Martins Pereira - Serviço de Informação e Documentação (SESID)

**DOCUMENT REVIEW:**

Simone Angélica Del Ducca Barbedo - Serviço de Informação e Documentação  
(SESID)  
André Luis Dias Fernandes - Serviço de Informação e Documentação (SESID)

**ELECTRONIC EDITING:**

Ivone Martins - Serviço de Informação e Documentação (SESID)  
Cauê Silva Fróes - Serviço de Informação e Documentação (SESID)



MINISTÉRIO DA CIÊNCIA, TECNOLOGIA, INOVAÇÕES E COMUNICAÇÕES  
**INSTITUTO NACIONAL DE PESQUISAS ESPACIAIS**

sid.inpe.br/mtc-m21c/2019/11.21.08.24-TDI

**MAPPING SUCCESSIONAL FOREST STAGES AND  
TREE SPECIES IN SUBTROPICAL AREAS  
INTEGRATING UAV-BASED PHOTOGRAMMETRIC  
POINT CLOUD AND HYPERSPECTRAL DATA:  
COMPARISON OF MACHINE AND DEEP LEARNING  
ALGORITHMS**

Camile Söthe

Doctorate Thesis of the Graduate  
Course in Remote Sensing, guided  
by Drs. Claudia Maria de Almeida,  
and Marcos Benedito Schimalski,  
approved in December 18, 2019.

URL of the original document:

<<http://urlib.net/8JMKD3MGP3W34R/3UED6S2>>

INPE  
São José dos Campos  
2019

## Cataloging in Publication Data

---

Söthe, Camile.

So77m Mapping successional forest stages and tree species in subtropical areas integrating UAV-based photogrammetric point cloud and hyperspectral data: comparison of machine and deep learning algorithms / Camile Söthe. – São José dos Campos : INPE, 2019.

xxvi + 186 p. ; (sid.inpe.br/mtc-m21c/2019/11.21.08.24-TDI)

Thesis (Doctorate in Remote Sensing) – Instituto Nacional de Pesquisas Espaciais, São José dos Campos, 2019.

Guiding : Drs. Claudia Maria de Almeida, and Marcos Benedito Schimalski.

1. Tropical biodiversity. 2. Imaging spectroscopy. 3. Photogrammetry. 4. WorldView-2. 5. Individual tree crown delineation. I.Title.

CDU 528.8:630\*1

---



Esta obra foi licenciada sob uma Licença [Creative Commons Atribuição-NãoComercial 3.0 Não Adaptada](https://creativecommons.org/licenses/by-nc/3.0/).

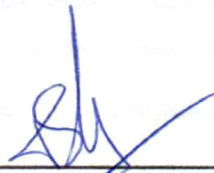
This work is licensed under a [Creative Commons Attribution-NonCommercial 3.0 Unported License](https://creativecommons.org/licenses/by-nc/3.0/).

Aluno (a): **Camille Söthe**

Título: "MAPPING SUCCESSIONAL FOREST STAGES AND TREE SPECIES IN SUBTROPICAL AREAS INTEGRATING UAV-BASED PHOTOGRAMMETRIC POINT CLOUD AND HYPERSPECTRAL DATA: COMPARISON OF MACHINE AND DEEP LEARNING ALGORITHMS"

Aprovado (a) pela Banca Examinadora em cumprimento ao requisito exigido para obtenção do Título de **Doutor(a)** em **Sensoriamento Remoto**

Dr. Thales Sehn Körting



\_\_\_\_\_  
**Presidente / INPE / São José dos Campos - SP**

Participação por Vídeo - Conferência

**Aprovado**       **Reprovado**

Dra. Claudia Maria de Almeida

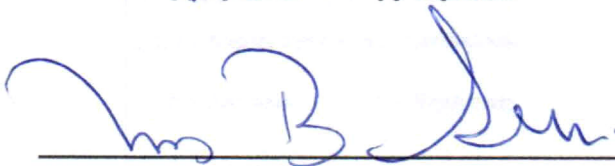


\_\_\_\_\_  
**Orientador(a) / INPE / São José dos Campos - SP**

Participação por Vídeo - Conferência

**Aprovado**       **Reprovado**

Dr. Marcos Benedito Schimalski

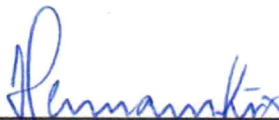


\_\_\_\_\_  
**Orientador(a) / UDESC / Lages - SC**

Participação por Vídeo - Conferência

**Aprovado**       **Reprovado**

Dr. Hermann Johann Heinrich Kux



\_\_\_\_\_  
**Membro da Banca / INPE / SJC Campos - SP**

Participação por Vídeo - Conferência

**Aprovado**       **Reprovado**

**Este trabalho foi aprovado por:**

**maioria simples**

**unanimidade**

**São José dos Campos, 18 de dezembro de 2019**



*“The two most important days in your life are the day you are born and the day you find out why”.*

*Mark Twain*





## ACKNOWLEDGEMENTS

Primeiramente agradeço à minha orientadora, Dra. Cláudia Almeida, por todo o suporte durante o Doutorado, por sempre ter acreditado no meu potencial para o meio acadêmico, por compartilhar seus conhecimentos, experiências e conselhos acadêmicos e pessoais. Por sempre responder prontamente todas as dúvidas e apoiar minhas decisões. Muito obrigada!

À Universidade do Estado de Santa Catarina (UDESC), em especial ao meu coorientador Dr. Marcos Benedito Schimalski que desde o Mestrado tem acompanhado o meu trabalho, por ter auxiliado na coordenação do trabalho de campo e por todas as valiosas contribuições ao longo da pesquisa. Também deixo meus agradecimentos ao Dr. Veraldo Liesenberg e aos colegas da UDESC, Carla Lima, Felipe Pinto e Carla Pertille por contribuírem com sugestões e com o trabalho de campo.

Ao Instituto Nacional de Pesquisas Espaciais (INPE) e a todo o corpo docente do curso de Sensoriamento Remoto, que foi essencial para meu crescimento e aprendizado, em especial aos Drs. Thales Körting e Hermann Kux, que contribuíram com suas sugestões na qualificação e proposta de Doutorado, e a coordenadora do curso de Sensoriamento Remoto, Dra. Ieda Sanches, pela eficiência e pronta-resposta em todas as minhas dúvidas e demandas sobre o curso.

Agradeço a todos os meus colegas de curso da turma de Sensoriamento Remoto de 2016, pelos conhecimentos compartilhados, pelos momentos de alegrias e de 'sofrimento' sempre com uma boa dose de bom humor, em especial aos amigos Bárbara Hass, Jéssica Gerente, Priscila Negrão e Alindomar Lacerda. Ainda deixo meus agradecimentos às amigas do INPE que dividiram comigo o 'apê' nesse período, Jeanne Lima e Anielli Rosane, as quais foram minha família joiense.

À equipe da Universidade Estadual de São Paulo (UNESP) de Presidente Prudente, Dr. Antonio Tommaselli, Gabriela Miyoshi e Marcus Moraes, que contribuíram no levantamento e processamento dos dados hiperespectrais.

À equipe da Pontifícia Universidade Católica do Rio de Janeiro (PUC-Rio), Dr. Raul Feitosa, Laura Rosa, José Bermudez e Pedro Diaz, por me fornecerem conhecimentos de teoria e prática sobre o algoritmo de aprendizado profundo utilizado nesse trabalho.

Aos colegas da Fondazione Edmund Mach, onde realizei o Doutorado Sandúiche, em especial ao meu orientador Dr. Michele Dalponte, pela sua

recepção, suporte e contribuições com esse trabalho, e a amiga Soraya Versace, por ter sido uma grande companheira durante meu período na Itália.

À Coordenação de Aperfeiçoamento de Pessoal de Nível Superior (CAPES) pelas bolsas de estudo concedidas nesse período, processos número 88882.330700/2018-01 e 88881.190545/2018-01 (PDSE), além do apoio financeiro para participação em evento internacional.

Meus profundos agradecimentos aos meus pais, Vilmar e Ceci, pelo apoio incondicional. Mesmo pensando que 'largar tudo' para iniciar o Doutorado não era uma decisão muito racional, estiveram ao meu lado em todos os momentos dessa trajetória.

Por fim gostaria de agradecer ao Dr. Silvio Rafaeli Neto que durante minha graduação na UDESC me concedeu uma bolsa de iniciação científica na área de Sensoriamento Remoto, despertando meu interesse por essa área. Hoje não tenho dúvidas da minha escolha.

## ABSTRACT

The use of Remote Sensing for successional stages and tree species mapping in (sub)tropical forests is a challenging task, due to high floristic and spectral diversity in these environments. Fortunately, in the latest decades, mankind has witnessed a remarkable advancement of space technologies targeted to monitoring forest resources, such as the availability of high spatial and spectral data and advanced classification methods. Besides providing high spatial and spectral resolution images, unmanned aerial vehicle (UAV)-hyperspectral cameras operating in frame format enable to produce tridimensional (3D) hyperspectral point clouds. This study investigated two major topics concerning the successional stages and tree species mapping in a subtropical forest environment in Southern Brazil: a) the use of UAV-acquired hyperspectral images and UAV-photogrammetric point cloud (PPC) for the classification of successional stages, comparing these data with classifications using multispectral images acquired by the WorldView-2 (WV-2) satellite and Light Detection and Ranging (LiDAR) data and; b) the use of UAV-acquired hyperspectral images and UAV-PPC for individual tree crown (ITC) delineation and semiautomatic classification of 16 major tree species in two subtropical forest fragments. For both goals, different datasets containing hyperspectral visible/near-infrared (VNIR) bands, PPC features, canopy height model (CHM), and other features extracted from hyperspectral or WV-2 data (e.g., texture, vegetation indices-VIs, and minimum noise fraction-MNF) were tested. To classify the successional forest stages, an object-based image analysis (OBIA) was conducted using two conventional machine learning classifiers, support vector machine (SVM) and random forest (RF). For tree species classification, two conventional machine learning, SVM and RF, and one deep learning classifier, the convolutional neural network (CNN), were tested in a pixel-based approach. Besides these classifiers, a new SVM approach focused on an imbalanced sample set was also tested, the weighted SVM (wSVM). For ITC delineation, three methods were tested: two using hyperspectral bands, the multiresolution region growing (MRG) and the itcIMG, and the other one using the PPC, named multiclass cut followed by recursive cut (MCRC). The best segmentation result was used in two classification approaches tested using the conventional machine learning methods: OBIA and the majority vote (MV) rule. The results showed that the successional forest stages were successfully classified with accuracies over 80% when the WV-2 data were applied, and over 90% with the UAV-hyperspectral data. The best result reached an overall accuracy (OA) of 99.28% using the hyperspectral data associated with the CHM and RF classifier. The CHM and features derived from WV-2 and hyperspectral data increased between 5% and 13% the classification accuracies. Regarding the tree species classification, the CNN outperformed the RF and SVM for both areas, with an OA of 84.4% in Area 1, and 74.95% in Area 2, using only the VNIR bands. This method was 22% to 26% more accurate than the SVM and RF when considering the VNIR dataset. The inclusion of PPC features and the CHM provided a great increase in tree species classification results when machine learning methods were applied (SVM, wSVM and RF), between 13%

and 17% depending on the selected classifier and the study area. However, a decrease was observed when these features were included in the CNN classification. The OBIA approach did not increase the OA for the SVM classifier, while a slightly increase was observed for the RF algorithm in comparison with the RF using the pixel-based classification. The MV rule approach, on the other hand, brought a marked increase in accuracy for both study areas (5% for Area 1 and 11% for Area 2). When using PPC features and the CHM, associated with the MV approach, the machine learning classifiers reached accuracies similar to the ones achieved by the CNN (82.52% for Area 1 and 75.45% for Area 2). The wSVM provided a slightly increase in accuracy not only for some lesser represented classes, but also for some major classes in Area 2. None of the three ITC delineation methods reached a suitable result for all reference ITCs. The MRG method tended to oversegment most ITCs, while the itcIMG and MCRC tended to undersegment or missed some suppressed ITCs. With the inclusion of the CHM in the MRG segmentation and merging homogenous segments with the Jeffries Matusita (JM) distance, visually and according to supervised evaluation metrics, a better delineation was reached. The results found in this study are relevant to favor the conservation of the Atlantic Rain Forest, a severely threatened biome, optimizing the mapping and monitoring of its forest remnants, and also to subsidize actions within the scope of the rural environmental register (*Cadastro Ambiental Rural- CAR*) in Brazil. In addition, the methodology can be used to map specific tree species, such as the endangered ones, in this case *Araucaria angustifolia* and *Cedrela fissilis*.

Keywords: Tropical Biodiversity. Imaging Spectroscopy. Photogrammetry. WorldView-2. Individual Tree Crown Delineation. Support Vector Machine. Random Forest. Convolutional Neural Network.

# MAPEAMENTO DE ESTÁDIOS SUCESSIONAIS DA VEGETAÇÃO E ESPÉCIES ARBÓREAS EM ÁREAS SUBTROPICAIS INTEGRANDO NUVEM DE PONTOS FOTOGRAFÉTRICA E DADOS HIPERESPECTRAIS BASEADOS EM VANT: COMPARAÇÃO ENTRE ALGORITMOS DE APRENDIZADO DE MÁQUINA E APRENDIZADO PROFUNDO

## RESUMO

O uso de Sensoriamento Remoto para o mapeamento de estádios sucessionais e espécies arbóreas em florestas (sub)tropicais é uma tarefa desafiadora, devido à alta diversidade florística e espectral desses ambientes. Felizmente, nas últimas décadas, a humanidade testemunhou um notável avanço das tecnologias espaciais voltadas ao monitoramento dos recursos florestais, como a disponibilidade de dados com alta resolução espacial e espectral e métodos de classificação sofisticados. Além da aquisição de imagens de alta resolução espacial e espectral, câmeras hiperespectrais a bordo de veículos aéreos não tripulados (VANT) operando em formato de quadro permitem produzir nuvens de pontos hiperespectrais tridimensionais (3D). Este estudo investigou dois grandes tópicos referentes ao mapeamento de estádios sucessionais e de espécies arbóreas em um ambiente de floresta subtropical do sul do Brasil: a) o uso de imagens hiperespectrais adquiridas por VANT e sua nuvem de pontos fotogramétrica (*photogrammetric point cloud* - PPC) para a classificação de três estádios sucessionais da vegetação, comparando esses dados com classificações usando imagens multiespectrais adquiridas pelo satélite WorldView-2 (WV-2) associados a dados *Light Detection and Ranging* (LiDAR); e b) o uso de imagens hiperespectrais adquiridas por VANT e informações da PPC para o delineamento de copas de árvore individual (*individual tree crown* - ITC) e para a classificação semiautomática de 16 espécies arbóreas dominantes em dois fragmentos de floresta subtropical. Para ambos os objetivos, foram testados diferentes conjuntos de dados contendo bandas do espectro visível/infravermelho próximo (*visible/near infrared* - VNIR), atributos derivados da PPC, modelo de altura de dossel (*canopy height model* - CHM) e outros atributos extraídos de dados hiperespectrais ou WV-2 (e.g., textura, índices de vegetação-VIs, e fração de ruído mínima-MNF). Para classificar os estádios sucessionais, foi conduzida uma análise de imagem baseada em objetos (*object-based image analysis* - OBIA) usando dois classificadores de aprendizado de máquina, máquinas de vetor de suporte (*support vector machine* - SVM) e floresta aleatória (*random forest* - RF). Para a classificação de espécies arbóreas, dois algoritmos de aprendizado de máquina convencionais, SVM e RF, e um classificador de aprendizagem profunda, rede neural convolucional (*convolutional neural network* - CNN), foram testados em uma abordagem baseada em pixels. Além destes, também foi testada uma nova abordagem SVM para lidar com o conjunto de amostras desbalanceadas, o SVM ponderado (*weighted SVM* - wSVM). Para o delineamento de ITC, três métodos foram testados: dois utilizando bandas hiperespectrais, o algoritmo multirresolução por crescimento de regiões (*multiresolution region growing* - MRG) e o itcIMG, e o

terceiro método utilizando a nuvem de pontos PPC, denominado corte multiclasse seguido de corte recursivo (*multiclass cut followed by recursive cut* - MCRC). O melhor resultado de segmentação foi usado em duas abordagens de classificação testadas com os métodos convencionais de aprendizado de máquina: OBIA e regra de voto majoritário (*majority vote* - MV). Os resultados mostraram que a classificação dos estádios sucessionais da vegetação, em geral, foi bem-sucedida, alcançando precisões acima de 80% quando empregados os dados do WV-2, e acima de 90% quando usados os dados hiperespectrais. O melhor resultado alcançou uma precisão global (*overall accuracy* - OA) de 99,28% usando os dados hiperespectrais associados ao CHM e ao classificador RF. O CHM e os atributos derivados dos dados do WV-2 e hiperespectrais aumentaram entre 5% e 13% a precisão da classificação. Em relação à classificação das espécies arbóreas, a CNN superou os classificadores RF e SVM em ambas as áreas, com uma OA de 84,4% na Área 1 e 74,95% na Área 2, utilizando apenas as bandas espectrais VNIR. Este método foi 22% a 26% mais preciso do que SVM e RF quando considerado apenas o conjunto de dados VNIR. A inclusão de atributos da PPC e do CHM levou a um significativo aumento na precisão da classificação de espécies arbóreas quando métodos de aprendizado de máquina foram aplicados (SVM, wSVM e RF), entre 13% e 17% dependendo do classificador e da área de estudo. No entanto, uma diminuição na OA foi observada quando esses atributos foram incluídos na classificação da CNN. A abordagem OBIA não aumentou a OA para o SVM, enquanto um pequeno aumento foi observado no algoritmo RF em comparação com o RF usando a classificação baseada em pixels. A abordagem MV, por outro lado, trouxe um aumento acentuado na precisão para ambas as áreas de estudo (5% para a Área 1 e 11% para a Área 2). Ao usar atributos derivados da PPC e o CHM, associadas à abordagem MV, os classificadores de aprendizado de máquina alcançaram precisões similares à CNN (82,52% para a Área 1 e 75,45% para a Área 2). O wSVM aumentou a precisão, não apenas de classes com menos amostras, mas também de algumas classes majoritárias na Área 2. Nenhum dos três métodos de delineamento de ITC alcançou um resultado adequado para todas as ITCs de referência. O método MRG tendeu a superssegmentar a maioria das ITCs, enquanto o itcIMG e o MCRC tenderam à sobressegmentação, ou então, não segmentaram algumas ITCs suprimidas sob o dossel. Com a inclusão do CHM na segmentação usando o MRG, e a fusão de segmentos homogêneos usando a distância Jeffries Matusita (JM), tanto visualmente quanto de acordo com métricas de avaliação, conseguiu-se um melhor delineamento das copas das árvores. Os resultados encontrados nesse estudo são relevantes para incentivar a conservação da Mata Atlântica, um bioma severamente ameaçado, otimizando o mapeamento e monitoramento de seus remanescentes florestais, e também para subsidiar ações no âmbito do Cadastro Ambiental Rural (CAR) no Brasil. Além disso, a metodologia pode ser usada para mapear espécies arbóreas específicas, como as ameaçadas de extinção, neste caso, *Araucaria angustifolia* e *Cedrela fissilis*.

Palavras-chave: Biodiversidade Tropical. Espectroscopia de Imageamento. Fotogrametria. WorldView-2. Delineamento de Árvores Individuais. Máquinas de Vetor de Suporte. Floresta Aleatória. Rede Neural Convolutacional.

## LIST OF FIGURES

	<u>Pg.</u>
Figure 2.1- Structure of a SVM classifier.....	25
Figure 2.2- Structure of a RF classifier.....	28
Figure 2.3- Structure of a CNN classifier.....	29
Figure 3.1- Methodological framework developed in this study.....	30
Figure 3.2- Study areas location. (A) Santa Catarina State and (B) Curitiba municipality (IBGE, 2019); (C) Google Earth image showing their location; (D) Area 1; (E) Area 2. ....	31
Figure 3.3- Distribution of the plots to identify the successional forest stages in both areas. ....	32
Figure 3.4 - Examples of forest cover of Area 1: (A-B) internal view, (C) external view; (D) aerial view using an UAV-RGB camera.....	33
Figure 3.5- Photos showing the weather conditions of the flight days. ....	37
Figure 3.6- Ground control points (GPPs) locations and an example of lime mark. ....	39
Figure 3.7- Dense photogrammetric point cloud (PPC) and digital surface model (DSM) of each area. ....	40
Figure 3.8- Digital terrain model (DTM) and digital surface model (DSM) generated from LiDAR data.....	41
Figure 3.9- Distribution of samples from forest successional stages over the Area 1 according to the input data.....	42
Figure 3.10- Tree species manually delineated as samples for both areas: UAV-RGB image with 4 cm spatial resolution and the corresponding crown in the hyperspectral images (used in this study). ....	43
Figure 3.11- Spatial distribution of the individual tree crown (ITC) samples over Area 1 (A) and Area 2 (B).....	45
Figure 3.12- Canopy height models (CHMs) used in this study.....	48
Figure 3.13- Illustration of the Precision and Recall (P&R) metric used as optimization function and evaluation metric.....	53

Figure 3.14- Methodological flowchart of successional forest stages classification using the OBIA approach.....	56
Figure 3.15- Methodological flowchart of tree species classification using machine learning methods (SVM, wSVM and RF), pixel-based and MV rule approaches. Example considering two species (sp1 and sp2).....	58
Figure 3.16- CNN architecture for Area 1 with 25 bands and 15 classes (14 tree species plus 'background' class).....	60
Figure 3.17- Methodological flowchart of tree species classification using the CNN method.....	60
Figure 4.1- MDG values reported as the Gini index of the feature selected for the forest successional stages classification according to the data.....	65
Figure 4.2- Mean reflectance (with standard deviation) of successional forest stages samples according to the data. A) Hyperspectral data; B) WV-2 data. .	66
Figure 4.3- Boxplots showing the distribution of CHM values of the successional stages samples used in each data. The central lines within each box are the medians. The box edges represent the upper and lower quartiles. Outliers are plotted individually. ....	67
Figure 4.4- <i>Kappa</i> and overall accuracy (OA) of successional forest stages classification for each classifier/dataset according to the data used. ....	68
Figure 4.5- F-measure of successional stages classes according to the data and classifier. The black bars indicate the minimum and maximum values varying according to the dataset.....	69
Figure 4.6- Classification maps using the hyperspectral data. A) Hyperspectral image (R14G23B4 composition) with the sample locations; B) SVM classifier associated with the VNIR dataset; C) SVM classifier associated with the VNIR_CHM_PPC dataset; D) RF classifier associated with the VNIR_CHM_MNF.....	70
Figure 4.7- Classification maps using the WV-2 data. A) WV-2 image (R3G8B5 composition) with the sample locations; B) SVM classifier associated with the VNIR dataset; C) SVM classifier associated with the VNIR_CHM dataset; D) RF classifier associated with the FSRF dataset. ....	71



Figure 4.8- Clearing areas highlighted in the hyperspectral data. A) Best classification result using the hyperspectral data (RF with VNIR_CHM_MNF dataset); B) Best classification result using the WV-2 data (RF with FSRF dataset). .....	72
Figure 4.9- Example of segmentation results for Area 1: A) and a) MRG_CHM result; B) and b) itcIMG result; C) and c) MCRC result.....	73
Figure 4.10 – Example of segmentation results for Area 2. A) MRG result; B) itcIMG result. ....	73
Figure 4.11- Details of segmentation results in Area 1 with reference ITCs highlighted in red color. (A) Reference and the MRG segmentation result; (B) Reference and the MRG_CHM result refined by the JM distance.....	75
Figure 4.12- Variable importance according to JM distance for each area.....	76
Figure 4.13- Mean reflectance (with standard deviation) of tree species classified in this study.....	77
Figure 4.14- Spectral profile mean of all tree species for Area 1 (A) and Area 2 (B). 77	
Figure 4.15- Boxplots showing the distribution of the PPC and the CHM values of the tree species samples in Area 1 (A, B) and Area 2 (C, D). The central lines within each box are the medians. The boxes edges represent the upper and lower quartiles. Outliers are plotted individually.....	79
Figure 4.16- Summary of the best results reached by each classifier/dataset/approach according to the study area.....	82
Figure 4.17- Differences in overall accuracy with the inclusion of features and approaches in relation to VNIR dataset, SVM and RF classifiers.....	84
Figure 4.18- F-measure of each tree species class for Area 1 according to the classifier. Black bars indicate the minimum and maximum values varying according to the dataset. ....	85
Figure 4.19- F-measure of tree species according to the best dataset result for each classifier in Area 1 considering the pixel approach.....	86
Figure 4.20- Difference in F-measure accuracy for each species and classifier according to the dataset/approach in relation to the pixel-based classification using the VNIR dataset in Area 1. ....	87

Figure 4.21- F-measure of each tree species class for Area 2 according to the classifier. Black bars indicate the minimum and maximum values varying according to the dataset. .... 89

Figure 4.22- F-measure of tree species according to the best dataset result for each classifier in Area 2 considering the pixel approach..... 90

Figure 4.23- Difference in F-measure accuracy for each species and classifier according to the dataset/approach in relation to the pixel-based classification using the VNIR dataset in Area 2. .... 91

Figure 4.24- Species-level recall and precision percentage accuracy across 36 classification models for Area 1. Precision is equivalent to user’s accuracy; recall is equivalent to producer’s accuracy. Higher precision relative to recall means the species has lower commission errors than omission errors..... 93

Figure 4.25- Species-level recall and precision percentage accuracy across 33 classification models for Area 2. Precision is equivalent to user’s accuracy; recall is equivalent to producer’s accuracy. Higher precision relative to recall means the species has lower commission errors than omission errors..... 94

Figure 4.26- F-measure of each tree species when either the SVM or wSVM were employed in relation to the number of pixel samples per class. Species ordered according to the number of pixel samples..... 95

Figure 4.27- Details of classification maps using the best dataset result for SVM, RF and CNN classifiers in Area 1. A) Reference samples; B) the SVM classifier (VNIR\_CHM\_PPC dataset) after the MV rule – the red circle shows missing ITCs of *Podocarpus*; C) OBIA associated with the RF classifier and the VNIR\_CHM\_PPC\_VI\_MNF dataset – the red circles show two missing ITCs of *Nectandra* and one of *Podocarpus*; D) the CNN classifier with VNIR dataset – the red circle shows one missing ITC of *Nectandra*; E)The SVM classifier associated with VNIR\_CHM\_PPC dataset in a pixel-based classification- the red circle shows missing ITCs of *Podocarpus*; F)The RF classifier associated with VNIR\_CHM dataset in a pixel-based classification- the red circles show two missing ITCs of *Podocarpus* and one of *Nectandra*. .... 97

Figure 4.28- Details of classification maps using the best dataset result for SVM, RF and CNN classifiers in Area 2. A) Reference samples; B) the SVM

classifier (VNIR\_CHM dataset) after the MV rule – the red circles show missing ITCs of *Nectandra* and a poorly detected ITC of *Campomanesia*; C) the RF classifier and the VNIR\_CHM dataset – the red circles show one missing ITC of *Nectandra*, one of *Erythrina*, and a poorly detected ITC of *Campomanesia*; D) the CNN classifier with the VNIR dataset – the red circles show one missing ITC of *Nectandra* and one of *Campomanesia*..... 98

Figure 4.29- Classification maps of Area 1: the SVM associated with the VNIR\_CHM\_PPC\_VI dataset and the MV rule; the CNN associated with the VNIR dataset..... 100

Figure 4.30- Percentage of tree species coverage area based on classification results of the SVM and CNN maps of Figure 4.29..... 100

Figure 4.31- Classification maps of Area 2: the SVM associated with the VNIR\_CHM dataset and the MV rule; the CNN associated with the VNIR dataset. .... 101

Figure 4.32- Percentage of tree species coverage area based on the classification results of the SVM and CNN maps of Figure 4.31. .... 101



## TABLE LIST

	<u>Pg.</u>
Table 2.1- Summary of studies exploring the forest successional stage classification with remote sensing data. ....	13
Table 2.2- Summary of studies exploring tree species classification using hyperspectral data. Works developed in tropical or subtropical forests are highlighted in gray. Those combining hyperspectral + LiDAR data contain the point density information at the 'Spatial resolution' column. ....	15
Table 3.1- Structural characteristics of each plot regarding its successional forest stage.....	33
Table 3.2- Tree species and their successional group identified in both areas.	34
Table 3.3- Description of VNIR bands used in this study. ( $\lambda$ = central wavelength of the spectral band).....	36
Table 3.4- Strip sizes and overlap of each area. ....	36
Table 3.5- Characteristics of the camera, flight and data acquired in the study areas. ....	36
Table 3.6- Spectral bands and spatial resolution of WorldView-2 data. ....	37
Table 3.7- Characteristics of the flight and LiDAR data acquired over the study areas. ....	38
Table 3.8- Number of samples collected for each forest successional stage according to the data for Area 1. ....	42
Table 3.9- Number of ITCs and pixels for each tree species used in the classification process. ....	44
Table 3.10- Texture features computed in this study for hyperspectral and WV-2 data. ....	46
Table 3.11- Vegetation indices extracted from hyperspectral (hyper) and WorldView-2 (WV-2) data.....	47
Table 3.12- Features extracted from the high density photogrammetric point clouds.....	49
Table 3.13- Description of the datasets according to the features used in the classification process. Hyperspectral (Hyper) and WorldView-2 (WV-2) data. .	51

Table 3.14- Segmentation parameters of multiresolution region growing (MRG) algorithm used in successional forest stages classification. ....	52
Table 3.15- Final parameters chosen for MRG and itcIMG segmentation methods.....	54
Table 3.16- Metrics used to evaluate the ITC delineation. ....	55
Table 4.1- Evaluation metrics for each segmentation result according to the study area.....	75
Table 4.2- Classification results according to the area/classifier/dataset/approach. Best result for each classifier/approach is highlighted. <sup>1</sup> Best results for each area that does not significantly differ among themselves. ....	80
Table 4.3- Summary of classifiers, approaches, datasets and accuracies related to tree species classification in both areas. ....	81
Table A1- Confusion matrices of successional forest stages classification using WV-2 data. ....	154
Table A2- Confusion matrices of successional forest stages classification using Hyperspectral data. ....	156
Table B.1- Confusion matrices using the SVM algorithm in Area 1. ....	158
Table B.2- Confusion matrices using the wSVM algorithm in Area 1. ....	165
Table B.3- Confusion matrices using the RF algorithm in Area 1. ....	167
Table B.4- Confusion matrices using the CNN algorithm in Area 1. ....	173
Table B.5- Confusion matrices using the SVM algorithm in Area 2. ....	175
Table B.6- Confusion matrices using the wSVM algorithm in Area 2. ....	180
Table B.7- Confusion matrices using the RF algorithm in Area 2. ....	181
Table B.8- Confusion matrices using the CNN algorithm in Area 2. ....	185

## ABBREVIATIONS LIST

AFI	Area Fit Index
ANN	Artificial Neural Network
AOP	Airborne Observation Platform
APEX	Airborne Prism EXperiment
C	Segmentation covering
CAR	Cadastral Ambiental Rural
CHM	Canopy Height Model
CNN	Convolutional neural network
DBH	Diameter at breast height
DSM	Digital Surface Model
DTM	Digital Terrain Model
FPI	Fabry-Perot interferometer
FS	Feature selection
GA	Genetic Algorithm
GLCM	Gray-level co-occurrence matrix
GNDVI	Green Normalized Vegetation Index
ITC	Individual tree crown
JM	Jeffries Matusita
KNN	K-nearest neighbor
LiDAR	Light Detection and Ranging
LOO	Leave-One-Out
MCRC	Multiclass Cut followed by Recursive Cut
MDA	Multiple Discriminant Analysis
MDG	Mean decrease in Gini index
MLC	Maximum Likelihood Classifier
MLP	Multilayer Perceptron
MNF	Minimum Noise Fraction
MOF	Mixed Ombrophilous Forest
MRG	Multiresolution region growing
MV	Majority-vote
NDVI	Normalized Difference Vegetation Index
NEON	National Ecological Observation Network
OA	Overall accuracy
OBIA	Object-based image analysis
OOB	Out-of-bag
OSAVI	Optimized Soil Adjusted Vegetation Index
P&R	Precision and Recall
PLSDA	Discriminant Analysis based on Partial Least Square
PPC	Photogrammetric point cloud
PSRI	Plant senescence reflectance index
PSSR	Pigment specific simple ratio
QDA	Quadratic Discriminant Analysis
RDA	Regularized Discriminant Analysis

ReLU	Rectified linear unit
RF	Random Forest
SAR	Synthetic Aperture Radar
SC	Santa Catarina
SPT	Segmentation Parameter Tuner
SR	Simple Ratio
SVM	Support Vector Machine
UAV	Unmanned aerial vehicle
USA	United States of America
VANT	Veículo aéreo não-tripulado
VI	Vegetation Index
VNIR	Visible/near-infrared
wSVM	Weighted SVM
WV-2	WorldView-2



## SUMMARY

	<u>Pg.</u>
1 INTRODUCTION .....	1
1.1 Hypotheses .....	6
1.2 Objectives .....	7
1.2.1 Main Objective .....	7
1.2.2 Specific Objectives .....	7
2 THEORETICAL BACKGROUND .....	9
2.1 Successional forest stages and the Mixed Ombrophilous Forest .....	9
2.2 Studies on forest and tree species mapping from remote sensing data ....	12
2.3 Segmentation and individual tree crown delineation .....	17
2.4 Feature extraction and feature selection .....	20
2.5 Image classification .....	23
2.5.1 Support vector machine .....	24
2.5.1.1 Weighted support vector machine .....	26
2.5.2 Random forest .....	27
2.5.3 Convolutional neural network .....	28
3 MATERIAL AND METHODS .....	30
3.1 Study areas .....	31
3.2 Field surveys .....	32
3.3 Input data .....	35
3.3.1 UAV-hyperspectral and PPC data .....	35
3.3.2 WorldView-2 data .....	37
3.3.3 LiDAR data .....	37
3.4 Data preprocessing .....	38
3.4.1 Hyperspectral data .....	38
3.4.2 WorldView-2 data .....	40
3.4.3 LiDAR data .....	41
3.5 Sample collection .....	42
3.6 Feature extraction .....	45
3.7 Feature selection and variable importance .....	49

3.8 Dataset composition .....	50
3.9 Segmentation and ITC delineation.....	51
3.10 Successional forest stages classification .....	55
3.11 Tree species classification .....	56
3.11.1 Machine learning methods .....	57
3.11.2 Deep learning method.....	58
3.12 Accuracy assessment and classification maps .....	60
4 RESULTS .....	64
4.1 Successional forest stages mapping .....	64
4.1.1 Feature selection and variable importance.....	64
4.1.2 Classification results.....	67
4.1.3 Classification maps .....	70
4.2 Tree species mapping.....	72
4.2.1 Individual tree crown delineation .....	72
4.2.2 Feature selection and variable importance.....	75
4.2.3 Classification results.....	80
4.2.3.1 Overall results .....	80
4.2.3.2 Tree species classification accuracies in Area 1 .....	84
4.2.3.3 Tree species classification accuracies in Area 2.....	88
4.2.3.4 Species prediction errors and imbalanced sample set.....	92
4.2.4 Tree species maps .....	96
5 DISCUSSION .....	102
5.1 Considerations about the successional forest stages classification .....	102
5.2 Considerations about the ITC delineation .....	106
5.3 Considerations about variable importance and tree species classification using machine learning methods.....	109
5.4 Considerations about tree species classification using the deep learning method .....	117
5.5 Considerations about the number of ITC samples, tree species classes and evaluation method .....	121
5.6 Considerations about the use of UAV-borne data.....	123
6 CONCLUSION AND FUTURE STUDIES .....	125

REFERENCES.....	129
APPENDIX A – CONFUSION MATRICES OF SUCCESSIONAL FOREST STAGES CLASSIFICATION .....	154
APPENDIX B – CONFUSION MATRICES OF TREE SPECIES CLASSIFICATION.....	158



## 1 INTRODUCTION

Tropical forests are among the most complex ecosystems on Earth. Hosting an overwhelming proportion of global tree diversity, approximately 53,000 tree species in contrast to only 124 across temperate Europe (SLIK et al., 2015), they play a crucial role in biodiversity conservation and in ecological dynamics at global scale (ZHANG Z. et al., 2016).

According to Viana and Tabanez (1996), the Atlantic Rain Forest (*Mata Atlântica*) is one of the most endangered tropical biomes in the world. Current estimates of remaining vegetation cover range from 16% (RIBEIRO et al., 2009) to 28% (REZENDE et al., 2018). This biome has been particularly affected by anthropogenic disturbances, such as industrial activities, urbanization, and agricultural expansion, which transformed it in an archipelago of different successional forest stages patches embedded into a mosaic of degraded areas, pasture, agriculture, forestry, and urban areas (JOLY et al., 2014).

The natural regeneration of abandoned areas can improve the provision of ecosystem services and habitat availability (STRASSBURG et al., 2016). However, more information is needed regarding how these forests recover during secondary succession, to enable the estimation of the ecosystem services that it provides (WORLD RESOURCES INSTITUTE, 2005). Currently, one of the major challenges for conservation is to obtain reliable and accurate information on a large scale to monitor biodiversity, resources, as well as the human impact on natural ecosystems (WAGNER et al., 2019). Remote sensing is considered an effective means for this effort, not only because of the increased spatial and temporal resolutions of the datasets, which enable identifying elements of biodiversity, such as tree species, but also because of the increase in available data and in the associated computational capacity to process such data (GHOSH et al., 2014; HE et al., 2015; KWOK, 2018).

During the last years, significant efforts have been made to map forest cover and its changes, mainly based on medium spatial resolution data, and a 1-year temporal resolution, such as the Global Forest Change map (HANSEN et al., 2013) and project MapBiomass specifically for Brazil (MAPBIOMASS, 2018). Such

resolution has revealed that fragmentation is increasing in all tropical forests (TAUBERT et al., 2018). However, it is still too coarse to retrieve information regarding species or the distribution of individual trees that can inform on the successional stage, diversity or disturbance levels of these ecosystems, which play key roles in maintaining environmental processes such as the water cycle, soil conservation, carbon sequestration and habitat protection (FAO, 2016).

In this regard, the improvement of the spatial resolution of the remote sensing sensors in the last decades enables the identification of isolated trees even in dense forest canopies. Hyperspectral sensors mounted on manned aircrafts, for instance, could provide data at both high spatial and spectral resolution, being extensively used in tree species classification in different environments, as tropical (CLARK et al., 2005; CLARK; ROBERTS 2012; FERÉT; ASNER, 2013; BALDECK et al., 2015; FERREIRA et al., 2016; SHEN; CAO, 2017), temperate or boreal forests (DALPONTE et al., 2012; 2013; 2014; GHOSH et al., 2014; RACZKO; ZAGAJEWSKI, 2017; MASCHLER et al., 2018) and savannas (CHO et al., 2012; COLGAN et al., 2012; NAIDOO et al., 2012; PIIROINEN et al., 2017).

Recently, small-format hyperspectral cameras on-board unmanned aerial vehicles (UAV) have been on the spotlight and they began to be explored for tree species classification in boreal (NEVALAINEN et al., 2017; TUOMINEN et al., 2018) and subtropical forests (SOTHE et al., 2019a). Compared to satellite and airborne manned data acquisition, UAV-borne methods have many advantages, such as the possibility to collect data even under poor imaging conditions, e.g., under cloud cover, which makes it very operational in a wide range of environmental measuring applications (HONKAVAARA et al., 2013); the cost-efficient data collection with the desired spatial and temporal resolutions; and the non-dependence on airports for take-off, or satellite availability in the desired area (PANEQUE-GÁLVEZ et al., 2014). As they operate at a lower flight height than conventional aerial platforms, they offer a finer spatial resolution (NEVALAINEN et al., 2017).

Besides the high spatial resolution and a considerable number of spectral bands, UAV-borne sensors operating in frame-format record spectral data in two spatial dimensions within every exposure, opening new ways of imaging spectroscopy (AASEN et al., 2018), in which spectral and 3D information can be retrieved from the same data and to compose (hyper)spectral digital surface models (HONKAVAARA et al., 2013; AASEN et al., 2015). This 3D information can capture differences in vertical structure among species (i.e. tree height, tree patterns and leaf distributions) (NÄSI et al., 2015; TUOMINEN et al., 2018) that can be useful for tree species classification. In fact, many studies have shown some improvement in accuracy when integrating multispectral or hyperspectral data with 3D information (i.e. acquired from Light Detection and Ranging-LiDAR data or from a photogrammetric point cloud - PPC) for successional forest stages (SOTHE et al., 2019b) or tree species classification (DALPONTE et al., 2012; GHOSH et al., 2014; BALDECK et al., 2015; PIIROINEN et al., 2017; TUOMINEN et al., 2018; SOTHE et al., 2019a). This combination allows to obtain a richer description of the vegetation analyzed, as their information are complementary to each other (GHOSH et al., 2014), but until now it has been poorly explored in tropical forests.

A fact that must be considered when dealing with very high spatial resolution data, as those acquired by UAV, is the existence of the intra-class variability. In this case, the presence of noise, differences in lighting conditions and spectral variability within the canopies of successional stages and tree species may negatively affect the classification results when the pixel is considered the classification unit (YU et al., 2006; PIAZZA et al., 2016). The intra-class variability of such data can be accommodated into segments, generated previously to the classification process, conducting the classification as an object-based image analysis (OBIA). In the case of tree species classification, OBIA approaches usually consider an individual tree crown (ITC) as the classification unit, which can reduce the negative effects of spectral variability of pixels inside the crowns (HEINZEL; KOCH, 2012), such as branches, presence of lianas, background, shadow, among others. In this sense, many studies showed that the classification of tree species at the ITC level using OBIA or

accommodating a pixel classification into segments with a majority vote rule (MV) procedure has proved to be more accurate than that executed at a pixel scale (CLARK et al., 2005; CLARK; ROBERTS, 2012; DALPONTE et al., 2013; FÉRET; ASNER, 2013). Furthermore, a classification map at an ITC level may be more easily related to the biophysical and biochemical properties of the species and has practical applications in studies of individual trees (DALPONTE et al., 2014; SHEN; CAO, 2017).

In fact, the delineation of ITCs not only helps the classification process, but also is a prerequisite for individual tree inventory over large spatial extents (CLARK et al., 2005), providing information such as tree count, location, crown size, distance between individuals, and tree species (FASSNACHT et al., 2016). Regarding that, numerous algorithms exist for automatic ITC delineation, but most of them have been developed for temperate or boreal forest stands (KE; QUACKENBUSH, 2011; DUNCANSON et al., 2014; DALPONTE et al., 2015a; LEE et al., 2016) and their application to deciduous and tropical forests has proven to be much more challenging (FÉRET; ASNER, 2013; TOCHON et al., 2015; FERREIRA et al., 2016; WAGNER et al., 2018). In a review study made by Zhen et al. (2016), they related that most of the published studies involving the ITC delineation are concentrated in coniferous forests (40.6%), because most algorithms assume a basic conical crown shape, which is more appropriate for conifers. Only 21.7% of the studies were in closed mixed forests and barely 6% in closed hardwood forests. Deng et al. (2016) reported that ITC delineation algorithms tend to have lower precision when applied to more structurally complex forests, especially multi-stratified ones with overlapping or interconnected canopies, such as tropical forests. Therefore, it is still necessary to explore the ITC delineation methods in tropical forests.

Besides the data and the classification level approach, a proper choice of the classification method is also decisive for a successful land use/ land cover mapping (LU; WENG, 2007). In this respect, machine learning algorithms, such as support vector machine (SVM) and random forest (RF), have been on the spotlight for tree species classification over the last years (DALPONTE et al., 2012; GHOSH et al., 2014; BALDECK et al., 2015; BALLANTI et al., 2016;



FERREIRA et al., 2016; PIIRONEN et al., 2017; FRANKLIN; AHMED, 2017; MASCHLER et al., 2018; FERREIRA et al., 2019; SOTHE et al., 2019a). These methods are considered robust and work well in the presence of a wide range of class distributions (ANDRADE et al., 2014) and with high dimensionality and multisource data (GHOSH et al., 2014).

Nevertheless, even with the availability of high spectral and spatial resolution data and robust classifiers, it is observed that studies involving tropical forests have been limited to the classification of three to eight dominant canopy species e.g., (CLARK et al., 2005; CLARK; ROBERTS, 2012; BALDECK et al., 2015; FERREIRA et al., 2016; SHEN; CAO, 2017). Among the issues that hamper the classification of a high number of tree species in such environments, the presence of dominant and minority classes is to be mentioned, resulting in an imbalanced sample set, in which only a small number of samples are available for the less often found tree species (MELLOR et al., 2015). In this case, sampling the natural abundance of species would lead to highly skewed samples size across classes, while increasing the sample size of rare species would be time-consuming and costly (GRAVES et al., 2016). Concerning this, some approaches relying on machine learning have been adapted to deal with small or imbalanced sample sets (DALPONTE et al., 2015; GRAVES et al., 2016; NGUYEN, 2019). Dalponte et al. (2015) proposed a semi-supervised SVM to combine the information from both labeled and unlabeled sets as a way to increase the number of samples. Graves et al. (2016) investigated the imbalanced classes problem with two strategies: i) creating a dataset where every class has the same amount of training samples, equal to the number of samples of the smallest class; and ii) allowing different cost parameters for each class while using the SVM classifier. Nguyen et al. (2019) proposed a weighted SVM (wSVM) method specifically developed to solve the problems of unbalancing, unreliability, and size of the training sets for tree species classification at an ITC level.

Although conventional machine learning methods are very well established in literature, these methods are based on hand-engineered features, and are thus highly dependent on domain knowledge (LI Y. et al., 2017). Recently, deep

learning has been introduced into hyperspectral images classification and is able to extract deep spatial and spectral features from hyperspectral data (SIGNORONI et al., 2019). Much of the pioneering work on deep learning applied to hyperspectral data classification has given evidence that the identification of deep features leads to higher classification accuracies for hyperspectral data (CHEN et al., 2014; LI W. et al., 2017; WAGNER et al., 2019). Among these methods, the convolutional neural network (CNN) algorithm is a supervised deep learning model that has been producing promising results in the classification of remotely sensed images (YUE et al., 2015; LI Y. et al., 2017; WANG et al., 2017; GAO et al., 2018), including tree species classification purposes in particular (PÖLÖNEN et al., 2018; FRICKER et al., 2019; HARTLING et al., 2019). Despite its great potential, there are no studies involving CNN for tree species classification in tropical or subtropical forests. Hereafter this study uses the term ‘machine learning’ to refer to conventional machine learning approaches that do not rely on deep learning.

## **1.1 Hypotheses**

This work is based on the following hypotheses:

- a) The successional forest stages can be well discriminated with both multispectral (WV-2) and hyperspectral data associated with machine learning methods.
- b) The integration of 3D features derived from the PPC and the 2D hyperspectral data improves the successional stages and tree species classification.
- c) The use of UAV-based PPC or hyperspectral data is effective for ITC delineation in subtropical forests.
- d) The use of ITC as a classification unit (i.e. OBIA or the MV rule) increases the tree species classification accuracies of machine learning methods in relation to the pixel-based classification.

- e) Classifiers dealing with the imbalanced samples can increase the accuracy of less represented tree species classes.
- f) Different of machine learning methods, the CNN algorithm can effectively classify tree species without the need of hand-engineered features with comparable accuracy indices.

## **1.2 Objectives**

### **1.2.1 Main objective**

The main goal of this study is to evaluate the exclusive and combined use of multisource data (i.e. WV-2, LiDAR, UAV-hyperspectral and UAV-based PPC) associated with machine learning methods and OBIA for the classification of successional forest stages of a mixed Atlantic Rain Forest area, and to evaluate the pure and combined use of multisource data (i.e. UAV-hyperspectral and UAV-based PPC) associated with machine and deep learning methods for the classification of a large number of tree species.

### **1.2.2 Specific objectives**

- a) To compare two machine learning methods (SVM and RF) and multisource data (UAV-hyperspectral data and UAV-based PPC; and WV-2 and LiDAR data) for the classification of successional forest stages.
- b) To test UAV-hyperspectral images and their integration with 3D features derived from the PPC for ITC delineation and tree species classification.
- c) To test a different SVM approach focused on an imbalanced sample set (wSVM) for tree species classification.
- d) To test a deep learning architecture based on CNN for tree species classification.

- e) To compare the results of the above-mentioned classifications with conventional classification methods, SVM and RF.
- f) To compare different classification approaches, per-pixel, OBIA and the MV rule, associated with machine learning methods for tree species classification.

## 2 THEORETICAL BACKGROUND

### 2.1 Successional forest stages and the Mixed Ombrophilous Forest

Tropical forests can be roughly grouped into categories of primary forest and successional forests. Primary forest corresponds to a forest that is barely disturbed by natural disasters or human activities (LU et al., 2003). Successional forest is defined as a regrowth forest following a disturbance such as deforestation, in which secondary succession describes the changes of plants that live in a particular community over time (FINEGAN, 1984). Due to the importance and different capability of successional forests in restoration of degraded moist tropical environments, accurately differentiating them into different stages is valuable to better understand their role and their relationships with ecosystem changes (LU et al., 2003).

The Mixed Ombrophilous Forest (MOF) is a phytophysiology of the Atlantic Rain Forest and one of the main formations in the southern region of Brazil (HIGUCHI et al., 2012). It is characterized by a heterogeneous formation of vegetation with primitive genera such as *Drimys*, *Araucaria* (Australasian) and *Podocarpus* (Afro-Asian), being *Araucaria angustifolia* a physiognomic marker of this forest type (BACKES; NILSON, 1983). The MOF designation originates from the phytogeographic classification of Veloso et al. (1991), who named as "Ombrophilous" the characteristic formations of humid environments and used the term "Mixed" to refer to the formation composed both by species originated in the temperate region, such as Andina, and the tropical region (VELOSO et al., 1991). Currently, the MOF is considered one of the most threatened phytophysionomies among the country's forest formations, remaining only 24.4% of its original cover in Santa Catarina (SC) (VIBRANS et al., 2013). Most of its remnants are composed of small isolated fragments (<50 ha) of secondary forests in early and intermediate forest stages (RIBEIRO et al., 2009).

The Resolution of the Brazilian Council for the Environment (*Conselho Nacional do Meio Ambiente* – CONAMA) nº 04/1994 (BRASIL, 1994) determines the observation of a set of qualitative and quantitative (structural) criteria and

indicators for the characterization of secondary vegetation in the early, intermediate and advanced stages for the SC state, which includes the MOF. Among the criteria mentioned in the Resolution, there are characteristics related to vegetation size, such as tree height, diameter at breast height (DBH) and basal area; forest formation characteristics, such as the number of strata, presence of epiphytes and lianas, litter thickness; and the floristic composition. The characterization of each stage according to the current Brazilian Laws is described as follows:

- a) Early successional stage ( $SS_1$ ): also called a pioneer stage, the vegetation is dominated by shrubs, herbs and grasses, with less diversity of species. This stage usually lasts between 6 and 10 years, depending on the degree of degradation of the soil, and the environment. The average height of the vegetation does not exceed 4 m, and the average diameter in the DBH reaches a maximum of 8 cm. In general, it has a small number of woody species, it presents a low complexity of vegetation structure and the occurrence of vascular epiphytes is rare.
- b) Intermediate successional stage ( $SS_2$ ): this stage can occur between 6 and 15 years after the area has been abandoned. The diversity increases, there is a greater number of woody trees than shrubs and herbs, with predominance of pioneer tree species. The average stage is characterized by moderate diameter amplitude, ranging from 8 to 15 cm DBH and height up to 12 m. Vascular epiphytes are present in greater number than the previous stage and the litter layer presents different thickness. It represents a stage of transition between the early and advanced stages.
- c) Advanced successional stage ( $SS_3$ ): at this stage, the woody tree physiognomy is dominant over the others, forming a closed and relatively uniform canopy, presenting dominant trees. The average height of the vegetation is over 12 m, and the DBH mean varies from 15 to 25 cm. In this physiognomy, there is a predominance of woody

species, with complexity in the vegetation structure and great diversity of species. Vascular epiphytes are found in abundance, woody creepers are well developed, and there is a thick layer.

Indicative species of each successional stage are defined according to their ecological group (pioneers, early or late secondary, and climax) (BUDOWSKI, 1965). The species are assigned to one of these ecological groups according to the strategy adopted in the forest dynamics, which can be determined by their tolerance or not to luminosity. In this case, for instance, the predominance of species considered pioneers or early secondary could serve as an indicator that the fragment is in the early or secondary successional stage. However, one must consider that some tree species may belong to different successional groups. Different altitudinal levels indicate relevant floristic differences for each of the sub-formations of the ombrophilous forest, and therefore, the pattern of indicator species is not uniform (VELOSO et al., 1991; RODERJAN et al., 2002; BLUM; RODERJAN, 2007). In addition, edaphic variations in the environment promote differences in the structure and composition of mature and secondary forests, reflecting on different indicator species even for close environments (VELOSO; KLEIN, 1961; CLARK et al., 1999; FINEGAN; DELGADO, 2000; RODERJAN et al., 2002). Therefore, the species that are socially more important in the community structure permeate different successional stages (SIMINSKI et al., 2011), making it difficult to use this as a criterion to define the successional stage (ANDREACCI; MARENZI, 2017).

Studies made by Higuchi et al. (2012) and Manfredi et al. (2015) highlighted the predominant species of MOF environments in SC. They pointed out that this phytophysognomy is characterized not only by the remarkable presence of *Araucaria angustifolia*, which is already a common sense, but also by an important set of typical broadleaf species, such as *Matayba elaeagnoides*, *Ocotea pulchella*, *Lamanonia ternata* and *Lithraea brasiliensis*. Although it is one of the most important species of this environment, araucaria trees are diminishing rapidly in their natural habitat and therefore they are categorized as “Critically endangered” according to the “List of Threatened Species” of the

International Union for Conservation of Nature (IUCN, 2017). Another endangered species of MOF is *Cedrela fissilis*, classified as “vulnerable” according to the IUCN red list.

## **2.2 Studies on forest and tree species mapping from remote sensing data**

The potential of remote sensing for vegetation mapping was verified in the 1980s, when the first images with a high spectral resolution were obtained (GOETZ; VANE, 1985). In the last decades, there was a remarkable advance in space technologies for forest resources monitoring. The recent refinement of both spatial and spectral settings of orbital sensors and the increased improvement in the classification algorithms have strengthened the use of remote sensing data as a source for land cover and land use mapping (ADAM et al., 2014). Remote sensing data is considerably more advantageous when compared to conventional *in situ* mapping, not only because these data are systematically acquired, allowing their application at large scales, but also because they involve a less capital- and labor-intensive acquisition (JANOTH et al., 2007).

On the last decades, several authors have committed themselves to characterize and classify successional stages of vegetation using remote sensed imagery (Table 2.1). At this level, recent efforts show that even when using medium spatial resolution images one can reach accuracies over 90% when machine learning methods are applied. Despite the optimistic results, until now there are no studies exploring very high spatial resolution images acquired by orbital satellites (such as WV-2 and WV-3) or UAV-borne data for this purpose. This is an interesting topic to be studied, since medium spatial resolution data may not capture different successional stages of very small forest fragments, which is a common reality in MOF environments.



Table 2.1- Summary of studies exploring the forest successional stage classification with remote sensing data.

Study	Sensor	Spatial resolution	Forest/ Country	Classifier	Best accuracy (%)
Vieira et al. (2003)	ETM/Landsat7	30 m	Tropical Forest, Brazil	Non reported	81
Amaral et al. (2009)	CBERS-2, IRS-P6 e Quickbird	20, 6 and 0.61 m	Tropical Forest, Brazil	MLC and Mahalanobis distance	54
Galvão et al. (2009)	CHRIS/PROBA	40 m	Tropical Forest, Brazil	MDA	82
Falkowski et al. (2009)	Optech ALTM30 (LiDAR)	0.26 points.m <sup>2</sup>	Temperate Mixed-conifer Forest, USA	RF	95
Li et al. (2011)	TM/Landsat5	30 m	Tropical Forest, Brazil	MLC, ANN, CTA, OBC	82.8
Castillo et al. (2012)	LVIS	Non reported	Tropical Dry Forest, Costa Rica	ISODATA	-
Lu et al. (2012)	TM/Landsat5 ALOS Palsar	30 m	Tropical Forest, Brazil	MLC	85.9
Berveglieri et al. (2016)	Dense DSM generated from stereoscopic optical images	0.45 m	Subtropical Forest, Brazil	Local height variance from the DSM	-
Piazza et al. (2016)	SAAPI orthoimages	0.39 m	Subtropical Forest, Brazil	Decision tree C4.5	91
Sothe et al. (2017a)	OLI/Landsat 8 and RapidEye	15 and 5 m	Subtropical Forest, Brazil	MLC, SVM and RF	90.8
Sothe et al. (2017b)	OLI/Landsat8 and Sentinel-2	15 and 10 m	Subtropical Forest, Brazil	SVM and RF	98.4
Zhang et al. (2017)	Leica ADS-40	0.4 m	Boreal Mixed Forest, Canada	RF	89
Pinto (2018)	CMOS 20MP	0.33 m	Tropical Forest, Brazil	RT	88
Bispo et al. (2019)	TanDEM-X	-	Tropical Forest, Brazil	MLC	87

Note: DSM= Digital Surface Model; MDA= Multiple Discriminant Analysis; MLC= Maximum Likelihood Classifier; RF= Random Forest; RT= Random Tree; SVM= Support Vector Machine.

Source: Author's production.

Not only the successional forest stages, but also mapping tree species distributions in tropical landscapes has been a major goal of the remote sensing community (NAGENDRA, 2001), due to its relevance in forest management and conservation sectors. It includes ecological applications for understanding spatial patterns of tree populations and species co-occurrence (COLGAN et al., 2014), conservation applications to identify regions of high diversity (LUCAS et al., 2008; GRAVES et al., 2016), invasive species (USTIN et al., 2002; HE et

al., 2011; KHARE et al., 2019), rare and ecologically important species (CLARK et al., 2005), and questions linked to resource inventories (VAN AARDT; WYNNE, 2007). High spatial resolution imaging spectroscopy, that can discriminate individual tree crowns and capture small differences in reflectance patterns among species, is pointed as the most suitable data to achieve these goals (NAGENDRA et al., 2008; FASSNACHT et al., 2016).

Mainly since the beginning of the 2010s, hyperspectral sensors have been on the spotlight for the classification of tree species in different forest types (Table 2.2). Nevertheless, research on tree species classification using hyperspectral for tropical environments is not so widespread (FASSNACHT et al., 2016). Among the first studies involving tree species classification in these environments, Clark et al. (2005) should be mentioned, who have applied reflectance of narrow bands of hyperspectral data to classify seven tree species at leaf, pixel, and tree crown levels respectively. Later, Clark and Roberts (2012) studied the potential of vegetation indices, absorption based metrics and spectral derivative metrics in improving classification accuracy of their previous study. Another pioneer study involving tree species classification in tropical forests was made by Féret and Asner (2013) using airborne hyperspectral data for the classification of 10 to 17 tree species. They pointed out that the accuracy was gradually reduced as the number of tree species for classification increased. Indeed, a particular challenge for operational species mapping in tropical forest ecosystems is the high species diversity, which requires identifying many species, most of them have few individuals in the landscape (GRAVES et al., 2016).

At the foliar level, the interaction of electromagnetic radiation with vegetation is basically controlled by three parameters: pigment concentration, structure and amount of water (GATES et al., 1965). Therefore, different species have very similar spectral behavior. The basic condition that must be satisfied to discriminate tree species is that the intraspecific variability is significantly smaller than the interspecific variability. In tropical forests, the verification of this condition is essential to evaluate the potential of reflectance data, in particular hyperspectral data, for species discrimination. Since it is rarely satisfied when

dealing with a large number of tree species and few samples, the combination of hyperspectral data with 3D features can be of great value to improve the discrimination of tree species classes. These features can provide other information besides the spectral characteristics, such as height, crown shape and species structure.

At Table 2.2 it can be noticed that studies exploring the combination of hyperspectral and 3D features (i.e. derived from LiDAR or PPC) are concentrated in temperate or boreal forests, as also indicated in the review paper elaborated by Fassnacht et al. (2016). So, it is necessary to explore the inclusion of such features as a means to improve the classification accuracy when studying a large number of tree species in tropical forests.

Table 2.2- Summary of studies exploring tree species classification using hyperspectral data. Works developed in tropical or subtropical forests are highlighted in gray. Those combining hyperspectral + LiDAR data contain the point density information at the 'Spatial resolution' column.

Study	Sensor	Spatial resolution (m)	Spectral resolution	Forest/ Country	Classifier	Number of species	Best accuracy (%)
Clark et al. (2005)	HYDICE	1.6	VNIR-SWIR (400–2500 nm; reduced to 30 bands selected)	Tropical Forest, Costa Rica	LDA, MLC, SAM	7	92
Jones et al. (2010)	AISA Dual	2 (0.4 points/m <sup>2</sup> )	VNIR-SWIR (429–2400 nm, reduced to 40 spectral bands)	Boreal Forest, Canada	SVM	11	72
Clark; Roberts (2012)	HYDICE	1.6	VNIR-SWIR (400–2500 nm; 210 bands)	Tropical Forest, Costa Rica	RF	7	87
Cho et al. (2012)	CAO Alpha	1.1	VNIR (384–1054 nm; 72 bands)	Savanna, South Africa	MLC	6	65
Dalponte et al. (2012)	AISA Eagle, GeoEye and ALS Optech ALTM	1 and 0.5 (8.6 and 0.48 points/m <sup>2</sup> )	VNIR (400–990 nm; 126 bands)	Temperate Forest, Italy	SVM e RF	7 species + non forest class	74
Naidoo et al. (2012)	CAO Alpha System	1.1 (1.3 point/m <sup>2</sup> )	VNIR (348-1054 nm, 72 bands)	Savanna, South Africa	RF	8	87.7

continue

Table 2.2- Continuation.

Study	Sensor	Spatial resolution (m)	Spectral resolution	Forest/Country	Classifier	Number of species	Best accuracy (%)
Ferét; Asner (2013)	CAO Alpha	0.56	VNIR (390–1044 nm; 24 bands)	Tropical Forest, Hawaii	LDA, QDA, RDA, KNN, ANN and SVM	17	73
Dalponte et al. (2014)	HySpex VNIR-160 and ALS Optech ALTM	0.4 (7.4 point/m <sup>2</sup> )	VNIR (410-990 nm, 160 bands)	Boreal Forest, Norway	SVM	2 species + mixed class	93
Ghosh et al. (2014)	HyMap and Hyperion	4, 8 and 30 (12 point density)	VNIR-SWIR (450-2500 nm, 128 bands)	Temperate Forest, Germany	SVM and RF	5	86
Baldeck and Asner (2015)	CAO AToMS	1.12	VNIR-SWIR (380–2512 nm, 167 bands)	Tropical Forest, Panama	Single-class SVM	3	94
Ferreira et al. (2016)	ProSpecTIR-VS	1	VNIR-SWIR (450-2400 nm, 357 bands)	Subtropical Forest, Brazil	LDA, SVM and RF	8	84.9
Ballanti et al. (2016)	AISA Eagle and Leica ALS60	2 (4 and 8 points/m <sup>2</sup> )	VNIR (397.78–997.96 nm, 128 bands)	Temperate Forest, USA	SVM and RF	8	90
Richter et al. (2016)	AISA dual	2	VNIR-SWIR (400- 2497 nm, 267 bands)	Temperate Forest, Germany	SVM, RF and PLSDA	10	78.4
Graves et al. (2016)	CAO AToMS	2	VNIR-SWIR (380–2512 nm)	Tropical Forest, Panama	SVM imbalanced	20 species + 1 mixed class	63
Nevalainen et al. (2017)	UAV-FPI	0.086	VNIR (507-819 nm, 33 bands)	Boreal Forest, Finland	RF, MLP, C4.5, KNN	4	95
Piironen et al. (2017)	AISA Eagle and Optech ALTM 300	1 (9.6 points/m <sup>2</sup> )	VNIR (400-1000 nm, 129 bands)	Agroforestry, Kenya	SVM and RF	31	57.1
Raczko; Zagajewski (2017)	APEX	3.35	VNIR-SWIR (413-2447 nm, 288 bands)	Temperate Forest, Poland	ANN, SVM and RF	5	77
Shen; Cao (2017)	AISA Eagle and RIEGL LMS-Q680i	0.6 (10 points/m <sup>2</sup> )	VNIR (398.55–994.44 nm, 64 bands)	Subtropical Forest, China	RF (object approach)	5	85.4

continue

Table 2.2- Conclusion.

Study	Sensor	Spatial resolution (m)	Spectral resolution	Forest/ Country	Classifier	Number of species	Best accuracy (%)
Tuominen et al. (2018)	UAV-FPI	0.08	VNIR-SWIR (409-1578 nm, 60 bands)	Arboretum, Finland	KNN+GA and RF	26	82.3
Maschler et al. (2018)	Hypex VNIR 1600 (160SB)	0.4	VNIR (415-991 nm, 80 bands)	Temperate Forest, Austria	RF (object approach)	13	91.7
Dabiri; Lang (2018)	APEX	2.5	VNIR-SWIR (413-2451 nm, 288 bands)	Temperate Forest, Austria	RF	6	90
Marrs; Ni-Meister (2019)	G-LIHT imager	1 m (6 points/m <sup>2</sup> )	VNIR (418-918 nm, 114 bands)	Temperate Forest, USA	SVM, CN2 rules, ANN	10 and 15	67 and 59
Sothe et al. (2019a)	UAV-FPI	0.11 (35 points/m <sup>2</sup> )	VNIR (506-819 nm, 25 bands)	Subtropical Forest, Brazil	SVM	12	72.4
Fricker et al. (2019)	NEON AOP	1 m	VNIR-SWIR (280- 2510, 426 bands)	Temperate Forest, USA	CNN	7	87

Note: ANN= Artificial Neural Network; CNN= Convolutional Neural Network; GA= Genetic Algorithm; KNN= K-nearest neighbor; LDA= Linear Discriminant Analysis; MDA= Multiple Discriminant Analysis; MLC= Maximum Likelihood Classifier; MLP= Multilayer Perceptron; PLSDA= Discriminant Analysis based on Partial Least Square; QDA= Quadratic Discriminant Analysis; RDA= Regularized Discriminant Analysis; RF= Random Forest; SVM= Support Vector Machine; SWIR=short-wave infrared.  
Source: Author's production.

### 2.3 Segmentation and individual tree crown delineation

In contrast to pixel-based analysis, in the OBIA framework segments are considered as the basic unit of analysis. The idea of segmentation is to spatially decompose complexity, in which resulting segments (grouped according to some homogeneity criteria) can maximize spectral homogeneity between segments while minimizing spectral variability within a segment (PAL; PAL, 1993). An optimal segment has minimum internal variations and, at the same time, maximum external difference from neighboring segments. These optimal segments, also referred to as "candidate objects", (BURNETT; BLASCHKE, 2003) strongly depend on segmentation methods.

In this sense, a variety of segmentation algorithms has been proposed in the last two decades. Among them, three segmentation approaches are the most often used for land cover mapping in general and for applications involving

forest environments: region growing (KE; QUACKENBUSH, 2011; SINGH et al., 2015; PIAZZA et al., 2016; NORDIN et al., 2018; SOTHE et al., 2019b), including multiresolution, graph-based (STRÎMBU; STRÎMBU, 2015; LEE et al., 2016) and mean shift (HU et al., 2017; MASCHLER et al., 2018).

The region growing stands out for its simplicity and it is implemented in many softwares. The multiresolution, for instance, is based on the region growing algorithm proposed by Baatz and Schäpe (2000). It starts with seed pixels and progressively grows regions by iteratively including adjacent pixels until a threshold of expansion or stopping criteria is met. This algorithm has three main parameters: the color (and shape) weight, the compactness (and smoothness) weight and the scale parameter. While the color/shape weights control how much the segmentation is based on image spectral (color) information vs object shape information, the smoothness/compactness weights control how much the object shape tends to be spatially compact vs spectrally homogeneous (smooth) but less compact. The scale parameter defines the maximum standard deviation of the homogeneity criteria regarding the weighted image layers for generating image objects. It limits the heterogeneity of the final objects and, thus, controls the size of the final segments (QIAN et al., 2014; TORRES-SÁNCHEZ et al., 2015). In general, the greater the scale value, the larger the size of objects and the higher the heterogeneity (QIAN et al., 2014).

In the last years, segmentation approaches have been adapted or specifically developed for ITC delineation (VAUHKONEN et al., 2012; FERREIRA et al., 2014; DALPONTE et al., 2015a; STRÎMBU; STRÎMBU, 2015; FERRAZ et al., 2016; LEE et al., 2016; WAGNER et al., 2018). Studies focused on ITC delineation usually aim to obtain information at the ITC level to be used for a direct classification, where each ITC is treated as one observation; or in a post-classification approach, treating each pixel as one observation and aggregating the pixel level species classifications inside each ITC (i.e. using the MV rule) (DALPONTE et al., 2014).

An outcome of an ITC classification, based either on direct classification or post-classification, depends on the ITC delineation carried out prior to the

classification. In this respect, ITC can be obtained from an automatic delineation method using different types of remote sensing data (e.g., LiDAR, multispectral and hyperspectral data) and different segmentation methods.

Lee et al. (2016; 2017) proposed a graph cut approach, based on the normalized cuts (NC), the latter one inspired on the previous work of Shi and Malik (2000). NC is an established approach for grouping points and/or pixels into disjoint clusters (LEE et al., 2017). It starts with a matrix of similarity measures between all possible pairs of points and/or pixels and uses the eigenvectors of that matrix to distinguish groups (SHI; MALIK, 2000). In the case of LiDAR (or PPC) data, the similarity matrix is derived from the physical distance between points (nodes) in 3D space. The NC divides the graph into clusters that have great similarity between the nodes of the same clusters and a low similarity between nodes of different clusters. According to Lee et al. (2017), when using LiDAR data, this method can delineate ITC directly from the 3D point cloud, so ITCs are not influenced by interpolation or smoothing errors prevailing in CHM-based approaches. To start the segmentation, this algorithm depends on priors that can be computed based on the higher values of a CHM band.

Another method specifically developed for ITC delineation is the *itcSegment*, proposed by Dalponte et al. (2015a). This method has two variants: one exploring point cloud data (*itcLiDAR*) and the other one exploring optical data (*itcIMG*), tested in this study. Similar to multiresolution, this latter starts with seed points: first, a low pass filter is applied to one raster band selected among the bands of the image; second, seed points are defined using a moving window in which a pixel can be considered a seed point if it detains the maximum value inside the window. Then, initial regions are defined starting from the seed points and a label map is created. A neighbor pixel is added to the region if it meets the pre-defined criteria (distance and threshold). From each region in the label map, the central coordinates of each pixel are extracted, and a 2D convex hull is applied to these points, and the resulting polygons are the final ITCs (DALPONTE et al., 2015a).

## 2.4 Feature extraction and feature selection

Feature reduction methods can be further separated into feature selection (FS) (selecting a subset from the original bands) and feature extraction algorithms (applying statistical transformations to create a reduced number of new features which summarize the information content of the original features) (WEBB; COPSEY, 2011).

Among the feature extraction methods, the minimum noise fraction (MNF) (GREEN et al., 1988) transformation is commonly applied for forest types and tree species classification using hyperspectral data (FASSNACHT et al., 2014; GHOSH et al., 2014; PIIRONEN et al., 2017; RACZKO; ZAGAJEWSKI, 2017; DABIRI; LANG; 2018; MASCHLER et al., 2018). MNF is a well-known technique for imagery denoising. It is similar to principal component (PC) transformation, however, instead of grouping projected bands (features, components) based on their variance, MNF transforms a noisy data cube into a data cube with images with increasing noise levels, which means that the MNF output images contain steadily decreasing image quality (LUO et al., 2016). Both PC and MNF transformations are based on the calculation of the eigenvalue decomposition using a covariance matrix (RODARMEL; SHAN, 2002). The resulting components from the dimensionality reduction techniques can be examined by the eigenvalues' measures. Eigenvalues are an indicator for the separation of noise-dominated components (meaning the components with near-unity eigenvalues) from information-dominant components (eigenvalues greater than 1) and visual inspection for band selection (DABIRI; LANG; 2018).

Besides reducing the data, feature extraction methods can be applied to get more information from the original bands or reduce the effects caused by illumination angles, increasing the classification accuracy (TONG et al., 2014). As examples, the vegetation indices (VIs) and textural features can be mentioned. Texture-based methods are commonly used for effectively incorporating spatial information in image interpretation. In the case of tree crowns, texture information is mainly related to crown-internal shadows, foliage



properties (size, density, and reflectivity), and branching (SAYN-WITTGENSTEIN, 1978). Gray-level co-occurrence matrix (GLCM)-based textural metrics proposed by Haralick et al. (1973) is a common approach used to compute texture information for vegetation types (and successional stages) and tree species classification (JOHANSEN; PHINN, 2006; YU et al., 2006; MALLINIS et al., 2008; FRANKLIN; AHMED, 2017; SOTHE et al., 2017ab; 2019ab; MASCHLER et al., 2018; FERREIRA et al., 2019).

VIs have been developed based on specific absorption features in order to quantify biophysical and biochemical indicators. They allow combining information contained in different spectral bands and can normalize external effects, e.g., solar and viewing angles, and internal effects such as soil variation or topographic conditions (LIN et al., 2015). The first indices were meant to enhance the strong reflectance of vegetation in the NIR region in relation to its marked absorption due to chlorophyll in the red region of the spectrum, such as the Simple Ratio (SR) (BIRTH; MACVEY, 1968) and the Normalized Difference Vegetation Index (NDVI) (ROUSE et al., 1973). More recently, some refinements were made in the conception of these indices, such as the Optimized Soil Adjusted Vegetation Index (OSAVI), which employs a soil adjustment coefficient (0.16) to minimize NDVI's sensitivity to variation in soil background under a wide range of environmental conditions and; the Green Normalized Vegetation Index (GNDVI) replaces the red band by the green band. Hyperspectral and newer multispectral sensors, such as WV-2 and WV-3, also allowed the calculation of the Red-edge Normalized Difference Vegetation Index (NDVI<sub>Red-edge</sub>) (GITELSON; MERZLYAK, 1994), which is composed by the spectral response of a band located in the red-edge region. According to Hatfield et al. (2008), the use of the green and red-edge channels avoids saturation and the concurrent loss of sensitivity to certain values of chlorophyll, besides being generally preferred because they are more sensitive to moderate and high contents of chlorophyll.

Hyperspectral sensors still make it possible to compute other indices at specific wavelengths, such as the photochemical reflectance index (PRI), the plant senescence reflectance index (PSRI), and the pigment specific simple ratio

(PSSR). According to Gamon et al. (1992), PRI is related to the changes in the xanthophyll cycle in the vegetation and the light efficiency in the photosynthesis process, which may not be perceived by NDVI. PSRI is sensitive to the ratio between carotenoids and leaf chlorophyll, which is altered during the senescence of the vegetation and also during its fruiting period (MERZLYAK et al., 1999), while PSSR was created for the study of chlorophyll concentration (BLACKBURN, 1998).

When dealing with hyperspectral data, or even with multispectral data associated with a high number of features extracted from them, FS can be a promising approach to reduce the data dimensionality. Removing redundant information, they reduce the computation complexity and generate a subset of the most relevant features (GUYON; ELISSEEFF, 2003; MALDONADO; WEBER, 2009; MA et al., 2017). Moreover, based on the selected features, assumptions can be made concerning which one is especially useful for the separation of land cover classes, such as successional forest stages and tree species (FASSNACHT et al., 2014).

FS algorithms are separated into three categories: filters, wrappers and embedded techniques (MALDONADO; WEBER, 2009; DURO et al., 2012; HIRA; GILLIES, 2015). Filter methods use statistical properties of the features to filter out poorly informative ones. This is done before applying any classification algorithm. Wrappers utilize the machine learning of interest as a black box to score subsets of variables according to their predictive power (MALDONADO; WEBER, 2009; MA et al., 2017). This approach tends to perform better in selecting features, since it takes the model hypothesis into account by training and testing it in the feature space (HIRA; GILLIES, 2015). However, it is computationally demanding. The third approach (embedded methods) performs FS in the process of model building. In contrast to filter and wrapper approaches, in embedded methods the learning part and the FS cannot be separated, and the class structure of the functions under consideration plays a crucial role (LAL et al., 2006).

Wrapper methods have a search strategy, which can be methodical, such as the best-first search; stochastic, such as a random hill-climbing algorithm; or it can use heuristics such as forward selection and backward selection to add and remove attributes (BROWNLEE, 2014). Sequential Forward Selection (SFS), a special case of sequential FS, is a greedy search algorithm that attempts to find the “optimal” feature subset by iteratively selecting features based on the classifier performance. It starts with an empty feature subset and add one feature at a time in each round; this feature is selected from the pool of all features that are not in the feature subset, and it is the feature that – when added – results in the best classifier performance (PUDIL et al., 1994).

Embedded methods include decision trees and RF algorithms. RF classifier, for instance, provides a ranking with the importance value of each feature using the ‘mean decrease in accuracy’ or ‘Gini index’ (LIAW; WIENER 2002). Variable importance in RF is based on the following heuristic: prediction errors based on the out-of-bag (OOB) samples are recorded for each tree and again after randomly shuffling the OOB samples. The difference between the prediction accuracy of the OOB samples and the permuted OOB samples is averaged over all trees and then normalized by the standard deviation of the differences (LIAW; WIENER 2002). Variables with larger scores are thought to be more important to the classification than variables with lower scores. However, this method does not provide a subset of features, depending on the user to choose how many will select based on importance values.

## **2.5 Image classification**

Digital image classification is a technique that seeks to recognize homogeneous patterns in the image and associate them with a given class (PONZONI et al., 2012). In the case of the supervised classification, training samples are collected, which are used to generate the patterns and thus label the pixels as belonging to a given class (NOVO, 2011).

Among the classification methods, parametric classifiers have been criticized for their limited ability to classify high-dimensional and multisource data (GHOSH et al., 2014). When applied to these situations, they may result in the so-called

Hughes phenomenon (HUGHES, 1968), which occurs when the ratio between the number of training samples available and the number of attributes is small, making it difficult to estimate the classifier parameters (DALPONTE et al., 2012).

In forest species classification studies, the acquisition of a sufficient amount of training data that exceeds the total number of spectral bands, especially when using hyperspectral data, is an impractical task. Consequently, non-parametric methods, such as those based on machine learning, have received increasing attention in these applications (DENG et al., 2016). Among the machine learning methods, RF and SVM are the most commonly applied for tree species classification (c.f. Table 2.2).

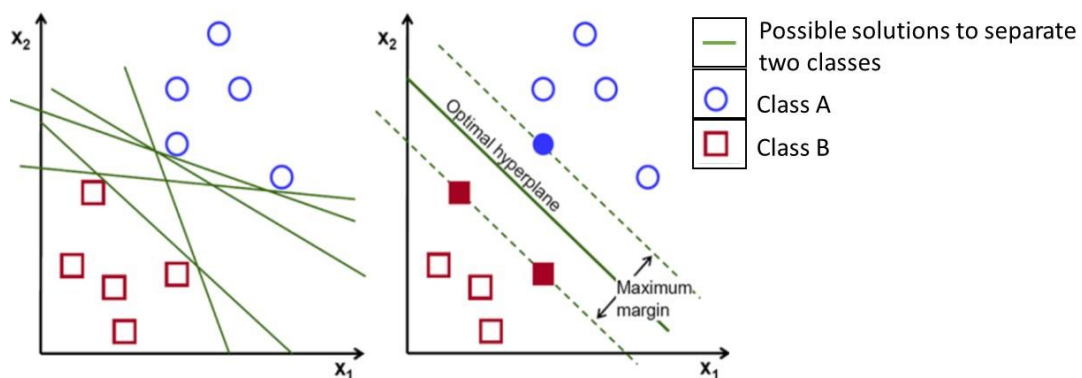
The above-mentioned algorithms can be considered as "shallow" learning models, because their architectures contain one or few processing layers (PASUPA; SUNHEM, 2016). Zhang, L. et al. (2016) report that such classifiers are highly dependent on the user's knowledge to choose the attributes and parameters to be used in the classification, which makes it difficult to achieve an optimal balance between discrimination and robustness for many types of data. In this sense, the main advantage of methods termed as 'deep' learning is that they take raw data and automatically learn features through training, with minimal prior knowledge about the task (LECUN et al., 1998). Such capacities have made deep learning emerged as the next generation learning technique with great potential for classification of remote sensing data (YUE et al., 2015; ZHANG, L. et al., 2016; LI, Y. et al., 2017; WANG et al., 2017; GAO et al., 2018; HARTLING et al., 2019). Among the deep learning algorithms, CNN stands out because it allows handling data in two or three dimensions, which is desirable in the classification of remote sensing images (LI, Y. et al., 2017).

### **2.5.1 Support vector machine**

The SVM classifier (VAPNIK, 1995) is a supervised, non-parametric statistical learning technique, which aims at finding an optimal hyperplane for solving the class separation problem (Figure 2.1). The optimal hyperplane is the one that maximizes the distance between closest training samples and the separating

hyperplane (MELGANI; BRUZZONE, 2004). Since the feature space is partitioned among the classes by a hyperplane, low accuracies are obtained for solving non-linear class boundary problems. Hence, SVMs uses the “kernel-trick” to map the data into a higher dimensional feature space (FASSNACHT et al., 2014), allowing for non-linear class boundaries. The SVM has four main kernel functions: (1) linear, (2) quadratic, (3) polynomial and (4) radial basis function (RBF) (LORENA; CARVALHO, 2007).

Figure 2.1- Structure of a SVM classifier.



Source: Drakos (2018).

Steinwart and Christmann (2008) identified three reasons for the success of SVM: ability to learn well with a small number of parameters; robustness in face of different types of variations and diversity of models and; computational efficiency compared to other methods. The robustness in the treatment of data of high dimensionality is related to the capacity of discernment of data with greater entropy by the SVM, that is, the amount of uncertainty (randomness) in the image (ANDRADE et al., 2014). Normally, other classifiers find problems with higher entropy data, due to the great occurrence of overfitting. The SVM, in addition to extracting the general parameters that allow generalization, store the noise and peculiarities, tolerating the recognition of patterns not observed during the training phase (ANDRADE et al., 2014). More detailed information about SVM can be found in Melgani and Bruzzone (2004) and Mountrakis et al. (2011).

### 2.5.1.1 Weighted support vector machine

According to Nguyen et al. (2019), a standard SVM algorithm gives the same weight to all the training samples and, therefore, in the case of wrongly labeled samples in the dataset, or a highly imbalanced distribution of the samples among the classes, the classification performance could significantly decrease. Motivated by that, the authors proposed the wSVM to solve the problems of unbalancing, unreliability, and size of the training sets for tree species classification at an ITC level. This algorithm gives distinct weights to different samples and to different classes based on three strategies: i) using the class abundances to differently weight the samples of the different classes and; ii) using the training samples and their distribution in the feature space to differently weight each training sample, and; iii) exploiting the unlabeled samples (that could be extracted from the study area) and their distribution in the feature space to weight differently each training sample. Since this method is not widely known, more details of the formulation regarding the two first strategies, which were explored in this study, will be given below.

Given a training dataset composed by  $x$  classes, and give that each class has  $N_k$  elements, the inter-class weight ( $CW$ ) can be formulated as (Equation 2.1):

$$CW_k = \frac{\max(N_{i=1\dots x})}{N_k} \quad (2.1)$$

with  $k=1,\dots,x$ . However, if the inter-class weights of majority classes are much smaller compared to the inter-class weights of minority classes, some information could be lost from the majority classes leading to a decrease of their accuracy. To deal with this problem, the inter-class weight of majority classes could be set to the mean values of all the inter-class weights (NGUYEN, 2019).

For the prediction of the intra-class component ( $SW$ ) of the sample weights, the training samples of each class are divided into  $G$  clusters. The density of each cluster is used to estimate the density of the samples in the feature space. Considering one class, if most training samples are grouped in one cluster while the remaining samples are sparsely distributed, the latter is considered less

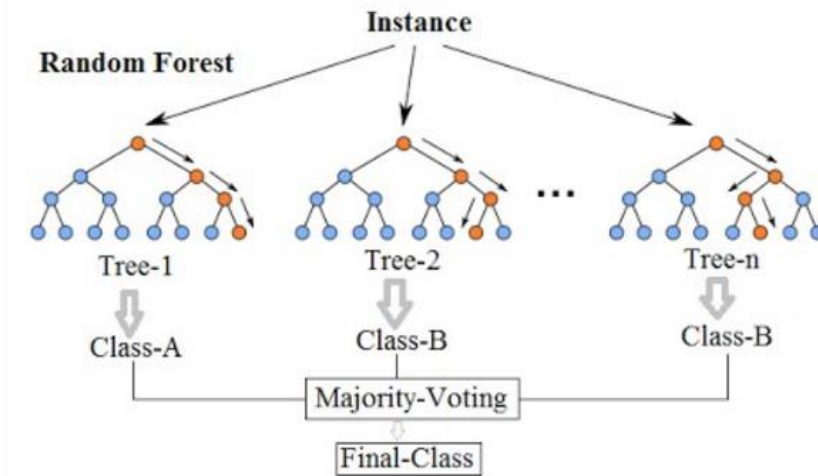
reliable than others. Hence, higher weights will be assigned to the samples that are in clusters characterized by a higher number of samples. In greater detail, this strategy follows three steps for each class (NGUYEN, 2019):

1. the k-means clustering is applied to the training set of each class to identify a set  $\Omega = \{c_1, c_2, \dots, c_G\}$  of  $G$ -clusters. The number of clusters  $G$  is defined as the square root of the half of the total number of samples in that class (DEMIR; BRUZZONE, 2014);
2. the density of the cluster  $c_i$  is determined by the number of samples located in that cluster. In this way, labeled samples that fall into the high-density clusters are more important for the classification problem and vice versa;
3. weights are normalized in the interval  $[0, 1]$ .

### **2.5.2 Random forest**

The RF is an algorithm designed by Breiman (2001) aiming to improve the accuracy of classification or regression by combining a large number of trees trained upon random subsets of the available labeled samples and features. In the first case, each tree contributes only one class vote to each instance, and the final classification is determined by the majority votes of all the forest trees (HASTIE et al., 2009) (Figure 2.2). In its simplest form, this algorithm requires the definition of a few parameters: the number of trees to form the "forest" (*ntree*) and the number of features/predictors considered for each node in the trees (*mtry*).

Figure 2.2- Structure of a RF classifier.



Source: Koehrsen (2017).

The method provides a way to evaluate statistical quality by means of an internal sampling procedure called OOB, which can be used to estimate classification errors. For this, the RF algorithm collects about 2/3 of the training data with substitution, while the remainders are left OOB. These samples of OOB are attributed to trees that have not yet been used, and the difference between the expected and the actual class is used to evaluate the classification accuracy (PRASAD et al., 2006). In addition to estimating the error, the OOB samples also allow to estimate the importance of each feature in the classification process, which is calculated based on the decrease in the accuracy of general or class classification when the feature is permuted in OOB samples (BREIMAN, 2001). This give to RF the ability to efficiently select the best predictor features from a large set of correlated features, without a previous step of FS (CLARK; ROBERTS, 2012). There is a rich and well-known literature on RF e.g., (BREIMAN, 2001; MURPHY, 2012; KUNCHEVA, 2014).

### 2.5.3 Convolutional neural network

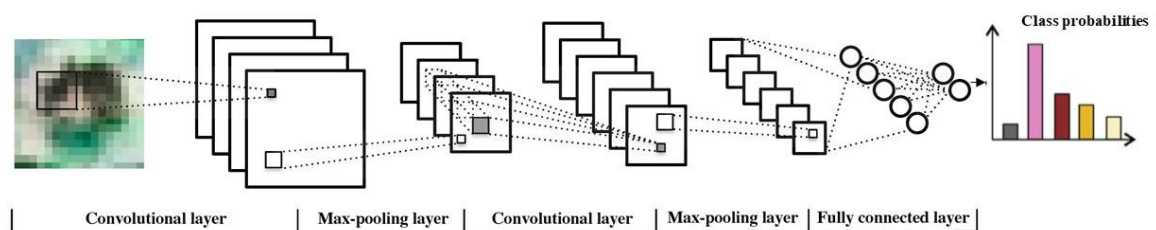
The first deep learning technique called CNN was introduced by Fukushima (1980), inspired by the biological learning process. Similar to the function of the human brain, CNNs are made up of neurons with learnable weights and biases. Each neuron receives several inputs, takes a weighted sum over them, passes it through an activation function and responds with an output (HARTLING et al.,



2019). The four key components of a CNN are: a) convolutional layer; b) activation function or non-linearity; c) pooling layer e; d) fully connected layer (ZHANG, L. et al., 2016) (Figure 2.3).

The original input image is convolved with a set of trainable kernels that scan across the entire input image resulting in a group of feature maps. Each feature map results from the convolution of the kernel, with its corresponding local region on the original input image. Moreover, an element wise non-linear activation function (e.g., sigmoid, rectified linear unit- ReLU, hyperbolic tangent) is taken out of the results of a convolutional layer for non-linearity amplification. The pooling layer is usually computed immediately after a convolutional layer and is used to down/sub-sample output of the convolutional layer to generate a condensed set of feature maps. The max-pooling is the most common and widely used pooling layer, which makes it possible to keep only the maximal values of the feature maps. It reduces the spatial size of feature maps significantly and, consequently, the computation volume for the next layers to be processed (GHORBANZADEH et al. 2019; HARTLING et al., 2019). The fully-connected layers finally follow several stacked convolutional and pooling layers. The last fully-connected layer (usually a softmax function) allows interpreting the output layer values as posterior probabilities for each defined class (WANG et al., 2017). More details about CNN can be found in Goodfellow et al. (2016) and Gao et al. (2018).

Figure 2.3- Structure of a CNN classifier.

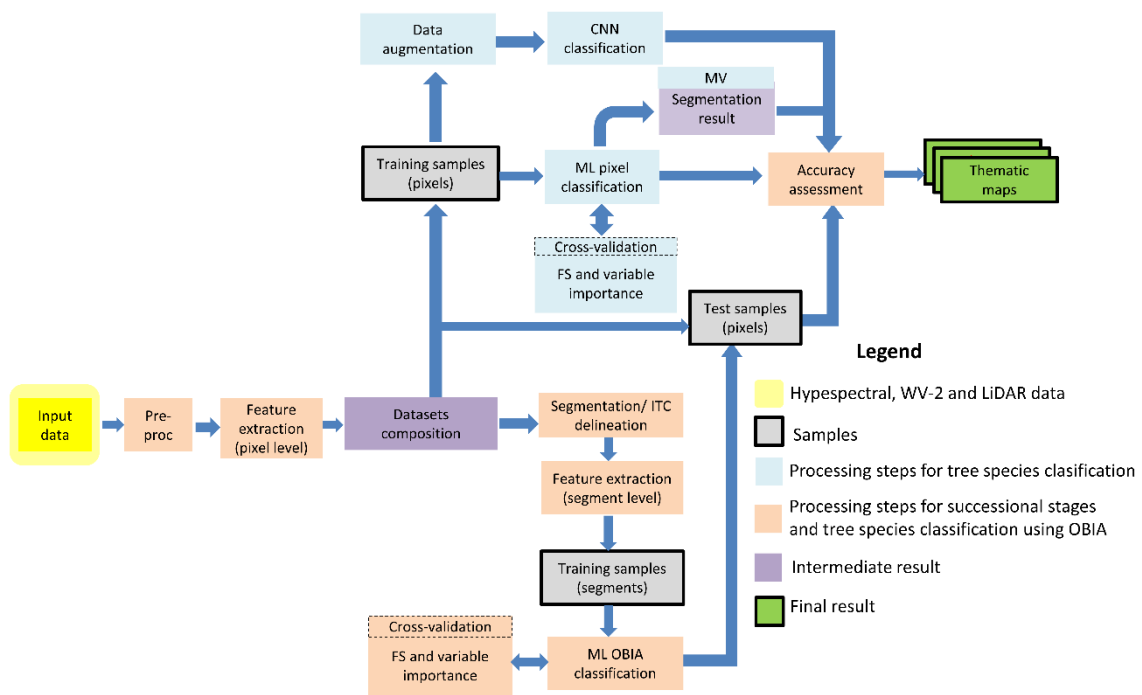


Source: Adapted from Li, W et al. (2017).

### 3 MATERIAL AND METHODS

The methodological framework developed for this research is shown in Figure 3.1. Refer to Figures 3.14, 3.15 and 3.17 for detailed flowcharts of each classification scheme. The common steps for both the successional stages and tree species classification are in light pink color boxes, while the light blue boxes comprise only steps performed for tree species classification.

Figure 3.1- Methodological framework developed in this study.



Note: Pre-proc= preprocessing; FS= feature selection; ML= machine learning.

Source: Author's production.

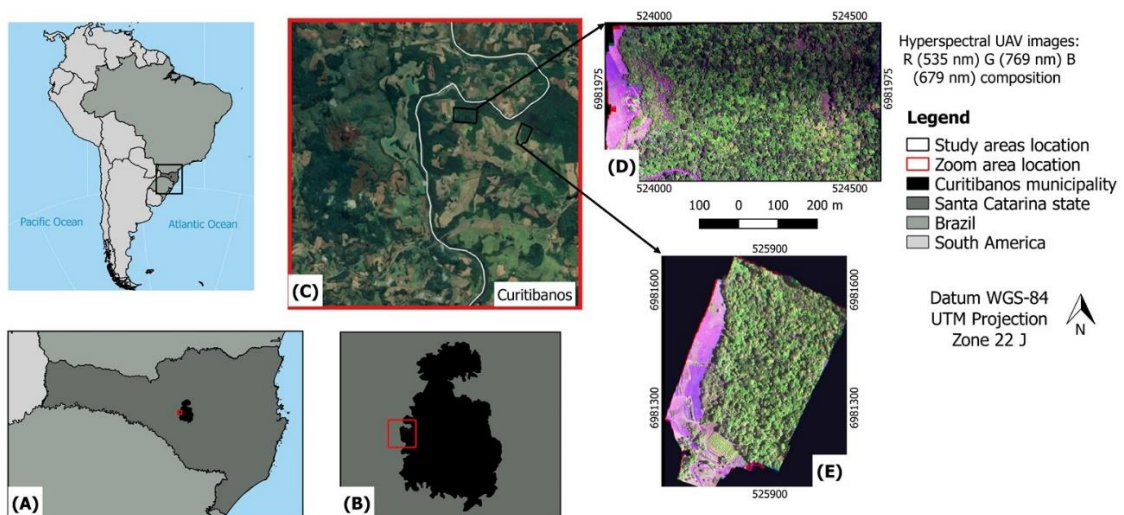
The first step comprised the preprocessing of the input data (hyperspectral, PPC, WV-2 and LiDAR), followed by the feature extraction at the pixel level, compilation of datasets and collection of training samples. For the OBIA approach and for the ITC delineation, the segmentation was performed prior to the classification. Afterwards, the spectral means corresponding to each layer of the training segments were used for the classification process. In this step, the feature selection and variable importance were performed. For tree species

classification at the pixel level, FS and variable importance were executed based on the *full* dataset and training samples associated with the JM and SFFS methods. Following, the classifications using the machine learning methods were performed and evaluated at the pixel level, and after the MV rule approach. For the CNN, a data augmentation was initially applied to the training samples and, in the sequence, a pixel-based classification was executed. The classification results were evaluated, and the final thematic maps were produced.

### 3.1 Study areas

The study areas are located in the municipality of Curitibaanos, SC state, southern Brazil (Figure 3.2), near the Marombas River. These areas are approximately 30 ha (Area 1) and 19 ha large (Area 2) and are part of the Atlantic Rain Forest biome and MOF phytophysiology. The climate, according to Köppen–Geiger classification, is Cfb, moist mesothermal with no clearly defined dry season, mild summers, and an average annual temperature of 15 °C (PEEL et al., 2007).

Figure 3.2- Study areas location. (A) Santa Catarina State and (B) Curitibaanos municipality (IBGE, 2019); (C) Google Earth image showing their location; (D) Area 1; (E) Area 2.

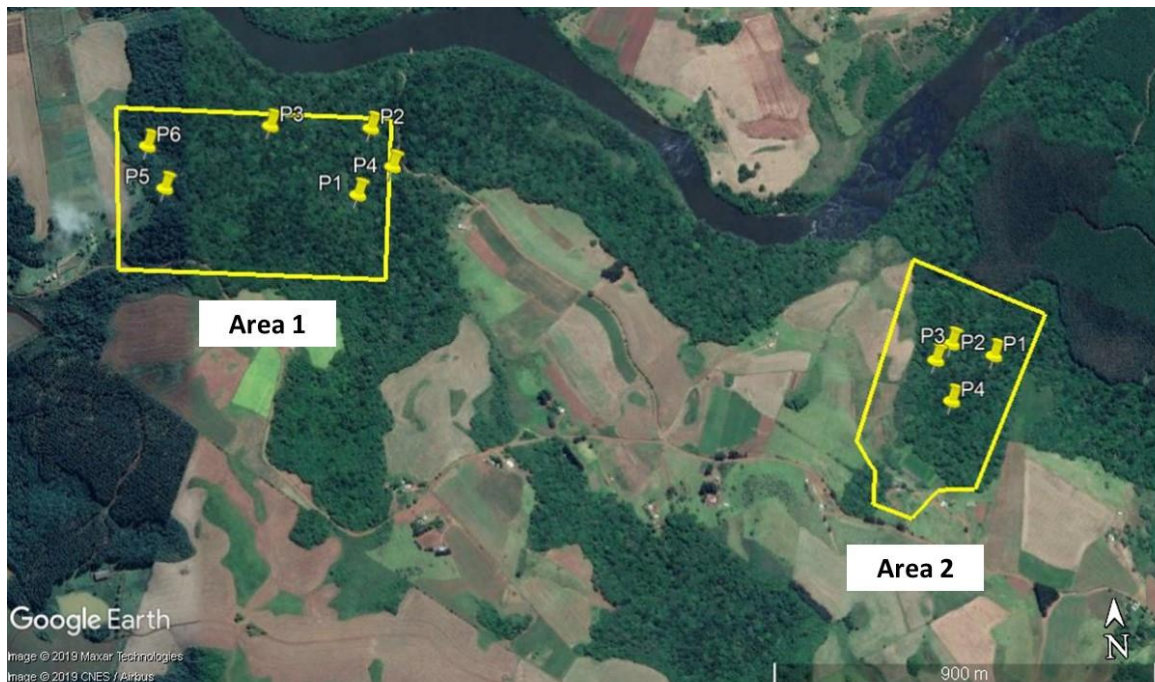


Source: Author's production.

### 3.2 Field surveys

Two fieldworks were carried out over both areas, the first one in December of 2017 and the second one in October of 2018. In the first one, a survey was conducted regarding the tree species diversity and structure and the successional stages of the forest fragments. For this task, six plots with 400 m<sup>2</sup> were delimited in Area 1 and four in Area 2 (Figure 3.3). Inside each plot, all the trees with DBH greater than 5 cm were measured and identified. Characteristics like the number of forest strata, presence of lianas and bromeliads and litter thickness were also reported to help at the successional stage classification of each plot. Table 3.1 shows the average DBH, height, basal area (BA), number of tree species and successional stage classified according to CONAMA Resolution 04/1994 (BRASIL, 1994) and Siminski et al. (2013). Figure 3.4 (A-D) shows examples of vegetation cover obtained from different views in Area 1.

Figure 3.3- Distribution of the plots to identify the successional forest stages in both areas.



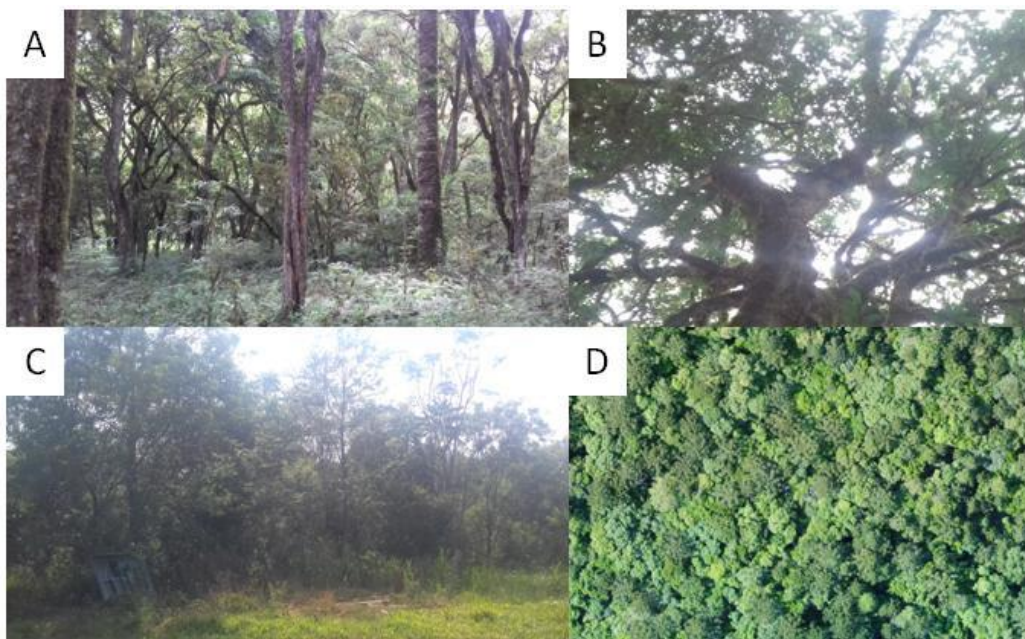
Source: Adapted from Google Earth (2019).

Table 3.1- Structural characteristics of each plot regarding its successional forest stage.

		DBH (cm)	Height (m)	BA (m <sup>2</sup> )	Number of tree species	Stage
Area 1	Plot 1	25.61	13	1.31	18	SS <sub>3</sub>
	Plot 2	19.35	9.77	1.19	24	SS <sub>3</sub>
	Plot 3	19.76	13	0.91	21	SS <sub>3</sub>
	Plot 4	21.75	16.7	0.75	16	SS <sub>3</sub>
	Plot 5	13.89	8	0.85	41	SS <sub>2</sub>
	Plot 6	12.27	7.31	0.26	16	SS <sub>2</sub>
Area 2	Plot 1	20.51	13.97	1.42	31	SS <sub>3</sub>
	Plot 2	21.65	12.1	1.29	21	SS <sub>3</sub>
	Plot 3	19.04	13.61	0.80	18	SS <sub>3</sub>
	Plot 4	16.39	12.15	0.7	17	SS <sub>3</sub>

Source: Author's production.

Figure 3.4 - Examples of forest cover of Area 1: (A-B) internal view, (C) external view; (D) aerial view using an UAV-RGB camera.



Source: Author's production.

Although all the plots comprised SS<sub>3</sub> and SS<sub>2</sub> stages (Table 3.1), SS<sub>1</sub> stage areas were also found in Area 1. However, plots were not installed in these areas because most trees did not reach the minimum DBH considered (5 cm). Therefore, the coordinates of such areas were collected to provide samples of this stage, in order to perform the successional stages classification.

Considering that Area 2 is mainly composed by the SS<sub>3</sub> stage, the successional forest stages classification was restricted to Area 1.

The second fieldwork was carried out after the acquisition of the UAV data. Differentiating from what is observed for land-use/land-cover assessment in field inspections, the species identification of an individual tree must be checked and determined by a trained specialist in situ (GRAVES et al., 2016). Therefore, it was not possible to implement a randomization scheme for collecting field data, and only the tree species which had clearly visible crowns in the images were inspected and identified in the field. Trees with ambiguous appearance were discarded.

In total, 17 tree species belonging to 11 families were originally identified in both areas (Table 3.2). Due to the low number of samples of *Ocotea puberula*, this particular tree species was associated with the *Ocotea pulchella* species, composing the *Ocotea* sp. class. Based on the first fieldwork, it was estimated that these species represent nearly 55% and 48% of all the trees species (including suppressed and co-dominant trees) of Areas 1 and 2, respectively. Considering only the dominant trees, they represent approximately 80% of the tree species in both areas.

Table 3.2- Tree species and their successional group identified in both areas.

ID	Species	Family	Successional group
1	<i>Luehea divaricata</i>	Malvaceae	initial or late secondary, climatic
2	<i>Araucaria angustifolia</i>	Araucariaceae	pioneer or secondary
3	<i>Mimosa scabrella</i>	Fabaceae	pioneer
4	<i>Lithraea brasiliensis</i>	Anacardiaceae	pioneer, initial secondary or climatic
5	<i>Campomanesia xanthocarpa</i>	Myrtaceae	initial or late secondary
6	<i>Cedrela fissilis</i>	Meliaceae	initial or late secondary, climatic
7	<i>Cinnamodendron dinisii</i>	Canellaceae	late secondary
8	<i>Cupania vernalis</i>	Sapindaceae	initial or late secondary
9	<i>Matayba elaeagnoides</i>	Sapindaceae	late secondary
10	<i>Nectandra megapotamica</i>	Lauraceae	initial or late secondary
11	<i>Ocotea</i> sp.	Lauraceae	initial secondary
12	<i>Podocarpus lambertii</i>	Podocarpaceae	late secondary or climatic
13	<i>Schinus terebenthifolius</i> (sp1)	Anacardiaceae	pioneer, initial or late secondary
14	<i>Schinus lentiscifolius</i> (sp2)	Anacardiaceae	initial or late secondary

continue

Table 3.2- Conclusion.

ID	Species	Family	Successional group
15	<i>Erythrina falcata</i>	Fabaceae	initial secondary or climatic
16	<i>Sebastiania commersoniana</i>	Euphorbiaceae	initial secondary

Source: Author's production.

### 3.3 Input data

#### 3.3.1 UAV-hyperspectral and PPC data

The flight to acquire the hyperspectral data was conducted in December 2017, at the end of the spring season, by means of a quadcopter UAV (UX4 model) and a frame format hyperspectral camera based on a Fabry–Perot interferometer (FPI), model 2015 (DT-0011). This camera was supplied by the São Paulo State University (UNESP) and built by Senop Ltd. (2018). It comprises one irradiance sensor and one global navigation satellite system (GNSS) receiver. A single frequency GNSS receiver (NSRAW) was integrated to acquire raw data which can be post-processed to provide the coordinates of the exposure station of the first band (MIYOSHI et al., 2018a).

The FPI technology offers a frame-format hyperspectral imager operating on the time-sequential principle (HONKAVAARA et al., 2017). The camera has an adjustable air gap, which allows for the acquisition of 25 spectral bands in the range from 500 to 900 nm with the best spectral resolution of 10 nm at the full width at half maximum (FWHM) (MIYOSHI et al., 2018b). While this camera allows for flexibility in selecting the spectral bands, increasing therefore the number of acquired bands, it simultaneously increases the acquisition time. In mobile applications, the bands in individual cubes have spatial offsets that need to be corrected in the processing phase (c.f. Section 3.4.1) (HONKAVAARA et al., 2013; HONKAVAARA et al., 2017; AASEN et al., 2018). Regarding the spectral bands, the configuration shown in Table 3.3 was adopted, comprising the visible and near infrared regions (VNIR) of the electromagnetic spectrum.

Table 3.3- Description of VNIR bands used in this study. ( $\lambda$  = central wavelength of the spectral band).

$\lambda$ (nm)	FWHM (nm)	$\lambda$ (nm)	FWHM (nm)	$\lambda$ (nm)	FWHM (nm)	$\lambda$ (nm)	FWHM (nm)	$\lambda$ (nm)	FWHM (nm)
506	15.65	580	15.14	650	15.85	700	21.89	750	19.43
519	17.51	591	14.81	659	24.11	710	20.78	769	19.39
535	16.41	609	13.77	669	21.7	720	20.76	780	18.25
550	15.18	620	14.59	679	21	729	21.44	790	18.5
565	16.6	628	12.84	690	21.67	740	20.64	819	18.17

Source: Author's production.

The aerial surveys were carried out in two consecutive days between 12:55 and 13:16 (UTC-3) in Area 1, and between 10:59 and 11:06 (UTC-3) in Area 2. The flights were conducted keeping a great overlap between the strips (Table 3.4), which allowed the creation of high spatial resolution PPCs. On both occasions, the illumination conditions were stable, and the weather was sunny (Figure 3.5). The characteristics of the camera, the flight and the data acquired in the study areas are shown in Table 3.5. Further details about the camera can be found in Oliveira et al. (2016) and Miyoshi et al. (2018b).

Table 3.4- Strip sizes and overlap of each area.

	Number of strips	Size of strips (m)	Forward overlap (%)	Side overlap (%)	PPC density (points/m <sup>2</sup> )
Area 1	8	700 x 35	70	60	35
Area 2	6	450 x 40	60	50	25

Source: Author's production.

Table 3.5- Characteristics of the camera, flight and data acquired in the study areas.

<b>Sensor</b>	CMOSIS CMV400 sensors
<b>Spectral bands</b>	25 spectral bands ranging from 506 to 819 nm
<b>FWHM</b>	Ranging from 12.84 to 21.89 nm
<b>Focal length</b>	8.6 mm
<b>Field of view (FOV)</b>	37°
<b>Ground sampling distance (GSD)</b>	11 cm (Area 1) 12 cm (Area 2)
<b>Image dimensions</b>	1,023 × 648 pixels
<b>Flight height</b>	150 m
<b>Flight speed</b>	4 m/s

Source: Author's production.



Figure 3.5- Photos showing the weather conditions of the flight days.



Source: Author's production.

### 3.3.2 WorldView-2 data

The cloud-free WV-2 scene (ID 103001005CAA7100) was acquired in August 2016 with 28.2° off Nadir and 42.7° Sun Elevation. The images have eight multispectral bands and one panchromatic band (Table 3.6). The scene is classified as standard 2A, which means that the radiometric, sensor, and geometric corrections were already applied.

Table 3.6- Spectral bands and spatial resolution of WorldView-2 data.

Spectral band	Wavelength (µm)	Spatial resolution (m)
Panchromatic	0.46–0.80	0.5
Coastal	0.40–0.45	2
Blue	0.45–0.51	2
Green	0.51–0.58	2
Yellow	0.59–0.63	2
Red	0.63–0.69	2
Red-edge	0.71–0.75	2
Near Infrared 1	0.77–0.90	2
Near Infrared 2	0.86–1.04	2

Source: Author's production.

### 3.3.3 LiDAR data

The LiDAR data were acquired by the company SAI Brasil, which performed a laser surveying in the study area using the Optech Model 3033 sensor in 2013, with a density of 1 point/m<sup>2</sup>. The characteristics of the flight are shown in Table 3.7.

Table 3.7- Characteristics of the flight and LiDAR data acquired over the study areas.

<b>Sensor</b>	Optech Model 3033
<b>Airborne</b>	Helicopter B2 Esquilo
<b>Flight height</b>	1,000 m
<b>Flight speed</b>	140 km/h
<b>Strip width</b>	700 m
<b>Forward overlap</b>	30°
<b>Points/m<sup>2</sup></b>	1
<b>Scanning angle</b>	20°

Source: Author's production.

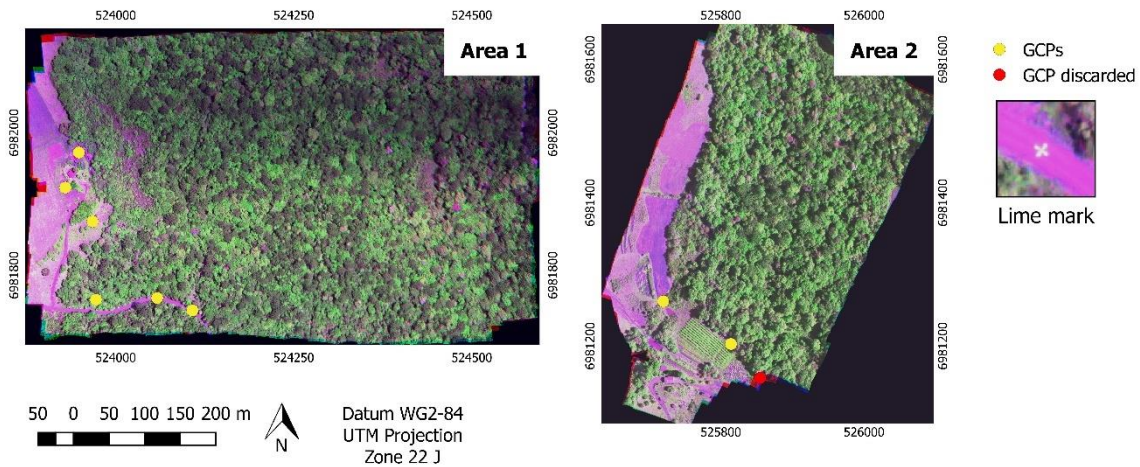
### 3.4 Data preprocessing

#### 3.4.1 Hyperspectral data

In this stage, digital numbers (DN) from the images were initially transformed into radiance values with photon units  $\text{pixel}^{-1} \text{s}^{-1}$ . Afterwards, the dark signal correction was calculated using a black image collected just before the data capture with the lens covered. The software Hyperspectral Imager, provided by Senop Ltd., was used for this step.

The next phase involved the geometric processing of the data using the Agisoft PhotoScan Professional software. Both the interior orientation parameters (IOPs) and the exterior orientation parameters (EOPs) were estimated using the so-called on-the-job calibration to reconstruct the camera geometry and the orientation of each band, which were refined based on the initial values. The initial values for the camera positions were determined by the GNSS receiver, comprising latitude, longitude, and altitude (flight height plus the average terrain height). The coordinates of six ground control points (GCPs) for Area 1 and three for Area 2 were added to the project and measured in the corresponding reference images (Figure 3.6). These points were previously located and surveyed in the field (signalized with lime mortar) on the same day of the flight and had their coordinates collected with a GNSS RTK Leica GS15. However, one point of Area 2 was discarded because it was situated at the border of the area and it did not appear in all the bands. After the bundle adjustment, the final errors of Area 1 in the GCPs (reprojection errors) were 0.03 pixels on the image and 0.003 m on the GCPs. At Area 2, the errors were 0.08 pixels on the image and 0.004 m on the GCPs.

Figure 3.6- Ground control points (GPPs) locations and an example of lime mark.

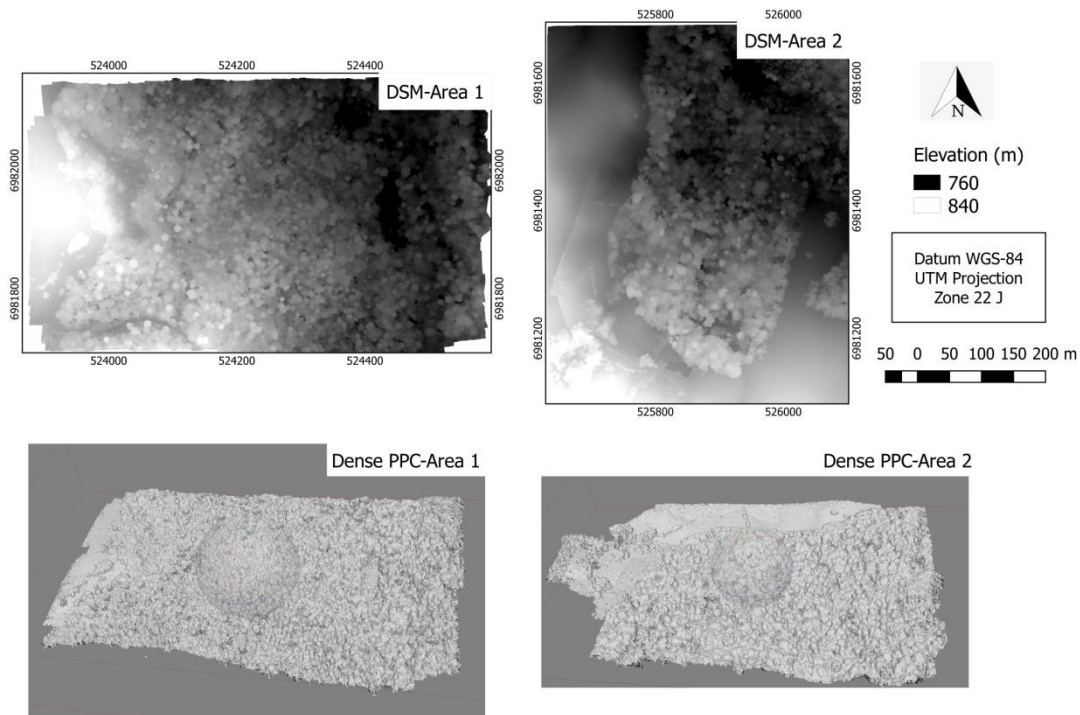


Source: Author's production.

Next, the orthorectification was performed starting with the generation of a dense point cloud. The dense matching method was used to generate the Digital Surface Models (DSMs) with a GSD of 11 cm for Area 1 and 12 cm for Area 2. In the last stage, the orthomosaics of all bands were generated from the orthoimages of each hypercube band. This whole procedure was repeated for each of the 25 spectral bands of each area in order to coregister them regarding the slight positioning difference among bands of the same image, caused by the time sequential operating principle of the camera (HONKAVAARA et al., 2013; MIYOSHI et al., 2018b). Afterwards, the final discrepancies among the orthorectified image bands were measured using the GCPs and four independent points chosen in the images for Area 1, and the GCPs plus two independent points for Area 2. An error was verified in x and y of about  $0.03 \pm 0.06$  m among the bands of Area 1, and about  $0.07 \pm 0.08$  m in Area 2, which was considered acceptable for the classification purpose in this study.

The orthomosaics of all the bands were stacked to compose the VNIR dataset. The PPC of the band centered at the 565 nm wavelength and its DSM (Figure 3.7), which is, in fact, an interpolated raster data, were exported to be used in further steps: generation of the PPC features and the canopy height model (CHM).

Figure 3.7- Dense photogrammetric point cloud (PPC) and digital surface model (DSM) of each area.



Source: Author's production.

### 3.4.2 WorldView-2 data

Initially, the WV-2 images were converted to radiance images, using the Radiometric Calibration tool of ENVI 5.3. Next, they were once again converted to surface reflectance using the Fast Line-of-sight Atmospheric Analysis of Spectral Hypercubes (FLAASH). In order to use this tool, it is necessary to enter some parameters of the scene and the sensor, such as: filter response functions (available at ENVI 5.3 for WV-2), central coordinates of the scene, terrain elevation, sensor altitude, pixel size, date and time of image acquisition, atmospheric model and aerosol model.

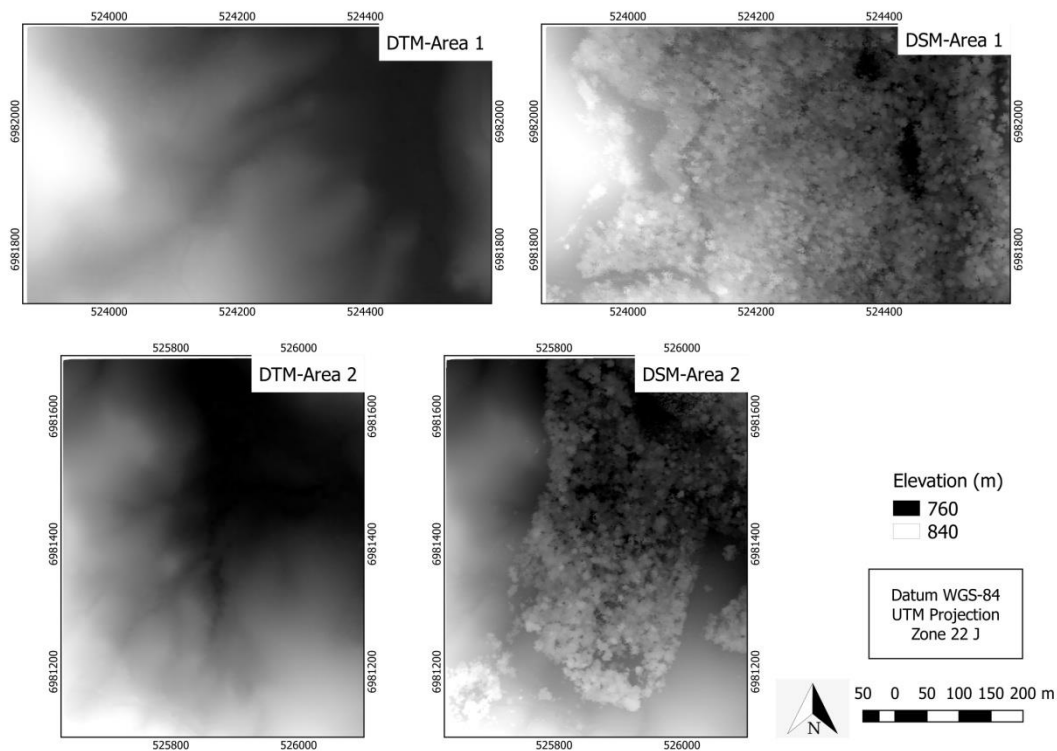
After the atmospheric correction, the WV-2 multispectral bands were pansharpened with the WV-2 panchromatic band using the Gram-Schmidt method. This method was chosen because it does not improve nor decrease the classification accuracy (BRUZZONE et al., 2006), keeping a high degree of spectral similarity with the original multispectral bands, and it did not impose a limit on the number of input bands (ANJOS, 2016). Finally, the WV-2 scene was

orthorectified based on the rational polynomial coefficients, using parameters provided by the metadata and the Digital Terrain Model (DTM) extracted from LiDAR data (Section 3.4.3).

### 3.4.3 LiDAR data

The filter Adaptive Triangular Irregular Network (AXELSSON, 2000) was applied to the LiDAR point cloud using the LAStools software (ISENBURG, 2018) to remove the outliers and to separate the ground from the non-ground points. To generate the DSM, the function *las2dem* of LAStools was applied. This function has a command called *thin\_with\_grid* which transforms the filtered points into a regular network with a user-defined spatial resolution. Due to the lower points density of LiDAR data, the DSM spatial resolution was set to 1 m. The same function was applied to generate the DTM, but in this case, only the points classified as 'ground' were interpolated (Figure 3.8).

Figure 3.8- Digital terrain model (DTM) and digital surface model (DSM) generated from LiDAR data.



Source: Author's production.

### 3.5 Sample collection

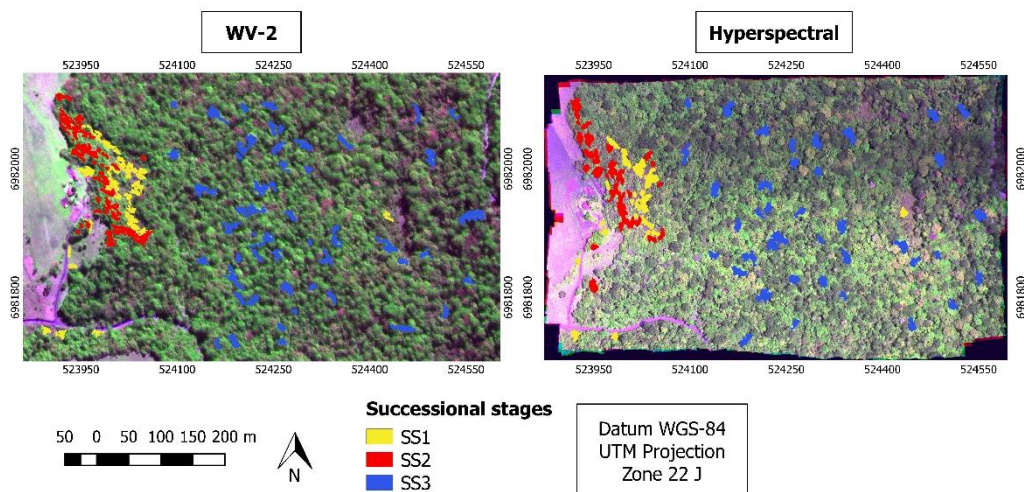
The samples used for the successional forest stages classification were defined based on field observations, UAV-RGB images with 4 cm spatial resolution and UAV-hyperspectral data with 11 cm spatial resolution. The samples correspond to segments resulting from the segmentation process described in Section 3.9, covering all the existing spectral variability in each class and input data (WV-2 and hyperspectral). Because of the smaller proportion of areas with SS<sub>1</sub> and SS<sub>2</sub> classes, fewer samples of them were collected and they were also more spatially concentrated (Figure 3.9). Due to differences in spatial resolution and segmentation results, the number of pixel samples varied for the WV-2 and hyperspectral data (Table 3.8).

Table 3.8- Number of samples collected for each forest successional stage according to the data for Area 1.

Class	WV-2		Hyperspectral	
	Nº segments	Nº pixels	Nº segments	Nº pixels
SS <sub>1</sub>	40	9,426	45	196,131
SS <sub>2</sub>	55	11,437	55	284,006
SS <sub>3</sub>	98	24,779	120	485,855

Source: Author's production.

Figure 3.9- Distribution of samples from forest successional stages over the Area 1 according to the input data.

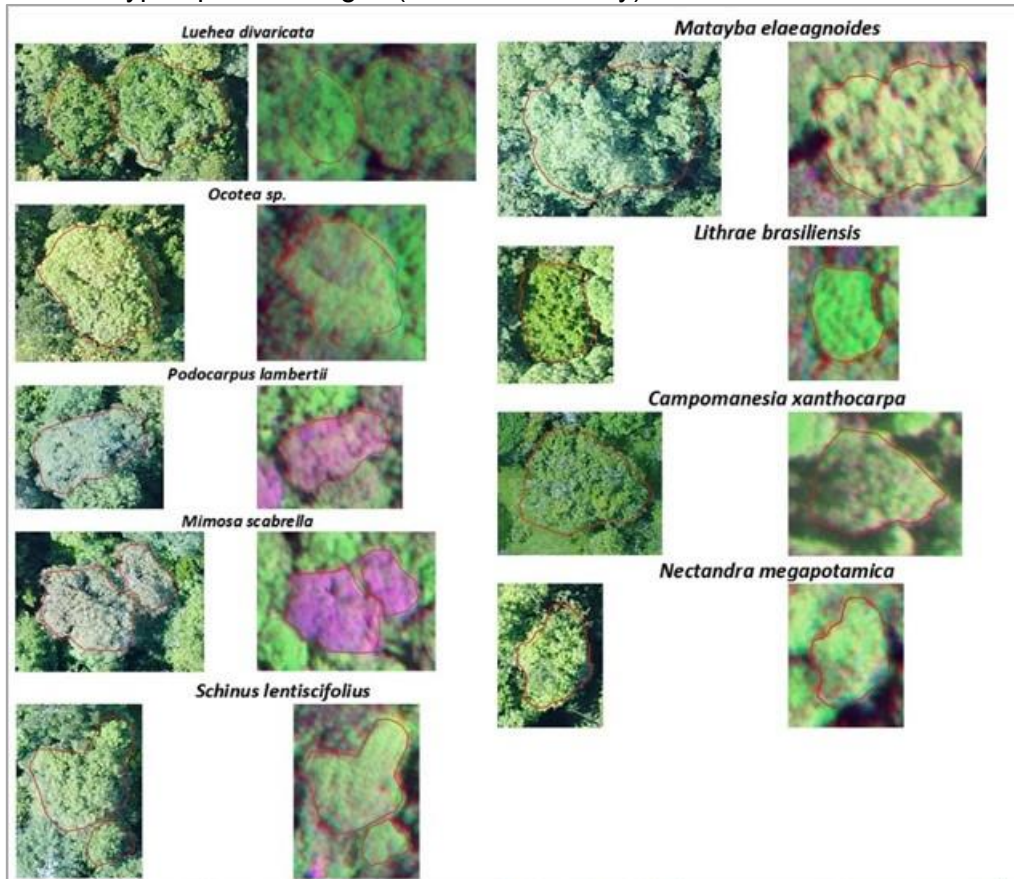


Source: Author's production.

Only the ITCs visited and identified in the field work were used as samples for tree species classification (Figure 3.10). The number of ITCs manually

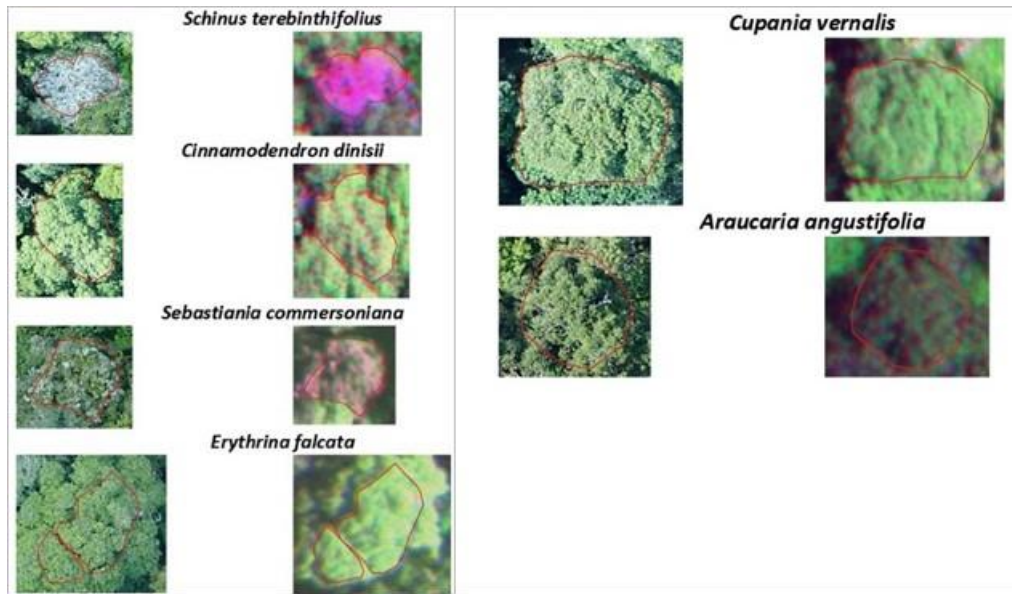
delineated and the corresponding number of pixels per class is shown in Table 3.9 and its distribution in Figure 3.11. Eighty ITCs representing 14 tree species were selected and identified in Area 1, and 41 ITCs representing 11 tree species for Area 2.

Figure 3.10- Tree species manually delineated as samples for both areas: UAV-RGB image with 4 cm spatial resolution and the corresponding crown in the hyperspectral images (used in this study).



continue

Figure 3.10- Conclusion



Source: Author's production.

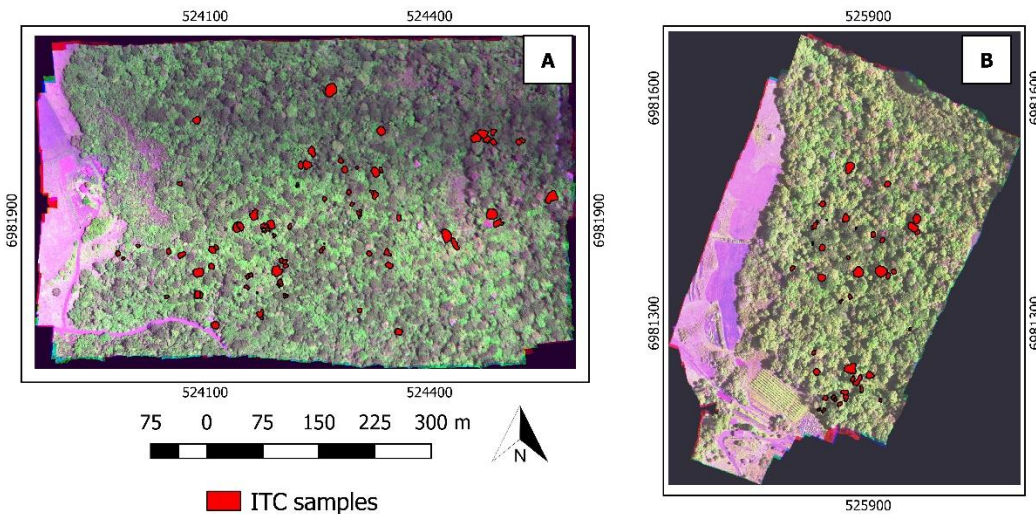
Table 3.9- Number of ITCs and pixels for each tree species used in the classification process.

Area 1			Area 2		
Species	ITC	Nº pixels	Species	ITC	Nº pixels
<i>Luehea divaricata</i>	5	23,624	<i>Luehea divaricata</i>	4	15,259
<i>Araucaria angustifolia</i>	8	27,191	<i>Araucaria angustifolia</i>	6	32,925
<i>Mimosa scabrella</i>	7	25,449	<i>Lithraea brasiliensis</i>	8	13,553
<i>Lithraea brasiliensis</i>	5	17,458	<i>Campomanesia xanthocarpa</i>	3	7,565
<i>Campomanesia xanthocarpa</i>	5	18,837	<i>Cedrela fissilis</i>	2	12,910
<i>Cedrela fissilis</i>	5	24,368	<i>Erythrina falcata</i>	2	3,663
<i>Cinnamodendron dinisii</i>	5	6,927	<i>Nectandra megapotamica</i>	4	4,862
<i>Cupania vernalis</i>	5	12,475	<i>Ocotea sp.</i>	3	12,991
<i>Matayba elaeagnoides</i>	8	48,231	<i>Podocarpus lambertii</i>	4	21,391
<i>Nectandra megapotamica</i>	8	11,247	<i>Schinus terebethifolius</i>	2	2,646
<i>Ocotea sp.</i>	9	101,884	<i>Sebastiania commersoniana</i>	3	3,396
<i>Podocarpus lambertii</i>	6	12,387			
<i>Schinus terebethifolius</i> (sp1)	2	4,491			
<i>Schinus lentiscifolius</i> (sp2)	2	6,083			
Total	80	340,652	Total	41	131,161

Source: Author's production.



Figure 3.11- Spatial distribution of the individual tree crown (ITC) samples over Area 1 (A) and Area 2 (B).



Source: Author's production.

### 3.6 Feature extraction

This step consisted in the extraction of features from the data (hyperspectral, PPC, LiDAR and WV-2) to be used in the classification process. Six sets of features were considered: (i) VNIR: the VNIR bands of hyperspectral and WV-2 data; (ii) MNF: minimum noise fraction components extracted from the hyperspectral and WV-2 data; (iii) GLCM: gray-level co-occurrence matrix textural features extracted from the hyperspectral and WV-2 data; (iv) VI: vegetation indices also extracted from hyperspectral and WV-2; (v) CHM: canopy height model, extracted from PPC and LiDAR data; and (vi) PPC: features extracted from the PPC.

The MNFs were computed in ENVI 5.3 using all the VNIR bands of hyperspectral and WV-2 data. Based on eigenvalue stats of the output uncorrelated bands, the first eight MNF components of hyperspectral data and five components of WV-2 data were selected, which had the highest values.

For texture information, the six GLCM features considered the most relevant for the analysis of remote sensing images were chosen: angular second moment (SM), contrast (con), variance (var), homogeneity (hom), correlation (cor), and entropy (ent) (LU et al., 2014) (Table 3.10). In addition to these six features, the dissimilarity (dis) and the textural mean (mean) were also computed because

previous studies conducted by Sothe et al. (2017b) showed that these two features were among the most important ones for identifying successional forest stages in a patch of Atlantic Rain Forest. The GLCM-based textural features were generated in ENVI 5.3, where it was necessary to define four parameters: window size, spectral bands, level of quantization, and the spatial component. The latter corresponds to the distance between the pixels and the angle (direction). The window size has an impact on the GLCM textural features performance for land use/ land cover classification. Small windows may amplify differences and increase the noise content in the texture image, while larger windows cannot effectively extract texture information due to the smoothing of the texture variation (LU et al., 2012; ATTARCHI; GLOAGUEN, 2014). Preliminary tests using the Jeffries–Matusita (JM) distance (RICHARDS; JIA, 2006) indicated that the textural parameters extracted using a 5 × 5 window size, in the southwest direction and at the level of quantization of 64 bits were the most appropriate for separating the classes in both data. In order to select different regions of the spectrum and less correlated bands without greatly increasing the dataset, the textural metrics were calculated for three spectral bands corresponding to green, red and NIR regions of hyperspectral data (565, 679, and 780 nm), and four bands corresponding to blue, green, red and NIR regions of WV-2 data (480, 550, 660 and 800 nm).

Table 3.10- Texture features computed in this study for hyperspectral and WV-2 data.

Texture feature	Abbreviation	Equation
Angular second moment	SM	$SM = \sum_{i,j=0}^{N-1} \{p(i,j)^2\}$
Contrast	Con	$Con = \sum_{i,j=0}^{N-1} p_{i,j}(i-j)^2$
Variance	Var	$Var = \sum_{i,j=0}^{N-1} (i-\mu)^2 p(i,j)$
Homogeneity	Hom	$Hom = \sum_{i,j=0}^N \frac{p_{i,j}}{1+(i-j)^2}$
Correlation	Cor	$Cor = \sum_{i,j=0}^N p_{i,j} \frac{[(i-\mu)(j-\mu)]}{\sqrt{(\sigma^2 i)(\sigma^2 j)}}$
Entropy	Ent	$Ent = \sum_{i,j=0}^{N-1} p_{i,j}(-\ln p_{i,j})$
Dissimilarity	Dis	$Dis = \sum_{i,j=0}^{N-1} p_{i,j} 1-j $
Textural mean	Mean	$Mean = \frac{\sum_{i=1}^N p_{xi}}{N}$

Note:  $i$  is the row number;  $j$  is the the column number;  $p_{ij}$  is the normalized value in the cell  $i,j$ ;  $N$  is the number of rows or columns.

Source: Author's production.

Different VIs were computed using the ENVI 5.3 according to the specific wavelengths available in each data. For the hyperspectral data, besides the NDVI, the PRI, PSRI and PSSR were computed (Table 3.11). Due to the lower number of spectral bands in comparison with the hyperspectral data, and for being more influenced by the illumination angles, more VIs were computed for the WV-2 data. In this case, different band combinations were used to calculate NDVI and SR indices.

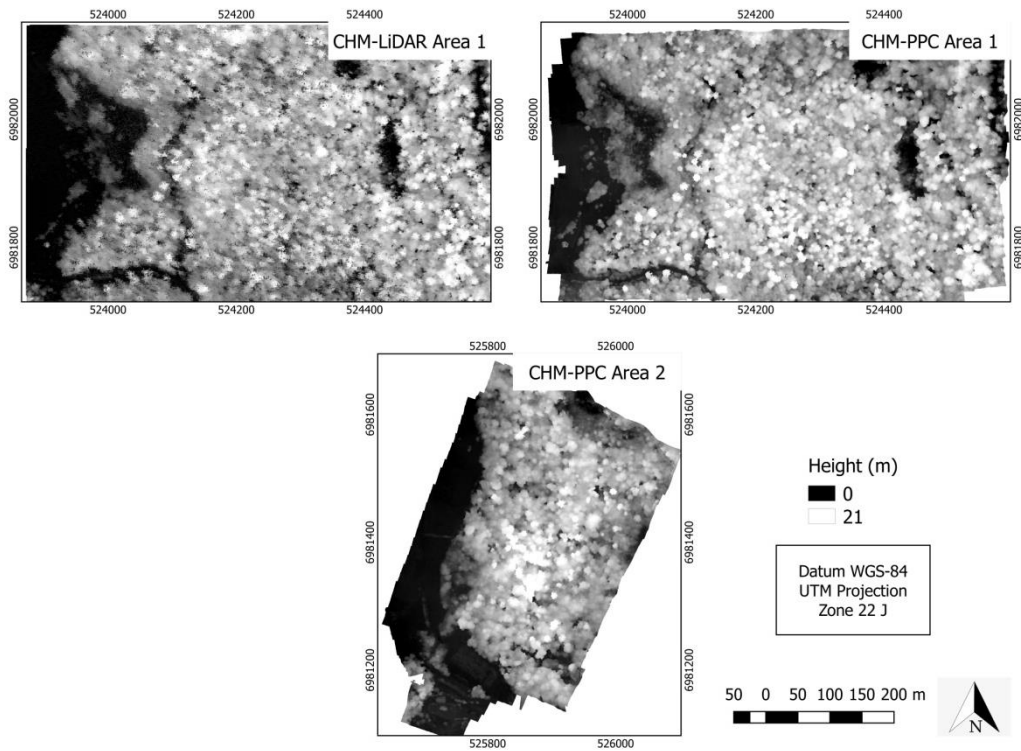
Table 3.11- Vegetation indices extracted from hyperspectral (hyper) and WorldView-2 (WV-2) data.

Data	Vegetation Index	Equation	Reference
Hyper	Normalized Difference Vegetation Index	$NDVI = \frac{\rho_{750} - \rho_{650}}{\rho_{750} + \rho_{650}}$	Rouse et al. (1973)
	Photochemical Reflectance Index	$PRI = \frac{\rho_{535} - \rho_{565}}{\rho_{535} + \rho_{565}}$	Gamon et al. (1992)
	Plant Senescence Reflectance Index	$PSRI = \frac{\rho_{679} - \rho_{506}}{\rho_{750}}$	Merzlyak et al. (1999)
	Pigment Specific Simple Ratio	$PSSR = \frac{\rho_{819}}{\rho_{679}}$	Blackburn (1998)
WV-2	Simple Ratio	$SR(6,5) = \frac{\rho_{720}}{\rho_{660}}$	Birth and Macvey (1968)
	Simple Ratio	$SR(7,5) = \frac{\rho_{810}}{\rho_{660}}$	
	Simple Ratio	$SR(8,5) = \frac{\rho_{910}}{\rho_{660}}$	
	Normalized Difference Vegetation Index	$NDVI(6,5) = \frac{\rho_{720} - \rho_{660}}{\rho_{720} + \rho_{660}}$	Rouse et al. (1973)
	Normalized Difference Vegetation Index	$NDVI(7,5) = \frac{\rho_{810} - \rho_{660}}{\rho_{810} + \rho_{660}}$	
	Normalized Difference Vegetation Index	$NDVI(8,5) = \frac{\rho_{910} - \rho_{660}}{\rho_{910} + \rho_{660}}$	
	Normalized Difference Vegetation Index	$NDVI(8,4) = \frac{\rho_{910} - \rho_{610}}{\rho_{910} + \rho_{610}}$	
	Green Normalized Difference Vegetation Index	$GNDVI(7,3) = \frac{\rho_{810} - 550}{\rho_{810} + \rho_{550}}$	Gitelson et al. (1996)
	Optimized Soil Adjusted Vegetation Index	$OSAVI = \frac{\rho_{810} - \rho_{660}}{\rho_{810} + \rho_{660} + 0.16}$	Rondeaux et al. (1996)

Source: Author's production.

Two CHMs were computed in this study (Figure 3.12) using the raster calculator tool of QGIS (QGIS DEVELOPMENT TEAM, 2017). One of them was calculated by the subtraction between the DSM, derived from the PPC, and the DTM, derived from LiDAR data. The spatial resolution was 0.22 m for Area 1, and 0.24 m for Area 2. The second CHM was calculated with both DSM and DTM extracted from LiDAR data, called CHM-LiDAR. Due to the lower density of points of the LiDAR data, the CHM-LiDAR was calculated with 1 m of spatial resolution. The latter one was used only in association with the WV-2 data for the successional forest stages classification.

Figure 3.12- Canopy height models (CHMs) used in this study.



Source: Author's production.

The last set of features comprehends six elevation metrics (Table 3.12) extracted from the UAV-PPC. The features were computed using the lidR package (ROUSSEL et al., 2018) in the R program (R DEVELOPMENT TEAM, 2018). To compute these features, an area-based approach with 0.5 m spatial resolution was adopted, chosen to ensure that there were no missing values in the resulting data. It was verified that the features extracted from a normalized PPC did not bring significant information to the datasets, because the values were very close to those obtained using the CHM. In order to check which one would be used in this study, classification tests were conducted in both areas using features derived from the non-normalized PPC (raw PPC data) and features resulting from the normalized PPC, where there was a subtraction between the points elevation values and the corresponding DTM values conducted point-by-point, i.e. individually. For Area 1, the non-normalized PPC features greatly improved the accuracy of the classification results, while for Area 2 the results coming from both data sets, non-normalized and normalized PPC features, were very similar. This can be probably ascribed to the fact that

the analyzed species in Area 1 present subtle variations in elevation (positioning in the terrain) and height, and such variations can be masked by the normalization procedure (Figures 3.7 and 3.8). Such assumptions may not hold for Area 2. Anyway, the non-normalized PPC features were kept in both cases for the sake of standardization.

Table 3.12- Features extracted from the high density photogrammetric point clouds.

PPC Feature	Description
zmax	maximum height of all points within each pixel
zmean	mean of all height points within each pixel
zq90	90th percentile of height distribution within each pixel
zq70	70th percentile of height distribution within each pixel
zq5	5th percentile of height distribution within each pixel
zentropy	entropy of height distribution within each pixel

Source: Author's production.

### 3.7 Feature selection and variable importance

In order to check the importance of each feature in tree species classification, the JM distance was considered because was widely used in such application (DALPONTE et al., 2012; 2013; 2015; FERREIRA, 2019; SOTHE et al., 2019a). The JM distance among the distributions of two classes  $\omega_i$  and  $\omega_j$  is as follows (Equation 3.1):

$$JM_{ij} = \left\{ \int_x \left[ \sqrt{p(x|\omega_i)} - \sqrt{p(x|\omega_j)} \right]^2 dx \right\}^{1/2} \quad (3.1)$$

It can be rewritten according to the Bhattacharyya distance  $B_{ij}$  (Equation 3.2):

$$JM_{ij} = \sqrt{2\{1 - \exp[-B_{ij}]\}} \quad (3.2)$$

The JM has upper and lower bounds that vary between 0 and  $\sqrt{2}$  ( $\approx 1.414$ ), with higher values indicating the total separability of the class pairs in the bands being used (RICHARDS; JIA, 2006). Besides the feature importance, the JM distance was also used as a separability criterion of a search strategy for the FS process. In this situation, a wrapper method, the sequential forward floating selection (SFFS) algorithm (PUDIL et al., 1994) was adopted because it is considered a fast suboptimal search strategy (DALPONTE et al., 2013). It is characterized by the presence of both forward and backward selection steps at each iteration. This “floating” behavior allows one to reconsider the selected features at each step, reducing the possibility to stop in a local maximum of the separability measure

(DALPONTE et al., 2012; 2013). When associated with a search strategy, the JM distance tends to saturate when the optimal number of features is reached. After the saturation point, any feature added does not increase the class separability. In this study, the set of features that corresponds to the saturation point of the distance was selected. The process was conducted in the R program using the hyperspectral dataset composed by all the features (*full* dataset described in Section 3.8) and the ITC samples.

To check the importance of the variables used in successional forest stages classification, the mean decrease in Gini index (MDG) was used. The MDG is a feature importance statistic produced by RF averaging Gini indices of the individual trees (BREIMAN, 2001). A higher MDG indicates higher variable importance, conversely, the least important variable will have the smallest MDG values (LOUPPE et al., 2013). The MDG was computed using the *full* dataset of hyperspectral and WV-2 data associated with the RF algorithm available in Waikato Environment Knowledge Analysis (WEKA) (HALL et al., 2009). Because the MDG only provides the importance value of each feature, not selecting a set of features, the selection was made performing a cross validation each time that one less important band was removed. If the accuracy started to decrease, no more features were removed.

### **3.8 Dataset composition**

After the feature extraction and selection, different datasets were composed to perform the classifications of tree species and successional stages (Table 3.13).

Table 3.13- Description of the datasets according to the features used in the classification process. Hyperspectral (Hyper) and WorldView-2 (WV-2) data.

Data	Dataset Name	VNIR	CHM	PPC	MNF	GLCM	VI	Total features
Hyper	VNIR	25	-	-	-	-	-	25
	VNIR_CHM	25	1	-	-	-	-	26
	VNIR_PPC	25	-	6	-	-	-	31
	VNIR_PPC_CHM	25	1	6	-	-	-	32
	VNIR_PPC_CHM_MNF	25	1	6	8	-	-	40
	VNIR_PPC_CHM_GLCM	25	1	6	-	24	-	56
	VNIR_PPC_CHM_VI	25	1	6	-	-	4	36
	VNIR_PPC_CHM_MNF_VI	25	1	6	8	-	4	44
	VNIR_MNF_GLCM_VI	25	-	-	8	24	4	61
	MNF_PPC_CHM	-	1	6	8	-	-	15
	MNF_PPC_CHM_VI <sup>1</sup>	-	1	6	8	-	4	19
	MNF_CHM <sup>2</sup>	-	1	-	8	-	-	09
	FSRF <sup>2</sup>	6	1	5	3	15	-	30
	FSJM-A1 <sup>1</sup>	18	1	6	7	10	4	46
	FSJM-A2 <sup>1</sup>	21	1	6	4	14	3	49
<i>full</i>	25	1	6	8	24	4	68	
WV-2	VNIR <sup>2</sup>	8	-	-	-	-	-	08
	VNIR_CHM- LiDAR <sup>2</sup>	8	1	-	-	-	-	09
	VNIR_CHM-LiDAR_MNF <sup>2</sup>	8	1	-	5	-	-	14
	VNIR_CHM- LiDAR_GLCM <sup>2</sup>	8	1	-	5	32	-	46
	VNIR_CHM- LiDAR_VI <sup>2</sup>	8	1	-	-	-	9	18
	VNIR_MNF_GLCM_VI <sup>2</sup>	8	-	-	5	32	9	54
	MNF_CHM- LiDAR <sup>2</sup>	-	1	-	5	-	-	06
	FSRF <sup>2</sup>	3	1	-	-	6	5	15
<i>full</i> <sup>2</sup>	8	1	-	5	32	9	55	

Note: <sup>1</sup>Dataset only used in tree species classification; <sup>2</sup>Dataset only used in successional forest stages classification; A1= Area 1; A2= Area 2; FSRF= Feature Selection Random Forest; FSJM= Feature Selection Jeffries-Matusita.  
Source: Author's production.

### 3.9 Segmentation and ITC delineation

For the classification of the successional forest stages, the multiresolution region growing (MRG) segmentation available in eCognition was applied to both the hyperspectral and WV-2 data. Three spectral bands of each data and the CHM (CHM-LiDAR in the case of WV-2) were used as input data. Since this level of classification is less detailed comparing with ITC delineation, the segmentation parameters were empirically chosen using a trial-and-error approach (Table 3.14).

Table 3.14- Segmentation parameters of multiresolution region growing (MRG) algorithm used in successional forest stages classification.

<b>Parameter</b>	<b>Hyperspectral</b>	<b>WV-2</b>
w_color	0.5	0.5
w_shape	0.5	0.5
w_compact	0.5	0.5
w_smooth	0.5	0.5
Scale	60	50

Source: Author's production.

For the ITC delineation, more careful tests were conducted, and three segmentation methods were tested: the MRG segmentation; the `itcIMG` function of `itcSegment` package (DALPONTE et al., 2015); and a graph cut method named multiclass cut followed by recursive cut (MCRC), proposed by Lee et al. (2016; 2017).

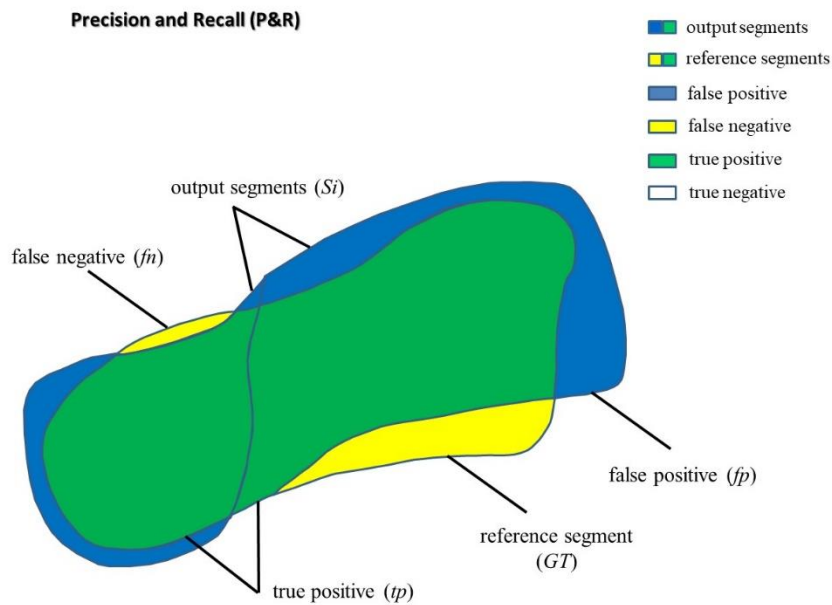
Three experiments were conducted using the MRG algorithm. For the first one, only three hyperspectral bands were used, two in the visible region (565 and 679 nm) and one in the NIR region (780 nm). In the second experiment, besides the bands, the CHM was also considered in the segmentation process (MRG\_CHM experiment). The segmentation parameters were optimized using the Segmentation Parameter Tuner (SPT) software (ACHANCCARAY et al., 2014). Based on reference ITCs, an optimization function (in this case, Precision and Recall- P&R) (Figure 3.13) interacts with the segmentation algorithm to determine the optimal set of parameters. As an optimization method, a hybrid strategy was adopted (QUIRITA et al., 2016; SOTHE et al., 2019c) in which, first, the Differential Evolution (STORN; PRICE, 1997) is applied to identify a promising initial solution, and then it is refined by the Nelder-Mead (NELDER; MEAD, 1965) function. The segmentation parameter tuning for the MRG algorithm was executed with 30 iterations and each of them was run three times in order to avoid a bias selection of a minimum local as seed point, and to ensure that the algorithm converges prior to that. The parameters automatically chosen were visually refined in the segmentation process executed in eCognition (Table 3.15).

The third experiment with the MRG method consisted in refining the segmentation results by means of the JM distance (MRG\_CHM\_JM



experiment). This distance was used as a criterion to merge homogeneous segments based on their spectral separability (FERREIRA et al., 2014; 2016). The JM distance was computed using the mean of the pixels in each tested segment and estimated using all the VNIR bands. Two neighboring segments with a low JM distance may belong to the same class and therefore can be merged if the distance is below a pre-defined threshold. After a set of empirical tests, the combination of parameters for the segmentation algorithm that produced the best result was: minimum size of a region (T)=40 pixels; JM threshold=0.2. To avoid an excessive merging, a criterion in which each segment could be merged only one time was applied. The results were visually verified after each iteration.

Figure 3.13- Illustration of the Precision and Recall (P&R) metric used as optimization function and one of the evaluation metrics.



As for the second segmentation method, the itcIMG function of the itcSegment package was tested using the NIR band centered at 819 nm. The segmentation parameters of itcIMG were empirically defined (Table 3.15).

Table 3.15- Final parameters chosen for MRG and itcIMG segmentation methods.

<b>Method</b>	<b>Parameter</b>	<b>Area 1</b>	<b>Area 2</b>
<b>MRG</b>	w_color	0.4	0.5
	w_shape	0.6	0.5
	w_compact	0.4	0.6
	w_smoot	0.6	0.4
	Scale	20	20
<b>itcIMG</b>	searchWinSize	25	25
	TRESHSeed	0.65	0.65
	TRESHCrown	0.3	0.35
	DIST	10	10
	th	0.2	0.1

Source: Author's production.

The MCRC segmentation was conducted in Matlab (MATHWORKS, 1996) program using the code available at <https://github.com/jl626/MCRC>. First, priors were computed based on the CHM, using a localmaxima function in QGIS software. These priors correspond to the highest values of CHM, which are usually associated with the top of the crowns. After that, the segmentation was driven using the raw PPC keeping the default parameters of the code.

Besides the visual assessment, some metrics were used to evaluate the ITC delineation results. The metrics were computed in SPT based on 20 reference ITCs manually delineated in the images. Räsänen et al. (2013) state that different segmentations may stand out as being best when different metrics are used, because each metric may evaluate different aspects of the generated segments (e.g., area, shape). Thus, three different metrics were used for this task: a) P&R (PONT-TUSET; MARQUES, 2013); b) Area Fit Index (AFI) (LUCIEER; STEIN, 2002); and c) Segmentation Covering (C) (PONT-TUSET; MARQUES, 2013). Brief introductions to these methods are summarized on Table 3.16.

Table 3.16- Metrics used to evaluate the ITC delineation.

Metric	Equation	Description
<i>P&amp;R</i>	$P = \frac{tp}{tp + fp}$ $R = \frac{tp}{tp + fn}$ $P\&R = 1 - \frac{2PR}{P + R}$	<p>Measures the trade-off between Precision and Recall considering segmentation as a classification process (Pont-Tuset and Marques 2013). Given a segment from the segmentation outcome <i>S</i> and its respective reference (or ground truth) segment <i>GT</i>, four different regions can be defined:</p> <p>True positives (tp): correspond to the pixels that belong to both <i>S</i> and <i>GT</i>;</p> <p>False positives (fp): pixels that belong to <i>S</i> but not to <i>GT</i>.</p> <p>False negatives (fn): pixels that belong to <i>GT</i> but not to <i>S</i>.</p> <p>True negatives (tn): pixels that do not belong to <i>S</i> or <i>GT</i>.</p> <p>Range [0,1], where “<i>P&amp;R</i> = 0” correspond to a perfect segmentation.</p>
<i>AFI</i>	$AFI = \frac{1}{N_{GT}} \sum_{k=1}^{N_{GT}} \frac{A_k - Al.i.k}{A_k}$	<p>Addresses the polygon form, being over/undersegmentation evaluated by analyzing the overlapping area between segmentation and reference (Lucieer and Stein 2002). It is defined as the ratio between the area and the perimeter of a segment.</p> <p><i>A<sub>k</sub></i> is the area, in pixels, of a reference segment <i>C<sub>k</sub></i> in the <i>GT</i> image and <i>Al.i.k</i> is the area, in pixels, of the segment, in the segmentation outcome, with the largest intersection with the reference segment. <i>N<sub>GT</sub></i> is the number of segments in the <i>GT</i> image.</p> <p>“<i>AFI</i> = 0” indicates a perfect overlap.</p>
<i>C</i>	$O(C_i, C_j) = \frac{ C_i \cap C_j }{ C_i \cup C_j }$ $= 1 - \frac{1}{N_{GT}} \sum_{C_t \in GT}  C_t  \cdot \max_{C_i \in S} O(C_i, C_t)$	<p>Measures the overlap between two segments, <i>C<sub>i</sub></i> in a segmentation <i>S</i> and <i>C<sub>j</sub></i> in its <i>GT</i>, where <math>\sum N_{GT}</math> is the total number of pixels in the original image. The segmentation covering (<i>C</i>) only considers the segments with the maximum overlap between them. It matches each proposed segment to a true segment, with which the proposed segment has the largest overlapping ratio and computes the sum of such optimal overlapping ratios weighted by relative segment sizes.</p> <p>Range [0,1], and “<i>C</i> = 0” stands for a perfect segmentation.</p>

Source: Adapted from Gu et al. (2018) and Sothe et al. (2019c).

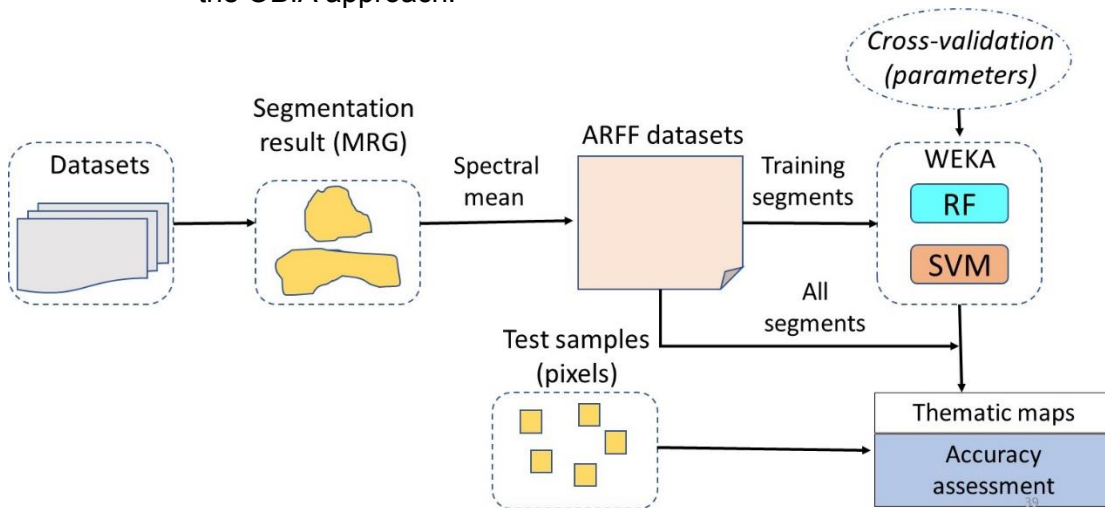
### 3.10 Successional forest stages classification

For the successional stages classification, the OBIA approach was executed using the image corresponding to the *full* datasets of WV-2 and hyperspectral data. From these datasets, the spectral means corresponding to each feature of the segments (generated in the segmentation step) were extracted. Then, the segments labeled in the samples collection were separated to compose the training datasets. These datasets were converted to Attribute-Relation File

Format (ARFF) and the classifications were performed in the software WEKA (HALL et al., 2009). The *libSVM* library was used for SVM, and the *RandomForest* library for RF algorithm. Different feature combinations were tested in these classifications, described in Table 3.13.

The classification parameters were selected based on a 10-fold cross-validation. The best result for each algorithm and dataset was applied to the full database to generate the maps and to evaluate the final results. Figure 3.14 depicts the OBIA classification scheme used in successional forest stages classification.

Figure 3.14- Methodological flowchart of successional forest stages classification using the OBIA approach.



Source: Author's production.

### 3.11 Tree species classification

Three machine learning (SVM, wSVM and RF) and one deep learning method (CNN) were tested. For the wSVM and CNN algorithms, only the pixel-based classification was conducted, while for the SVM and RF, three approaches were compared: a) the pixel-based classification, b) the pixel-based classification associated with the MV rule, and c) OBIA. Details on these experiments and adopted parameters are given below.

### 3.11.1 Machine learning methods

At the pixel-based classification, all the hyperspectral datasets described in Table 3.13 were used in SVM and RF algorithms. For wSVM classifier, only the VNIR, VNIR\_CHM\_PPC and the best result of SVM for each area were tested.

The pixel-based classifications using RF, SVM and wSVM were conducted in R program. The *randomForest* package (LIAW; WIENER, 2002) was used for RF classification, while the *kernlab* package (KARATZOGLOU et al., 2004) for SVM and wSVM. The algorithm parameters were defined based on a 5-fold cross validation process.

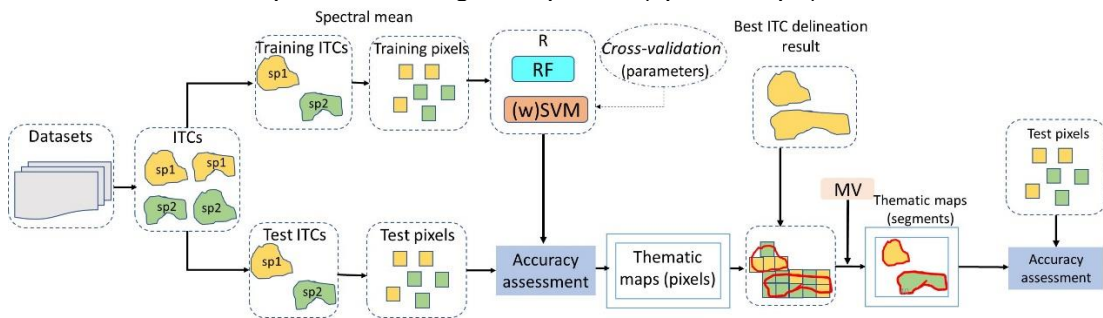
For RF, the *n tree* parameter was set to 500 trees in all the experiments. Regarding the *m try* parameter, the default value was kept, which corresponds to the square root of the total number of features used in each experiment (BREIMAN et al., 2001).

For both SVM and wSVM, the one-against-one multiclass strategy and the RBF were adopted, due to its superiority in relation to the other functions has been demonstrated in several studies (HUANG et al., 2002; DURO et al., 2012). This function has two user-defined parameters that can affect the classification accuracy: cost ( $C$ ) value used to fit the classification errors in the training data set (ADAM et al., 2014), and gamma ( $g$ ). A high value of  $C$  may overfit the model to data, while the adjustment of the  $g$  parameter will have an influence on the shape of the separating hyperplane (LI; DU, 2015). Based on cross-validation, it was observed that by varying the value of  $C$  between 1, 10, 100 and 1000, the results did not change substantially. The value 100 for this parameter presented a slightly better accuracy and was adopted for all datasets, while the  $g$  value was set during the classification process with the function *sigest* of the *kernlab*. The same process was adopted for wSVM classification. However, in this case, different weights were applied for both: each class and each sample. The algorithms for the computation of the class and sample weights were implemented in R using clustering based on k-means (NGUYEN, 2019).

For the MV rule approach, the class of each segment was assigned based on the majority class of its classified pixels. This process was conducted in the

TerraView software (INPE-DPI, 2018), using the resulting segments described in Section 3.5 associated with the best pixel-based classification results maps for each area. Figure 3.15 shows the methodological flowchart of tree species classification using the machine learning methods and the pixel-based classification and MV rule approaches.

Figure 3.15- Methodological flowchart of tree species classification using machine learning methods (SVM, wSVM and RF), pixel and MV rule approaches. Example considering two species (sp1 and sp2).



Source: Author's production.

Due the limited number of ITCs in Area 2, the OBIA approach was executed only in Area 1, using the image corresponding to the *full* dataset. From this image, spectral means of the segments belonging to the training ITCs were extracted to be used as training data. Since only few ITC samples are available, the use of one spectral mean per ITC would drastically reduce the training set. Thus, an oversegmentation result provided by the MRG algorithm was adopted, in which each ITC was represented by more than one homogeneous segment. The classification was conducted in the same way as the successional forest stages classification in WEKA, using RF and SVM algorithms (c.f. Section 3.10, Figure 3.14), but only the best dataset result according to a 5-fold cross validation was used for the final map and accuracy assessment.

### 3.11.2 Deep learning method

In this study, a CNN architecture was adopted and executed in a Python environment using Keras with TensorFlow backend (ABADI et al., 2015). The CNN architecture consisted of five convolutional layers, three pooling layers, a fully-connected layer and a classification layer (Figure 3.16). The number of kernels for each convolutional layer was 32, 32, 48, 48, 64, and 128 for the

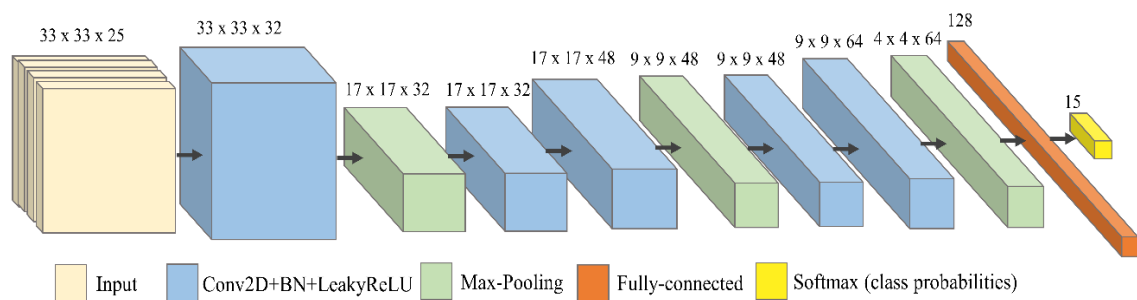
fully-connected layer, with a learning rate of  $10e^{-4}$ . After every convolution operation and the fully-connected layer, a batch normalization, followed by a leaky rectified linear unit (Leaky ReLU) activation function, was applied. In terms of training time with gradient descent, the non-saturating activation function Leaky ReLU tends to be faster than other saturating activation functions (LI Y. et al., 2017). The Adam optimizer (KINGMA; BA, 2015) parameters were set to default values. To deal with overfitting, the network was trained using early stopping and dropout regularization of 0.35 after the fully-connected layer and before the top layer. The last layer of the network (classification layer) is composed by the softmax activation function that performs a pixel-wise classification upon the learned representative features.

Considering the requirement of CNN regarding the high-dimensional number of training samples (PASUPA; SUNHEM, 2016) and aiming to balance the samples set, a data augmentation process using flip and rotation operations was applied to increase the number of training samples for the less representative classes. According to Yu et al. (2017), these operations preserve the scene topologies in remote sensing data, which is especially important for consistent classifications, but enhance the intra-class data diversity. To this end, the samples were replicated as the feature space was rotated and flipped in different directions until an amount of 15,000 pixels per class was reached. The few classes with training samples exceeding 15,000 pixels, however, were downsampled. The total number of CNN parameters varied according to the dataset: 186,896 (VNIR dataset), 194,372 (VNIR\_CHM dataset) and 239,227 (VNIR\_CHM\_PPC dataset).

In the inference step, the trained network was applied over the image to generate the classifications. To that, the CNN classifier was applied to overlapping image patches to predict the class of their central pixel using a sliding window technique with stride 1. Next, each query was spatially concatenated to obtain a classification at the same resolution of the input image. The evaluated network was designed to receive a patch of 33x33 pixels (which was defined after testing different patch sizes) and to output a probabilistic vector of size equal to the number of classes, where the index location of the highest value indicates the most probable class.

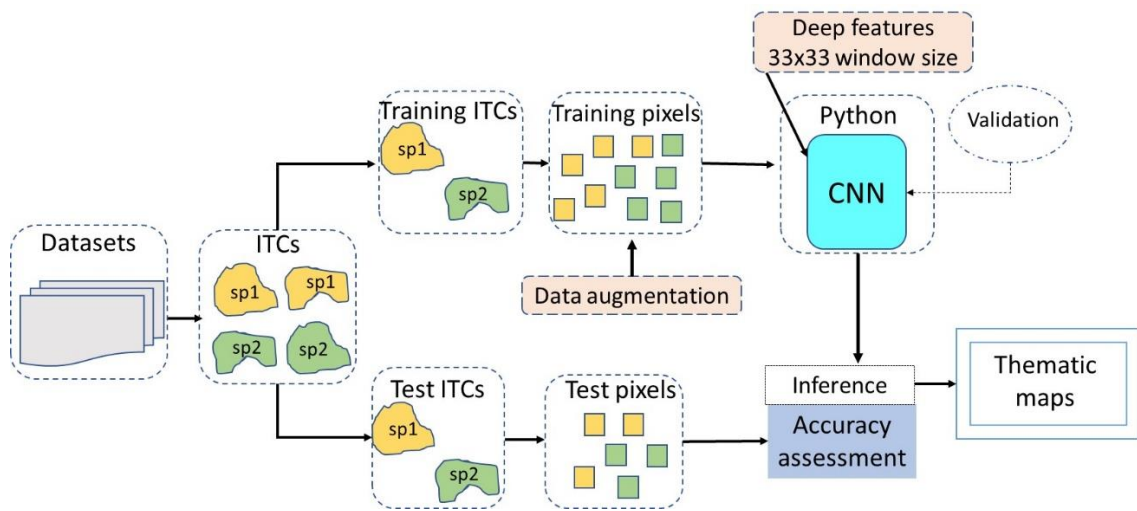
Because the CNN computes its features employing the user-defined window size, it was necessary to include a 'background' class. This procedure avoids classification errors caused by the influence of pixels related to disregarded classes, such as ground and black areas corresponding to the borders of the images. However, it is important to note that pixels classified as 'background' were not considered in the confusion matrices. Figure 3.17 depicts the methodological flowchart of tree species classification using the CNN method.

Figure 3.16- CNN architecture for Area 1 with 25 bands and 15 classes (14 tree species plus 'background' class).



Source: Author's production.

Figure 3.17- Methodological flowchart of tree species classification using the CNN method.



Source: Author's production.

### 3.12 Accuracy assessment and classification maps

To evaluate the classification results, the confusion matrices were generated based on a cross-check between the classified results and the test samples. In this case, the test samples of the successional forest stages correspond to



independent sets of random points generated for each classification result in a two-stage process. Initially, irregular polygons not including the training samples were manually delimited for each class directly in the images of both sensors, based on field observations and very high spatial resolution images as ancillary data. In a second stage, inside each of these polygons, a stratified random sampling was conducted, where 200 and 400 pixels for SS<sub>1</sub>, and 200 and 400 pixels for SS<sub>2</sub> were selected in the WV-2 and hyperspectral data, respectively. Due to the greater representativeness of SS<sub>3</sub>, 500 and 1,000 pixels were selected for this class in the WV-2 and hyperspectral data, respectively. More pixels were selected for the hyperspectral data due to their higher spatial resolution (smaller pixel size). The random selection procedure was repeated for each classification to maintain the independence among the test sets. The test samples of tree species correspond to 50% of ITCs not used in the training or validation steps. In this way, the ITC identity was kept, the classifier had no contact with the test samples during the training step and the evaluation was able to provide an unbiased sense of model effectiveness (RUSSEL; NORVIG, 2009).

From the confusion matrices, different agreement indices were calculated: (a) overall accuracy (OA); (b) precision (i. e. producer's accuracy), (c) recall (i. e. user's accuracies); (d) F-measure and; (e) *Kappa* index. The OA was calculated as the total number of correctly classified samples divided by the total number of samples. The *Kappa* index measures the agreement of prediction with the true class. This metric compares an observed accuracy with an expected accuracy, considering the random chance of classifying correctly (COHEN, 1960). Precision is the proportion of the samples that truly belong to a specific class among all those classified as that class, while recall is the proportion of samples which were classified to a specific class among all samples that truly belong to that class (NEVALAINEN et al., 2017).

In tree species classification, for a given class, differences in precision and recall accuracy indicate if the species is more or less abundant in test data predictions relative to its true abundance. High precision values relative to recall (alternatively low commission error and high omission error) means that the model was careful when predicting the species, but in doing so, there were

many individuals of that species that were not predicted. Ultimately, the species is underpredicted or had fewer individuals of that species than the ones actually existing in reality. Lower precision values relative to recall (high commission error and low omission error) means that the model was able to include all the individuals which belong to that species, but it also included individuals of other classes. Lastly, the species is overpredicted or included more individuals of that species than the ones actually existing in reality. Evaluating the relative magnitude of precision and recall for a given class is useful when the application of the classification is to determine relative abundances of species (GRAVES et al., 2016). Finally, the F-measure is a harmonic mean of precision and recall and was calculated to measure the performance at the class level (Equation 3.3):

$$F = 2 \times \frac{(\textit{precision} \times \textit{recall})}{(\textit{precision} + \textit{recall})} \quad (3.3)$$

F-measure increases with higher precision and recall and/or greater similarity between precision and recall. While the F-measure does indicate the similarity of precision and recall measurements (more similarity implies a higher F-measure), it does not indicate which metric is larger or smaller.

The z test was applied to the *Kappa* indices of all classifications with a significance level of 5%, i.e., a confidence interval of 95%. The value of the normal distribution of z is obtained by the ratio of the difference between two given Kappa indices to the difference between their respective variances (SKIDMORE, 1999). If  $z > 1.96$ , the test is significant, and the null hypothesis is rejected, leading us to conclude that there exists a significant difference between the obtained results.

All the classification maps of the successional forest stages were generated, and the non-forest areas were removed by a CHM mask, considering pixel values below 0.5 m and a spectral mean of NDVI < 0.2. These thresholds were visually chosen because they separated forest from non-forest areas, including few buildings existing in Area 1. On the other hand, mapping of tree species were restricted to the sample locations, since the production of species maps in tropical ecosystems is puzzling, as hundreds of species compose the canopy

and a large degree of uncertainty is obtained when classifying all the image pixels (FÉRET; ASNER, 2013; FERREIRA et al., 2016). For the visualization of correctly classified ITCs, the raster calculator of QGIS was used. When the raster with the sample ITC species was equal to the classified species, the sample locations were classified accordingly. Otherwise, a zero value was assigned. This procedure aimed to evaluate the potential of each method to correctly label the pixels within the ITCs when considering all the samples (training and test sets). A probability approach has not been used in this case, as reported by Ferreira et al. (2016), because in some cases it was verified that even correctly classified ITCs presented low probability.

As a final step, even aware of the uncertainties in expanding the tree species classification over the entire area, the maps of the two best classification results of each area were made to analyze the representativeness and abundance of each species, and to evaluate if two different classifiers present some agreement in classification. In this case, the non-forest areas were removed by a CHM mask, considering pixel values below 2 m. Expanding the classification, the species that were not included in this study were misclassified, but they were not included in the confusion matrices reckoning.

## **4 RESULTS**

### **4.1 Successional forest stages mapping**

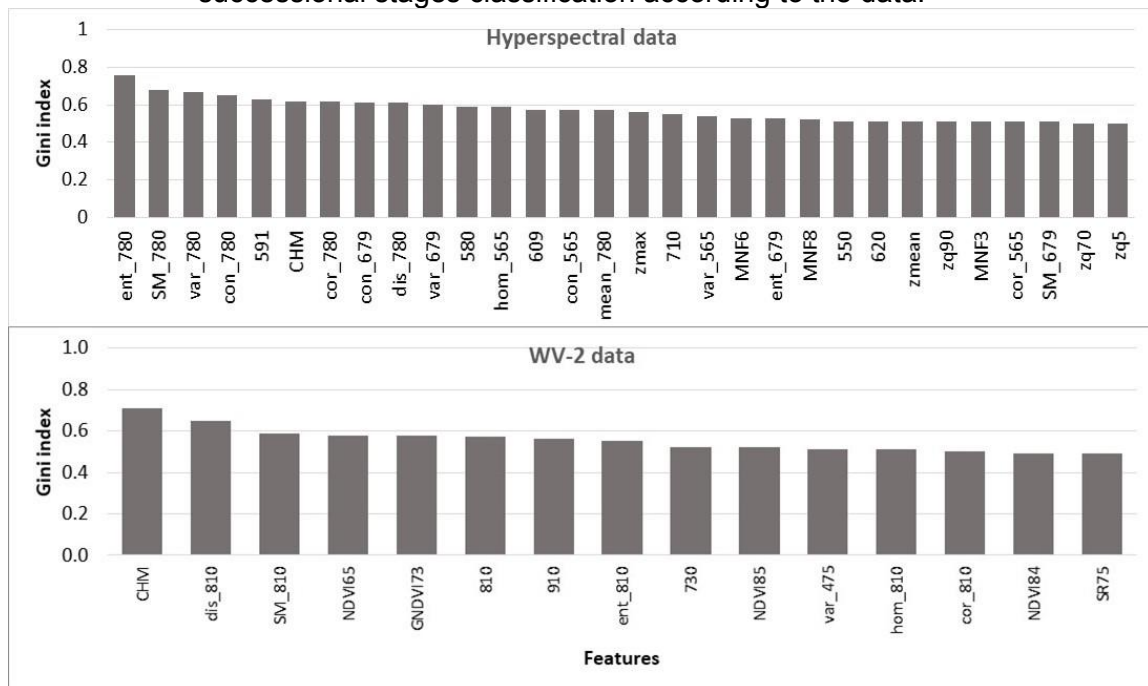
#### **4.1.1 Feature selection and variable importance**

Figure 4.1 shows the importance values of the most important variables for successional forest stages classification according to the data. When hyperspectral data were used, the most important features were four textural metrics extracted from the band centered at 780 nm (ent, SM, var and con – Table 3.10), followed by the CHM. The VNIR bands centered at the green region (580, 591 and 609 nm) stand out from the other spectral bands, while the sixth and eighth MNFs were more important than the first ones. Regarding the PPC features, only the zmax presented a higher importance value compared to other features.

For WV-2, the CHM was the most important feature, followed by two textural metrics of the NIR band (SM and dis) and two VIs (NDVI65 and GNDVI73). The NIR bands centered at 810 and 910 nm were more important compared to other bands. In these data, the VIs presented higher values than the hyperspectral data.

In the FSRF dataset, 15 features of WV-2 and 30 of the hyperspectral data were selected (Figure 4.1). The feature selected from the WV-2 data comprised three VNIR bands, the CHM, six texture features and five VIs. From the hyperspectral data, six VNIR bands, the CHM, five PPC features, three MNF and 15 texture features were selected.

Figure 4.1- MDG values reported as the Gini index of the feature selected for the forest successional stages classification according to the data.

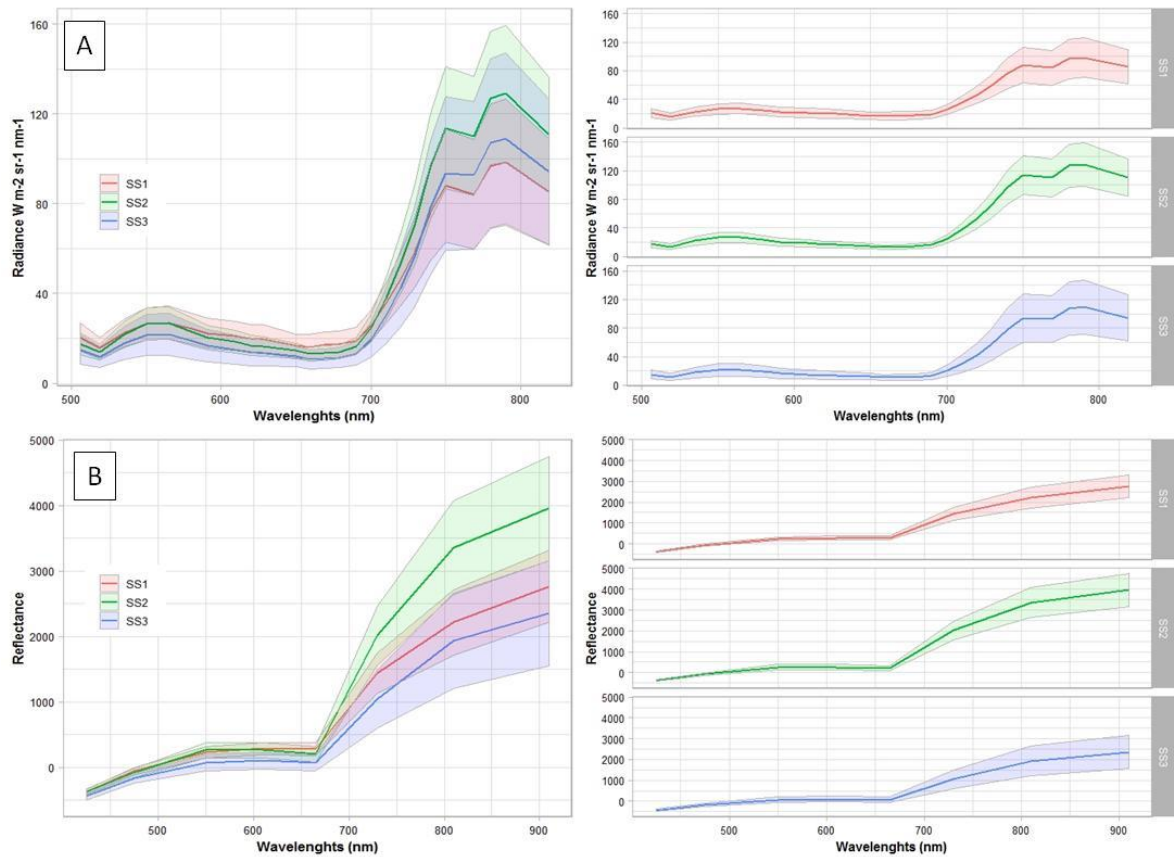


Source: Author's production.

In order to check the spectral separability among the classes, reflectance (WV-2 data) and radiance (hyperspectral data) curves of the three successional stages were generated considering the mean spectral response and the standard deviation of the training samples (Figure 4.2). It can be observed that in the visible region (480–660 nm) the successional stages present similar reflectance values, while in the NIR region (700–900 nm) the stages tend to be more separable from each other. In the NIR range of both data, the SS<sub>2</sub> presented relatively higher radiance values than the other stages, followed by the SS<sub>1</sub> in the hyperspectral data and the SS<sub>3</sub> in the WV-2 data.

The use of hyperspectral data allowed the construction of more detailed spectral curves in comparison with multispectral data. For instance, it can be noticed that the curves presented a slight decrease at the 775 nm region that does not appear in the WV-2 data.

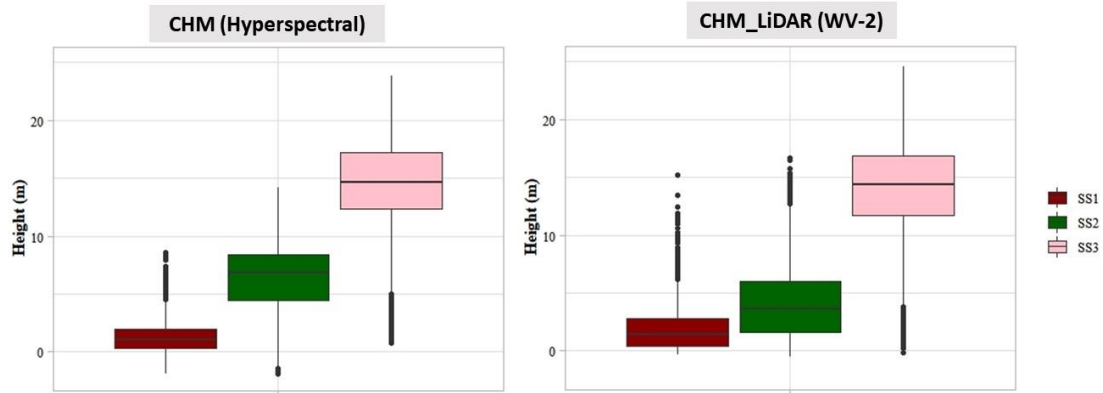
Figure 4.2- Mean reflectance (with standard deviation) of successional forest stages samples according to the data. A) Hyperspectral data; B) WV-2 data.



Source: Author's production.

The CHM was considered one of the most important features in both data. In Figure 4.3, it can be observed that it clearly discriminates the successional stages classes. As expected, the SS<sub>3</sub> presented higher height values, followed by the SS<sub>2</sub> and SS<sub>1</sub> classes. In the case of the WV-2 data, when the CHM using both DTM and DSM from LiDAR data was employed, more overlap between the SS<sub>2</sub> and SS<sub>1</sub> was observed, which can be due to the lower points density that generated the DSM in comparison with the DSM-PPC.

Figure 4.3- Boxplots showing the distribution of CHM values of the successional stages samples used in each data. The central lines within each box are the medians. The box edges represent the upper and lower quartiles. Outliers are plotted individually.

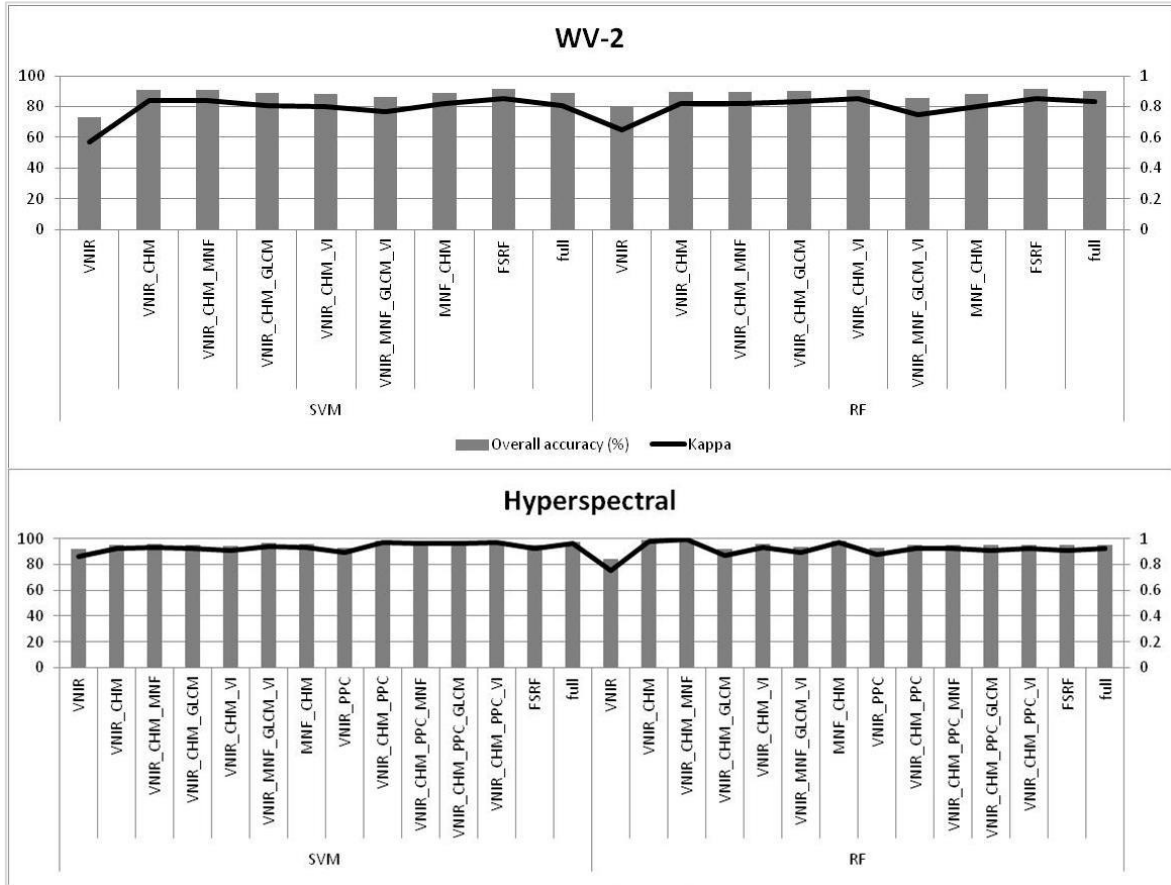


Source: Author's production.

#### 4.1.2 Classification results

Figure 4.4 shows the classification results according to the dataset and classifier for the WV-2 and the hyperspectral data. The best general result was achieved with the RF classifier associated with the VNIR\_CHM\_MNF dataset of the hyperspectral data (99.28% of OA and 0.99 of *Kappa*), similar to the VNIR\_CHM dataset performance that reached 99% of OA. The worst result using the hyperspectral data was achieved with the VNIR dataset and the RF classifier, with 84.28% of OA and *Kappa* of 0.75. For the WV-2, the best result was achieved using the RF classifier and the FSRF dataset (OA of 91.22% and *Kappa* of 0.85). Similarly to the hyperspectral data, the WV-2 data had the worst accuracy when only the VNIR dataset was employed, 73.44% of OA and 0.57 of *Kappa*, but in this case using the SVM classifier. Globally, the OAs were higher than 80% and 90% when the WV-2 and the hyperspectral data were respectively employed.

Figure 4.4- *Kappa* and overall accuracy (OA) of successional forest stages classification for each classifier/dataset according to the data used.



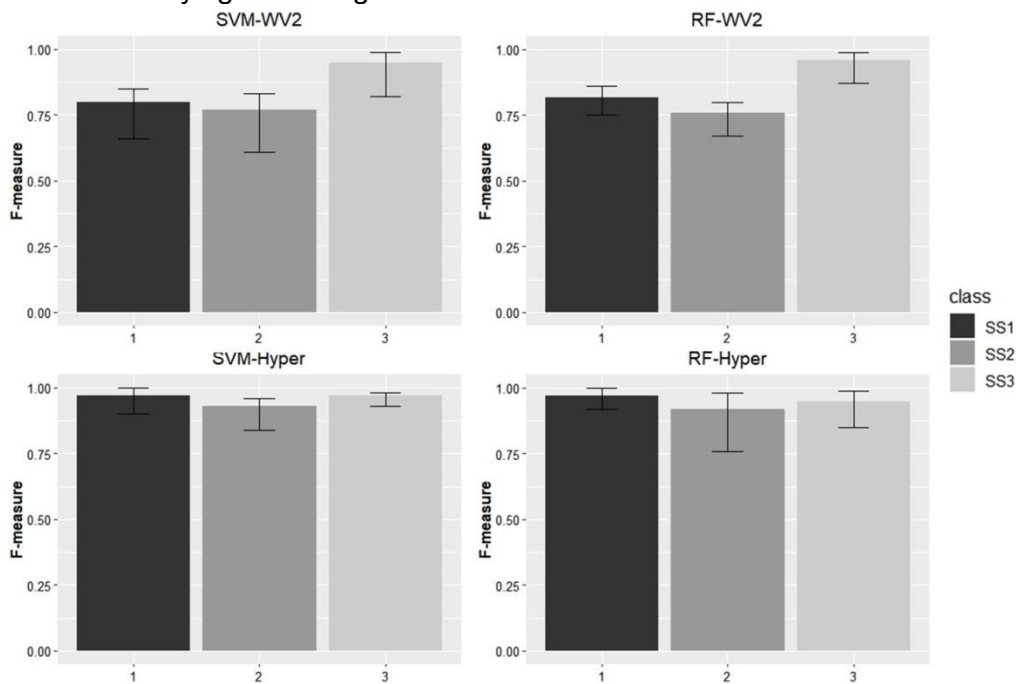
Source: Author's production.

The incorporation of the CHM-LiDAR to the WV-2 VNIR dataset led to a marked increase of 17.34% and 9% in OA when the SVM and RF were respectively employed. When the CHM was added to the VNIR dataset of the hyperspectral data, an increase of 3.17% and 14.72% for each classifier (SVM and RF) was observed. The incorporation of the PPC features to the VNIR dataset of the hyperspectral data led to a smaller increase in comparison with the addition of the CHM, 1.39% and 8.45% for SVM and RF classifiers, respectively. When the CHM and the PPC features were applied together with the VNIR bands of the hyperspectral data, the accuracy increased up to 6.34% and 11% for the SVM and RF in relation to the VNIR dataset. The inclusion of other features, such as GLCM, MNF and VIs, to the VNIR dataset also led to a significant increase in comparison with the VNIR dataset for both data. For WV-2, the increase was about 5% to 13% when the RF and SVM were respectively employed, while for the hyperspectral data, these values reached 9% and 5%.



Figure 4.5 shows the F-measure of each successional stage class. Using the hyperspectral data, except for the VNIR dataset, all the classes presented F-measures higher than 0.85. The SS<sub>1</sub> and SS<sub>3</sub> classes reached F-measures equal to 1 in some datasets. When the WV-2 data were employed, an F-measure higher than 0.75 for all classes in most datasets was reached. In these data, the SS<sub>3</sub> reached a better accuracy than the other two stages, with an F-measure higher than 0.9 in most cases. This can be explained by the fact that in these data the CHM presented some overlap between SS<sub>1</sub> and SS<sub>2</sub> as shown in Figure 4.3.

Figure 4.5- F-measure of successional stages classes according to the data and classifier. The black bars indicate the minimum and maximum values varying according to the dataset.



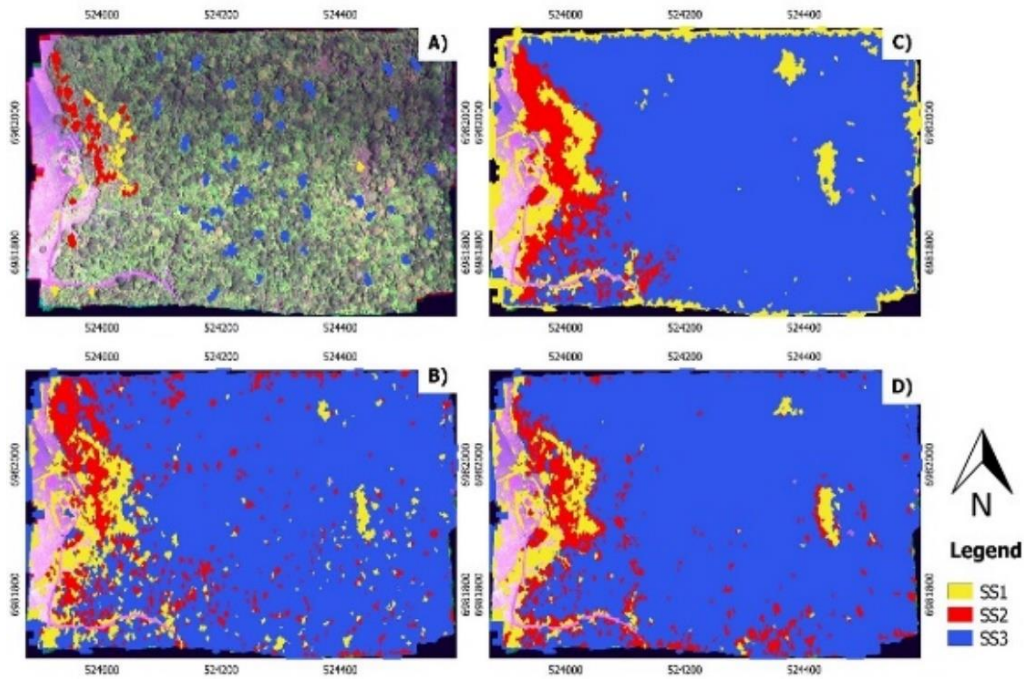
Source: Author's production.

In the confusion matrices (Appendix A), it can be observed a higher confusion occurred in the SS<sub>2</sub> stage. It was somehow expected, since this stage presents characteristics of both SS<sub>1</sub> and SS<sub>3</sub> stages. When the WV-2 data were employed, more confusion occurred between SS<sub>1</sub> and SS<sub>2</sub> stages, while for the hyperspectral data, the highest confusion was between the SS<sub>2</sub> and SS<sub>3</sub> stages.

### 4.1.3 Classification maps

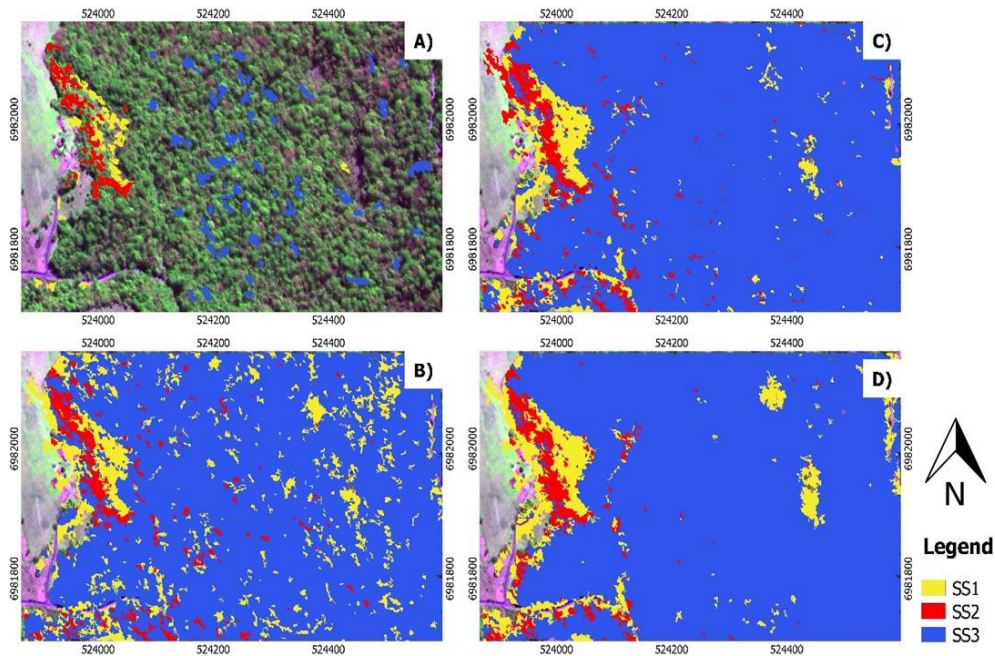
Figure 4.6 shows the classification maps using the hyperspectral and the WV-2 data and different datasets. In general, the classification results agreed with the sampled classes (Figure 4.6 A and 4.7 A). It can be observed that when only the VNIR bands were used, more SS<sub>3</sub> segments were wrongly classified as SS<sub>1</sub> or SS<sub>2</sub> stages in both data (WV-2 and hyperspectral). In this case, the incorporation of height information of the CHM provided a better discrimination of this stage (Figure 4.6, C-D and 4.7, C-D).

Figure 4.6- Classification maps using the hyperspectral data. A) Hyperspectral image (R14G23B4 composition) with the sample locations; B) SVM classifier associated with the VNIR dataset; C) SVM classifier associated with the VNIR\_CHM\_PPC dataset; D) RF classifier associated with the VNIR\_CHM\_MNF.



Source: Author's production.

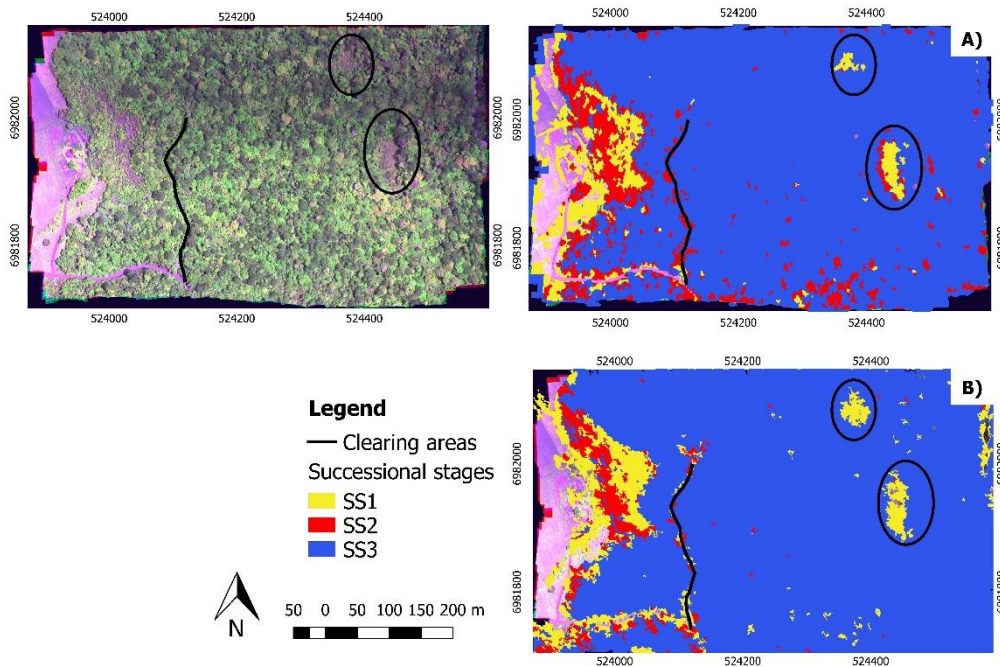
Figure 4.7- Classification maps using the WV-2 data. A) WV-2 image (R3G8B5 composition) with the sample locations; B) SVM classifier associated with the VNIR dataset; C) SVM classifier associated with the VNIR\_CHM dataset; D) RF classifier associated with the FSRF dataset.



Source: Author's production.

One visible difference in the classification maps that did not appear in the confusion matrices concerns two clearings existing in the area (rounded shape), and one deforestation trail (linear shape) (Figure 4.8). These regions were classified as SS<sub>1</sub> or SS<sub>2</sub> in the classification maps generated by the best result of each input data (Figure 4.8, A-B), which is somehow expected, because they have shorter vegetation when comparing with its surroundings. On the other hand, parts of them were wrongly classified as SS<sub>3</sub> when using the VNIR dataset (Figures 4.6 and 4.7, B).

Figure 4.8- Clearing areas highlighted in the hyperspectral data. A) Best classification result using the hyperspectral data (RF with VNIR\_CHM\_MNF dataset); B) Best classification result using the WV-2 data (RF with FSRF dataset).



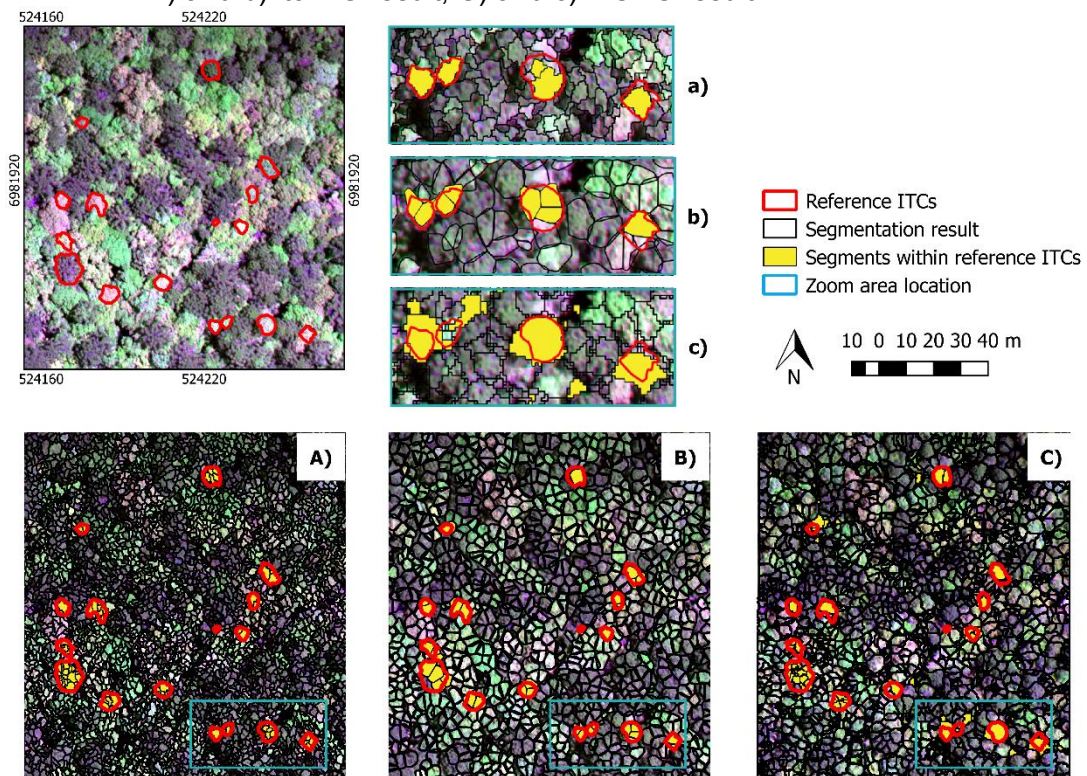
Source: Author's production.

## 4.2 Tree species mapping

### 4.2.1 Individual tree crown delineation

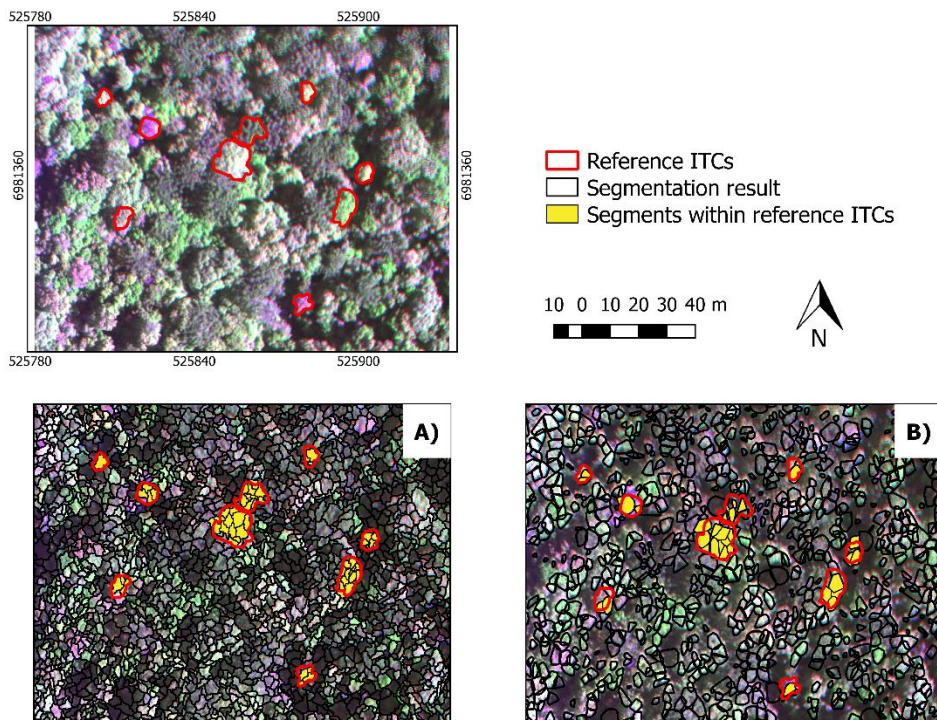
The three methods tested for ITC delineation provided different results. Even with the parameter optimization, the MRG algorithm resulted in an oversegmentation for most of the crowns in both areas (Figure 4.9 and 4.10). The MCRC method (only applied to Area 1) tended to group more than one ITC, even different species, into the same segment (Figure 4.9, C), while the itcIMG missed some ITCs, mainly in Area 2 (Figure 4.10, B).

Figure 4.9- Example of segmentation results for Area 1: A) and a) MRG\_CHM result; B) and b) itcIMG result; C) and c) MCRC result.



Source: Author's production.

Figure 4.10 – Example of segmentation results for Area 2. A) MRG result; B) itcIMG result.



Source: Author's production.

The segmentation results according to the evaluation metrics are presented in Table 4.1. Except for MRG and MCRC experiments in Area 1, the metric values of P&R were relatively low, demonstrating that the segmentation results had a good balance between over and undersegmentation. The closer the value is to zero, the better the spatial match between reference and the resulting segments, and thus the larger the overlapping area between them (EISANK et al., 2014). For all methods in both areas, AFI presented a value higher than 0, suggesting that the reference polygons are usually larger in size compared with the references (GU et al., 2018).

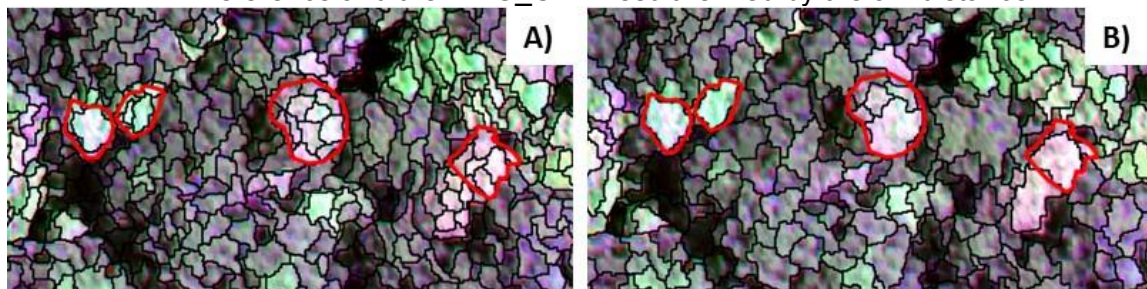
Despite its oversegmentation, the MRG had in general a good performance in capturing the edges of the ITCs (Figure 4.11, A). The inclusion of the CHM in the MRG method reduced the excessive number of segments, bringing some improvement in delineation. After the MRG\_CHM has been refined by the JM distance (MRG\_CHM\_JM), a better delineation was reached (Figure 4.11, B), with some ITCs represented by only one segment. The visual evaluation corroborates the metric values, since the *P&R* values reduced from 0.29 to 0.15, the *AFI* values reduced from 0.58 to 0.45, and the *C* values from 0.74 to 0.62 with the MRG\_CHM\_JM experiment. This result indicates that besides reducing the oversegmentation, the definition of the edges from the crowns was also improved according to the *C* metric. The itcIMG method also achieved a good result in Area 1 according to the evaluation metrics (Figure 4.9, B). The *AFI* values suggested an oversegmentation when using the MCRC, which occurred for some ITCs (Figure 4.9, C). This method was not suitable to capture the edges of the ITCs, missing some trees and involving different species in the same segment, which can be due to the use of the PPC instead of an optical image. The MRG results for Area 2 were similar to those obtained for Area 1, while the itcIMG results missed some ITCs in that area, what can be observed in Figure 4.10 (B).

Table 4.1- Evaluation metrics for each segmentation result according to the study area.

Metric	Area 1					Area 2		
	MRG	MRG_CHM	MRG_CHM_JM	itcIMG	MCRC	MRG	CHM	itcIMG
P&R	0.29	0.17	0.15	0.15	0.57	0.19	0.17	0.22
AFI	0.58	0.45	0.45	0.43	0.77	0.45	0.55	0.46
C	0.74	0.62	0.62	0.62	0.91	0.69	0.41	0.74

Source: Author's production.

Figure 4.11- Details of segmentation results in Area 1 with reference ITCs highlighted in red color. (A) Reference and the MRG segmentation result; (B) Reference and the MRG\_CHM result refined by the JM distance.



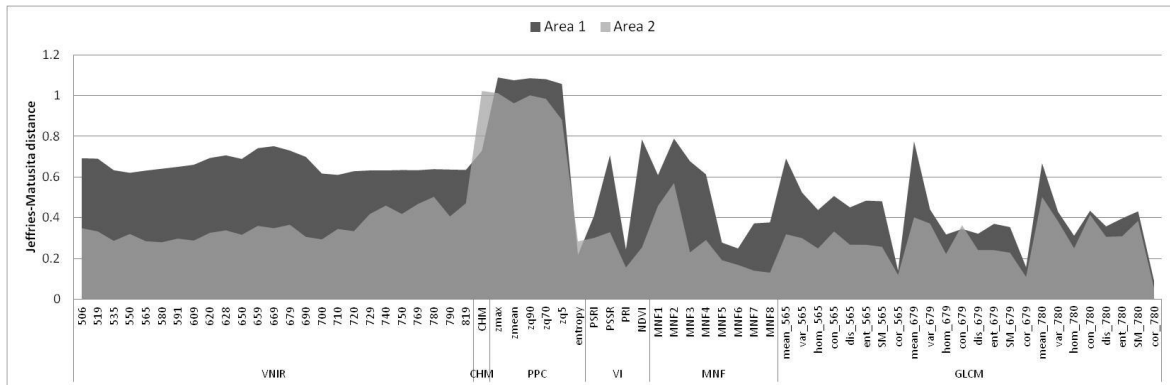
Source: Author's production.

#### 4.2.2 Feature selection and variable importance

Figure 4.12 shows the importance of each feature according to the JM distance. The elevation metrics extracted from the PPC and the CHM were the most important features to discriminate the tree species classes of both areas. Other important features for Area 1 were two VIs (PSSR and NDVI), the GLCM texture mean of the band centered at 679 nm, and the second and the third MNF output bands. In this area, all the VNIR spectral bands showed similar JM values, except for a slight increase in the red region.

For Area 2, besides the CHM and PPC features, the first and second MNF together with the GLCM texture mean of the bands centered at 679 and 780 nm were regarded as the most important ones. The bands located in the NIR region were slightly more important than the visible bands for this area, while the VIs were less important as compared with Area 1. For Area 2, all the features presented a lower JM value than Area 1, what probably impacted the classification accuracies (c.f. Section 4.2.3).

Figure 4.12- Variable importance according to JM distance for each area.

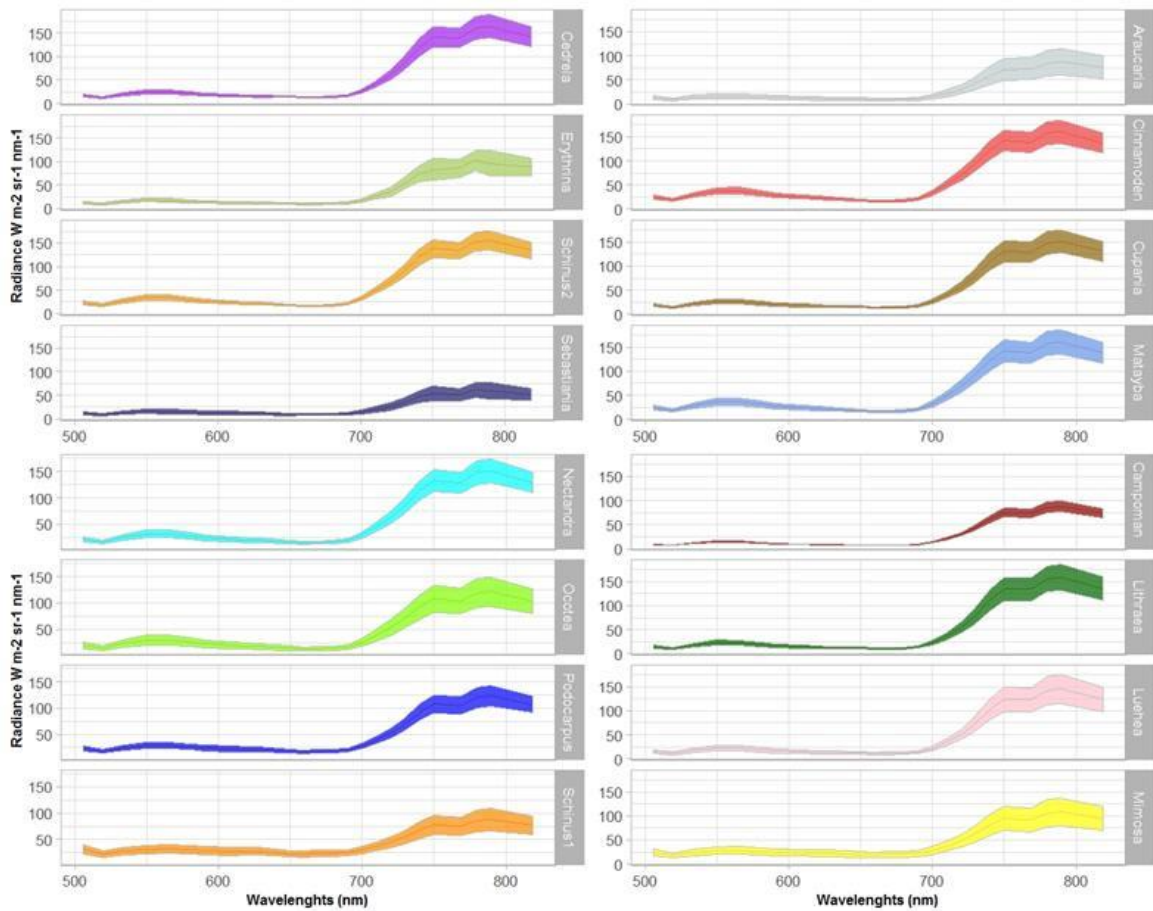


Source: Author's production.

Figures 4.13 and 4.14 show the spectral profile (and standard deviation) of each class separately and together, respectively. It can be observed that in the region corresponding to the visible range (506–700 nm), the difference in radiance values of the tree species is limited. *Araucaria angustifolia* had the lowest radiance values in the entire spectrum for both areas. The discrimination among the tree species seems to be more pronounced in the NIR range (700–819 nm). However, even in this region, some groups of species are hardly discernible, mainly for Area 1, such as: *Araucaria angustifolia*, *Campomanesia xanthocarpa* and *Schinus sp1*; *Podocarpus lambertii*, *Mimosa scabrella* and *Ocotea sp.*; and *Cinnamodendron dinisii* and *Schinus sp2*. For Area 2, three species are clearly distinguishable in this region: *Araucaria angustifolia*, *Sebastiania commersoniana* and *Schinus sp1*, what explains the higher JM values in the NIR region for this area.

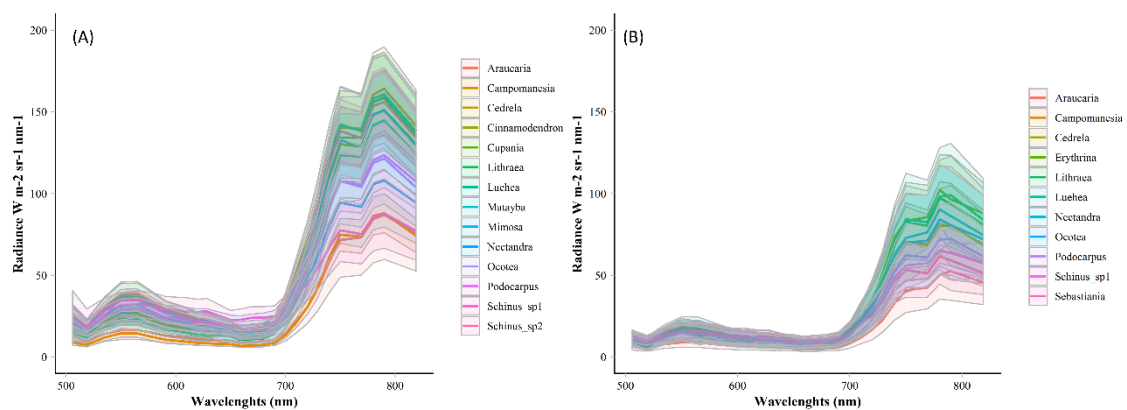


Figure 4.13- Mean reflectance (with standard deviation) of tree species classified in this study.



Source: Author's production.

Figure 4.14- Spectral profile mean of all tree species for Area 1 (A) and Area 2 (B).



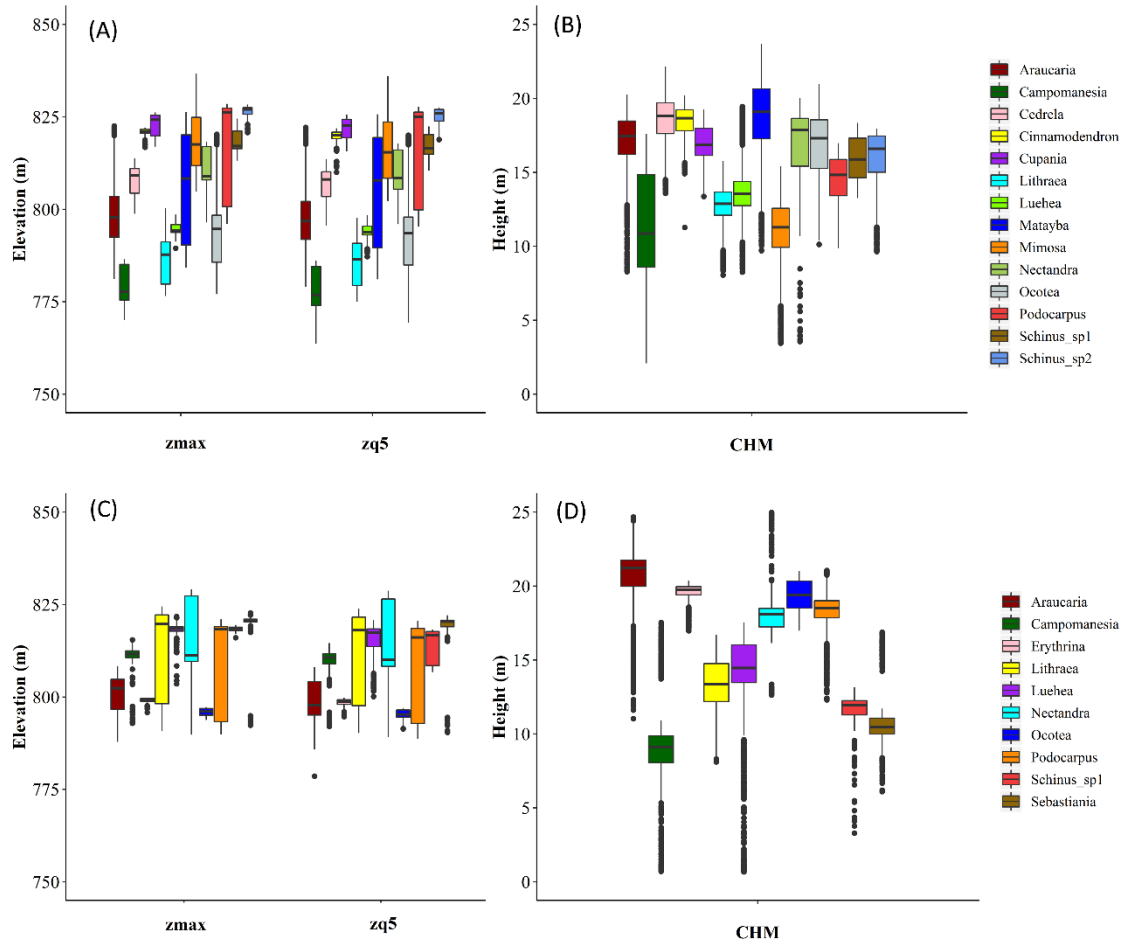
Source: Author's production.

Figure 4.15 shows the distribution of two PPC features (zmax and zq5) and the CHM values extracted from the samples of each class. It can be noticed that the CHM clearly separates some tree species classes. *Campomanesia*

*xanthocarpa* presented lower height values in both study areas. Besides this species, *Mimosa scabrella*, *Luehea divaricata* and *Lithraea brasiliensis* can be discriminated from other species due to their lower heights in Area 1 (Figure 4.15, B). In Area 2, even more species can be differentiated with the CHM, what justifies the higher importance value assigned to this feature in this area (Figure 4.15, D).

It can be observed in Figure 4.15 (A) that the PPC features discriminate some classes that were not separated with the CHM in Area 1, such as both *Schinus* classes, *Campomanesia xanthocarpa*, *Lithraea brasiliensis*, *Luehea divaricata*, and *Ocotea* sp. On the other hand, in Area 2 (Figure 4.15, C), with the exception of *Ocotea* sp. and *Sebastiania commersoniana*, other species presented great overlaps in PPC values, which accounts for the smaller increase in accuracy when these features were employed (c. f. Section 4.2.3).

Figure 4.15- Boxplots showing the distribution of the PPC and the CHM values of the tree species samples in Area 1 (A, B) and Area 2 (C, D). The central lines within each box are the medians. The boxes edges represent the upper and lower quartiles. Outliers are plotted individually.



Source: Author's production.

In the FS using the SFFS method associated with the JM distance, 46 features were selected for Area 1, comprising all the groups of generated features: 18 of the 25 VNIR bands corresponding to different regions of the spectrum, all the PPC features, the CHM, 7 MNFs, 10 textural features and all the VIs. For Area 2, 49 features were selected: 21 VNIR bands, all the PPC features, the CHM, 4 MNFs, 3 VIs and 14 textural features.

### 4.2.3 Classification results

#### 4.2.3.1 Overall results

The classification results employing different datasets, classifiers and approaches are presented in Table 4.2 and summarized in Table 4.3, while the best results are showed in Figure 4.16.

Table 4.2- Classification results according to the area/classifier/dataset/approach. Best result for each classifier/approach is highlighted. <sup>1</sup>Best results for each area that does not significantly differ among themselves.

Classifier	Dataset	Area 1		Area 2	
		OA (%)	Kappa	OA (%)	Kappa
SVM	VNIR	62.67	0.57	48.91	0.41
	VNIR_CHM	67.90	0.63	<b>63.93</b>	<b>0.58</b>
	VNIR_PPC	68.61	0.64	51.50	0.44
	VNIR_CHM_PPC	76.04	0.73	63.10	0.57
	VNIR_CHM_PPC_MNF	76.55	0.73	62.35	0.57
	VNIR_CHM_PPC_GLCM	74.56	0.71	61.98	0.56
	VNIR_CHM_PPC_VI	<b>77.66</b>	<b>0.74</b>	62.94	0.57
	VNIR_CHM_PPC_MNF_VI	77.10	0.74	62.25	0.56
	VNIR_MNF_GLCM_VI	61.91	0.56	47.34	0.39
	MNF_CHM_PPC	68.97	0.64	56.47	0.50
	MNF_CHM_PPC_VI	73.60	0.70	59.06	0.53
	FSJM	74.68	0.71	57.66	0.52
	<i>full</i>	72.59	0.68	61.90	0.56
	MV best SVM result for each area*	<b>82.52</b>	<b>0.80<sup>1</sup></b>	<b>75.47</b>	<b>0.72<sup>1</sup></b>
	OBIA (VNIR_CHM_PPC_VI)	73.52	0.69	-	-
RF	VNIR	59.24	0.52	48.60	0.40
	VNIR_CHM	<b>66.06</b>	<b>0.60</b>	66.02	0.61
	VNIR_PPC	51.46	0.44	63.43	0.58
	VNIR_CHM_PPC	55.91	0.50	65.45	0.60
	VNIR_CHM_PPC_MNF	57.54	0.52	65.94	0.60
	VNIR_CHM_PPC_GLCM	56.60	0.50	66.51	0.61
	VNIR_CHM_PPC_VI	55.59	0.49	65.61	0.60
	VNIR_CHM_PPC_MNF_VI	56.71	0.51	66.21	0.61
	VNIR_MNF_GLCM_VI	59.17	0.52	48.97	0.40
	MNF_CHM_PPC	52.72	0.46	61.72	0.56
	MNF_CHM_PPC_VI	53.82	0.47	63.28	0.57
	FSJM	56.32	0.50	52.08	0.46
	<i>full</i>	57.74	0.52	<b>67.37</b>	<b>0.62</b>
	OBIA(VNIR_CHM_PPC_VI_MNF)	<b>68.00</b>	<b>0.63</b>	-	-

continue

Table 4.2- Conclusion.

Classifier	Dataset	Area 1		Area 2	
		OA (%)	Kappa	OA (%)	Kappa
wSVM	VNIR	56.42	0.51	48.98	0.42
	VNIR_CHM_PPC	74.37	0.71	65.15	0.60
	best SVM result for each area*	<b>75.03</b>	<b>0.72</b>	<b>65.60</b>	<b>0.60</b>
CNN	VNIR	<b>84.37</b>	<b>0.82<sup>1</sup></b>	<b>74.95</b>	<b>0.71<sup>1</sup></b>
	VNIR_CHM	79.19	0.76	73.12	0.69
	VNIR_CHM_PPC	77.17	0.74	70.36	0.65

\*Majority Vote (MV) rule and wSVM classifier applied to VNIR\_CHM\_PPC\_VI dataset in Area 1 and VNIR\_CHM dataset in Area 2.

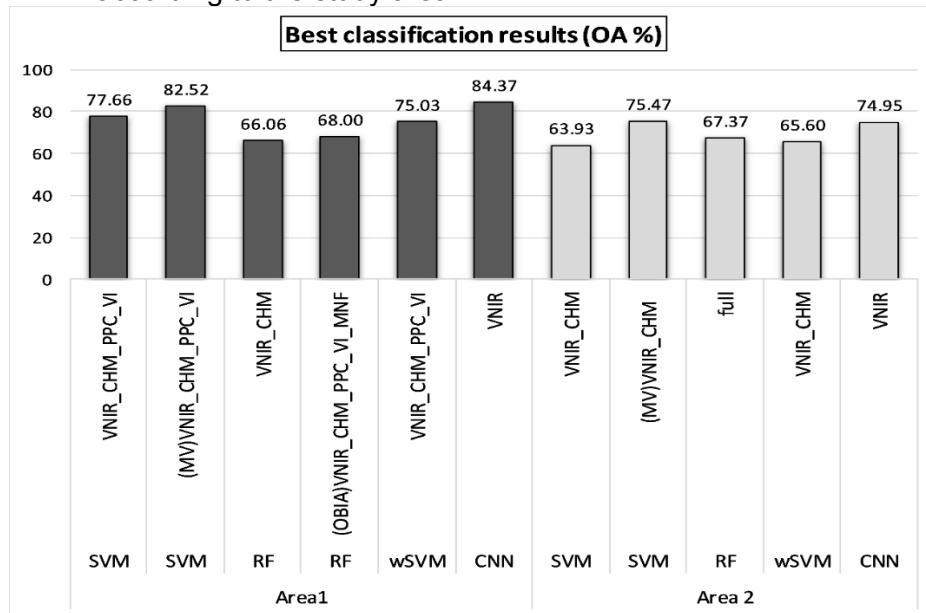
Source: Author's production.

Table 4.3- Summary of classifiers, approaches, datasets and accuracies related to tree species classification in both areas. Refer to Table 3.13 for a full description of features that compose the datasets.

Classifier	Approach	Area 1		Area 2	
		Number of datasets	Accuracy (%)	Number of datasets	Accuracy (%)
SVM	pixel	13	63-78	13	49-64
	OBIA	1	74	-	-
	MV rule	1	83	1	75
RF	pixel	13	53-66	13	49-67
	OBIA	1	68	-	-
	MV rule	1	-	1	75
wSVM	pixel	3	56-75	3	49-65
CNN	pixel	3	77-84	3	70-75

Source: Author's production.

Figure 4.16- Summary of the best results reached by each classifier/dataset/approach according to the study area.



Source: Author's production.

For Area 1, the best general result was achieved by the CNN classifier associated with the VNIR dataset (OA 84.37% and *Kappa* 0.82). The second best result for this area was reached when the MV rule approach was applied to the SVM classification associated with the VNIR\_CHM\_PPC\_VI dataset (OA 82.52% and *Kappa* 0.80). For Area 2, the opposite occurred: the best general result was achieved after the MV approach was applied to the SVM classification using the VNIR\_CHM dataset (OA 75.47% and *Kappa* 0.72), while the second best result was reached by the CNN algorithm associated with the VNIR dataset (OA of 74.95% and *Kappa* of 0.71).

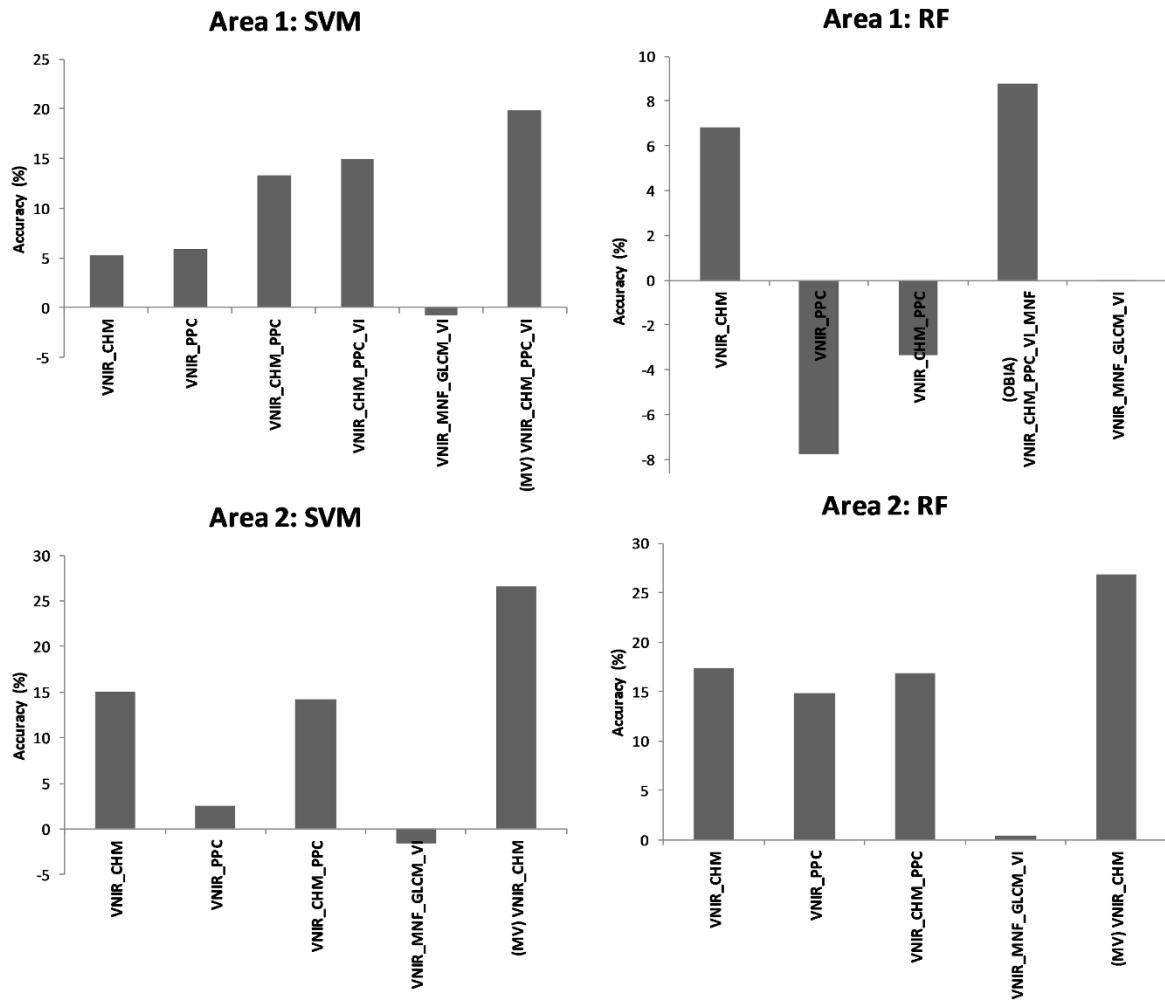
When the pixel-based approaches were compared, the CNN classifier reached the best results for both areas. The SVM classifier had a significant superior performance than the RF in Area 1. On the other hand, it was slightly below to the RF in Area 2. The OBIA approach (applied only to Area 1) using the SVM algorithm presented a lower accuracy comparing with the SVM adopting a pixel-based classification. In its turn, the RF classifier had a slight increase in OA with OBIA when compared with the pixel-based RF classification. The wSVM had a superior performance than the conventional SVM only in Area 2.

Figure 4.17 illustrates the increase (or decrease) in OA when different features were added, and different approaches were employed for the SVM and RF methods related to the classifications using only the VNIR dataset and the pixel-based approach. It is possible to notice that the performance of the classifiers varied according to the dataset and study area. Except for the RF applied to Area 1, the inclusion of the CHM and PPC features led to an increase between 13% and 17% in relation to the VNIR dataset. For Area 1, the SVM associated with the VNIR\_CHM\_PPC\_VI dataset reached the best result, with an increase of 15% in relation to the VNIR dataset. The same increase (15%) was observed for the SVM in Area 2 in relation to the VNIR dataset when the VNIR\_CHM and VNIR\_CHM\_PPC datasets were employed.

For the RF classifier in Area 1, the best result was achieved using the VNIR\_CHM, with an increase of 7% in OA compared to the VNIR dataset. When the OBIA approach was employed, the increase in relation to pixel-based classification using the VNIR dataset was about 9%, 2% more than the pixel-based approach. In Area 2, the *full* dataset allowed an increase of 19% in relation to the VNIR dataset. The inclusion of other hyperspectral features (i.e. VI, MNF and GLCM) to the VNIR dataset did not significantly change the results in both areas for neither the RF nor SVM classifiers.

When the best pixel-based classification result of the SVM algorithm was aggregated into segments using the MV rule, a marked increase of 20% and 27% was observed in relation to the VNIR dataset results for Areas 1 and 2, respectively. Comparing the MV and the pixel-based classification using the same dataset (VNIR\_CHM\_PPC\_VI for Area 1, and VNIR\_CHM for Area 2), the increase was nearly 5% and up to 11%, respectively. Contrary to machine learning classifiers, the addition of the CHM and PPC features to the VNIR dataset led to a decrease of approximately 7% and 4.5% in OA of both areas when the CNN classifier was employed.

Figure 4.17- Differences in overall accuracy with the inclusion of features and approaches in relation to VNIR dataset, SVM and RF classifiers.



Source: Author's production.

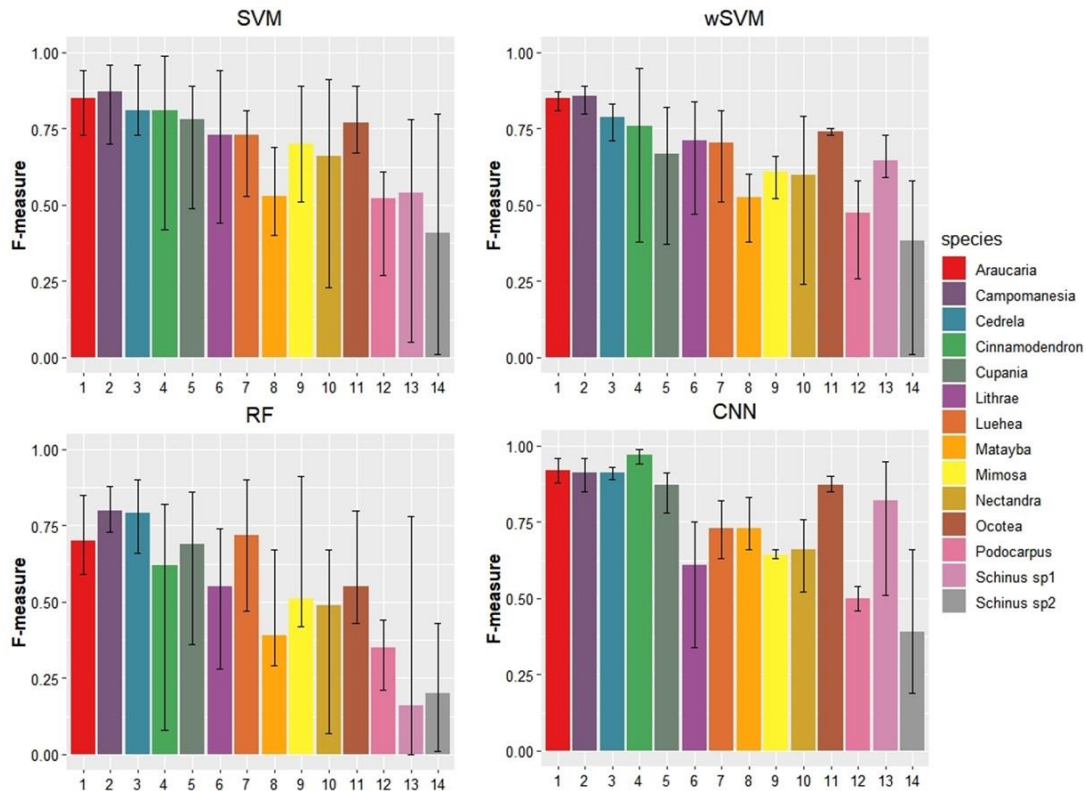
#### 4.2.3.2 Tree species classification accuracies in Area 1

Figure 4.18 shows the average F-measure of each tree species and classifier in Area 1. The black bars indicate the minimum and maximum F-values, which varied according to the dataset used by each classifier. As expected, the tree species were not equally classified, and some of them presented more variability in the F-measure values when different datasets/classifiers were employed. Regarding the classifiers, it can be observed that the RF presented higher variability in the F-measure results for most species as compared to other classifiers. Generally, classes with fewer samples presented more variability in accuracy, such as *Cinnamodendron dinisii* and both *Schinus* classes. In the case of the CNN, however, species as *Cinnamodendron dinisii*,



*Araucaria angustifolia*, *Campomanesia xanthocarpa*, *Cedrela fissilis*, *Mimosa scabrella*, *Ocotea* sp. and *Podocarpus lambertii* presented very low variability in the F-measure values, even when the dataset was altered.

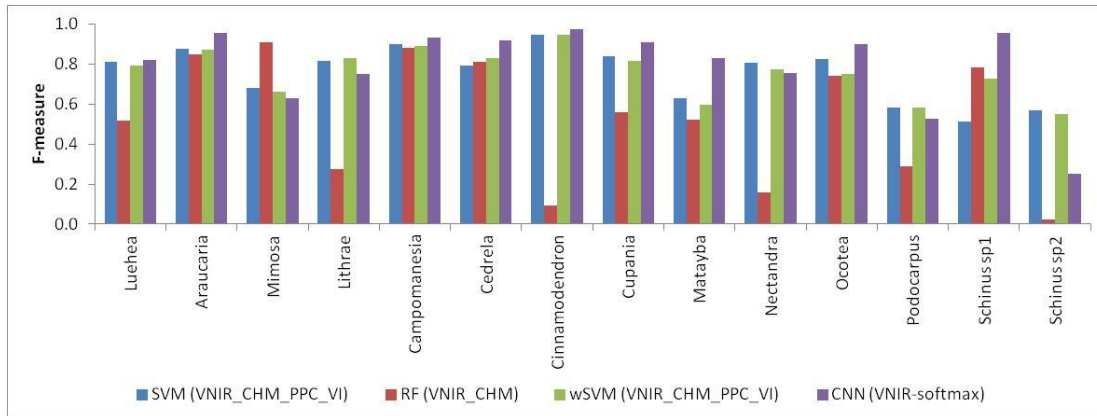
Figure 4.18- F-measure of each tree species class for Area 1 according to the classifier. Black bars indicate the minimum and maximum values varying according to the dataset.



Source: Author's production.

Figure 4.19 summarized the F-measure of tree species reached by the best result for each classifier. The CNN presented the best result for nine of fourteen tree species, with the F-measure varying between 0.8 and 1 for most of them. For *Lithraea brasiliensis*, *Nectandra megapotamica*, *Podocarpus lambertii* and *Schinus sp2*, the SVM and wSVM were the best classifiers, reaching similar results. The RF classifier achieved the highest accuracy for *Mimosa scabrella*. This classifier had the lowest performance for this area, with some species presenting F-measures below 0.5 even for the best dataset, as *Podocarpus lambertii* and *Schinus sp2*.

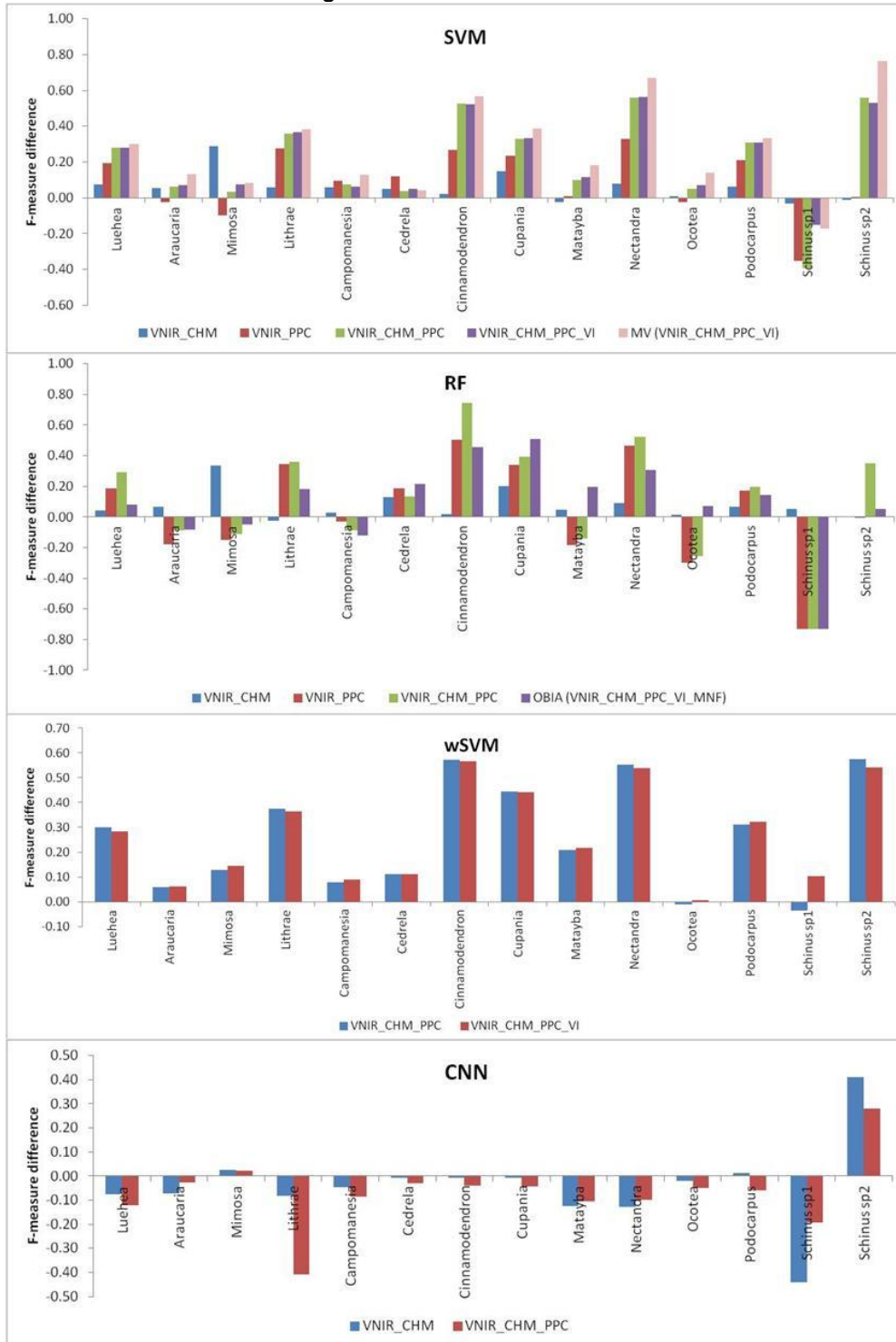
Figure 4.19- F-measure of tree species according to the best dataset result for each classifier in Area 1 considering the pixel approach.



Source: Author's production.

Regarding the datasets, when SVM, RF and wSVM classifiers were employed, the inclusion of PPC features or CHM led to a marked increase in accuracy for almost all the classes (Figure 4.20). For SVM and wSVM, the F-measure for most tree species were typically well over 0.7 when the PPC features were included in the dataset, and both methods reached similar results. When the MV rule was applied to the best SVM result, with exception of *Schinus sp1*, all the classes presented an increase in F-measure. Conversely, when the PPC features or the CHM were included in the CNN classifier, except for *Schinus sp2*, all the classes presented a decrease between 0.01 and 0.4 in F-measure. On the other hand, *Schinus sp2* presented an increase of 0.4 when the CHM was included in CNN classifier.

Figure 4.20- Difference in F-measure accuracy for each species and classifier according to the dataset/approach in relation to the pixel-based classification using the VNIR dataset in Area 1.



Source: Author's production.

The confusion matrices of Area 1 (Appendix B) depict that the incorporation of the PPC features helps to differentiate some specific classes when the SVM was used. In the datasets without the PPC features and the CHM, the main confusion among the species occurred with *Schinus sp2*, which was wrongly assigned to other classes such as *Podocarpus lambertii*, *Cupania vernalis* and *Cedrela fissilis*, and had other classes incorrectly assigned to it, namely: *Cinnamodendron dinisii*, *Matayba elaeagnoides* and *Nectandra megapotamica*. In these datasets, it also can be noticed that *Nectandra megapotamica* and *Matayba elaeagnoides* were incorrectly classified as *Ocotea sp.*, and *Nectandra megapotamica* and *Matayba elaeagnoides* confused with each other. When the PPC features and the CHM were incorporated to the datasets, these confusions were generally reduced, but *Schinus sp1* was incorrectly classified as *Mimosa scabrella*, what explains the decrease in the F-measure of that species in comparison with the use of the VNIR\_CHM dataset. The wSVM had a similar behavior to the SVM, with the difference that *Schinus sp1* presented an increase in the F-measure with the VNIR\_CHM\_PPC\_VI dataset.

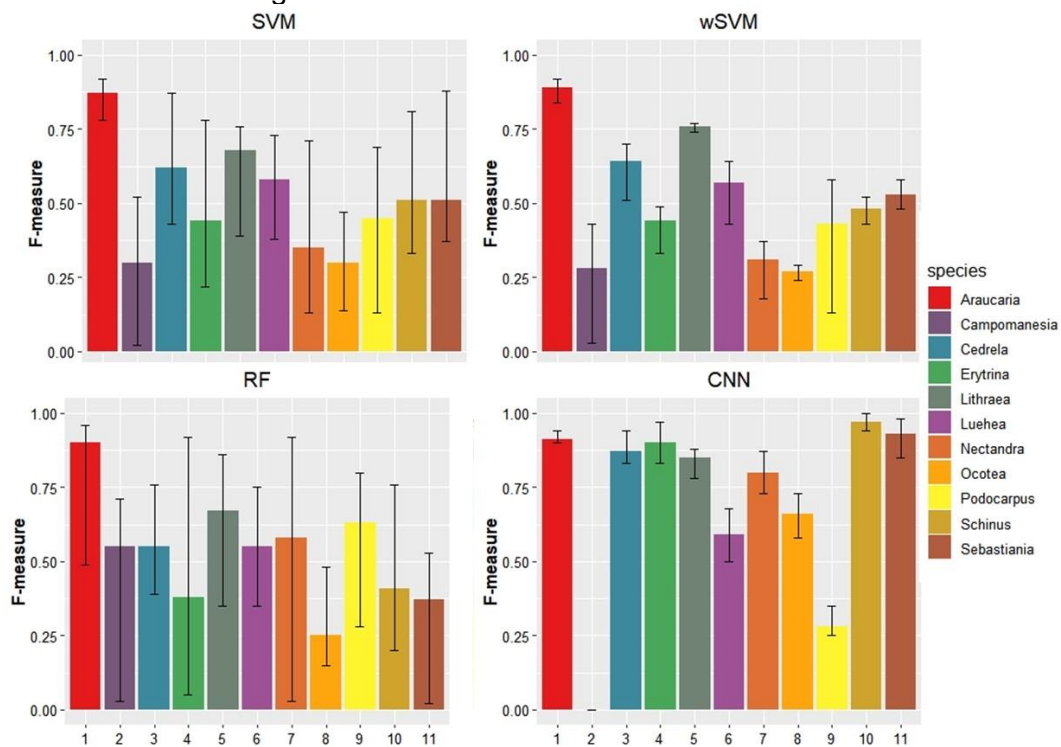
The inclusion of PPC features to RF classifier led to a decrease in F-measure of some species, which explains the lower OA of this method in comparison to the use of VNIR or VNIR\_CHM dataset. In this case, PPC features markedly decreased the accuracy of *Schinus sp1* that was wrongly assigned to *Mimosa scabrella*, and also increased the confusion among species as *Ocotea sp.* and *Matayba elaeagnoides*. Even looking the best results of each classifier, including CNN, some confusion among *Matayba elaeagnoides* and *Ocotea sp.* persisted.

#### **4.2.3.3 Tree species classification accuracies in Area 2**

Figure 4.21 shows the average, minimum and maximum F-measures for each tree species in Area 2 according to the classifier. It was observed that most tree species classes had a lower accuracy as compared with Area 1, many of them with F-measures lower than 0.6. For Area 2, the RF classifier reached a general better performance than the SVM, mainly for some tree species, such as *Campomanesia xanthocarpa*, *Nectandra megapotamica* and *Podocarpus*

*lambertii*. In this area, the wSVM classifier had a better performance than the conventional SVM, which was more evident for some classes, like *Campomanesia xanthocarpa*, *Cedrela fissilis* and *Erythrina falcata*. The CNN classifier outperformed other classifiers, presenting F-measures over 0.8 for many classes and less variability in F-measures accuracies. However, it totally misclassified the species *Campomanesia xanthocarpa*. Again, the RF presented more variability in the F-measure values.

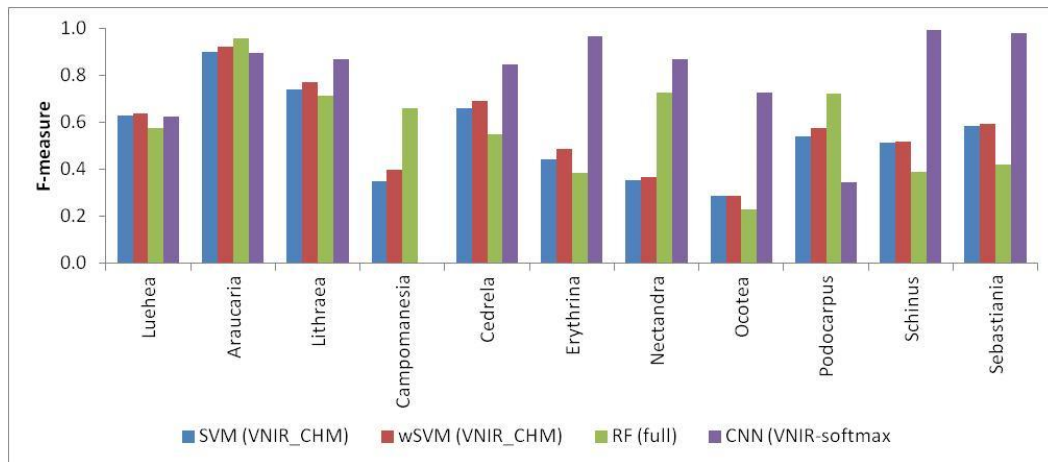
Figure 4.21- F-measure of each tree species class for Area 2 according to the classifier. Black bars indicate the minimum and maximum values varying according to the dataset.



Source: Author's production.

Figure 4.22 shows the species accuracies of the best dataset for each classifier used in the pixel approach for Area 2. The CNN achieved the best result for seven, of the 11 tree species, very notable for six classes, as *Cedrela fissilis*, *Erythrina falcata*, *Nectandra megapotamica*, *Ocotea* sp., *Schinus therebinthifolius* and *Sebastiania commersoniana*. RF reached the best result for *Araucaria angustifolia* and *Campomanesia xanthocarpa*, while wSVM had the best result for *Luehea divaricata*.

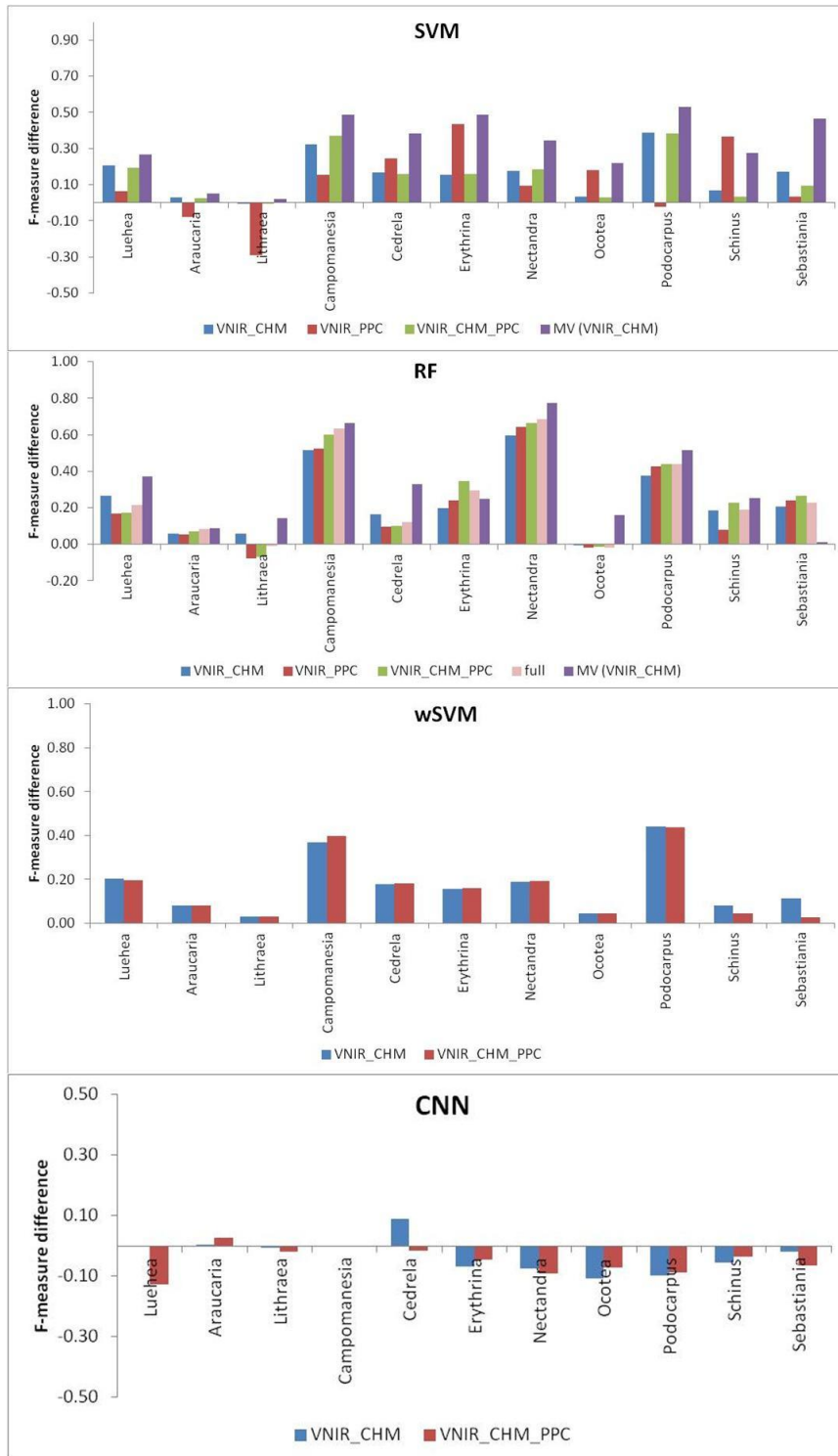
Figure 4.22- F-measure of tree species according to the best dataset result for each classifier in Area 2 considering the pixel approach.



Source: Author's production.

Similarly to Area 1, almost all the tree species presented an increase in F-measures when the CHM and PPC features were added to the VNIR dataset with the SVM, wSVM and RF classifiers (Figure 4.23). In the confusion matrices of the VNIR dataset (Appendix B), it can be noticed that *Podocarpus lambertii* was wrongly assigned to a lot of different species, such as *Ocotea* sp., *Cedrela fissilis*, *Campomanesia xanthocarpa* and *Araucaria angustifolia*, while *Luehea divaricata* was wrongly assigned to *Podocarpus lambertii*. *Campomanesia xanthocarpa* was wrongly classified as *Lithraea brasiliensis* and *Luehea divaricata* when only the VNIR bands were used. The incorporation of the CHM and PPC features markedly reduced the confusion among these classes in machine learning classifiers. Again, except for *Cedrela fissilis* and *Araucaria angustifolia*, all the tree species presented a decrease between 0.01 and 0.13 in F-measures when the PPC or the CHM were included in the CNN classifier.

Figure 4.23- Difference in F-measure accuracy for each species and classifier according to the dataset/approach in relation to the pixel-based classification using the VNIR dataset in Area 2.



Source: Author's production.

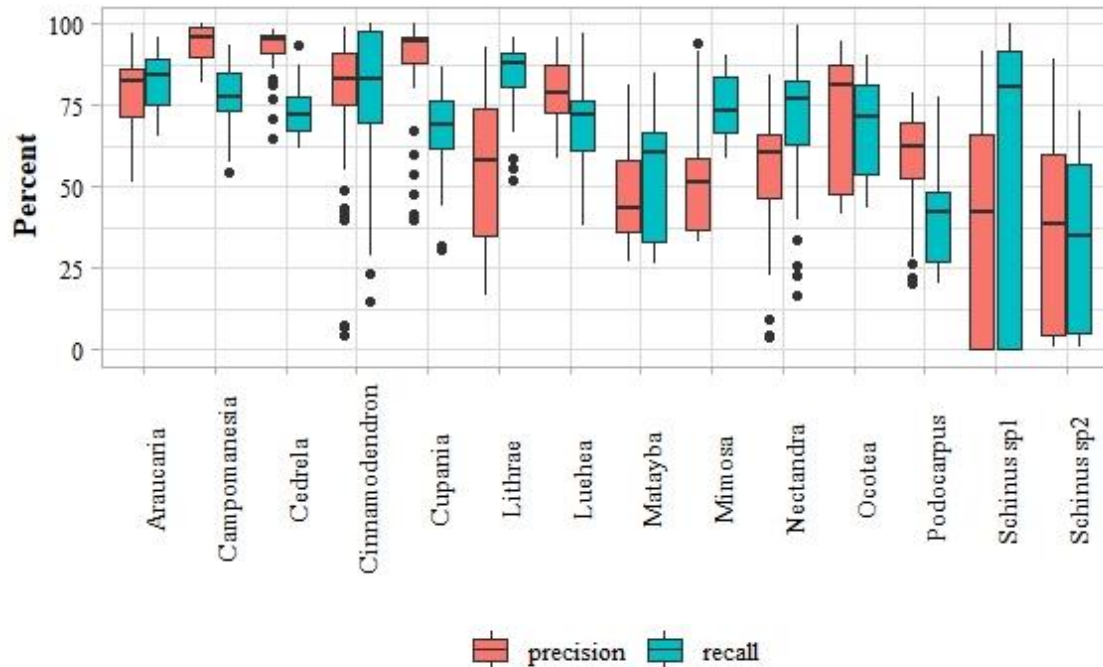
#### 4.2.3.4 Species prediction errors and imbalanced sample set

The boxplots of Figures 4.24 and 4.25 were built using the precision and recall values of 36 classification results for Area 1, and 33 for Area 2, considering all the variations regarding the dataset, classifier and approach. The differences between precision and recall for each species were highly variable, both regarding the level of accuracy of each class and the metric with the greatest value. Only one species (*Araucaria angustifolia*) had both high precision and recall values, and less variability in accuracies for both study areas, which was reflected in its higher F-measure.

Regarding Area 1 (Figure 4.24), species with more ITC samples, such as *Matayba elaeagnoides* and *Ocotea* sp., kept a balance between precision and recall, but their accuracies varied according to the dataset/classifier adopted. Both *Schinus* classes, with fewer ITC samples, presented high variability in precision and recall. In the classification results, it was observed that usually when one classifier/dataset improved the accuracy of one of these species, the other one tended to present a reduced accuracy. These species were not grouped into the same class, because despite belonging to the same genus, they have distinct spectral and structural characteristics. Even aware that their few ITC samples is the probable cause of the high variability in accuracies, these species were not discarded from the sample set, because the aim was to represent as many species as possible. Species such as *Campomanesia xathocarpa*, *Cupania vernalis*, *Luehea divaricata* and *Podocarpus lambertii* tended to present higher precision than recall. This trend indicates that these species are underpredicted in classification models. There were a few notable exceptions to this trend, particularly *Cinnamomum dinisii* that despite having few samples, presented higher values and a certain balance between precision and recall. On the other hand, species as *Lithraea brasiliensis*, *Mimosa scabrella* and *Nectandra megapotamica* presented higher recall than precision, indicating higher commission errors, i.e. these species were overpredicted and other species have been wrongly assigned to them.



Figure 4.24- Species-level recall and precision percentage accuracy across 36 classification models for Area 1. Precision is equivalent to user's accuracy; recall is equivalent to producer's accuracy. Higher precision relative to recall means the species has lower commission errors than omission errors.

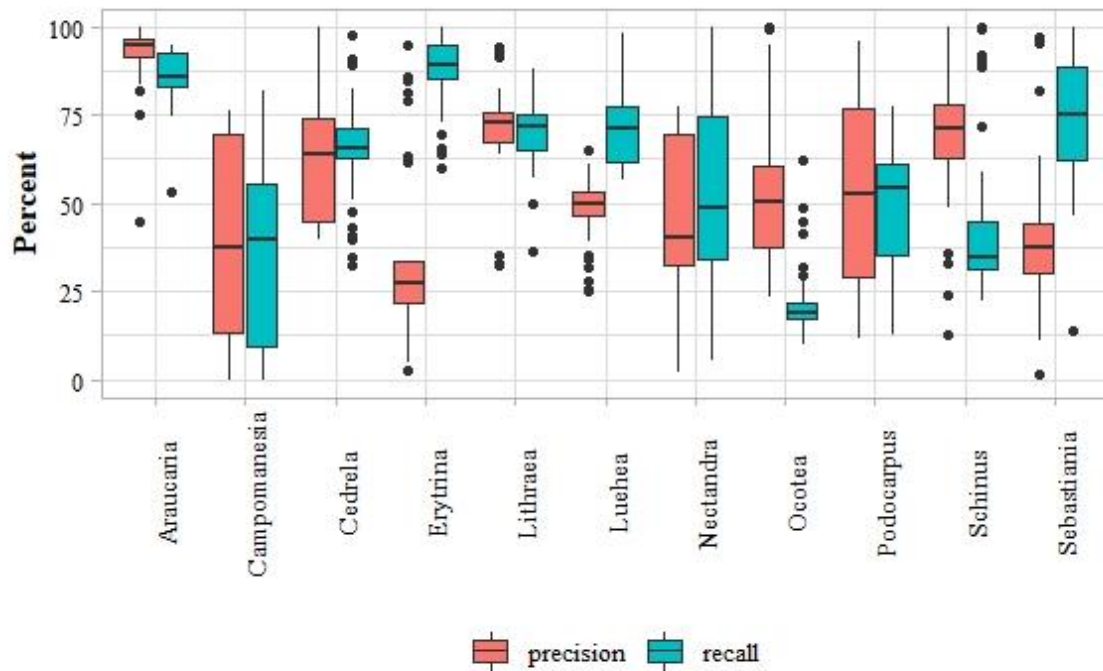


Source: Author's production.

Figure 4.25 shows the precision and recall values of tree species for Area 2. In this area, besides *Araucaria angustifolia*, *Lithraea brasiliensis* presented a balance and lower variability in precision and recall values. Other species also presented a balance between these metrics, but higher variability, such as *Campomanesia xathocarpa*, *Nectandra megapotamica* and *Podocarpus lambertii*. This means that the prediction of these species varied according to the dataset and the employed classifier. It should be emphasized that in the case of *Campomanesia xanthocarpa*, the three CNN classification models contributed to this higher variability, because this species was totally misclassified by this algorithm. This fact also increases the precision and recall of the classes that have been confused with it, such as *Erythrina falcata*, *Luehea divaricata* and *Nectandra megapotamica*. The classes with fewer ITC samples, such as *Erythrina falcata* and *Sebastiania commersoniana*, had higher recall than precision, what indicates that individuals from other classes were wrongly assigned to them. On the other hand, species such as *Ocotea* sp. and

*Schinus sp1*, had higher precision than recall; consequently, they tended to be wrongly classified as other classes.

Figure 4.25- Species-level recall and precision percentage accuracy across 33 classification models for Area 2. Precision is equivalent to user's accuracy; recall is equivalent to producer's accuracy. Higher precision relative to recall means the species has lower commission errors than omission errors.

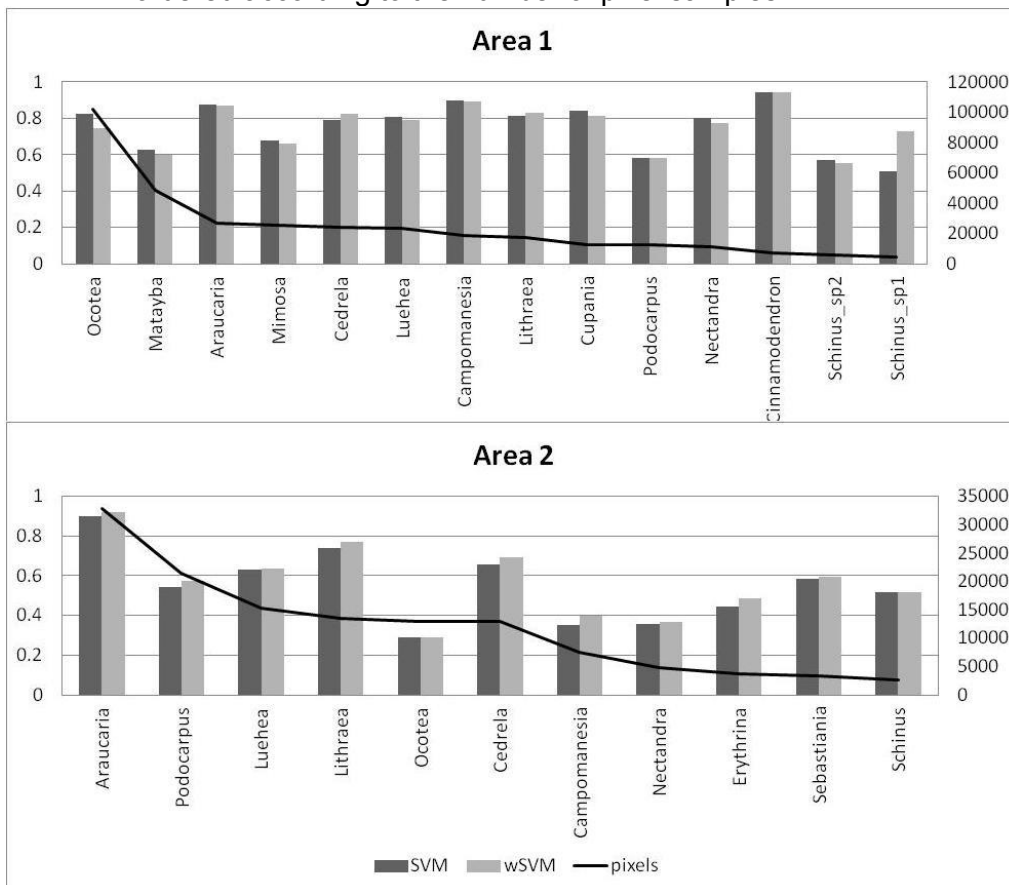


Source: Author's production.

In this study, a variation of the SVM classifier, the wSVM, was adopted as an attempt to deal with the imbalanced sample set problem. In Figure 4.26 it can be observed the F-measure of each tree species when either the SVM or the wSVM were employed, according to the number of pixel samples. It was expected that the wSVM would increase the accuracy of minority classes. In Area 1, when considering the same dataset (VNIR\_CHM\_PPC\_VI), the wSVM reached a better accuracy for *Schinus sp1*, with an F-measure of 0.73, in comparison with 0.51 reached by the conventional SVM. Conversely, *Ocotea sp.*, the species with the highest number of samples, had a decrease from 0.82 to 0.74 in the F-measure when the wSVM was employed. In this case, to favor minority classes, the algorithm can negatively affect the majority ones. For other classes, the accuracies of both methods were very similar.

In Area 2, the wSVM had an equal or better performance than the conventional SVM for all the classes. Classes with fewer samples, such as *Campomanesia xanthocarpa* and *Erythrina falcata*, had a more pronounced increase when the wSVM was employed. For the former one, the F-measure increased from 0.35 to 0.40, while for *Erythrina falcata* it raised from 0.44 to 0.49. In this area, the wSVM reached a better performance even for classes with more samples, such as *Podocarpus lambertii* and *Araucaria angustifolia*. The wSVM not only gives different weights to each class, but also to each sample. In this case, if one sample is not considered good, i.e. is not close to the class cluster, it will receive a smaller weight. Thus, this algorithm could improve the accuracy of majority classes as well.

Figure 4.26- F-measure of each tree species when either the SVM or wSVM were employed in relation to the number of pixel samples per class. Species ordered according to the number of pixel samples.



Source: Author's production.

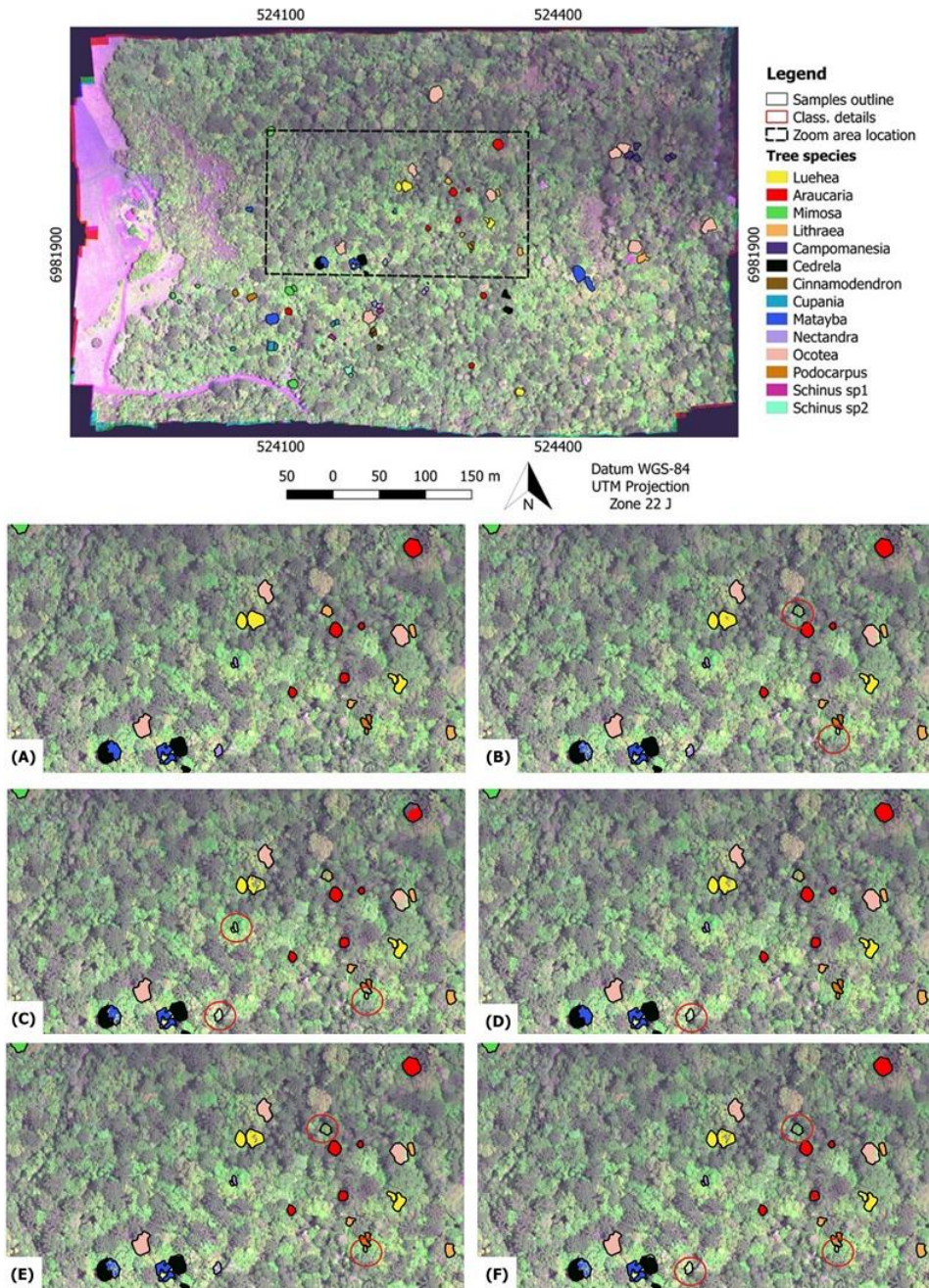
#### 4.2.4 Tree species maps

Figure 4.27 and 4.28 show the classification maps considering each ITC sample of Area 1 and Area 2 (training and test sets). The maps were produced in order to see the proportion of pixels correctly labeled within each ITC, and if the species were detected by the classification method. The proposed approach produced reliable results considering only the ITCs checked in the field.

In general, the methods detected the species and assigned the correct class to the ITCs. However, in some cases, only few pixels inside the ITCs were correctly classified, meaning that the method detected the species, but did not classify the entire ITC accordingly. In other minor cases, all the ITC was misclassified, which was mainly observed for the small-sized ones.

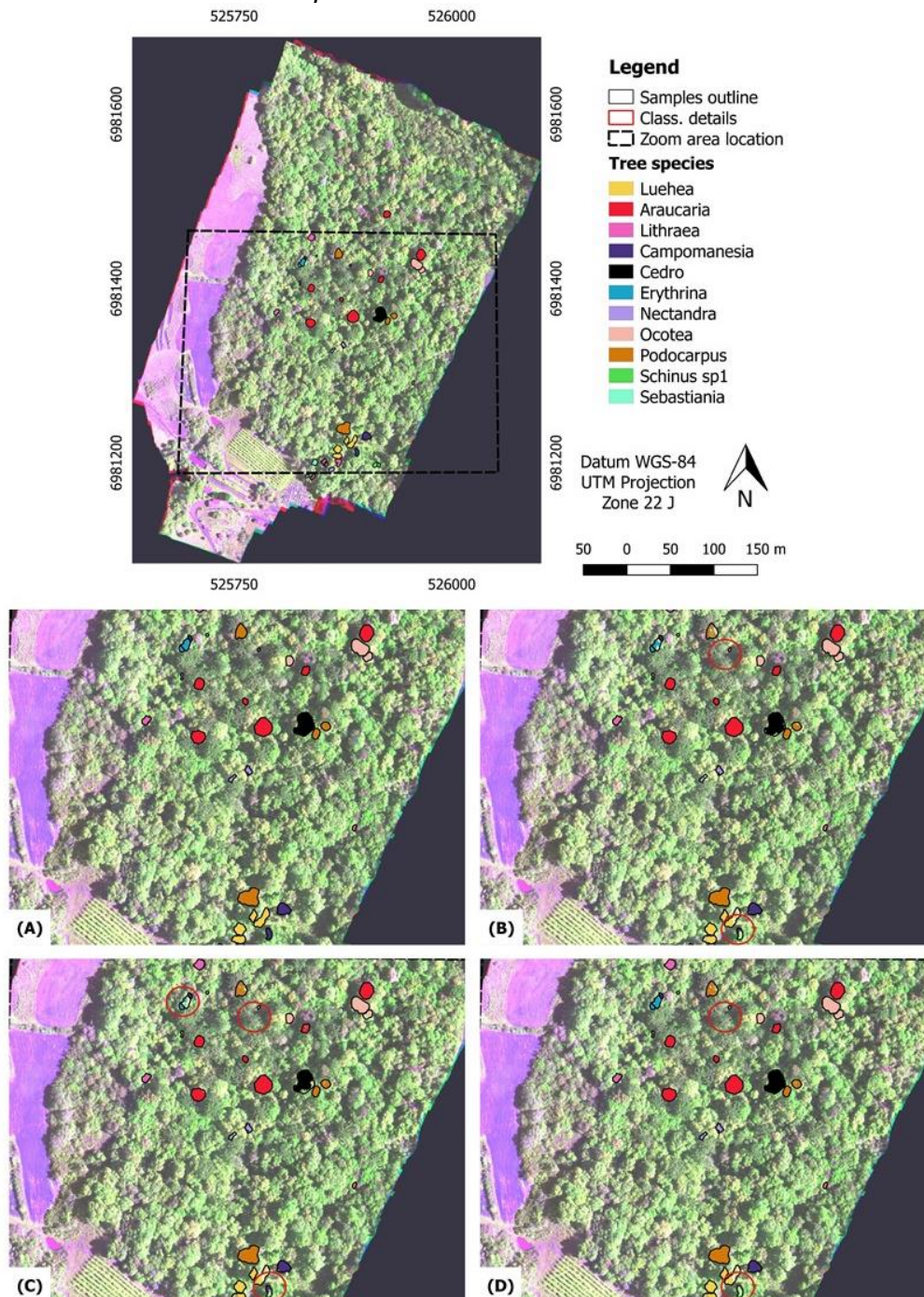
In Area 2 (Figure 4.28), the CNN totally misclassified one ITC of *Campomanesia xanthocarpa* used as test sample. However, the classified images allowed to observe that the two ITCs used as training samples were correctly classified. All the methods misclassified a small ITC of *Nectandra megapotamica*.

Figure 4.27- Details of classification maps using the best dataset result for SVM, RF and CNN classifiers in Area 1. A) Reference samples; B) the SVM classifier (VNIR\_CHM\_PPC dataset) after the MV rule – the red circle shows missing ITCs of *Podocarpus*; C) OBIA associated with the RF classifier and the VNIR\_CHM\_PPC\_VI\_MNF dataset – the red circles show two missing ITCs of *Nectandra* and one of *Podocarpus*; D) the CNN classifier with VNIR dataset – the red circle shows one missing ITC of *Nectandra*; E)The SVM classifier associated with VNIR\_CHM\_PPC dataset in a pixel-based classification- the red circle shows missing ITCs of *Podocarpus*; F)The RF classifier associated with VNIR\_CHM dataset in a pixel-based classification- the red circles show two missing ITCs of *Podocarpus* and one of *Nectandra*.



Source: Author's production.

Figure 4.28- Details of classification maps using the best dataset result for SVM, RF and CNN classifiers in Area 2. A) Reference samples; B) the SVM classifier (VNIR\_CHM dataset) after the MV rule – the red circles show missing ITCs of *Nectandra* and a poorly detected ITC of *Campomanesia*; C) the RF classifier and the VNIR\_CHM dataset – the red circles show one missing ITC of *Nectandra*, one of *Erythrina*, and a poorly detected ITC of *Campomanesia*; D) the CNN classifier with the VNIR dataset – the red circles show one missing ITC of *Nectandra* and one of *Campomanesia*.

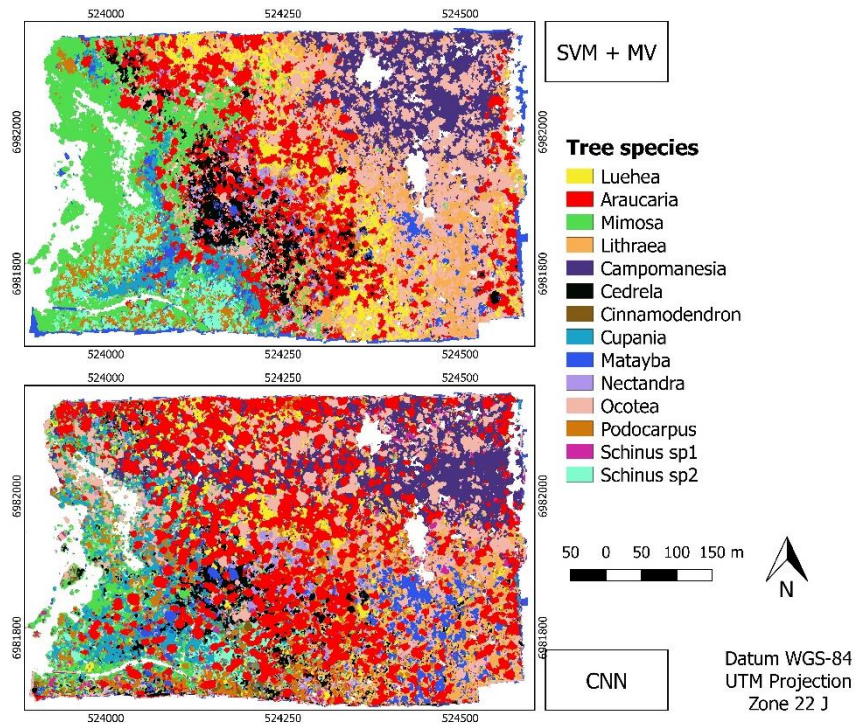


Source: Author's production.

In order to check if the classification maps present some agreement regarding the tree species abundance and distribution over the areas, the entire classification maps of the two best methods for each area (Figures 4.29 and 4.31) was considered, which were the SVM associated with the MV rule approach and the CNN. The percentage of coverage area by each tree species according to each map was also computed (Figures 4.30 and 4.32). No official information regarding real tree species distribution over the entire areas is available, and this analysis was only conducted to verify the differences among the methods.

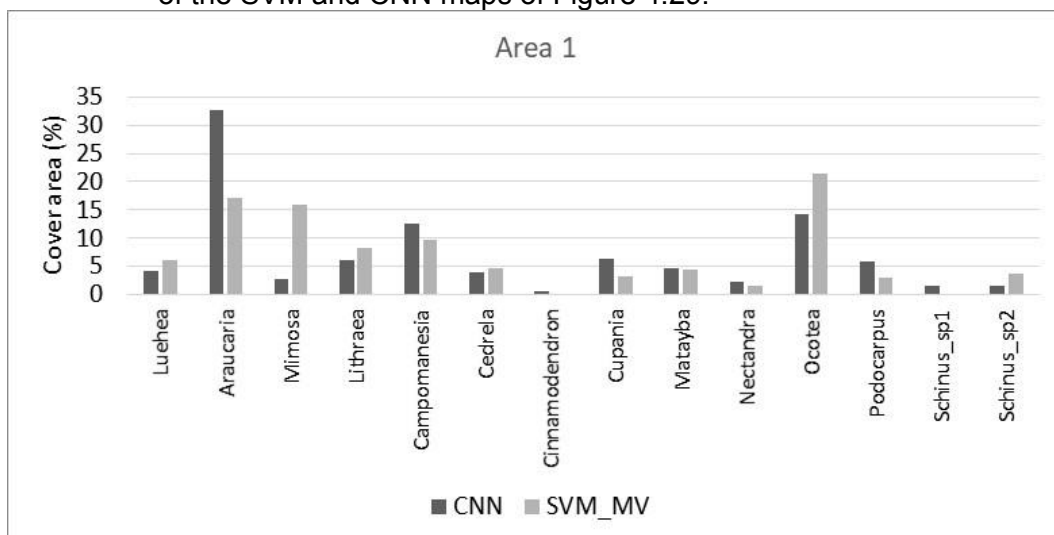
For Area 1, one can observe that the maps presented some disagreements regarding the distribution of the species over the area. It occurred mainly in the western part of the area, where the SS<sub>2</sub> stage predominates. The SVM model classified that portion as *Mimosa scabrella*, while the CNN confused several tree species among themselves. Also, it can be noticed in Figure 4.29 that the CNN has the tendency to classify much more areas as *Araucaria angustifolia*, and fewer ones as *Ocotea* sp. and *Mimosa scabrella* in comparison with the SVM. Despite the differences in species distribution, except for *Araucaria angustifolia*, *Mimosa scabrella* and *Ocotea* sp., the maps presented some agreement regarding the percentage of coverage area by each tree species (Figure 4.30).

Figure 4.29- Classification maps of Area 1: the SVM associated with the VNIR\_CHM\_PPC\_VI dataset and the MV rule; the CNN associated with the VNIR dataset.



Source: Author's production.

Figure 4.30- Percentage of tree species coverage area based on classification results of the SVM and CNN maps of Figure 4.29.



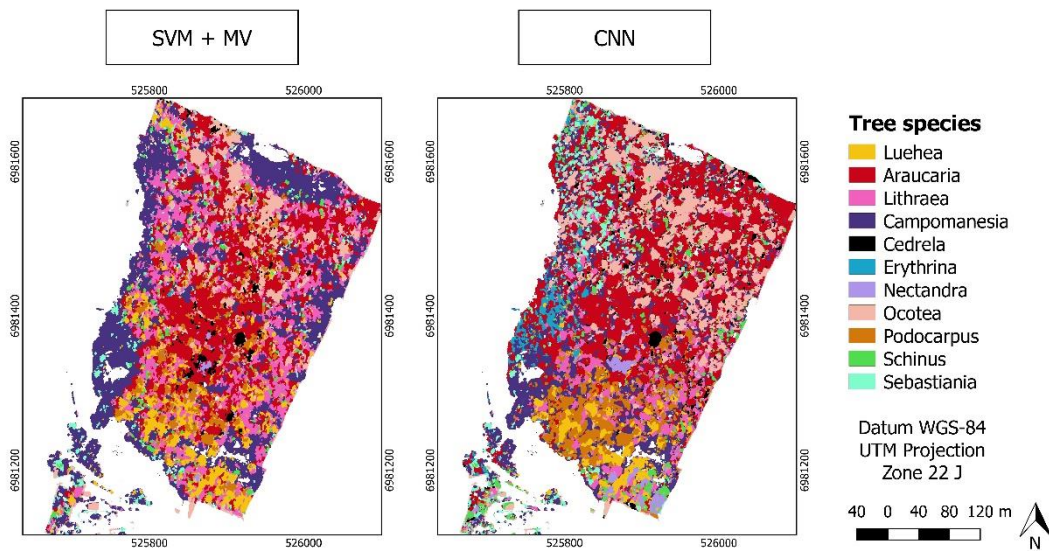
Source: Author's production.

For Area 2, more agreement can be observed regarding the distribution of species like *Araucaria angustifolia*, *Ocotea* sp., *Luehea divaricata* and



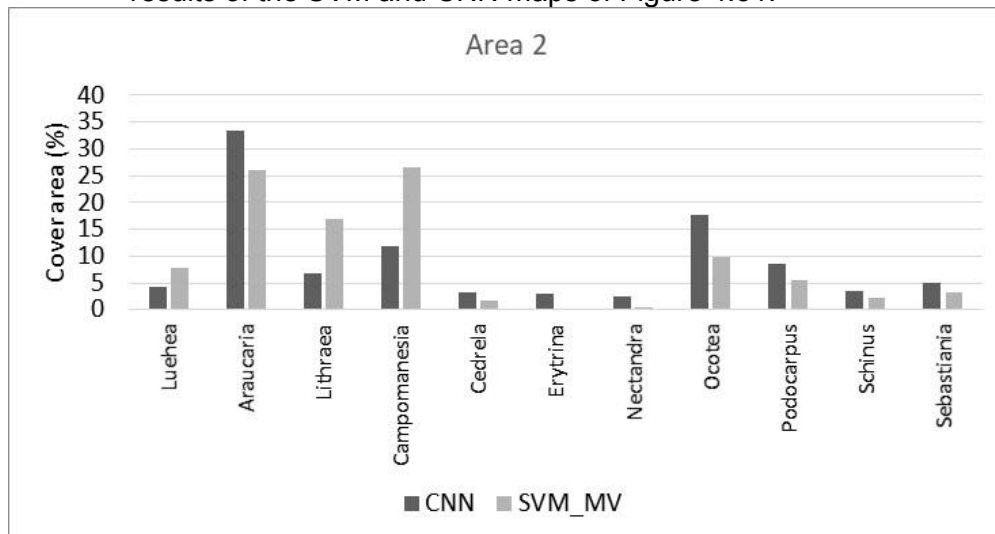
*Podocarpus lambertii* (Figure 4.31). Similarly to Area 1, the CNN classified more areas as *Araucaria angustifolia*, on the contrary to Area 1, more areas were classified as *Ocotea* sp. as well (Figure 4.32). The SVM, on the other hand, classified more areas as *Lithraea brasiliensis* and *Campomanesia xanthocarpa*. The latter one was totally misclassified by the CNN according to the test set; thus, it confirmed that this algorithm underestimates this class.

Figure 4.31- Classification maps of Area 2: the SVM associated with the VNIR\_CHM dataset and the MV rule; the CNN associated with the VNIR dataset.



Source: Author's production.

Figure 4.32- Percentage of tree species coverage area based on the classification results of the SVM and CNN maps of Figure 4.31.



Source: Author's production.

## 5 DISCUSSION

### 5.1 Considerations about the successional forest stages classification

Comparing the WV-2 and the hyperspectral data, the best accuracies for successional forest stages were reached when the latter one was used. With an OA of 99.28% and *Kappa* index of 0.99, this study surpassed previous works concerning the successional forest stages classification. In fact, to the best of our knowledge, this is the first study involving UAV and hyperspectral data for this purpose, which encourages further studies using remote sensing for the successional forest stages mapping. Different of what was observed in tree species maps, successional stages maps proved to be more stable regarding their distribution and coverage area when different classifiers and datasets are alternately used. Furthermore, they are produced more easily, because a person that has a relative knowledge of the study area can collect training samples using high spatial resolution images instead of conducting an extensive fieldwork. The WV-2 data also reached satisfactory accuracies, with the best OA of 91.22%.

Regarding the classifier's performance, it was observed that the SVM and RF reached similar accuracies, varying according to the dataset. The RF reached the best general performance, which corroborates the work of Sothe et al. (2017b), which compared both methods to classify successional forest stages using RapidEye and OLI/Landsat-8. However, the best general result achieved by Sothe et al. (2017a) for the same purpose but using MSI/Sentinel-2 instead of RapidEye, was reached with the SVM algorithm. In any case, both methods proved to be an attractive alternative for successional forest stages classification.

For both data (WV-2 and hyperspectral), the best general result had the CHM band included in the dataset. In fact, the CHM showed to be the most important feature to discriminate the successional forest stages when the WV-2 data was employed, and the sixth more important when using the hyperspectral data. This result was somehow expected, since the height is a good feature to discriminate such classes: SS<sub>1</sub>, besides the differences in the species

composition, has a shorter height and a smaller number of vertical strata than SS<sub>2</sub> that has a lower height than SS<sub>3</sub>. This was also pointed out by Castillo et al. (2012), who used LiDAR data from the LVIS sensor to classify three successional stages of vegetation in a tropical rainforest of Costa Rica. They demonstrated that changes in forest vertical structure (such as height) associated with the main successional stages of the forest can be effectively identified with LiDAR data. Berveglieri et al. (2016) developed an approach to classify successional stages based only on the vertical structure variations of DSM derived from optical images. Bispo et al. (2019) reached an accuracy of 87% when using height information extracted from the TanDEM-X synthetic aperture radar (SAR) interferometry to classify three successional forest stages and a primary forest class in the Amazon Forest. Sothe et al. (2019b) concluded that the inclusion of the CHM and LiDAR features to the WV-2 data improved the discrimination of vegetation classes, such as two successional stages, *Araucaria angustifolia* and reforestation. In this study, the use of a higher spatial resolution CHM, i.e. with DSM provided by a dense PPC instead of a sparse LiDAR point cloud, did not make substantially difference. Different from what occurred in tree species classification, the PPC features were not as useful as the CHM to classify successional forest stages.

Despite the great importance of the CHM, if this kind of data is lacking, an OA of 86.44% was reached when other multispectral features were included in the WV-2 data (MNF, GLCM, VIs). With the hyperspectral data, results without the CHM or PPC features were also promising, with an OA of 96.44% when the SVM algorithm and the VNIR\_MNF\_GLCM\_VI dataset were used. In this study, textural features were very important for the successional forest stages classification. Considering that these features aggregate contextual information through a neighborhood window, they smooth the image, reducing the impact of noisy pixels, shadows or small clearings that are eventually found throughout the vegetation, thus, also decreasing the spectral mixture at the pixel level (SOTHE et al., 2017a). This could be especially advantageous when hyperspectral data are applied, since the contextual window can smooth their great variability caused by their high spatial resolution. In fact, 15 texture

features were selected in the FS process for these data. On other hand, it may have masked spectral differences among tree species, since these features had few or negative effect for tree species classification.

The use of textural information was acknowledged as a strong attribute for differentiating vegetation classes by several authors (ARAÚJO, 2006; YU et al., 2006; SETTE; MAILLARD, 2011; ROSLANI et al., 2013; GOMES; MAILLARD, 2015; TOPALOGLU et al., 2016; SOTHE et al., 2017ab). Sette and Maillard (2011) classified successional forest stages of a Dense Ombrophilous Forest in the Atlantic Rain Forest with FORMOSAT-2 imagery and obtained an OA of 60.5% based only on visible bands, which rose to 91% when the classification also relied on textural attributes. Araújo (2006) verified an improvement in the discrimination between trees and grass with the introduction of an attribute indirectly based on texture, which considered the number of subobjects contained within each of these two classes in an immediately lower segmentation level. According to the author, since the texture of the tree class is rougher due to the presence of shadow amid the canopy leaves, this class tended to present a higher number of subobjects in comparison to grass.

VIs were more important for the WV-2 data than for the hyperspectral data. Band ratios and VIs generated using different band combinations have advantages for vegetation differentiation and biomass estimation, because these features can reduce Bi-directional Reflectance Distribution Function (BRDF) errors and do not saturate as quickly as single band data (COLGAN et al., 2012). In this study, the WV-2 scene presented more shadows due to the geometry of the data acquisition, thus VIs may have minimized this effect, besides being important features for the successional stages discrimination. According to Pu and Landry (2012), large view-angles (close to 30°) were found to be problematic when classifying tree species from the WV-2 data due to a notably increased amount of occlusion, and in the particular case of this work, also shading. This is one of the reasons why the WV-2 data were applied only for classifying successional stages and not tree species in the present case. Other authors also reported the importance of VIs for vegetation classification. Sothe et al. (2017a) reported that the VIs derived from OLI/Landsat-8 data had

great importance for successional forest stages classification, which was not observed when they used MSI/Sentinel-2 data. Maschler et al. (2018) found great improvement in tree species classification accuracies when VIs and principal components were aggregated to the classifications.

Regarding the spectral differences among the stages, in Figure 4.2 it was observed that in both WV-2 and hyperspectral data, the successional forest stages can be better discriminated in the NIR region, and the SS<sub>2</sub> was the stage with the highest reflectance and radiance values in this region. Ponzoni and Rezende (2004), when classifying the successional stages with TM/Landsat-5 images, also observed that the SS<sub>2</sub> presented higher reflectance values than the other stages in the NIR region. These authors were surprised by this behavior, as it would be expected that as the canopy's roughness increased, its reflectance in this spectral region should decrease due to the mutual shading of a stratum or dominant trees protruding from the upper canopy and thus, the SS<sub>1</sub>, with fewer vertical strata, would have higher values. However, the higher values of SS<sub>2</sub> can be explained by the fact that in this stage more multiple scattering of electromagnetic radiation by the leaves is expected than for the SS<sub>1</sub>, at the same time that it suffers lower effect of shadows than SS<sub>3</sub>, due to the lower number of vertical strata.

Followed by the SS<sub>2</sub>, in the WV-2 data, the SS<sub>1</sub> presented higher reflectance values than the SS<sub>3</sub>, while for the hyperspectral data, the opposite occurred. Since the WV-2 scene used in this study has a high off-nadir angle (28.2°), more shadows are present in comparison with the hyperspectral data. The shadow effects resulting from the geometry of the data acquisition are more pronounced in the SS<sub>3</sub> stages, due to their higher number of vertical strata and canopy's roughness, therefore reducing the reflectance response of this stage.

Although the WV-2 is a multispectral sensor, the bands situated in the yellow and red-edge regions and the two bands in the NIR region allow a better characterization of vegetation classes in comparison with further high spatial resolution multispectral sensors with only four bands (e.g., GeoEye, IKONOS, QuickBird). However, none of the data (hyperspectral, WV-2) include the short-

wave infrared (SWIR) region, which would be interesting for the successional forest stages classification, as pointed out by Sothe et al. (2017a).

Several authors highlighted the importance of both the SWIR and red-edge spectral regions for classifying forest types and agricultural fields (TIGGES et al., 2013; RAMOELO et al., 2015; IMMITZER et al., 2016; SOTHE et al., 2017a). Immitzer et al. (2016), when using Sentinel-2 data for discriminating vegetation species and cultures with the RF classifier, concluded that the SWIR and red-edge bands had a decisive importance for the image classification. Ramoelo et al. (2015), when using Sentinel-2 data and the RF algorithm, verified that the SWIR-1 and SWIR-2 bands together with the first red-edge band achieved the highest importance values for assessing leaf nitrogen content in the African savannah. Sothe et al. (2017a), when using MSI/Sentinel-2 and OLI/Landsat-8 data to classify successional forest stages of the MOF, found that textural means of SWIR bands were the most important variables for classification according to the RF ranking variable importance.

Despite its lowest OA, the use of a satellite data, instead of the UAV-hyperspectral data, allows mapping of larger areas and are less complex regarding processing tasks. On the other hand, UAV data can be more flexible regarding the field campaigns and weather conditions, but it is restricted to smaller areas. Both data enable the inspection and control of irregular activities (e.g., deforestation, illegal logging and forestry, etc.) as well as the conception of strategies for forest management and conservation. The information derived from these data can also support environmental regularization initiatives, such as the Rural Environmental Register (*Cadastro Ambiental Rural- CAR*), a governmental program in Brazil designed for the inventory of natural assets and land cover/land use in rural properties (SOTHE et al., 2017a).

## **5.2 Considerations about the ITC delineation**

This study tested three methods for ITC delineation, one traditional segmentation algorithm (MRG), and two specifically focused on ITC delineation (itcIMG and MCRC). Although the last two ones are specifically designed for ITC delineation, they need some improvement to be applied in this context (i.e.

tropical forests). While the itcIMG assumed a round shape for the ITCs and missed some suppressed trees, the MCRC led to an undersegmented result, where more ITCs, and even different species, were grouped into the same segment.

Despite being different methods, both itcIMG and MCRC start the segmentation assuming that the brightest points of the image correspond to treetops. For the MCRC method, these points are defined as priors and were computed based on the CHM, whereas for itcIMG the NIR band was used to compute the seeds or brightest points. While using the brightest points as the top of the trees is a reasonable approach in temperate or boreal forests, particularly in coniferous stands, this is likely too simplistic for tropical forest environments due to the variety of architectures and crown sizes existing in these areas. For a large rounded ITC, the brightest pixels may appear not at the point of maximum height but rather on the border exposed to the sun, while for flat ITCs there could be no difference in brightness at all (WAGNER et al., 2018). The irregular shapes and sizes of ITCs may also result in more than one prior per ITC. Furthermore, tropical forests have different strata with tree heights varying according to the species, resulting in cases that any prior (and consequently any segment) is generated for suppressed trees. Tochon et al. (2015) reported that brightness is not adequate to enhance spectral differences among individuals, particularly in high-resolution images with pixels that are smaller than ITCs.

The MRG is not a specific algorithm for ITC delineation, but because it allows the use of parameters as shape, compactness and color, it was the method that better captured the edges of the ITCs. Also, in the adopted case, instead of setting the seeds in the brightest points, they were randomly selected by the algorithm. However, conversely to what occurs when using the PPC data, the use of spectral bands alone in the MRG algorithm led to an oversegmentation, in which each ITC was represented by more than one segment. Wagner et al. (2018) listed three major limitations for delineating ITCs based on the spectral characteristics of tropical forests, which can be related to the oversegmentation results obtained in this work: (i) trees may be partially covered by lianas,

thereby altering the spectral response of species (KALACSKA et al., 2007), and generating more segments for the same ITC; (ii) a tree can have new leaves only in part of its crown, which results in marked different spectral responses for the same crown (LOPES et al., 2016), and also results in more segments per ITC, and; (iii) due to the diverse architecture and leaf characteristics of tropical trees, the intra-crown spectral variability among different species is also likely to be highly diverse (FERREIRA et al., 2016).

The same issue was approached by Tochon et al. (2015), when proposing a method based on the binary partition tree (BPT) to segment two tropical forests using hyperspectral data. The authors argued that the segmentation applied to dense tropical forests is an ill-posed task: a given image can often be segmented at several levels of details, due to the complex architecture of the top of the canopy. It was also observed by Wagner et al. (2018) when proposing a method based on interactive successive steps for ITC detection and delineation, which included the rolling ball algorithm and mathematical morphological operations, bimodal distribution parameters estimations and focal statistics, using WV-2 images. Despite their optimistic results, they indicated as the main limitations the underestimation of small trees and the oversegmentation of the large ITCs.

The MCRC method was tested using the raw PPC, which can also be related to its poor performance. Due to the passive nature of the optical sensor, it does not penetrate the vegetation as it occurs with LiDAR data, what makes it difficult to discriminate two close ITCs with similar heights or suppressed ITCs. Indeed, preliminary tests conducted with the other function of itcSegment package, the itcLIDAR, using the raw PPC led to the same problem and were discarded for further analyses.

Larsen et al. (2011) reported that especially when dealing with complex forest types, it is difficult to reach a good ITC delineation using only a common segmentation approach, and it may even require many processing steps e.g., (TOCHON et al., 2015; WAGNER et al., 2018). In a review article made by Zhen et al. (2016), it was verified that most of the studies in this line were



developed for coniferous forests, and only 11% of them explored the fusion of active and passive sensors for this purpose, even fewer encompassed distinct forest environments. In this study, methods involving the integration of hyperspectral data and 3D information, such as LiDAR and PPC, can be an alternative to improve the ITC delineation, providing a balance between over and undersegmentation. While the PPC avoids the generation of an excessive number of segments resulting from the spectral variability inside the ITCs, the spectral bands can provide information regarding the variability among species, avoiding two ITCs from being grouped into one segment. Another alternative to be explored is to include a consistent hierarchy of segmentations (TOCHON et al., 2015), keeping smaller ITCs at a more detailed segmentation level than larger ones e. g., (MASCHLER et al., 2018).

When the CHM band was included in the MRG algorithm, the oversegmentation was reduced and the borders of the ITC were still well delineated. Besides that, the use of the JM distance to merge homogeneous segments was considered a proper way to reduce oversegmentation, as also reported by Ferreira et al. (2014; 2016). Thus, the MRG method using the CHM and spectral bands refined by the JM, both visually and according to evaluation metrics, proved to be the best result obtained in this study.

### **5.3 Considerations about variable importance and tree species classification using machine learning methods**

This study showed that the combination of the CHM and PPC features with the VNIR bands led to a significant increase in classification accuracies when machine learning methods were applied (RF, SVM and wSVM). One of the first works involving the investigation of UAV-based photogrammetry and hyperspectral imagery for tree species classification was made by Nevalainen et al. (2017), in which they reached 95% of OA when classifying tree species in a boreal forest using features extracted from UAV-borne hyperspectral data and the thereof derived PPC. Later, Tuominen et al. (2018) tested the use of UAV-borne hyperspectral data and PPC features to classify 26 tree species in an arboretum located in Finland and reported an increase of 0.07 in the *Kappa*

index when they combined the VNIR bands with 3D features (*Kappa* of 0.77). The aforementioned studies reached better or similar accuracies to this study, but none of them involved tropical environments. Nevalainen et al. (2017) classified only four tree species in a boreal forest and, despite the high number of tree species, the study of Tuominen et al. (2018) was conducted in an arboretum area with the tree species distributed in homogeneous stands, which makes the area suitable for testing tree species recognition both at a stand and individual tree level.

The findings of this study using machine learning methods are consistent with other studies involving airborne hyperspectral data for tree species classification in tropical forest environments. Féret and Asner (2013) reached an OA of 73.2% using the pixel-based approach to classify 17 tree species in a Hawaiian tropical forest with airborne hyperspectral data, and 74.9% when they classified only 10 species, acknowledging the decline in the prediction accuracy when increasing the number of classes. When testing machine learning algorithms to classify eight tree species of a subtropical forest in Brazil, Ferreira et al. (2016) achieved an average classification accuracy of 70% using the VNIR hyperspectral bands. In that case, the inclusion of SWIR bands increased the accuracy to 84%. Using hyperspectral data with visible, NIR and SWIR bands, Clark and Roberts (2012) reached an OA of 71.5% in the pixel-based approach to classify seven emerged-canopy species in a tropical forest in Costa Rica. Regarding studies involving other highly diverse environments, Piironen et al. (2017) reached 57% of OA when classifying 31 tree species in a diverse agroforestry landscape in Africa. Graves et al. (2016) classified 20 tree species and one mixed-species class in a tropical agricultural landscape in Panama and reported an OA of 62%.

The importance of 3D information, such as that derived from LiDAR, for tree species classification has been reported in several studies. Deng et al. (2016) performed the classification of tree species in a temperate forest and obtained an improvement of up 14% when the LiDAR-derived features were employed together with an RGB orthophoto. Shen and Cao (2017) had an improvement of 0.4% to 5.6% when using both hyperspectral and airborne LiDAR features to

classify tree species in a subtropical forest. Similarly, Piironen et al. (2017) found an increase of 6% when LiDAR features were added to the hyperspectral bands for classifying tree species in a diverse African agroforestry. Dalponte et al. (2008) and Jones et al. (2010) reported that LiDAR combined with hyperspectral data increased the classification accuracy in approximately 2%, with a greater improvement for some tree species.

It can also be noticed that the improvement with 3D information was more evident for some species, such as *Schinus sp2*, *Ocotea sp.*, *Nectandra megapotamica* and *Matayba eleaeagnoides* in Area 1. *Ocotea sp.* class comprises two species of *Ocotea* genus (*O. pulchella* and *O. puberula*), which result in a more diverse spectral behavior. Furthermore, *Ocotea sp.* and *Nectandra megapotamica* belong to the same family (Lauraceae), having similar spectral characteristics. In this case, the spectral similarity among these tree species can be solved with the inclusion of the PPC features. The PPC features may also capture differences in the crown structure of *Matayba eleaeagnoides* and *Ocotea sp.*, since the former has a wider top with irregular branching, while the latter has a smaller and rounded top (LORENZI, 1992). For Area 2, when the VNIR dataset was used with machine learning methods, most of the confusion was associated with *Podocarpus lambertii*. This species is a conifer and presents irregular or cuneiform crowns. These structure differences could help in discriminating it from other broadleaves species when the PPC features were incorporated into the models.

The inclusion of the height information (CHM) improved the accuracies about 5% to 7% for Area 1, and 15 to 17% for Area 2. Indeed, the CHM was more important than the PPC features for Area 2, which may be due to the lower PPC density of this area, besides particularities of it and its individual trees. In the studies of Cho et al. (2012), Naidoo et al. (2012) and Asner et al. (2008), the tree height derived from LiDAR was an important variable for mapping tree species in two completely different forest ecosystems (savannas and tropical forest). On the other hand, Ghosh et al. (2014) concluded that there is no significant effect of the height information on tree species classification accuracies in a temperate forest. According to Fassnacht et al. (2016), the

canopy height per se is not a good predictor to classify tree species as the height of a tree varies with age, site conditions and competition and only to a minor degree with species. However, in tropical forests, this predictor can be useful to discriminate species belonging to different successional groups as pioneer, secondary and climatic, since they may have different heights according to their capacity to adjust to differentiated lighting levels (BOARDMAN, 1977). In Area 1, there was a great confusion between *Schinus sp1* and *Mimosa scabrella*, and between the latter and *Podocarpus lambertii* in the datasets without the CHM information. These three species belong to different successional groups: *Schinus sp1* and *Mimosa scabrella* are considered pioneer species, while *Podocarpus lambertii* is a late secondary or climatic shade-tolerant species (LORENZI, 1992). As a shade-tolerant species, *Podocarpus lambertii* can live under the shadow of other trees and, therefore, might present a lower height. Despite both are pioneer species, *Mimosa scabrella* and *Schinus sp1* have different heights (Figure 4.15), which can be due to particularities of the area. For instance, it was verified that *Mimosa scabrella* samples were located near the road or clearing areas. The lack of competition for light could have caused their limited growth in height. On the other hand, *Schinus sp1* samples were found in the middle of the forest, which could have led to their high growth rate, as this species searches for light. For this reason, when the height information was incorporated, there was an increase in classification accuracies of these species.

*Araucaria angustifolia*, the most frequent tree in the two study areas, presented stable accuracies even with the inclusion of 3D information, showing that even the use of the VNIR bands alone can discriminate this tree species. One observes that this species presents the lowest radiance values in the entire spectrum of the VNIR bands (Figure 4.2). According to Roberts et al. (2004), coniferous trees generally have lower reflectance values in the NIR region compared to broadleaf trees, which is closely related to their needle structure and the higher absorption of coniferous needles. Furthermore, the crown size and shape of coniferous trees influence the hemispherical directional reflectance factor (HDRF), and hence their reflectance as well (RAUTIAINEN;

STENBERG, 2005). On the other hand, *Podocarpus lambertii*, another conifer found in the study areas, tended to present more confusion with some broadleaf species, especially when the VNIR dataset was used. This may have occurred because its shape is not conical as a typical conifer, which confers this species a similar spectral response to other species in both study areas. Its branch structure brought about confusion with broadleaves species with small leaves, such as *Mimosa scabrella* in Area 1, even with the inclusion of the PPC features.

For both areas, the use of the MV rule significantly increased the accuracy of the pixel-based classification (5% and 11%), while OBIA approach (only applied to Area 1) did not make significant difference. These findings corroborate other studies that compared tree species classification using pixel-based and MV approaches (CLARK et al., 2005; DALPONTE et al., 2013; 2014; FERREIRA et al., 2016), and also further studies comparing these two approaches with OBIA (CLARK; ROBERTS 2012; FÉRET; ASNER, 2013). Clark and Roberts (2012) compared the OBIA approach, composed by the mean spectra of each ITC, with per-pixel and MV approaches. The pixel-based classification had roughly the same performance (nearly 70% OA) to the one achieved when using the average spectra from ITCs in an OBIA approach, however, when applying the MV, the accuracy rose to 87%. Féret and Asner (2013) reached better results when using the MV approach (83.6%), followed by the OBIA approach (79.6%) and lastly the pixel-based classification (74.9% of OA), when classifying species of a tropical forest. However, for the MV and OBIA classification, they had to reduce the number of classes from 17 to 10, due to the limited number of pixels and ITCs labeled to train the classifiers. Furthermore, similarly to this study, the authors pointed out that the segmentation did not delineate ITCs correctly, but each crown was instead composed by several segments.

According to Clark and Roberts (2012), considering the MV of pixels within ITCs, the error from any misclassified pixels within a crown is minimized, what leads to higher accuracies. However, in this approach, the ITCs may have high internal spectral variability, since they can receive the correct species label with only a fourth of the correctly classified pixels. The OBIA can be a better

alternative to deal with the spectral variability within the classes, which is common when high spectral resolution data is used, but in this case more ITC samples are needed. Furthermore, shadow, underlying objects, and other materials within an ITC may decrease the purity of its extracted spectra and further reduce classification accuracy (LIU; WU, 2018). Concerning this, Liu and Wu (2018) proposed a pixel weighting approach in which they extract the illuminated-leaf fraction at each pixel using a spectral mixture analysis (SMA) model and then calculate the ITC spectra using the illuminated-leaf fractions as weights.

For Area 1, all the VNIR bands showed similar importance according to the JM distance. Only slightly higher values can be noticed for the first two bands (506 to 519 nm), and four bands between 659 and 690 nm. These regions include the green peak and the chlorophyll absorption features, previously reported to contain useful information for the separation of tree species with hyperspectral data (NAIDOO et al., 2012; FASSNACHT et al., 2014; FERREIRA et al., 2016). The NIR bands, regarded as an important region for the tree species classification (CLARK; ROBERTS, 2012; DALPONTE et al., 2012; PIIRONEN et al., 2017), were not relevant for Area 1, while for Area 2 these bands had the highest JM values. In this region, the tree structure has the strongest impact (PONZONI et al., 2012) and the changes in the viewing angle may reduce the relative spectral differences among the species (NEVALAINEN et al., 2017). Due to the limited spectral range of the FPI camera (500–900 nm), the complete infrared region (including SWIR) could not be fully tested and evaluated in this study. Ferreira et al. (2016) reported 14% of increase in accuracy when including SWIR bands for tree species classification. Tuominen et al. (2018) reached the best result when combining VNIR and SWIR bands with 3D features extracted from the PPC. Nevertheless, their second-best result was achieved using only VNIR bands and 3D features, suggesting that these features can somehow compensate for the lack of the SWIR data.

In fact, the CHM and PPC features were markedly more important than the hyperspectral features (i.e. VI, MNF and GLCM features). The use of all the VNIR bands, hyperspectral features, the CHM and PPC features in the *full*

dataset did not improve the accuracy when compared to the use of the VNIR\_CHM\_PPC dataset (except for the RF in Area 2). For Area 1, using the SVM algorithm, an increase of 1.6% was observed when the VIs were added to the VNIR\_CHM\_PPC dataset, while the addition of the GLCM features led to a decrease in accuracy for most cases. Ferreira et al. (2016) reported an increase in the classification accuracy (of up to 5%) adding the VIs to the VNIR dataset. Maschler et al. (2018) found great improvement in tree species classification accuracies when VIs and principal components were aggregated to the classifications, while the inclusion of textural metrics had only a small effect. Although it was not the most important spectral region according to the JM distance for Area 1, the VIs containing at least one NIR band (PSSR and NDVI) were more important than the PSRI and PRI for the tree species classification in this work. In the study of Naidoo et al. (2012), the NDVI was also scored as one of the most important VIs to classify eight savanna tree species with hyperspectral data. The use of MNF features (MNF\_CHM\_PPC dataset) instead of the VNIR bands (MNF\_CHM\_PPC dataset) led to a decrease of 2.34% to 7% in OA when considering both areas and the SVM and RF classifiers. Ghosh et al. (2014) and Piironen et al. (2017) reported an improvement when MNF components were used instead of spectral bands, but it is worth stressing that in those cases they had hyperspectral data with more than 100 bands. The MNF transformation reduced the dimensionality and redundancy inherent in high spectral resolution data and, thus, provided better accuracies (GHOSH et al., 2014).

In the FS process, 46 out of the original 68 features were selected for Area 1, and 49 for Area 2, which mostly resulted in a non-significant increase in accuracy when compared with the *full* dataset for both areas. Similarly to the use of MNF components, studies that performed the FS in the hyperspectral data for tree species classification generally dealt with more than 100 spectral bands (DALPONTE et al., 2012; FASSNACHT et al., 2014; FERREIRA et al., 2016; PIIRONEN et al., 2017; MASCHLER et al., 2018). However, the hyperspectral data of this study contain only 25 bands, and thus the spectral information is not as redundant as when more than 100 hyperspectral bands

are used. Furthermore, according to Fassnacht et al. (2014), the FS is commonly applied to reduce the processing time and to enable a meaningful interpretation of the selected predictors, not necessarily resulting in significant increases of classification accuracies. Deng et al. (2016), when testing a FS process for tree species classification, stated that for the same feature there were different contribution degrees to species classification in different loops, indicating that the importance of a feature is changeable and greatly depends on the combination with other features. Therefore, it is difficult to determine a combination of features that can benefit all the tree species classes at the same time. Piironen et al. (2017) reported that the FS process had only a small impact on tree species classification accuracies, but they highlighted its importance to achieve the same level of accuracy with a smaller number of input features.

Regarding the classifiers, the SVM clearly outperformed the RF for Area 1, but it was worse than the RF in Area 2. Studies comparing both methods for tree species classification indicated that the SVM had a similar (GHOSH et al., 2014; BALLANTI et al., 2016) or superior performance than the RF (DALPONTE et al., 2012; DENG et al., 2016; FERREIRA et al., 2016; PIIRONEN et al., 2017; RACZKO; ZAGAJEWSKI, 2017). Some studies showed that the SVM performs better than the RF in the presence of small or imbalanced datasets. In this situation, the RF tends to focus more on the prediction accuracy of the majority class, which often results in poor accuracy for the minority classes (CHEN et al., 2004; DALPONTE et al., 2012). However, this was not verified in this study, since Area 2 also presents a small and imbalanced sample set, and the RF was superior to the SVM in that case. Piironen et al. (2017) observed that the fusion of LiDAR features with MNF components improved significantly the accuracy for the SVM algorithm, while for the RF classifier there was not a statistically significant improvement between these datasets. Similar behavior was reported by Deng et al. (2016), when comparing the SVM and RF algorithms for tree species classification. They observed more accuracy gain when features were added to the SVM classifier instead of the RF. In this study, the RF performance decreased with the addition of other features, including the PPC features, for



the VNIR\_CHM dataset in Area 1, but it remained relatively stable in Area 2. In such situations, the impact of data fusion depends on the classifier (PIIROINEN et al., 2017) and, in our case, also on the study area peculiarities. In fact, it is difficult to keep the generalization of the classification process when changing the datasets and study areas, and this is one of the reasons underlying the findings of Fassnacht et al. (2016), who reported on the importance of integrating more than a single test site in any comparative study of tree species classification.

The wSVM outperformed the SVM only in Area 2. Since the wSVM assigns different weights to different classes (or samples), it forces the new separating hyperplane to pay more attention to the minority class samples (NGUYEN, 2019), which are more remarkable in this area. Another fact to consider is that besides the class, this algorithm also assigns different weights to each sample. Area 2 presents larger coregistration errors among the bands than Area 1, such as non reliable pixel samples, e.g., those situated on the border of ITCs where these errors can be more noticeable, and hence may receive a lower weight in the classification process. In fact, it was verified that for Area 2, even classes with more samples had an increase in accuracy when the wSVM was applied.

Finally, although all the machine learning classifiers have parameters to be optimized, the parameter values used in this work provided an output similar or even more accurate when compared to other studies e. g., (DALPONTE et al. 2012; IMMITZER et al. 2016; RACZKO; ZAGAJEWSKI; 2017). According to Maxwell et al. (2018), some algorithms have been reported to be robust to parameter settings, and machine learning may still outperform parametric classifiers, such as maximum likelihood, even with little effort to tune hyperparameters.

#### **5.4 Considerations about tree species classification using the deep learning method**

The CNN classifier outperformed machine learning classifiers for both areas, reaching the best performance when the VNIR dataset was used. Conversely, machine learning methods had a poorer performance when only the VNIR

bands were employed. As pointed by Li Y. et al. (2017) and Gao et al. (2018), the main advantage of deep learning methods, as CNN, is that they can extract spatial and spectral features automatically from the original images, learning features through training, with minimal prior knowledge about the task.

When the PPC features and CHM were added to the VNIR dataset in the machine learning classifiers, and the results were incorporated into segments by a MV approach, they reached a performance similar to the CNN in both areas. The MV rule includes spatial context when it aggregates the pixels into segments, leading to higher accuracies and reducing the 'salt and pepper' effect in classifications. Regarding CNN, it can be observed that the classification images, even without the further use of segments (MV), were more homogeneous and had the tendency to correct a larger proportion of pixels inside the ITCs than the pixel-based classifications using machine learning methods. This can be associated with the contextual window (patch sizes) used to reckon features, considering the information of the pixel neighborhood. In the case of trees, the spatial structure of canopies is related to the tree size: if a pixel falls in a specific tree, its neighbors are also likely to be in the same tree and have similar information. Information in neighboring pixels is related to the information in a focal pixel and these relationships decay with distance. CNN classifiers operate according to such principle of detecting patterns in groups of adjacent pixels and relate them to background information (FRICKER et al., 2019).

Another fact to consider is that besides the need of ITC segments in a MV rule approach, more features are necessary in machine learning methods to reach similar accuracies to those attained by the CNN. Indeed, contrary to machine learning methods, the CNN presented a decrease in accuracy for most classes when the PPC, the CHM or both are included in the dataset. This may be occurred due to the increase of training parameters when more bands were added to the dataset, leading to overfitting, i.e. a reduction in the generalization ability of the algorithm (LIU et al., 2019). Another possible explanation is that the PPC features were manually extracted before their inclusion in the algorithm. As a CNN automatically extracts its own features, the inclusion of the raw PPC instead of rasterized features could enable the extraction of more useful features

by this algorithm. A similar behavior was observed by Sothe et al. (2019b) when comparing CNN and ensemble methods using WV-2 data, LiDAR features, and their integration. Despite the difference was very small, the CNN had the best performance when WV-2 data were employed using only the spectral bands; and the worst accuracy when only LiDAR features were used. However, in that case, even for the CNN, an increase in accuracy was observed when LiDAR features were integrated into the WV-2 data, which can be due to the intensity features of LiDAR, and not the elevation ones. Hartling et al. (2019) also reached the best OA for a dense CNN when multispectral bands of WV-3 were employed together with LiDAR data, but they used only the intensity image instead of elevation features.

According to He et al. (2018), most of the existing methods do not extract informative features from LiDAR-derived rasterized data in a deep manner. Hamraz et al. (2018) pointed out that LiDAR point clouds are not easily processed by the human visual system, and hence the expert-designed features may as well be suboptimal and likely miss useful information. Qi et al. (2016; 2017) mentioned that 3D data have attracted less attention in view of their more costly acquisition/processing and their both less intuitive and conventional representation formats, which demand non-trivial pre-processing techniques to discretize the data and make them usable for deep learning methods. In this respect, some approaches can be explored in future works, such as voxel spaces to create representations that can drive and be processed by a 3D CNN (MATURANA; SCHERER, 2015; WU et al. 2015; GUAN et al., 2019) or even the use of morphological and multiattribute profiles to extract

Until the present moment, there are few recent studies exploring CNN for tree species classification purposes (PÖLÖNEN et al., 2018; FRICKER et al., 2019; GUAN et al., 2019; HARTLING et al., 2019). Pölönen et al. (2018) reached 96.2% of OA when classifying three tree species of a boreal forest using a 3D CNN and hyperspectral data, while Guan et al. (2019) reached 96.4% of OA when classifying 10 tree species using mobile LiDAR data and a 3D CNN in an urban environment. Such high OA values are usually associated with validation samples internally generated by the CNN during training. Hartling et al. (2019) compared a

dense CNN architecture to the RF and SVM methods to classify eight tree species in an urban area using WV-2, WV-3 and LiDAR data. In their study, the CNN classifier reached 82.6% of OA in comparison to 60% achieved by machine learning methods. Fricker et al. (2019) reached a F-score of 0.87 when classifying seven tree species in a mixed-conifer forest in USA. The results of this study are comparable to those of the above mentioned works, given that Pölönen et al. (2018) and Fricker et al. (2019) handled a limited number of species, none of them in tropical forests, and both Guan et al. (2019) and Hartling et al. (2019) studied urban areas, which represent a more controlled environment. Likewise our study, Hartling et al. (2019) emphasized the ability of the CNN to extract information from the input dataset and pointed out that the addition of features, such as VIs and texture, tended to decrease the OA of the CNN.

Although outperforming other methods for the majority of the analyzed tree species in both areas, the CNN totally misclassified *Campomanesia xanthocarpa* in Area 2. Even so, their training samples were correctly classified, which can be a specific case of overfitting, since different ITCs were used as test samples to evaluate the methods.

The non-dependence of former steps of feature extraction and segmentation before the classification makes the CNN concept an attractive solution for tree species classification in highly diverse environments, even in the presence of small sample sets, if a data augmentation process is applied. On the other hand, the processing time and computer power requirements are the biggest disadvantages of such method. Huang et al. (2002) noted that the higher accuracy of artificial neural networks (ANNs) algorithms compared to decision trees was offset by the larger computational cost. However, when considering the VNIR dataset and the pixel-based approach, this study showed that the CNN reached accuracies between 22% and 26% higher than those of RF and SVM for both areas, which can counterbalance the price of its high computational cost.

## 5.5 Considerations about the number of ITC samples, tree species classes and evaluation method

According to Ferét and Asner (2013), the minimum number of samples per species required to perform optimal classification is a limiting factor in tropical forest studies due to the difficulty and high cost of tree localization on the ground. While Baldeck and Asner (2014) suggest approximately 20 ITCs as the focal number to achieve optimal classification accuracy in an 11-class model, Graves et al. (2016) suggest that in a model with 21 classes, all the classes should have at least 20 to 30 ITCs per class to produce accurate and reliable classification predictions, allowing for a split of the ITCs into training and test groups. This study, similarly to other studies involving the classification of a considerable number of tree species e.g., (FÉRET; ASNER, 2013; LEE et al., 2016; PIIROINEN et al., 2017; TUOMINEN et al., 2018; BRABANT et al., 2019), had few ITC samples for some classes. This, coupled with the fact that not all the species were considered in the classification models, is an obstacle to extrapolate the classification over the entire area, because it may result in a map with many uncertainties.

It can be noticed, for instance, that the maps of Figures 4.29 and 4.31 presented similar accuracies according to confusion matrices but are different regarding the species distribution over the area. Even so, these classified images could be used in some general ecological applications, such as assessing patterns of species composition and abundance across environmental gradients or land management units, considering that such classifications are in compliance to a certain extent with each other regarding the proportion of every species. They can also be useful for the identification of areas of high or low tree cover and species diversity, the identification of ecological groups of tree species (like pioneer, secondary, and climax), to support the successional forest stages classification as well as to provide landscape estimates of aboveground biomass (GRAVES et al., 2016). For more focused applications, where accurate predictions of species location and identity is needed, such as monitoring endangered tree species (e.g., *Araucaria angustifolia* and *Cedrela fissilis*), other techniques, like semi-supervised methods where a focal group of species is identified from a background of unknown species

(BALDECK; ASNER, 2014; BALDECK et al., 2015), can be a better approach (GRAVES et al., 2016).

It was verified that not always the classes with fewer samples had the lowest classification accuracy. However, those classes with only two or three ITCs tended to present more variability in accuracies when changing the dataset and classifier and may eventually have their cover area underestimated in the classification results. Graves et al. (2016) observed that species with more training samples presented lower variability across the iterations of the classification process. Our study showed a similar pattern; here though, the iterations here regard changing datasets and classifiers, i.e. each classification scheme did run only once.

In such situations, another issue that deserves attention is the evaluation method. This study adopted a simple split in training and test sets, which is pointed out as one of the most popular approaches for statistically assessing tree species classifications (FASSNACHT et al., 2016). On the other hand, Lyons et al. (2018) reported that a simple split of data into training and test sets results in a large variance in estimates of accuracy and mapped area, mainly when dealing with small sample sets. In this case, when the classes are not completely representative of the full population of trees in the study area, the reported accuracies could be optimistic (FASSNACHT et al., 2016). Nevertheless, a study conducted by Sothe et al. (2019a) using the same dataset and the SVM classifier adopted the Leave-One-Out (LOO) strategy to evaluate the models in Area 1 and reached an accuracy of 72.4% for the best dataset (VNIR\_PPC\_CHM\_VI), which is about 5% below the present study. However, this strategy was not adopted in this work, since the use of LOO with the CNN algorithm would be extremely time-consuming. This is one of the main reasons why studies concerning CNN-based classifications followed the simple split strategy (LI Y. et al., 2017; GAO et al., 2018; ZHANG et al., 2018; PÖLÖNEN et al., 2018; FRICKER et al., 2019; HARTLING et al., 2019), which is ultimately able to provide a fair comparison among classifiers.

## 5.6 Considerations about the use of UAV-borne data

The use of an UAV hyperspectral camera proved to be a cheap and fast way to acquire data for successional stages and tree species classification in a highly diverse forest. When considering different UAV sensors, the advantages of the image-frame approach over the traditional pushbroom or whiskbroom scanning approaches include the possibility to collect image blocks with stereoscopic multiple object views maintaining the geometric and radiometric constraints provided by the rigid rectangular image geometry (HONKAVAARA et al., 2013). Although the UAV laser scanning technique has developed rapidly in recent years, the high prices of the sensors still render this technique expensive, and cameras which are mounted on the UAVs, are less expensive and more accessible than light laser scanners (SALACH et al., 2018). Regardless of that, the main disadvantage of the PPC is the lack of vegetation penetration which can be an obstacle for ITC delineation and estimation of structure parameters.

When machine learning methods were applied, the use of the PPC features increased strongly the classification accuracy of Area 1, however, due to the lower density of points and particularities of the area, this increase was not so pronounced as the CHM for Area 2. This suggests that the flight campaigns should be planned in order to acquire a higher overlap among the images and consequently, a denser PPC. The CHM generated from the DSM of the PPC proved to be very useful for tree species classification for both areas.

The disadvantages of the current first-generation frame format hyperspectral cameras are the poorer spectral resolution (FWHM of 10–30 nm) and the smaller number of spectral bands in respect to more mature pushbroom techniques, which typically provide hundreds of spectral bands with FWHMs of 2–10 nm (HONKAVAARA et al., 2016). Besides that, a special care must be taken to align the spectral bands during the preprocessing steps. Since fewer GCPs were used for band registration in Area 2, it presented more problems related to misalignments between the bands, which may have negatively affected the results. In the future, the spectral performance of the FPI cameras is expected to improve,

and the latest commercial cameras already offer improved performances ([www.rikola.fi](http://www.rikola.fi)) (HONKAVAARA et al., 2016; AASEN et al., 2018).



## 6 CONCLUSION AND FUTURE STUDIES

This study investigated two major topics concerning the mapping of subtropical forests: i) the ability of UAV-based PPC, UAV-hyperspectral and WV-2 data to map successional forest stages using machine learning methods; ii) the ability of UAV-based PPC and UAV-hyperspectral data for ITC delineation and tree species classification using machine and deep learning methods. For successional forest stages classification, the SVM and RF classifiers were tested using an OBIA approach and up to 14 datasets depending on the data (WV-2 and hyperspectral) (c.f. Table 3.13). For tree species classification, four different classifiers (SVM, wSVM, RF and CNN), three classification approaches (per-pixel, OBIA, MV rule) and 13 datasets composed of up to 68 features (c.f. Tables 3.13, 4.2 and 4.3) were tested. Regarding the hypotheses presented, the following considerations can be made:

- a) The successional forest stages can be well discriminated with either multispectral (WV-2) or hyperspectral data: both data showed a great potential for classifying the successional forest stages. The accuracies generally were over 80% for the WV-2 data and 90% for the hyperspectral data, reaching 99.28% with the latter one associated with the VNIR\_CHM\_MNF dataset and the RF classifier. The addition of textural features, MNF and VIs in the classification process was important to increase the accuracy of both input data as compared with the exclusive use of the VNIR dataset. The CHM was the most important feature when the WV-2 data were used, but not indispensable if other multispectral features are alternately incorporated. Texture features were among the most important ones for the employed hyperspectral data, which can be due to their property of smoothing the high level of information, a characteristic derived from their refined spatial and spectral resolution. VIs were more important for the WV-2 data, since they may have attenuated the shadow effects caused by the data acquisition geometry. It is worth mentioning that the adopted methodology may be easily applied to

further subtropical areas of the Atlantic Rain Forest with similar characteristics. Finally, the flexibility of the UAV data regarding weather conditions and temporal resolution must be highlighted, as well as the synoptic and systemic data acquisition capabilities of the WV-2 sensor.

- b) The inclusion of 3D features derived from the PPC improved the tree species and successional forest stages classification: the inclusion of PPC features and the CHM provided a marked accuracy increase in the tree species classification results when machine learning methods were applied (SVM, wSVM and RF), between 13% and 17% depending on the classifier and the study area. However, a decrease was observed when these features were included in the CNN classification. Regarding the successional forest stages, the inclusion of the PPC features and the CHM improved the accuracy between 6.3% and 13% in comparison with the VNIR dataset.
- c) The use of the UAV-based PPC and hyperspectral data is effective for ITCs delineation in subtropical forests: three segmentation algorithms were tested for the ITC delineation; however, none of them reached a proper result for all reference ITCs. The MRG method tended to oversegment the ITCs, while the itcIMG and MCRC undersegmented or even missed some suppressed ITCs. With the inclusion of the CHM in the MRG segmentation and merging homogenous segments with the JM distance, a better result was obtained.
- d) The use of ITCs as a classification unit (i.e. OBIA or the MV rule at an object level) increases the tree species classification accuracies of machine learning methods in relation to the pixel-based classification: The OBIA approach (only applied to Area 1) did not increase the OA for the SVM, while a slight increase was observed for the RF algorithm in comparison with the other pixel-based classifications. When the pixel-based classifications were aggregated into segments through a MV rule, it was observed a marked increase in accuracy for both study

areas (5% for Area 1 and 11% for Area 2), considering the same datasets individually. This can be explained by the fact that this procedure reduced the classification errors associated with the spectral variability of high spatial resolution data.

- e) Classifiers dealing with the imbalanced sample sets can increase the accuracy of less represented tree species classes: the wSVM, a new SVM approach to work with imbalanced sample sets and unreliable samples, improved the accuracy not only for some lesser represented classes, but for some major classes in Area 2 as well. The use of a CNN architecture associated with a previous step to balance the samples set was also a promising approach to classify tree species in both areas, since the method outperformed all the other algorithms when pixel-based approaches are compared.
- f) The CNN algorithm can effectively classify tree species using fewer features than machine learning methods with comparable accuracy indices: when considering the pixel-based approach, CNN outperformed the RF and SVM for both areas, with an OA of 84.4% in Area 1, and 74.95% in Area 2, using only the VNIR bands. In fact, this method was more accurate than the SVM and RF when considering only the VNIR dataset, between 22% and 26%.

As final considerations, it can be stated that machine learning methods also provided good results for tree species classification. The SVM and RF had a similar performance for Area 2, but the SVM was significantly better than the RF in Area 1. In both areas, when the best dataset result of the SVM was associated with the MV rule approach, a performance similar to that obtained by the CNN was reached. However, in the case of machine learning methods, besides the use of segments, the PPC features and the CHM were crucial to increase the accuracy. Neither the inclusion of hyperspectral features nor the FS process changed the results for the tree species classification.

This work indicated that the adopted approaches for the semiautomatic classification of three successional forest stages and 16 tree species in patches of a subtropical portion of the Atlantic Rain Forest are promising. The herein produced findings are relevant for the conservation of this severely threatened biome, being potentially useful for optimizing mapping and monitoring of its forest remnants. Furthermore, the methodology can be used to classify specific tree species, such as the endangered ones, like *Araucaria angustifolia* and *Cedrela fissilis*. In further studies, a feasible approach for improving the classification performance is envisaged so as to explore the ITC delineation methods for tropical forest environments, combining PPC and hyperspectral data. This proper delineation can be associated with an OBIA classification at an ITC level. Moreover, increasing the number of ITC samples in a way to enable a more robust model and consistent classification is also a goal to be pursued. The generalization of the classification is another issue to consider, since the use of two study areas, instead of one, showed that the particularities of each area should be duly taken into account when choosing the most reliable features and algorithms for the purpose of classifying tree species.

Finally, it is also necessary to explore methods involving the extraction of deep features directly from the PPC using the CNN classifier. This algorithm showed a great potential for classifying tree species using only the VNIR bands, but it did not benefit from the PPC features manually extracted before the classification. It is believed that this algorithm can perform even better if a more robust technique to extract 3D features is implemented.

## REFERENCES

AASEN, H.; BURKART, A.; BOLTEN, A.; BARETH, G. Generating 3D hyperspectral information with lightweight UAV snapshot cameras for vegetation monitoring: from camera calibration to quality assurance. **ISPRS Journal of Photogrammetry and Remote Sensing**, v. 108, p. 245–259, 2015.

AASEN, H.; HONKAVAARA, E.; LUCIEER, A.; ZARCO-TEJADA, P.J. Quantitative remote sensing at ultra-high resolution with UAV spectroscopy: a review of sensor technology, measurement procedures, and data correction workflows. **Remote Sensing**, v. 10, n. 7, p. 1091, 2018.

ABADI, M. et al. **TensorFlow**: large-scale machine learning on heterogeneous systems. 2015. Available from: <https://www.tensorflow.org>. Access in: Aug 6, 2018.

ACHANCCARAY, P. M. D.; AYMA, V. A.; IMENEZ, L.; GARCIA, S.; HAPP, P. N.; FEITOSA, R. Q.; PLAZA, A. A free software tool for automatic tuning of segmentation parameters. **South-Eastern European Journal of Earth Observation and Geomatics**, v. 3, p. 707-712, 2014.

ADAM, E.; MUTANGA, O.; ODINDI, J.; ABDEL-RAHMAN, E.M. Land-use/cover classification in a heterogeneous coastal landscape using RapidEye imagery: evaluating the performance of random forest and support vector machines classifiers. **International Journal of Remote Sensing**, v. 35, p. 3440–3458, 2014.

AMARAL, M.V.F.; SOUZA, A.L.; SOARES, V.P.; SOARES, C.P.B.; LEITE, H.G.; MARTINS, S.V.; FERNANDES FILHO, E.I.; LANA, J.M. Avaliação e comparação de métodos de classificação de imagens de satélites para o mapeamento de estádios de sucessão florestal. **Revista Árvore**, v. 33, p. 575–582, 2009.

ANDRADE, A. C.; FRANCISCO, C. N.; ALMEIDA, C. M. de. Desempenho de classificadores paramétrico e não paramétrico na classificação da fisionomia vegetal. **Revista Brasileira de Cartografia**, n. 66/2, p. 349-363, 2014.

ANDREACCI, F.; MARENZI, R. C. Avaliação da aplicação da Resolução CONAMA 04/94 na definição dos estágios sucessionais de fragmentos florestais da Floresta Ombrófila Densa de Santa Catarina. **Biotemas**, v. 30, n. 4, p. 117-128, 2017.

ANJOS, C. S. **Classificação de áreas urbanas com imagens multiespectrais e hiperespectrais utilizando métodos não-paramétricos**. Tese. 2016. 382 p. (Doutorado em Sensoriamento Remoto) - Instituto Nacional de Pesquisas Espaciais (INPE), São José dos Campos, Brasil, 2016.

ARAÚJO, E.H.G. **Análise multi-temporal de cenas do satélite QuickBird usando um novo paradigma de classificação de imagens e inferências espaciais** - estudo de caso: Belo Horizonte, MG. 2006. Dissertação (Mestrado em Sensoriamento Remoto) - Instituto Nacional de Pesquisas Espaciais (INPE), São José dos Campos, 2006.

ASNER, G.P.; KNAPP, D.E.; KENNEDY-BOWDOIN, T.; JONES, M.O.; MARTIN, R.E.; BOARDMAN, J.; HUGHES, R.F. Invasive species detection in Hawaiian rainforests using Airborne Imaging Spectroscopy and LiDAR. **Remote Sensing of Environment**, v. 112, n. 5, p. 1942–1955, 2008.

ATTARCHI, S.; GLOAGUEN, R. Classifying complex mountainous forests with L-band SAR and Landsat data integration: a comparison among different machine learning methods in the hyrcanian forest. **Remote Sensing**, v. 6, p. 3624–3647, 2014.

AXELSSON, P. DEM generation from LASE scanner data using adaptive TIN models. **International Archives of Photogrammetry and Remote Sensing**, Amsterdam, v. 33, part. B4, 2000.

BAATZ, M.; SCHÄPE, M. Multiresolution segmentation: an optimization approach for high quality multi-scale image segmentation. In: STROBL, J., BLASCHKE, T., GRIESEBNER, G. (Ed.). **Angewandte geographische informations- verarbeitung XII**. Karlsruhe: Wichmann Verlag, 2000. p. 12–23.

BACKES, A.; NILSON, A.D. Araucaria angustifolia (Bert.) O. Kuntze, o pinheiro-brasileiro. **Iheringia: Série Botânica**, Porto Alegre, n. 30, p.85-96, 1983.

BALDECK, C.A.; ASNER, G.P. Single-species detection with airborne imaging spectroscopy data: a comparison of support vector techniques. **IEEE Journal of Selected Topics in Applied Earth Observations and Remote Sensing**, v. 8, p. 2501–2512, 2014.

BALDECK, C.A.; ASNER, G.P.; MARTIN, R.E.; ANDERSON, C.B.; KNAPP, D.E.; KELLNER, J.R.; WRIGHT, S.J. Operational tree species mapping in a diverse tropical forest with airborne imaging spectroscopy. **PLoS ONE**, v.10, n. e0118403, 2015.

BALLANTI, L.; BLESIOUS, L.; HINES, E.; KRUSE, B. Tree species classification using hyperspectral imagery: a comparison of two classifiers. **Remote Sensing**, v. 8, n. 445, 2016.

BERVEGLIERI, A.; TOMMASELLI, A. M. G.; IMAI, N. N.; RIBEIRO, E. A. W.; GUIMARÃES, R. G. Identification of successional stages and cover changes of tropical forest based on digital surface model analysis. **IEEE Journal of Selected Topics in Applied Earth Observations and Remote Sensing**, v. 9, n. 12, p. 5385 – 5397, 2016.

BIRTH, G.S.; MCVEY, G. Measuring the color of growing turf with a reflectance spectroradiometer. **Agronomy Journal**, v. 60, p. 640-643, 1968.

BISPO, P. D. C.; PARDINI, M.; PAPATHANASSIOU, K. P.; KUGLER, F.; BALZTER, H.; RAINS, D.; SANTOS, J. R.; RIZAEV, I. G.; TANSEY, K.; SANTOS, M. N.; SPINELLI ARAUJO, L. Mapping forest successional stages in the Brazilian Amazon using forest heights derived from TanDEM-X SAR interferometry. **Remote Sensing of Environment**, v. 232, n. 111194, 2019.

BLACKBURN, G. A. Spectral indices for estimating photosynthetic pigment concentrations: a test using senescent tree leaves. **The International Journal of Remote Sensing**, v. 19, n. 4, p. 657-675, 1998.

BLUM, C. T.; RODERJAN, C. V. Espécies indicadoras em um gradiente da Floresta Ombrófila Densa na Serra da Prata, Paraná, Brasil. **Revista Brasileira de Biociências**, v. 5, n. 2, p. 873-875, 2007.

BOARDMAN, N. K. Comparative photosynthesis of sun and shade plants. **Annual Review of Plant Physiology**, Palo Alto, v. 28, p. 355-377, 1977.

BRABANT, C.; ALVAREZ-VANHARD, E.; LARIBI, A.; MORIN, G.; NGUYEN, K. T.; THOMAS, A.; HOUET, T. Comparison of hyperspectral techniques for urban tree diversity classification. **Remote Sensing**, 11, n. 11, p. 1269, 2019.

BRASIL. CONSELHO NACIONAL DO MEIO AMBIENTE. Resolução CONAMA nº 04/94, de 4 de maio de 1994. **Diário Oficial da União**, n.114, 17 jun. 1994.

BREIMAN, L. Random forests. **Machine Learning**, v. 45, n. 1, p. 5–32, 2001.

BROWNLEE, J. **An introduction to feature selection**. 2014. Available from: <https://machinelearningmastery.com/an-introduction-to-feature-selection/>. Access in: Jun 28, 2018.

BRUZZONE, L.; CARLIN, L.; ALPARONE, L.; BARONTI, S.; GARZELLI, A.; NENCINI, F. Can multiresolution fusion techniques improve classification accuracy? In: SPIE, IMAGE AND SIGNAL PROCESSING FOR REMOTE SENSING, 12., Boston, USA. **Proceedings...Boston**, 2006. v. 6365.

BUDOWSKI, G. Distribution of tropical American rain forest species in the light of successional processes. **Turrialba**, v. 15, n. 1, p. 40-42, 1965.

BURNETT, C.; BLASCHKE, T. A multi-scale segmentation/object relationship modelling methodology for landscape analysis. **Ecological Modelling**, v. 168, p. 233–249, 2003.

CASTILLO, M; RIVARD, B.; SÁNCHEZ-AZOFEIFA, A; CALVO-ALVARADO, J.; DUBAYAH, R. LIDAR remote sensing for secondary tropical dry forest identification. **Remote Sensing of Environment**, v. 121, p. 132–143, 2012.

CHEN, C.; LIAW, A.; BREIMAN, L. **Using random forest to learn imbalanced data**. Berkeley: University of California, 2004.

CHEN, Z.; GAO, B.; DEVEREUX, B. State-of-the-art: DTM generation using airborne LIDAR data. **Sensors**, v. 17, n. 150, 2017.

CHEN, Y.; LIN, Z.; ZHAO, X.; WANG, G.; GU, Y. Deep learning-based classification of hyperspectral data. **IEEE Journal of Selected Topics in Applied Earth Observations and Remote Sensing**, 2014.

CHO, M. A.; MATHIEU, R.; ASNER, G. P.; NAIDOO, L.; VAN AARDT, J.; RAMOELO, A.; DEBBA, P.; WESSELS, K.; MAIN, R.; SMIT, I. P. J.; ERASMUS, B. Mapping tree species composition in South African savannas using an integrated airborne spectral and LiDAR system. **Remote Sensing of Environment**, v. 125, p. 214–226, 2012.

CLARK, D. B., PALMER, M. W.; CLARK, D. A. Edaphic factors and the landscape-scale distributions of tropical rain-forest trees. **Ecology**, v. 80, n. 8, p. 2662-2675, 1999.

CLARK, M.L.; ROBERTS, D.A. Species-level differences in hyperspectral metrics among tropical rainforest trees as determined by a tree-based classifier. **Remote Sensing**, v. 4, p. 1820–1855, 2012.

CLARK, M.L.; ROBERTS, D.A.; CLARK, D.B. Hyperspectral discrimination of tropical rain forest tree species at leaf to crown scales. **Remote Sensing of Environment**, v. 96, p. 375–398, 2005.

COHEN, J. A coefficient of agreement for nominal scales. **Educational and Psychological Measurement**, v. 20, n. 1, p. 37-46, 1960.

COLGAN, M.S.; ASNER, G.P. Coexistence and environmental filtering of species-specific biomass in an African savanna. **Ecology**, v. 95, p. 1579–1590, 2014.

COLGAN, M.S.; BALDECK, C.A.; FÉRET, J.-B.; ASNER, G.P. Mapping savanna tree species at ecosystem scales using support vector machine classification and BRDF correction on airborne hyperspectral and LiDAR data. **Remote Sensing**, v. 4, p. 3462–3480, 2012.



DABIRI, Z.; LANG, S. Comparison of independent component analysis, principal component analysis, and minimum noise fraction transformation for tree species classification using APEX hyperspectral imagery. **ISPRS International Journal of Geoinformation**, v. 7, n. 12, p. 488, 2018.

DALPONTE, M.; REYES, F.; KANDARE, K.; GIANELLE, D. Delineation of individual tree crowns from ALS and hyperspectral data: a comparison among four methods. **European Journal of Remote Sensing**, v. 48, n. 1, p. 365-382, 2015a.

DALPONTE, M.; ENE, L. T.; MARCONCINI, M.; GOBAKKEN, T.; NÆSSET, E. Semi-supervised SVM for individual tree crown species classification. **ISPRS Journal of Photogrammetry and Remote Sensing**, v. 110, p. 77–87, 2015b.

DALPONTE, M.; BRUZZONE, L.; GIANELLE, D. Fusion of hyperspectral and LIDAR remote sensing data for classification of complex forest areas. **IEEE Transactions on Geoscience and Remote Sensing**, v. 46, p. 1416–1427, 2008.

DALPONTE, M.; BRUZZONE, L.; GIANELLE, D. Tree species classification in the Southern Alps based on the fusion of very high geometrical resolution multispectral/hyperspectral images and LiDAR data. **Remote Sensing of Environment**, v. 123, p. 258–270, 2012.

DALPONTE, M.; ØRKA, H.O.; ENE, L.T.; GOBAKKEN, T.; NÆSSET, E. Tree crown delineation and tree species classification in boreal forests using hyperspectral and ALS data. **Remote Sensing of Environment**, v. 140, p. 306–317, 2014.

DALPONTE, M.; ØRKA, H.O.; GOBAKKEN, T.; GIANELLE, D., NÆSSET, E. Tree species classification in boreal forests with hyperspectral data. **IEEE Transactions on Geoscience and Remote Sensing**, v. 51, p. 2632–2645, 2013.

DEMIR, B.; BRUZZONE, L. A multiple criteria active learning method for support vector regression. **Pattern Recognition**, v. 47, n. 2558–2567, 2014.

DENG, S.; KATOH, M.; XIAOWEI, Y.; HYYPPÄ, J.; GAO, T. Comparison of tree species classifications at the individual tree level by combining ALS data and RGB images using different algorithms. **Remote Sensing**, v. 8, n. 12, p. 1034, 2016.

DRAKOS, G. **Support vector machine vs logistic regression**. 2018. Available from: <https://towardsdatascience.com/support-vector-machine-vs-logistic-regression-94cc2975433f>. Access in: Nov 3, 2018.

DUNCANSON, L.; COOK, B.; HURTT, G.; DUBAYAH, R. An efficient, multi-layered crown delineation algorithm for mapping individual tree structure across multiple ecosystems. **Remote Sensing of Environment**, v. 154, p. 378 -386, 2014.

DURO, D.C.; FRANKLIN, S.E.; DUBE, M.G. A comparison of pixel-based and object-based image analysis with selected machine learning algorithms for the classification of agricultural landscapes using SPOT-5 HRG imagery. **Remote Sensing of Environment**, v. 118, p. 259–272, 2012.

EISANK, C.; SMITH, M.; HILLIER, J. Assessment of multiresolution segmentation for delimiting drumlins in digital elevation models. **Geomorphology**, v. 214, n. 100, p. 452–464, 2014.

FALKOWSKI, J.; EVANS, J. S.; MARTINUZZI, S.; GESSLER, P. E.; HUDAK, A. T. Characterizing forest succession with lidar data: an evaluation for the Inland Northwest, USA. **Remote Sensing of Environment**, v. 113, p. 946–956, 2009.

FASSNACHT, F.E.; LATIFI, H.; STERECZAK, K.; MODZELEWSKA, A.; LEFSKY, M.; WASER, L.T.; STRAUB, C.; GHOSH, A. Review of studies on tree species classification from remotely sensed data. **Remote Sensing of Environment**, v. 186, p. 64–87, 2016.

FASSNACHT, F.E.; NEUMANN, C.; FÖRSTER, M.; BUDDENBAUM, H.; GHOSH, A.; CLASEN, A.; JOSHI, P.K.; KOCH, B. Comparison of feature reduction algorithms for classifying tree species with hyperspectral data on three central European test sites. **IEEE Journal of Selected Topics in Applied Earth Observations and Remote Sensing**, v. 7, n. 6, p. 2547–2561, 2014.

FÉRET, J.; ASNER, G.P. Tree species discrimination in tropical forests using airborne imaging spectroscopy. **IEEE Transactions on Geoscience and Remote Sensing**, v. 51, p. 73–84, 2013.

FERRAZ, A.; SAATCHI, S.; MALLET, C.; MEYER, V. Lidar detection of individual tree size in tropical forests, **Remote Sensing of Environment**, v. 183, p. 318-333, 2016.

FERREIRA, M. P.; WAGNER, F. H.; ARAGAO, L. E. O. C.; SHIMABUKURO, Y. E.; SOUZA FILHO, C. R. Tree species classification in tropical forests using visible to shortwave infrared WorldView-3 images and texture analysis. **ISPRS Journal of Photogrammetry and Remote Sensing**, v. 149, p.119-131, 2019.

FERREIRA, M. P.; ZANOTTA, D. C.; ZORTEA, M.; KORTING, T. S.; FONSECA, L. M. G.; SHIMABUKURO, Y. E.; SOUZA FILHO, C. R. Automatic tree crown delineation in tropical forest using hyperspectral data. In: INTERNATIONAL GEOSCIENCE AND REMOTE SENSING SYMPOSIUM (IGARSS), Québec, Canada. **Proceedings...** Québec, 2014. p. 784–787.

FERREIRA, M.P.; ZORTEA, M.; ZANOTTA, D.C.; SHIMABUKURO, Y.E.; SOUZA FILHO, C.R. Mapping tree species in tropical seasonal semi-deciduous forests with hyperspectral and multispectral data. **Remote Sensing of Environment**, v. 179, p. 66–78, 2016.

FINEGAN, B. Forest succession. **Nature**, v. 312, n. 8, p. 109-114, 1984.

FINEGAN, B.; DELGADO, D. Structural and floristic heterogeneity in a 30-year-old Costa Rican rain forest restored on pasture through natural secondary succession. **Restoration Ecology**, Crawley, v. 8, n. 4, p. 380-393, 2000.

FOOD AND AGRICULTURE ORGANIZATION - FAO **Forests and agriculture: land-use challenges and opportunities**. Rome: FAO, 2016.

FRANKLIN, S.E.; AHMED, O.S. Deciduous tree species classification using object-based analysis and machine learning with unmanned aerial vehicle multispectral data. **International Journal of Remote Sensing**, v. 39, p. 5236–5245, 2017.

FREDRICH, C.M.B.; FEITOSA, R.Q. Automatic adaptation of segmentation parameters applied to inhomogeneous objects detection. In: CONFERENCE ON GEOGRAPHIC OBJECT-BASED IMAGE ANALYSIS, 2008, Calgary, Canada. **Proceedings...** University of Calgary, 2008.

FRICKER, G. A.; VENTURA J. D.; WOLF, J. A.; NORTH, M. P; DAVIS, F. W.; FRANKLIN, J. A. Convolutional neural network classifier identifies tree species in mixed-conifer forest from hyperspectral imagery. **Remote Sensing**, v. 11, n. 2326, 2019.

FUKUSHIMA, K. Neocognitron: a self-organizing neural network model for a mechanism of pattern recognition unaffected by shift in position. **Biological Cybernetics**, v. 36, n.4, p. 193–202, 1980.

GALVÃO, L.S.; PONZONI, F.J.; LIESENBERG, V.; SANTOS, J.R.D. Possibilities of discriminating tropical secondary succession in Amazônia using hyperspectral and multiangular CHRIS/PROBA data. **International Journal of Applied Earth Observation and Geoinformation**, v. 11, p. 8–14, 2009.

GAMON, J.A.; PEÑUELAS, J.; FIELD, C.B. A narrow-waveband spectral index that tracks diurnal changes in photosynthetic efficiency. **Remote Sensing of Environment**, v. 41, p. 35–44, 1992.

GAO, Q.; LIM, S.; JIA, X. Hyperspectral image classification using convolutional neural networks and multiple feature learning. **Remote Sensing**, v. 10, n. 2, p. 299, 2018.

GATES, D. M.; KEEGAN, H. J.; SCHLETER, J. C.; WEIDNER, V. R. Spectral properties of plants. **Applied Optics**, v. 4, n. 1, 1965.

GHORBANZADEH, O.; BLASCHKE, T.; GHOLAMNIA, K.; MEENA, S. R.; TIEDE D.; ARYAL J. Evaluation of different machine learning methods and deep-learning convolutional neural networks for landslide detection. **Remote Sensing**, v. 11, n. 196, 2019.

GHOSH, A.; FASSNACHT, E. F.; JOSHI, P. K.; KOCH, B. A framework for mapping tree species combining hyperspectral and LiDAR data: role of selected classifiers and sensor across three spatial scales. **International Journal of Applied Earth Observation and Geoinformation**, v. 26, p. 49–63, 2014.

GITELSON, A. A.; KAUFMAN, Y. J.; MERZLYAK, M. N. Use of a green channel in remote sensing of global vegetation from EOS-MODIS. **Remote Sensing of Environment**, v. 58, p. 289-298, 1996.

GITELSON, A.A.; MERZLYAK, M.N. Quantitative estimation of chlorophyll-a using reflectance spectra: experiments with autumn chestnut and maple leaves. **Journal of Photochemistry and Photobiology B: Biology**, v. 22, p. 247-252, 1994.

GOETZ, A.; VANE, G. Imaging spectrometry for earth remote sensing. **Science**, v. 228, n. 4704, p. 1147-1153, 1985.

GOMES, M.F.; MAILLARD, P. Using spectral and textural features from RapidEye images to estimate age and structural parameters of Cerrado vegetation. **International Journal of Remote Sensing**, v. 36, p. 3058–3076, 2015.

GOODFELLOW, I.; Y. BENGIO, Y.; COURVILLE, A. **Deep learning**. Cambridge: MIT Press, 2016.

GOOGLE EARTH. Available from: <http://earth.google.com/web>. Access in: July 23, 2019.

GRAVES, S.J.; ASNER, G.P.; MARTIN, R.E.; ANDERSON, C.B.; COLGAN, M.S.; KALANTARI, L.; BOHLMAN, S. Tree species abundance predictions in a tropical agricultural landscape with a supervised classification model and imbalanced data. **Remote Sensing**, v. 8, n. 2, p. 161, 2016.

GREEN, A. A.; BERMAN, M.; SWITZER, P.; CRAIG, M. D. A transformation for ordering multispectral data in terms of image quality with implications for noise removal. **IEEE Transactions on Geoscience and Remote Sensing**, v. 26, p. 65–74, 1988.

GU, H.; HAN, Y; YANG, Y.; LI, H.; LIU, Z.; SOERGEL, U.; BLASCHKE, T.; CUI, S. An efficient parallel multi-scale segmentation method for remote sensing imagery. **Remote Sensing**, v. 10, n. 4, p. 590, 2018.

GUAN, H.; YU, Y.; YAN, W.; LI, D.; LI, J. 3D CNN based tree species classification using mobile LiDAR data. In: THE INTERNATIONAL ARCHIVES OF THE PHOTOGRAMMETRY, REMOTE SENSING AND SPATIAL INFORMATION SCIENCES, 42., 2019. **Proceedings...** Enschede, The Netherlands, 2019.

GUYON, I.; ELISSEEFF, A. An introduction to variable and feature selection. **Journal of Machine Learning Research**, v. 3, p. 1157-1182, 2003.

HALL, M.; FRANK, E.; HOLMES, G.; PFAHRINGER, B.; REUTEMANN, P.; WITTEN I. H. The weka data mining software: an update. **ACM SIGKDD Explorations Newsletters**, v. 11, n. 1, p. 10–8, 2009.

HAMRAZ, H.; JACOBS, N. B.; CONTRERAS, M. A.; CLARK, C. H. Deep learning for conifer/deciduous classification of airborne LiDAR 3D point clouds representing individual trees. **arXiv:1802.08872**, 2018.

HANSEN, M. C.; POTAPOV, P. V.; MOORE, R.; HANCHER, M.; TURUBANOVA, S. A.; TYUKAVINA, A. et al. High-resolution global maps of 21st-century forest cover change. **Science**, v. 342, p. 850–853, 2013.

HALL, M.; FRANK, E.; HOLMES, G.; PFAHRINGER, P. R., WITTEN, I. H. The WEKA data mining software: an update. **SIGKDD Explorations Newsletter**, v.11, n.1, p.10-18, 2009.

HARALICK, R. M.; SHANMUGAM, K.; DINSTEN, I. H. Textural features for image classification. **IEEE Transactions on Systems, Man, and Cybernetics**, v. 3, p. 610–621, 1973.

HARTLING, S.; SAGAN, V.; SIDIKE, P.; MAJMAITIJANG, M.; CARRON, J. Urban tree species classification using a WorldView-2/3 and LiDAR data fusion approach and deep learning, **Sensors**, v. 19, n. 6, p. 1284, 2019.

HASTIE, T. J.; TIBSHIRANI, R. J.; FRIEDMAN, J. H. **The elements of statistical learning: data mining, inference, and prediction**. New York: Springer, 2009.

HATFIELD, J. L.; GITELSON, A. A.; SCHEPERS, J. S.; WALTHALL, C. L. Application of spectral remote sensing for agronomic decisions. **A Supplement to Agronomy Journal**, p. 117-131, 2008.

HE, K. S. et al. Will remote sensing shape the next generation of species distribution models? **Remote Sensing in Ecology and Conservation**, v. 1, p. 4–18, 2015.

HE, K. S.; ROCCHINI, D.; NETELER, M.; NAGENDRA, H. Benefits of hyperspectral remote sensing for tracking plant invasions. **Diversity And Distribution**, v. 17, p. 381–392, 2011.

HE, X.; WANG, A.; GHAMISI, P.; LI, G.; CHEN, Y. LiDAR data classification using spatial transformation and CNN. **IEEE Geoscience and Remote Sensing Letters**, p. 1-5, 2018.

HEINZEL, J.; KOCH, B. Investigating multiple data sources for tree species classification in temperate forest and use for single tree delineation. **International Journal of Applied Earth Observation And Geoinformation**, v. 18, p. 101–110, 2012.

HIGUCHI, P.; SILVA, A. C.; FERREIRA, T. S.; SOUZA, S. T.; GOMES, J. P.; SILVA, K. M.; SANTOS, K. F.; LINKE, C.; PAULINO, P. S. Influência de variáveis ambientais sobre o padrão estrutural e florístico do componente arbóreo, em um fragmento de Floresta Ombrófila Mista Montana em Lages, SC. **Ciência Florestal**, v. 22, n. 1, p. 79 - 90, 2012.

HIRA, Z.M.; GILLIES, D.F. A review of feature selection and feature extraction methods applied on microarray data. **Advances in Bioinformatics**, n. 198363, 2015.

HONKAVAARA, E. et al. Remote sensing of 3-D geometry and surface moisture of a peat production area using hyperspectral frame cameras in visible to short-wave infrared spectral ranges onboard a small Unmanned Airborne Vehicle (UAV). **IEEE Transactions on Geoscience and Remote Sensing**, v. 54, 2016.

HONKAVAARA, E.; ROSNELL, T.; OLIVEIRA, R.; TOMMASELLI, A. Band registration of tuneable frame format hyperspectral UAV imagers in complex scenes. **ISPRS Journal of Photogrammetry and Remote Sensing**, v. 134, p. 96–109, 2017.

HONKAVAARA, E.; SAARI, H.; KAIVOSOJA, J.; PÖLÖNEN, I.; HAKALA, T.; LITKEY, P.; MÄKYNEN, J.; PESONEN, L. Processing and assessment of spectrometric, stereoscopic imagery collected using a lightweight UAV spectral camera for precision agriculture. **Remote Sensing**, v. 5, p. 5006-5039, 2013.

HU, X.; CHEN, W.; XU, W. Adaptive mean shift-based identification of individual trees using airborne LiDAR data. **Remote Sensing**, v. 9, n. 2, p. 148, 2017.

HUANG, C.; DAVIS, L.S.; TOWNSHEND, J.R.G. An assessment of support vector machines for land cover classification. **Remote Sensing**, v. 23, p. 725–749, 2002.

HUGHES, G. F. On the mean accuracy of statistical pattern recognizers. **IEEE Transactions on Information Theory**, v. 14, n. 1, p. 55–63, 1968.

IMMITZER, M.; VUOLO, F.; CLEMENT ATZBERGER, C. First experience with Sentinel-2 data for crop and tree species classifications in Central Europe. **Remote Sensing**, v. 8, p. 166, 2016.

INSTITUTO BRASILEIRO DE GEOGRAFIA E ESTATÍSTICA - IBGE. **Instituto Brasileiro de Geografia e Estatística**. Available from: <<https://downloads.ibge.gov.br/>>. Access in: Mar 12, 2019.

INSTITUTO NACIONAL DE PESQUISAS ESPACIAIS - INPE. **O aplicativo TerraView**. Available from: <http://www.dpi.inpe.br/cursos/ser301/software.html>. Access in: Oct 24, 2018.

INTERNATIONAL UNION FOR CONSERVATION OF NATURE - IUCN. **The IUCN red list of threatened species**. 2017. Available from: <http://www.iucnredlist.org/>. Access in: Jan 8, 2018.

ISENBURG, M. **LAStools**: software for rapid LiDAR processing. Available from: <http://www.cs.unc.edu/~isenburg/lastools/>. Access in: July 7, 2018.

JANOTH, J.; EISL, M.; KLAUSHOFER, F.; LUCKEL, W. Procedimentos baseados em segmentação para a análise de mudanças e classificação florestais com dados de satélite de alta resolução. In: BLASCHKE, T.; KUX, H. (Ed.). **Sensoriamento remoto e SIG avançados**. 2. ed. São Paulo: Oficina de Textos, 2007.

JOHANSEN, K.; PHINN, S. Mapping structural parameters and species composition of riparian vegetation using IKONOS and Landsat ETM+ data in Australian tropical savannahs. **Photogrammetric Engineering and Remote Sensing**, v. 72, p. 71–80, 2006.

JOLY, C.A.; METZGER, J.P.; TABARELLI, M. Experiences from the Brazilian Atlantic forest: ecological findings and conservation initiatives. **New Phytologist**, v. 204, p. 459–473, 2014.

JONES, T. G.; COOPS, N. C.; SHARMA, T. Assessing the utility of airborne hyperspectral and LiDAR data for species distribution mapping in the coastal Pacific Northwest, Canada. **Remote Sensing of Environment**, v. 114, p. 2841–2852, 2010.

KALACSKA, M.; BOHLMAN, S.; SANCHEZ-AZOFEIFA, G.; CASTRO ESAU, K.; CAELLI, T. Hyperspectral discrimination of tropical dry forest lianas and trees: comparative data reduction approaches at the leaf and canopy levels **Remote Sensing of Environment**, v. 109, p. 406-415, 2007.

KARATZOGLOU, A.; SMOLA, A.; HORNIK, K.; ZEILEIS, A. kernlab - an S4 package for kernel methods in R. **Journal of Statistical Software**, v. 11, n. 9, p. 1–20, 2004.

KE, Y.; QUACKENBUSH, L. J. A comparison of three methods for automatic tree crown detection and delineation from high spatial resolution imagery.” **International Journal of Remote Sensing**, v. 32, n. 13, p. 3625–3647, 2011.

KHARE, S.; LAFITI, H.; ROSSI, S.; GHOSH, S. K. Fractional cover mapping of invasive plant species by combining very high-resolution stereo and multi-sensor multispectral imageries. **Forests**, v. 10, n. 7, p. 540, 2019.

KINGMA, D. P.; BA, J. L. Adam: a method for stochastic optimization. **International Conference on Learning Representations**, p. 1–13, 2015.

KOEHRSEN, W. Random forest simple explanation. 2017. Available from: <https://medium.com/@williamkoehrsen/random-forest-simple-explanation-377895a60d2d>. Access in: Nov 3, 2018.

KUNCHEVA, L. I. **Combining pattern classifiers: methods and algorithms**. 2.ed.. New Jersey: John Wiley & Sons, 2014.

KWOK, R. Ecology’s remote-sensing revolution. **Nature**, v. 556, p. 137–138, 2018.

LAL, T. N.; CHAPELLE, O.; WESTON, J. Embedded methods. GUYON, I.; NIKWAVESH, M.; GUNN, S.; ZADEH, L. A. (Ed.). **Feature extraction**. Heidelberg: Springer, 2006. p. 137-165.

LARSEN, M.; ERIKSSON, M.; DESCOMBES, X.; PERRIN, G.; BRANDTBERG, T.; GOUGEON, F. A. Comparison of six individual tree crown detection algorithms evaluated under varying forest conditions. **International Journal of Remote Sensing**, v. 32, p. 5827–5852, 2011.

LECUN, Y.; BOTTOU, L.; BENGIO, Y.; HAFFNER, P. Gradient-based learning applied to document recognition. **Proceedings of the IEEE**, p. 2278–2324, 1998.

LEE, J.; CAI, X.; LELLMANN, J.; DALPONTE, M.; MALHI, Y.; BUTT, N.; MORECROFT, M.; SCHÖNLIEB, C-B.; COOMES, D. A. Individual tree species classification from airborne multisensor imagery using robust PCA. **IEEE Journal of Selected Topics in Applied Earth Observations and Remote Sensing**, v. 9, n. 6, 2016.

LEE, J.; COOMES, D. A.; SCHÖNLIEB, C-B.; CAI, X.; LELLMANN, J.; DALPONTE, M.; MALHI, Y.; BUTT, N.; MORECROFT, M. A graph cut approach to 3D tree delineation, using integrated airborne LiDAR and hyperspectral imagery. **CoRR**, abs/1701.06715, 2017.

LI, G.; LU, D.; MORAN, E.; HETRICK, S. Land-cover classification in a moist tropical region of Brazil with Landsat thematic mapper imagery. **International Journal of Remote Sensing**, v. 32, p. 8207–8230, 2011.



LI, W.; DU, Q. Support vector machine with adaptive composite kernel for hyperspectral image classification. In: SATELLITE DATA COMPRESSION, COMMUNICATIONS, AND PROCESSING, 11., 2015, **Proceedings...** SPIE, 2015.

LI, W.; HAOHUAN, F.; YU, L.; CRACKNELL, A. Deep learning based oil palm tree detection and counting for high-resolution remote sensing images. **Remote Sensing**, v. 9, n. 22, 2017.

LI, Y.; ZHANG, H.; SHEN, Q. Spectral–spatial classification of hyperspectral imagery with 3D convolutional neural network. **Remote Sensing**, v. 9, n. 67, 2017.

LIAW, A.; WIENER, M. Classification and regression by random forest. **R News**, v. 2, n. 3, p. 18–22, 2002.

LIN, C.; POPESCU, S.C.; THOMSON, G.; TSOGT, K.; CHANG, C.-I. Classification of tree species in overstorey canopy of subtropical forest using QuickBird images. **PLoS ONE**, v. 10, e0125554, 2015.

LIU, B.; LI, Y.; LI, G.; LIU, A. A Spectral Feature Based Convolutional Neural Network for Classification of Sea Surface Oil Spill. **ISPRS International Journal of Geo-Information**, v. 8, n. 160, 2019.

LIU, H.; WU, C. Crown-level tree species classification from AISA hyperspectral imagery using an innovative pixel-weighting approach. **International Journal of Applied Earth Observation and Geoinformation**, v. 68, p. 298-307, 2018.

LOPES, A.; NELSON, B.; WU, J.; GRAA, P.; TAVARES, J.; PROHASKA, N.; MARTINS, G.; SALESKA, S. Leaf flush drives dry season green-up of the central amazon. **Remote Sensing of Environment**, v. 182, p. 90-98, 2016.

LORENA, A. C.; CARVALHO, A. C. P. L. F. Uma introdução às support vectors machines - tutorial. **Revista de Informática Teórica e Aplicada**, v. 14, n. 2, p. 43-67, 2007.

LORENZI, H. **Árvores brasileiras**: manual de identificação e cultivo de plantas arbóreas nativas do Brasil. Plantarum: Nova Odessa, 1992. 351 p.

LOUPPE, G.; WEHENKEL, L.; SUTERA, A.; GEURTS, P. Understanding variable importances in forests of randomized trees. In: INTERNATIONAL CONFERENCE ON NEURAL INFORMATION PROCESSING SYSTEMS, 26., 2013. **Proceedings...** 2013. p. 431-439.

- LU, D.; BATISTELLA, M.; LI, G.; MORAN, E.; HETRICK, S.; FREITAS, C.; DUTRA, L.; SANT'ANNA, S.J.S. Land use/cover classification in the Brazilian Amazon using satellite images. **Brazilian Journal of Agricultural Research**, v. 47, p. 1185–1208, 2012.
- LU, D.; LI, G.; MORAN, E.; KUANG, W. A comparative analysis of approaches for successional vegetation classification in the Brazilian Amazon. **GIScience And Remote Sensing**, v. 51, p. 695–709, 2014.
- LU, D.; MAUSEL, P.; BRONDÍZIO, E.; MORAN, E. Classification of successional forest stages in the Brazilian Amazon basin. **Forest Ecology and Management**, v. 181, n. 3, p. 301–312, 2003.
- LU, D.; WENG, Q. A survey of image classification methods and techniques for improving classification performance. **International Journal of Remote Sensing**, v. 28, p. 823–870, 2007.
- LUCAS, R.; BUNTING, P.; PATERSON, M.; CHISHOLM, L. Classification of Australian forest communities using aerial photography, CASI and HyMap data. **Remote Sensing of Environment**, v. 112, p. 2088–2103, 2008.
- LUCIEER, A.; STEIN, A. Existential uncertainty of spatial objects segmented from satellite sensor imagery. **IEEE Transactions on Geoscience and Remote Sensing**, v. 40, p. 2518–2521, 2002.
- LUO, G.; CHEN, G.; TIAN, L.; QIN, K.; QIAN, S.-E. Minimum noise fraction versus principal component analysis as a preprocessing step for hyperspectral imagery denoising. **Canadian Journal of Remote Sensing**, v. 42, p. 106–116, 2016.
- LYONS, M. B.; KEITH, D. A.; PHINN, S. R.; MASON, T. J.; ELITH, J. A comparison of resampling methods for remote sensing classification and accuracy assessment. **Remote Sensing of Environment**, v. 208, p. 145–153, 2018.
- MA, L.; LI, M.; GAO, Y.; CHEN, T.; MA, X.; QU, L. A novel wrapper approach for feature selection in object-based image classification using polygon-based cross-validation. **IEEE Geoscience and Remote Sensing Letters**, v. 14, p. 409–413, 2017.
- MALDONADO, S.; WEBER, R. A wrapper method for feature selection using support vector machines. **Information Sciences**, v. 179, p. 2208–2217, 2009.
- MALLINIS, G.; KOUTSIAS, N.; TSAKIRI-STRATI, M.; KARTERIS, M. Object-based classification using Quickbird imagery for delineating forest vegetation polygons in a Mediterranean test site. **ISPRS Journal of Photogrammetry and Remote Sensing**, v. 63, p. 237–250, 2008.

MANFREDI, S.; GOMES, J. P.; FERREIRA, P. I.; BORTOLUZZI, R. L. C.; MANTOVANI, A. dissimilaridade florística e espécies indicadoras de Floresta Ombrófila Mista e Ecótonos no Planalto Sul Catarinense. **Floresta**, v. 45, n. 3, p. 497 - 506, 2015.

MAPBIOMAS. **Project MapBiomias**: collection 2.3 of Brazilian land cover & use map Series. 2018. Available from: [http://mapbiomas.org/pages/database/mapbiomas\\_collection](http://mapbiomas.org/pages/database/mapbiomas_collection). Access in: July 31, 2018.

MARRS, J.; NI-MEISTER, W. Machine learning techniques for tree species classification using co-registered LiDAR and hyperspectral data. **Remote Sensing**, v. 11, n. 7, p. 819, 2019.

MASCHLER, J.; ATZBERGER, C.; IMMITZER, M. Individual tree crown segmentation and classification of 13 tree species using airborne hyperspectral data. **Remote Sensing**, v. 10, p. 1218, 2018.

MATHWORKS, INC. **MATLAB**: the language of technical computing: computation, visualization: programming: installation guide for UNIX version 5. Natick: Math Works Inc., 1996.

MATURANA, D.; SCHERER, S. Voxnet: a 3d convolutional neural network for real-time object recognition. In: IEEE/RSJ INTERNATIONAL CONFERENCE ON INTELLIGENT ROBOTS AND SYSTEMS (IROS), 2015. **Proceedings...** 2015. p. 922–928.

MAXWELL, A. E.; WARNER, T. A.; FANG, F. Implementation of machine-learning classification in remote sensing: an applied review. **International Journal of Remote Sensing**, v. 39, n. 9, p. 2784-2817, 2018.

MELGANI, F.; BRUZZONE, L. Classification of hyperspectral remote sensing images with support vector machines. **IEEE Transactions on Geoscience and Remote Sensing**, v. 42, n. 8, p. 1778–1790, 2004.

MELLOR, A.; BOUKIR, S.; HAYWOOD, A.; JONES, S. Exploring issues of training data imbalance and mislabelling on random forest performance for large area land cover classification using the ensemble margin. **ISPRS Journal of Photogrammetry and Remote Sensing**, v. 105, p.155–168, 2015.

MERZLYAK, M. N.; GITELSON, A. A.; CHIVKUNOVA, O. B; RAKITIN, V. Y. Non-destructive optical detection of pigment changes during leaf senescence and fruit ripening. **Physiologia Plantarum**, v. 106, n. 1, p. 135-141, 1999.

MIYOSHI, G.T.; IMAI, N.N.; TOMMASELLI, A.M.G.; HONKAVAARA, E. Impact of reduction of radiometric resolution in hyperspectral images acquired over forest field. In: THE INTERNATIONAL ARCHIVES OF THE PHOTOGRAMMETRY, REMOTE SENSING AND SPATIAL INFORMATION SCIENCES, 42., 2018. **Proceedings.... 2018a.**

MIYOSHI, G.T.; IMAI, N.N.; TOMMASELLI, A.M.G.; HONKAVAARA, E.; NÄSI, R.; MORIYA, É.A.S. Radiometric block adjustment of hyperspectral image blocks in the Brazilian environment. **International Journal of Remote Sensing**, v. 39, p. 4910–4930, 2018b.

MOUNTRAKIS, G.; IM, J.J.; OGOLE, C. Support vector machines in remote sensing: a review. **ISPRS Journal of Photogrammetry and Remote Sensing**, v. 66, p. 247–259, 2011.

MURPHY, K. P. **Machine learning: a probabilistic perspective.** Cambridge: The MIT Press, 2012.

NAGENDRA, H. Using remote sensing to assess biodiversity. **International Journal of Remote Sensing**, v.22, p.2377–2400, 2001.

NAGENDRA, H.; ROCCHINI, D. High resolution satellite imagery for tropical biodiversity studies: the devil is in the detail. **Biodiversity and Conservation**, v. 17, p. 3431–3442, 2008.

NAIDOO, L.; CHO, M.A.; MATHIEU, R.; ASNER, G. Classification of savanna tree species, in the Greater Kruger National Park region, by integrating hyperspectral and LiDAR data in a Random Forest data mining environment. **ISPRS Journal of Photogrammetry and Remote Sensing**, v. 69, p. 167–179, 2012.

NÄSI, R.; HONKAVAARA, E.; LYYTIKÄINEN-SAARENMAA, P.; BLOMQVIST, M.; LITKEY, P.; HAKALA, T.; VILJANEN, N.; KANTOLA, T.; TANHUANPÄÄ, T.; HOLOPAINEN, M. Using UAV-based photogrammetry and hyperspectral imaging for mapping bark beetle damage at tree-level. **Remote Sensing**, v. 7, p. 15467–15493, 2015.

NELDER, J.; MEAD, R. A simplex method for function minimization. **The Computer Journal**, v. 7, n. 4, p. 308-313, 1965.

NEVALAINEN, O.; HONKAVAARA, E.; TUOMINEN, S.; VILJANEN, N.; HAKALA, T.; YU, X.; HYYPA, J.; SAARI, H.; POLONEN, I.; IMAI, N. N.; TOMASELLI, A. M. G. Individual tree detection and classification with UAV-based photogrammetric point clouds and hyperspectral imaging. **Remote Sensing**, v. 9, n. 185, 2017.

NGUYEN, M. H. **A system for Individual tree Crown detection and classification based on elevation and intensity LiDAR data**. 2019. 72 p. Dissertation (Master in Information and Communication Engineering)- Department of Information Engineering and Computer Science, University of Trento, Trento, Italy, 2019.

NGUYEN, M. H.; DEMIR, B.; DALPONTE, M. Weighted support vector machines for tree species classification using LiDAR data. In: INTERNATIONAL GEOSCIENCE AND REMOTE SENSING SYMPOSIUM (IGARSS), 2019, Yokohama, Japan. **Proceedings...** 2019.

NORDIN, S. A.; LATIF, Z. A.; OMAR, H. Individual tree crown segmentation in tropical peat swamp forest using airborne hyperspectral data. **Geocarto International**, v.34, n.11, p.1218-1236, 2018.

NOVO, E. M. L. M. **Sensoriamento remoto: princípios e aplicações**. 4.ed. São Paulo: Edgard Blücher, 2011.

OLIVEIRA, R. A.; TOMMASELLI, A.M.; HONKAVAARA, E. Geometric calibration of a hyperspectral frame camera. **Photogrammetric Record**, v. 31, p. 325–347, 2016.

PAL, N.R.; PAL, S.K. A review on image segmentation techniques. **Pattern Recognition**, v. 26, p. 1277–1294, 1993.

PANEQUE-GÁLVEZ, J.; MCCALL, M.K.; NAPOLETANO, B.M.; WICH, S.A.; KOH, L.P. Small drones for community-based forest monitoring: an assessment of their feasibility and potential in tropical areas. **Forests**, v. 5, p. 1481–1507, 2014.

PASUPA, K.; SUNHEM, W. A. Comparison between shallow and deep architecture classifiers on small dataset. In: INTERNATIONAL CONFERENCE ON INFORMATION TECHNOLOGY AND ELECTRICAL ENGINEERING (ICITEE), 8., 2016. **Proceedings...** 2016.

PEEL, M.C.; FINLAYSON, B.L.; MCMAHON, T.A. Updated world map of the Köppen-Geiger climate classification. **Hydrology and Earth System Sciences**, v. 11, p. 1633–1644, 2007.

PIAZZA, A.G.; VIBRANS, A.C.; LIESENBERG, V.; REFOSCO, J.C. Object-oriented and pixel-based classification approaches to classify tropical successional stages using airborne high-spatial resolution images. **GIScience and Remote Sensing**, v. 53, p. 206–226, 2016.

PIIROINEN, R.; HEISKANEN, J.; MAEDA, E.; VIINIKKA, A.; PELLIKKA, P. Classification of tree species in a diverse african agroforestry landscape using imaging spectroscopy and laser scanning. **Remote Sensing**, v. 9, p. 875, 2017.

PINTO, F. M. **Classificação do estágio sucessional da vegetação em áreas de floresta ombrófila mista (FOM) com o emprego de imagens digitais obtidas por VANT (Veículo Aéreo Não Tripulado)**. 2018. 89 p. (Mestrado em Engenharia Florestal)- Universidade do Estado de Santa Catarina (UDESC), Lages, Brasil, 2018.

PÖLÖNEN, I.; ANNALA, L.; RAHKONEN, S.; NAVALAINEN, O.; HONKAVAARA, E.; TUOMINEN, S.; VILJANEN, N.; HAKALA, T. Tree species identification using 3D spectral data and 3D convolutional neural network. In: WORKSHOP ON HYPERSPPECTRAL IMAGE AND SIGNAL PROCESSING: EVOLUTION IN REMOTE SENSING (WHISPERS), 9., 2018. **Proceedings...** 2018.

PONT-TUSET, J.; MARQUES, F. Measures and meta-measures for the supervised evaluation of image segmentation. In: IEEE CONFERENCE ON COMPUTER VISION AND PATTERN RECOGNITION, 2013, Portland, USA. **Proceedings...** 2013. p. 2131-2138.

PONZONI, F. J.; SHIMABUKURO, Y. E.; KUPLICH, T. M. **Sensoriamento remoto da vegetação**. 2. ed. São Paulo: Oficina de Textos, 2012.

PONZONI, F.J.; REZENDE, A.N.P. Caracterização espectral de estágios sucessionais de vegetação secundária arbórea em Altamira (PA), através de dados orbitais. **Revista Árvore**, v. 28, p. 535–545, 2004.

PRASAD, A. M.; IVERSON, L. R.; LIAW, A. Newer classification and regression tree techniques: bagging and random forests for ecological prediction. **Ecosystems**, v. 9, n. 2, p.181–199, 2006.

PU, R.; LANDRY, S. A comparative analysis of high spatial resolution IKONOS and WorldView-2 imagery for mapping urban tree species. **Remote Sensing of Environment**, v. 124, p. 516–533, 2012.

PUDIL, P.; NOVOVICOVÁ, J.; KITTLER, J. Floating search methods in feature selection. **Pattern Recognition Letters**, v.15, p. 1119–1125, 1994.

QGIS DEVELOPMENT TEAM. **QGIS Geographic Information System**. Open Source Geospatial Foundation, 2017. Available from: <http://qgis.osgeo.org>. Access in: Aug 24, 2018.

QI, C.R.; SU, H.; NIEßNER, M.; DAI, A.; YAN, M.; GUIBAS, L.J. Volumetric and multi-view CNNs for object classification on 3d data. In: IEEE CONFERENCE ON COMPUTER VISION AND PATTERN RECOGNITION, 2016, Las Vegas, USA. **Proceedings...** 2016. p. 5648-5656.

QI, C.R.; SU, H.; MO, K.; GUIBAS, L.J. Pointnet: deep learning on point sets for 3d classification and segmentation. **Computer Vision and Pattern Recognition (CVPR)**, v. 1, n. 4, 2017.

QIAN, Y.; W. ZHOU, J. YAN, W. LI, L. Han. Comparing machine learning classifiers for object-based land cover classification using very high resolution imagery. **Remote Sensing**, v. 7, p. 153-168, 2014.

QUIRITA, V. A. A.; ACHANCCARAY, P. M. D.; FEITOSA, R. Q.; HAPP, P. N.; COSTA, G. A. O. P.; KLINGER, T.; HEIPKE, C. Metaheuristics for supervised parameter tuning of multiresolution segmentation. **IEEE Geoscience and Remote Sensing Letters**, v. 13, n. 9, p. 1364-1368, 2016.

R DEVELOPMENT CORE TEAM. **R**: a language and environment for statistical computing. Available from: <http://www.r-project.org>. Access in: Mar 20, 2018.

RACZKO, E.; ZAGAJEWSKI, B. Comparison of support vector machine, random forest and neural network classifiers for tree species classification on airborne hyperspectral APEX images. **European Journal of Remote Sensing**, v. 50, p. 144–154, 2017.

RAMOELO, A.; CHO, M.; MATHIEU, R.; SKIDMORE, A.K. Potential of sentinel-2 spectral configuration to assess rangeland quality. **Journal of Applied Remote Sensing**, v. 9, n. 1, 2015.

RÄSÄNEN, A.; RUSANEN, A.; KUITUNEN, M.; LENSU, A. What makes segmentation good? a case study in boreal forest habitat mapping. **International Journal of Remote Sensing**, v. 34, n. 23, p. 8603-8627, 2013.

RAUTIAINEN, M.; STENBERG, P. Application of photon recollision probability in coniferous canopy reflectance simulations. **Remote Sensing of Environment**, v. 96, p. 98–107, 2005.

REZENDE, C. L.; SCARANO, F. R.; ASSAD, E. D.; JOLY, C. A.; METZGER, J.P.; STRASSBURG, B. B. N.; TABARELLI, M.; FONSE, G. A.; MITTERMEIER, R. A. From hotspot to hopespot: an opportunity for the Brazilian Atlantic Forest. **Perspectives in Ecology and Conservation**, v. 16, n. 4, p. 208-214, 2018.

RIBEIRO, M.; METZGER, J. P.; MARTENSEN, A. C.; PONZONI, F.J.; HIROTA, M. M. The Brazilian Atlantic Forest: how much is left, and how is the remaining forest distributed? implications for conservation. **Biological Conservation**, v. 142, p. 1141–1153, 2009.

RICHARDS, J.A.; JIA, X. **Remote sensing digital image analysis**: an introduction. 4.ed. New York: Springer, 2006.

RICHTER, R.; REU, B.; WIRTH, C.; DOKTOR, D.; VOHLAND, M. The use of airborne hyperspectral data for tree species classification in a species-rich Central European forest area. **International Journal of Applied Earth Observation and Geoinformation**, v. 52, p. 464–474, 2016.

ROBERTS, D.A.; USTIN, S.L.; OGUNJEMIYO, S.; GREENBERG, J.; DOBROWSKI, S.Z.; CHEN, J.; HINCKLEY, T.M. Spectral and structural measures of northwest forest vegetation at leaf to landscape scales. **Ecosystems**, v. 7, p. 545–562, 2004.

RODARMEL C.; SHAN, J. Principal component analysis for hyperspectral image classification. **Surveying and Land Information Science**, v. 62, n. 2, p. 115, 2002.

RODERJAN, C. V.; GALVÃO, F.; KUNIOSHI, Y. S.; HATSCHBACH, G. G. As unidades fitogeográficas do estado do Paraná, Brasil. **Ciência & Ambiente**, Santa Maria, v. 24, p. 75-92, 2002.

RONDEAUX, G.; STEVEN, M.; BARET, F. Optimization of soil-adjusted vegetation indices. **Remote Sensing of Environment**, v. 55, p. 95-107, 1996.

ROSLANI, M.A.; MUSTAPHA, M.A.; LIHAN, T.; WAN JULIANA, W.A. Classification of mangroves vegetation species using texture analysis on Rapideye satellite imagery. **AIP Conference Proceedings**, v. 1571, p. 480, 2013.

ROUSE, J. W.; HAAS, R. H.; SCHELL, J.A.; DEERING, W. D. Monitoring vegetation systems in the Great Plains with ERTS. In: ERTS SYMPOSIUM, 3., 1973. **Proceedings...** 1973. p.309-317. (NASA SP-351).

ROUSSEL, J.R.; AUTY, D.; DE BOISSIEU, F.; MEADOR, A.S. **lidR**: airborne LiDAR data manipulation and visualization for forestry applications. Available from: <https://cran.rproject.org/web/packages/lidR/index.html>. Access in: Aug 22, 2018.

RUSSELL, S.; NORVIG, P. **Artificial intelligence: a modern approach**. 3.ed. [S.l.]: Prentice Hall, 2009.

SALACH, A.; BAKULA, K.; PILARSKA, M.; OSTROWSKI, W.; GÓRSKI, K.; KURCZYNSKI, Z. Accuracy assessment of point clouds from LiDAR and dense image matching acquired using the UAV platform for DTM creation. **ISPRS International Journal of Geoinformation**, v. 7, n. 342, 2018.

SAYN-WITTGENSTEIN, L. **Recognition of tree species on aerial photographs**. Ottawa, Canada: Forest Management Institute, 1978. (Information Report FMR-X-118).



SENOP. **Datasheet VIS-NIR snapshot hyperspectral camera for UAVs.** Snapshot Hyperspectral Camera. Available from: <http://view.24mags.com/mera/datasheet-hyperspectralcamera>. Access in: Aug 2, 2018.

SETTE, P.G.C.; MAILLARD, P. Análise de textura de imagem de alta resolução para aprimorar a acurácia da classificação da mata atlântica no sul da Bahia. In: BRAZILIAN SYMPOSIUM ON REMOTE SENSING-SBSR, 15., 2011, Curitiba, PR, Brazil. **Proceedings...**Curitiba, 2011.

SHEN, X.; CAO, L. Tree-species classification in subtropical forests using airborne hyperspectral and LiDAR data. **Remote Sensing**, v. 9, p. 1180, 2017.

SHI, J.; MALIK, J. Normalized cuts and image segmentation. Pattern Analysis and Machine Intelligence. **IEEE Transactions on Pattern Analysis and Machine Intelligence**, v. 22, n. 8, p. 888–905, 2000.

SIGNORONI, A.; SAVARDI, M.; BARONIO, A.; BENINI, S. Deep learning meets hyperspectral image analysis: a multidisciplinary review. **Journal of Imaging**, v. 5, n. 52, 2019.

SIMINSKI, A.; FANTINI, A. C.; GURIES, R. P.; RUSCHEL, A. R.; REIS, M. S. Secondary forest succession in the Mata Atlantica, Brazil: floristic and phytosociological trends. **International Scholarly Research Notices Ecology**, 759893, p. 1-19, 2011.

SIMINSKI, A.; FANTINI, A. C.; REIS, M. S. Classificação da vegetação secundária em estágios de regeneração da Mata Atlântica em Santa Catarina. **Ciência Florestal**, v. 23, n. 3, p. 369-378, 2013.

SINGH, M.; EVANS, D.; TAN, B. S.; NIN, C. S. Mapping and characterizing selected canopy tree species at the Angkor World Heritage Site in Cambodia using aerial data. **PLoS ONE**, v. 11, n. 4, e0154548, 2015.

SKIDMORE, A.K. Accuracy assessment of spatial information. In: STEIN, A.; VAN DER MEER, F. D.; GORTE, B. (Ed.). **Spatial statistics for remote sensing**. Dordrecht: Kluwer Academic Publishers, 1999. p. 197–209.

SLIK, J. W. F. et al. An estimate of the number of tropical tree species. **Proceedings of the National Academy of Sciences**, v. 112, p.7472–7477, 2015.

SOTHE, C.; ALMEIDA, C. M.; LIESENBERG, V.; SCHIMALSKI, M. B. Evaluating Sentinel-2 and Landsat-8 data to map successional forest stages in a subtropical forest in southern Brazil, **Remote Sensing**, v. 9, n. 8, p. 838, 2017a.

SOTHE, C.; SCHIMALSKI, M.B.; LIESENBERG, V.; DE ALMEIDA, C.M. Approaches for classifying successional forest stages in São Joaquim National Park using Landsat-8 and RapidEye images. **Boletim de Ciências Geodésicas**, v. 23, 2017b.

SOTHE, C.; DALPONTE, M.; ALMEIDA, C. M. de; SCHIMALSKI, M. B.; LIMA, C. L.; LIESENBERG, V.; MIYOSHI, G. T.; TOMMASELLI, A. M. G. Tree species classification in a highly diverse subtropical forest integrating UAV-based photogrammetric point cloud and hyperspectral data. **Remote Sensing**, v. 11, n. 11, 2019a.

SOTHE, C.; ALMEIDA, C. M.; SCHIMALSKI, M. B.; LIESENBERG, V.; ROSA, L. C.; BERMUDEZ, J. D.; FEITOSA, R. Q. Comparison of machine and deep learning algorithms applied to multisource data for a subtropical forest area classification. **International Journal of Remote Sensing**, DOI:10.1080/01431161.2019.1681600. 2019b.

SOTHE, C.; ALMEIDA, C. M. DE; SCHIMALSKI, M. B.; LIESENBERG, V.; ACHANCCARAY DIAZ, P. Automatic tuning of segmentation parameters for tree crown delineation with VHR imagery. **Geocarto International**, DOI:10.1080/10106049.2019.1690056, 2019c.

STEINWART, I.; CHRISTMANN, A. **Support vector machines**. New York: Springer, 2008.

STORN, R.; PRICE, K. Differential evolution: a simple and efficient heuristic for global optimization over continuous spaces. **Journal of Global Optimization**, v. 11, n. 4, p. 341–359, 1997.

STRASSBURG, B. B. et al. The role of natural regeneration to ecosystem services provision and habitat availability: a case study in the Brazilian Atlantic Forest. **Biotropica**, v. 48, p. 890–899, 2016.

STRÎMBU, V. F.; STRÎMBU, B. M. A graph-based segmentation algorithm for tree crown extraction using airborne LiDAR data. **ISPRS Journal Photogrammetry**, v. 104, p. 30–43, 2015.

TAUBERT, F. et al. Global patterns of tropical forest fragmentation. **Nature**, v. 554, p. 519, 2018.

TIGGES, J.; LAKES, T.; HOSTERT, P. Urban vegetation classification: benefits of multitemporal RapidEye satellite data. **Remote Sensing of Environment**, v. 136, p. 66–75, 2013.

TOCHON, G.; FÉRET, J. B.; VALERO, S.; MARTIN, R. E.; KNAPP, D. E.; SALEMBIER, P.; ASNER, G. P. On the use of binary partition trees for the tree crown segmentation of tropical rainforest hyperspectral images. **Remote Sensing of Environment**, v. 159, p. 318–331, 2015.

TONG, X; XIE, H; WENG, Q. Urban land cover classification with airborne hyperspectral data: what features to use? **IEEE Journal of Selected Topics in Applied Earth Observations and Remote Sensing**, v. 7, n. 10, p. 3998-4009, 2014.

TOPALOGLU, R.H.; SERTELA, E.; MUSAOGLU, N. Assessment of classification accuracies of Sentinel-2 and Landsat-8 data for land cover/use mapping. In: INTERNATIONAL ARCHIVES OF THE PHOTOGRAMMETRY, REMOTE SENSING AND SPATIAL INFORMATION SCIENCES, 23., 2016, Prague, Czech Republic. **Proceedings...** 2016. p. 1055–1059.

TORRES-SÁNCHEZ, J.; LÓPEZ-GRANADOS, F.; PEÑA, J. M. An automatic object-based method for optimal thresholding in UAV images: application for vegetation detection in herbaceous crops. **Computers and Electronics in Agriculture**, v. 114, p. 43-52, 2015.

TUOMINEN, S.; NÄSI, R.; HONKAVAARA, E.; BALAZS, A.; HAKALA, T.; VILJANEN, N.; PÖLÖNEN, I.; SAARI, H.; OJANEN, H. Assessment of classifiers and remote sensing features of hyperspectral imagery and stereo-photogrammetric point clouds for recognition of tree species in a forest area of high species diversity. **Remote Sensing**, v. 10, p. 714, 2018.

USTIN, S. L.; DIPIETRO, D.; OLMSTEAD, K.; UNDERWOOD, E.; SCHEER, G. J. Hyperspectral remote sensing for invasive species detection and mapping. **IEEE International Geoscience and Remote Sensing Symposium**, v. 3, p. 1658–1660, 2002.

VAN AARDT, J. A. N.; WYNNE, R. H. Examining pine spectral separability using hyperspectral data from an airborne sensor: an extension of field-based results. **International Journal of Remote Sensing**, v. 28, n. 2, p. 431–436, 2007.

VAPNIK, V. N. **The nature of Statistical learning theory**. New York: Springer-Verlag, 1995. 314 p.

VAUHKONEN, J.; SEPPÄNEN, A.; PACKALÉN, P.; TOKOLA, T. Improving species-specific plot volume estimates based on airborne laser scanning and image data using alpha shape metrics and balanced field data. **Remote Sensing of Environment**, v. 124, p. 534–541, 2012.

VELOSO, H. P.; KLEIN, R. M. As comunidades e associações vegetais da mata pluvial do sul do Brasil. III. as associações das planícies costeiras do quaternário, situadas entre o Rio Itapocu, **Sellowia**, Itajaí, v. 13, p. 205-260, 1961.

VELOSO, H. P.; RANGEL FILHO, A. L. R.; LIMA, J. C. A. **Classificação da vegetação brasileira, adaptada a um sistema universal**. Rio de Janeiro: Fundação Instituto Brasileiro de Geografia e Estatística, 1991. 123p.

VIANA, V.; TABANEZ, A.J. Biology and conservation of forest: fragments in Brazilian Atlantic Moist Forest. In: SCHEILAS, J.; GREENBERG, R. (Ed.). **Forest patches in tropical landscapes**. Washington: Island Press, 1996.

VIBRANS, A. C.; SEVEGNANI L.; GASPER AL, LINGNER D. V. **Inventário florístico florestal de Santa Catarina**: Floresta Ombrófila Mista. Blumenau: Edifurb, v.3, 2013.

VIEIRA, I. C. G.; ALMEIDA, A. S.; DAVIDSON, E. A.; STONE, T. A.; CARVALHO, C. J. R.; GUERRERO, J. B. Classifying successional forests using Landsat spectral properties and ecological characteristics in Eastern Amazônia. **Remote Sensing of Environment**, v. 87, p. 470–481, 2003.

WAGNER, F. H.; FERREIRA, M. P.; SANCHEZ, A.; HIRYE, M. C. M.; ZORTEA, M.; GLOOR, E.; PHILLIPS, O. L.; SOUZA FILHO, C. R.; SHIMABUKURO, Y.E.; ARAGÃO, L.E.O.C. Individual tree crown delineation in a highly diverse tropical forest using very high resolution satellite images. **ISPRS Journal of Photogrammetry and Remote Sensing**, v. 145, Part B: 362-377, 2018.

WAGNER, F. H.; SANCHEZ, A.; TARABALKA, Y.; LOTTE, R. G.; FERREIRA, M. P.; AIDAR, M. P. M.; GLOOR, W.; PHILLIPS, O. L.; ARAGÃO, L. E. O. C. Using the U-net convolutional network to map forest types and disturbance in the Atlantic rainforest with very high resolution images. **Remote Sensing in Ecology and Conservation**, 2019.

WANG, J.; LUO, C.; HUANG, H.; ZHAO, H.; WANG, S. Transferring pre-trained deep CNNs for remote scene classification with general features learned from linear PCA network. **Remote Sensing**, v. 9, p. 225, 2017.

WEBB, A. R.; COPSEY, K. D. **Statistical pattern recognition**. 3.ed. Hoboken, NJ, USA: Wiley, 2011. 666 p, ISBN: 978-0-470-68227-2.

WORLD RESOURCES INSTITUTE. **Millennium ecosystem assessment: ecosystems and human well-being: biodiversity synthesis**. Washington: Island Press, 2005.

WU, Z.; SONG, S.; KHOSLA, A.; YU, F.; ZHANG, L.; TANG, X.; XIAO, J. 3D shapenets: a deep representation for volumetric shapes. In: CONFERENCE ON COMPUTER VISION AND PATTERN RECOGNITION, 2015. **Proceedings...** IEEE, 2015. p. 1912-1920.

YU, Q.; GONG, P.; CLINTON, N.; BIGING, G.; KELLY, M.; SCHIROKAUER, D. Object-based detailed vegetation classification with airborne high spatial resolution remote sensing imagery. **Photogrammetric Engineering & Remote Sensing**, v. 72, n. 7, p. 799–811, 2006.

YU, X.; WU, X.; LUO, C.; REN, P. Deep learning in remote sensing scene classification: a data augmentation enhanced convolutional neural network framework. **GIScience & Remote Sensing**, v. 54, n. 5, p. 741–758, 2017.

YUE, J.; ZHAO, W.; MAO, S.; LIU, H. Spectral–spatial classification of hyperspectral images using deep convolutional neural networks. **Remote Sensing Letters**, v. 6, p. 468–477, 2015.

ZHANG, C.; SARGENT, I.; PAN, X.; LI, H.; GARDINER, A.; HARE, J.; ATKINSON, P. M. An object-based convolutional neural network (OCNN) for urban land use classification. **Remote Sensing of Environment**, v. 216, p. 57–70, 2018.

ZHANG, L.; ZHANG, L.; DU, B. Deep learning for remote sensing data: a technical tutorial on the state of the art. **IEEE Geoscience and Remote Sensing Magazine**, v. 4, p. 22–40, 2016.

ZHANG, W.; HU, B.; WOODS, M.; BROWN, G. Characterizing forest succession stages for wildlife habitat assessment using multispectral airborne imagery. **Forests**, v. 8, n. 234, 2017.

ZHANG, Z.; ZANG, R.; WANG, G.; HUANG, X. Classification of landscape types based on land cover, successional stages and plant functional groups in a species-rich forest in Hainan Island, China. **Tropical Conservation Science**, v. 9, p. 135–152, 2016.

ZHEN, Z.; QUACKENBUSH, L. J.; ZHANG, L. Trends in automatic individual tree crown detection and delineation: evolution of LiDAR data. **Remote Sensing**, v. 8, p. 333, 2016.

## APPENDIX A – CONFUSION MATRICES OF SUCCESSIONAL FOREST STAGES CLASSIFICATION

Table A.1- Confusion matrices of successional forest stages classification using WV-2 data.

<b>SVM_VNIR</b>					<b>RF_VNIR</b>				
Class	SS1	SS2	SS3	Total	Class	SS1	SS2	SS3	Total
SS1	183	58	110	351	SS1	144	16	23	183
SS2	10	94	6	110	SS2	10	109	5	124
SS3	0	48	384	432	SS3	39	75	472	586
Total	200	200	500	900	Total	200	200	500	900

---

<b>SVM_VNIR_CHM</b>					<b>RF_VNIR_CHM</b>				
Class	SS1	SS2	SS3	Total	Class	SS1	SS2	SS3	Total
SS1	181	42	1	224	SS1	178	60	0	238
SS2	10	145	8	163	SS2	13	128	0	141
SS3	2	13	491	506	SS3	2	12	500	514
Total	200	200	500	900	Total	200	200	500	900

---

<b>SVM_VNIR_CHM_MNF</b>					<b>RF_VNIR_CHM_MNF</b>				
Class	SS1	SS2	SS3	Total	Class	SS1	SS2	SS3	Total
SS1	178	42	10	230	SS1	178	60	0	238
SS2	10	158	11	179	SS2	13	129	0	142
SS3	5	0	479	484	SS3	2	11	500	513
Total	200	200	500	900	Total	200	200	500	900

---

<b>SVM_VNIR_CHM_GLCM</b>					<b>RF_VNIR_CHM_GLCM</b>				
Class	SS1	SS2	SS3	Total	Class	SS1	SS2	SS3	Total
SS1	178	42	10	230	SS1	169	37	0	206
SS2	10	136	5	151	SS2	13	143	0	156
SS3	5	22	485	512	SS3	11	20	500	531
Total	200	200	500	900	Total	200	200	500	900

---

<b>SVM_VNIR_CHM_VI</b>					<b>RF_VNIR_CHM_VI</b>				
Class	SS1	SS2	SS3	Total	Class	SS1	SS2	SS3	Total
SS1	178	39	10	227	SS1	180	40	0	220
SS2	10	135	8	153	SS2	13	140	0	153
SS3	5	26	482	513	SS3	0	20	500	520
Total	200	200	500	900	Total	200	200	500	900

<b>SVM_VNIR_MNF_GLCM_VI</b>				
Class	SS1	SS2	SS3	Total
SS1	172	42	15	229
SS2	10	127	6	143
SS3	11	31	479	521
Total	200	200	500	900

<b>RF_VNIR_MNF_GLCM_VI</b>				
Class	SS1	SS2	SS3	Total
SS1	171	24	24	219
SS2	3	129	5	137
SS3	19	47	471	537
Total	200	200	500	900

<b>SVM_MNF_CHM</b>				
Class	SS1	SS2	SS3	Total
SS1	177	69	5	251
SS2	10	130	0	140
SS3	6	1	495	502
Total	200	200	500	900

<b>RF_MNF_CHM</b>				
Class	SS1	SS2	SS3	Total
SS1	181	77	0	258
SS2	10	112	0	122
SS3	2	11	500	513
Total	200	200	500	900

<b>SVM_FSRF</b>				
Class	SS1	SS2	SS3	Total
SS1	178	39	0	219
SS2	15	141	0	154
SS3	0	20	500	520
Total	200	200	500	900

<b>RF_FSRF</b>				
Class	SS1	SS2	SS3	Total
SS1	180	39	0	219
SS2	13	141	0	154
SS3	0	20	500	520
Total	200	200	500	900

<b>SVM_full</b>				
Class	SS1	SS2	SS3	Total
SS1	164	38	10	212
SS2	10	152	8	170
SS3	19	10	482	511
Total	200	200	500	900

<b>RF_full</b>				
Class	SS1	SS2	SS3	Total
SS1	174	42	5	221
SS2	13	141	0	154
SS3	6	17	495	518
Total	200	200	500	900

Table A.2- Confusion matrices of successional forest stages classification using Hyperspectral data.

<b>SVM_VNIR</b>					<b>RF_VNIR</b>				
Class	SS1	SS2	SS3	Total	Class	SS1	SS2	SS3	Total
SS1	400	56	34	490	SS1	400	10	64	474
SS2	0	306	21	327	SS2	0	352	171	523
SS3	0	38	945	983	SS3	0	38	765	803
Total	400	400	1,000	1,800	Total	400	400	1,000	1,800

<b>SVM_VNIR_CHM</b>					<b>RF_VNIR_CHM</b>				
Class	SS1	SS2	SS3	Total	Class	SS1	SS2	SS3	Total
SS1	400	21	13	434	SS1	400	0	0	400
SS2	0	379	58	437	SS2	0	400	18	418
SS3	0	0	929	929	SS3	0	0	982	982
Total	400	400	1,000	1,800	Total	400	400	1,000	1,800

<b>SVM_VNIR_CHM_MNF</b>					<b>RF_VNIR_CHM_MNF</b>				
Class	SS1	SS2	SS3	Total	Class	SS1	SS2	SS3	Total
SS1	400	13	10	423	SS1	400	0	0	400
SS2	0	387	48	435	SS2	0	400	13	413
SS3	0	0	942	942	SS3	0	0	987	987
Total	400	400	1,000	1,800	Total	400	400	1,000	1,800

<b>SVM_VNIR_CHM_GLCM</b>					<b>RF_VNIR_CHM_GLCM</b>				
Class	SS1	SS2	SS3	Total	Class	SS1	SS2	SS3	Total
SS1	400	21	13	434	SS1	400	0	24	424
SS2	0	379	50	429	SS2	0	390	111	501
SS3	0	0	937	937	SS3	0	10	865	875
Total	400	400	1,000	1,800	Total	400	400	1,000	1,800

<b>SVM_VNIR_CHM_VI</b>					<b>RF_VNIR_CHM_VI</b>				
Class	SS1	SS2	SS3	Total	Class	SS1	SS2	SS3	Total
SS1	400	13	10	423	SS1	400	0	26	426
SS2	0	387	78	465	SS2	0	399	51	450
SS3	0	0	912	912	SS3	0	1	923	924
Total	400	400	1,000	1,800	Total	400	400	1,000	1,800

<b>SVM_VNIR_MNF_GLCM_VI</b>					<b>RF_VNIR_MNF_GLCM_VI</b>				
Class	SS1	SS2	SS3	Total	Class	SS1	SS2	SS3	Total
SS1	400	25	31	456	SS1	400	0	44	444
SS2	0	375	8	383	SS2	0	386	57	443
SS3	0	0	961	961	SS3	0	14	899	913
Total	400	400	1,000	1,800	Total	400	400	1,000	1,800



<b>SVM_MNF_CHM</b>					<b>RF_MNF_CHM</b>				
Class	SS1	SS2	SS3	Total	Class	SS1	SS2	SS3	Total
SS1	400	0	0	400	SS1	400	0	0	400
SS2	0	400	79	479	SS2	0	385	21	406
SS3	0	0	921	921	SS3	0	15	979	994
Total	400	400	1,000	1,800	Total	400	400	1,000	1,800

<b>SVM_VNIR_PPC</b>					<b>RF_VNIR_PPC</b>				
Class	SS1	SS2	SS3	Total	Class	SS1	SS2	SS3	Total
SS1	400	0	60	460	SS1	400	13	38	451
SS2	0	388	52	440	SS2	0	387	79	466
SS3	0	12	888	900	SS3	0	0	883	883
Total	400	400	1,000	1,800	Total	400	400	1,000	1,800

<b>SVM_VNIR_CHM_PPC</b>					<b>RF_VNIR_CHM_PPC</b>				
Class	SS1	SS2	SS3	Total	Class	SS1	SS2	SS3	Total
SS1	400	0	0	400	SS1	400	0	24	424
SS2	0	400	35	435	SS2	0	400	60	460
SS3	0	0	965	965	SS3	0	0	916	916
Total	400	400	1,000	1,800	Total	400	400	1,000	1,800

<b>SVM_VNIR_CHM_PPC_MNF</b>					<b>RF_VNIR_CHM_PPC_MNF</b>				
Class	SS1	SS2	SS3	Total	Class	SS1	SS2	SS3	Total
SS1	400	0	0	400	SS1	400	0	26	426
SS2	0	400	39	439	SS2	0	400	65	465
SS3	0	0	961	961	SS3	0	0	909	909
Total	400	400	1,000	1,800	Total	400	400	1,000	1,800

## APPENDIX B – CONFUSION MATRICES OF TREE SPECIES CLASSIFICATION

Note: species ID according to Table 3.2.

Table B.1- Confusion matrices using the SVM algorithm in Area 1.

VNIR														
ID	1	2	3	4	5	6	7	8	9	10	11	12	13	14
1	6,087	234	1	4,820	230	1,053	0	339	227	170	141	301	0	79
2	355	11,349	515	113	241	22	7	18	192	93	901	352	50	54
3	2	923	5,104	4	0	0	0	1	2	14	127	297	502	7
4	148	40	0	3,278	1	725	0	2	38	50	81	10	0	0
5	564	235	4	190	6,168	5	0	7	6	0	818	1	0	0
6	387	139	1	933	10	10,207	56	880	1,028	646	549	254	2	65
7	0	0	3	6	0	1	1,080	21	741	362	98	50	2	4
8	255	85	163	94	45	80	26	2,350	658	306	349	372	0	564
9	79	371	123	323	1	98	415	165	9,822	897	2,615	711	60	45
10	80	1	10	199	0	73	127	30	2,488	1,461	1,073	114	8	20
11	1,376	366	186	164	35	54	748	92	7,027	2,087	31,622	1,265	72	4
12	3	113	3,590	108	0	15	4	7	161	87	315	1,671	114	104
13	0	48	148	0	0	0	0	0	0	7	138	400	1,532	0
14	1	1	19	22	0	3	262	28	380	299	80	65	3	42

VNIR_CHM														
ID	1	2	3	4	5	6	7	8	9	10	11	12	13	14
1	7,212	209	3	5,511	314	209	0	63	16	121	45	596	0	295
2	208	12,070	108	85	80	45	7	22	61	75	743	456	56	182
3	3	142	8,681	29	10	0	0	0	0	40	21	551	80	38
4	189	10	0	3,726	102	240	0	2	30	44	123	34	0	10
5	193	184	28	29	6,139	0	0	2	0	0	427	0	0	2
6	154	95	0	33	1	10,961	72	433	2,660	291	541	12	0	0
7	0	0	0	0	0	0	1,337	12	1,380	340	206	0	4	0
8	78	102	0	39	6	339	14	3,146	743	270	386	281	0	258
9	113	383	82	42	0	112	401	126	9,209	697	2,673	1,049	213	6
10	0	3	0	84	0	279	186	23	1,613	1,954	1,602	41	8	2
11	1,184	534	117	551	79	86	651	71	6,860	2,264	31,937	414	113	78
12	2	161	754	44	0	64	0	11	81	65	69	1,530	361	92
13	1	9	94	0	0	0	0	0	0	17	53	741	1,508	0
14	0	3	0	81	0	1	57	29	117	301	81	158	2	25

VNIR_PPC														
ID	1	2	3	4	5	6	7	8	9	10	11	12	13	14
1	7,979	32	0	2,098	0	0	0	0	132	14	1,828	611	0	0
2	159	10,594	986	11	0	101	67	8	141	46	758	230	22	47
3	0	16	3,978	0	0	0	0	0	16	4	3	64	1,730	0
4	96	12	0	6,248	6	58	0	0	183	54	306	70	0	0
5	0	271	0	13	6,684	0	0	0	0	0	627	0	0	0
6	0	503	10	0	0	11,866	0	7	1,954	855	0	16	2	0
7	0	0	12	0	0	0	2,045	81	1,056	9	0	0	0	1
8	0	0	284	0	0	0	86	3,651	1,023	25	0	15	0	828
9	0	131	306	1,861	0	140	362	113	11,117	123	5,492	504	13	50
10	4	3	9	0	0	25	13	11	1,011	3,003	1	16	8	0
11	1,089	2,289	44	23	41	85	152	52	6,134	2,345	29,400	110	120	0
12	10	54	4,157	0	0	61	0	6	2	0	492	3,420	0	21
13	0	0	79	0	0	0	0	0	1	1	0	28	450	0
14	0	0	2	0	0	0	0	11	0	0	0	779	0	41

VNIR_CHM_PPC														
ID	1	2	3	4	5	6	7	8	9	10	11	12	13	14
1	8,244	24	0	2,257	0	1	0	0	0	17	196	307	0	0
2	79	11,859	279	4	0	76	22	13	27	41	697	213	59	0
3	0	9	5,450	0	0	0	0	0	0	19	0	120	1,607	10
4	23	93	0	7,790	286	0	0	0	88	27	537	242	0	0
5	0	497	0	14	6,366	0	0	0	1	0	379	0	0	0
6	0	135	0	0	0	11,714	0	0	5,077	805	6	0	1	0
7	0	0	0	0	0	0	2,496	38	1	3	0	0	0	0
8	0	0	0	0	0	0	4	3,762	1,148	0	0	1	0	133
9	0	340	50	35	0	210	10	91	13,165	107	6,344	7	15	0
10	0	0	0	0	0	39	33	0	234	4,570	0	16	63	0
11	987	835	4	154	79	129	160	13	3,024	887	30,605	132	227	0
12	4	113	4,057	0	0	167	0	5	1	3	143	4,341	0	222
13	0	0	12	0	0	0	0	0	4	0	0	46	373	0
14	0	0	15	0	0	0	0	18	0	0	0	438	0	623

VNIR_CHM_PPC_MNF														
ID	1	2	3	4	5	6	7	8	9	10	11	12	13	14
1	8,258	33	0	2,513	0	6	0	0	0	19	193	391	0	0
2	61	12,211	240	7	0	57	23	7	32	38	610	203	79	1
3	0	7	5,809	0	0	0	0	0	0	15	0	112	1,123	11
4	20	80	0	7,593	68	0	0	0	126	14	422	172	0	0
5	1	601	0	6	6,587	0	0	0	0	0	529	0	0	0
6	0	227	0	0	0	11,772	0	0	4,356	550	5	1	1	0
7	0	0	0	0	0	0	2,461	44	0	0	0	0	0	0
8	0	0	0	0	0	0	8	3,773	1,001	0	0	1	0	116
9	4	260	37	16	0	190	19	93	11,426	94	5,065	45	24	0
10	0	2	0	0	0	55	39	0	378	4,702	0	18	38	0
11	991	375	3	119	76	129	175	13	5,442	1,036	31,760	213	199	0
12	2	109	3,755	0	0	127	0	5	6	11	323	4,204	0	199
13	0	0	3	0	0	0	0	0	3	0	0	76	881	0
14	0	0	20	0	0	0	0	5	0	0	0	427	0	661

VNIR_CHM_PPC_GLCM														
ID	1	2	3	4	5	6	7	8	9	10	11	12	13	14
1	8,064	23	0	4,053	0	25	0	0	14	55	463	546	0	0
2	149	11,592	338	15	2	124	21	2	36	160	544	254	105	4
3	0	1	7,054	0	0	0	0	0	0	15	0	384	663	7
4	87	0	0	6,095	55	0	0	0	110	27	187	85	0	0
5	0	1,373	0	21	6,632	0	0	0	0	0	764	0	0	0
6	10	430	0	0	0	11,862	0	3	2,707	406	31	0	2	0
7	0	0	0	0	0	0	2,347	6	67	11	0	0	0	0
8	0	0	0	0	0	0	16	3,810	1,451	2	0	8	0	329
9	12	57	85	6	0	91	39	96	10,447	98	5,525	158	3	0
10	0	0	0	0	0	85	32	0	1,027	4,286	0	16	14	0
11	1,015	326	0	64	42	38	270	1	6,903	1,352	31,290	136	56	0
12	0	103	2,334	0	0	111	0	6	7	64	103	3,799	61	179
13	0	0	10	0	0	0	0	0	1	3	0	122	1,441	0
14	0	0	46	0	0	0	0	16	0	0	0	355	0	469

VNIR_CHM_PPC_VI														
ID	1	2	3	4	5	6	7	8	9	10	11	12	13	14
1	8,323	19	0	2,247	0	0	0	0	2	19	314	294	0	0
2	62	12,051	302	3	1	73	24	11	17	45	688	208	72	1
3	0	2	5,771	0	0	0	0	0	0	16	0	119	1,192	16
4	23	90	0	7,819	240	1	0	0	92	34	379	227	0	0
5	0	642	0	19	6,436	0	0	0	0	0	469	0	0	0
6	0	146	0	0	0	11,788	0	3	4,805	715	2	0	0	0
7	0	0	0	0	0	0	2,482	44	0	0	0	0	0	0
8	0	0	0	0	0	0	7	3,764	1,099	0	0	10	0	142
9	0	334	17	11	0	152	15	96	13,013	113	4,933	11	17	0
10	0	1	0	0	0	48	24	0	344	4,676	0	14	53	0
11	927	505	3	155	54	126	173	10	3,394	850	31,919	172	180	0
12	2	115	3,757	0	0	148	0	6	2	10	203	4,264	0	238
13	0	0	1	0	0	0	0	0	2	1	0	73	831	0
14	0	0	16	0	0	0	0	6	0	0	0	471	0	591

VNIR_VI_MNF_GLCM														
ID	1	2	3	4	5	6	7	8	9	10	11	12	13	14
1	6,225	527	6	5,198	86	1,290	2	360	161	244	113	414	0	112
2	455	10,615	586	159	131	22	0	8	87	68	1,008	506	17	59
3	3	950	5,068	0	0	0	0	0	0	19	107	332	568	0
4	221	29	0	3,357	19	1,232	0	1	59	27	63	14	0	0
5	341	660	0	128	6,398	0	0	0	0	0	1,029	0	0	0
6	288	250	2	591	17	9,516	41	1,116	627	718	93	252	1	46
7	0	0	3	0	0	0	1,126	11	879	369	71	23	0	1
8	241	101	97	124	0	84	19	2,107	451	354	207	327	1	560
9	19	32	39	292	3	89	385	186	9,465	743	2,267	605	6	56
10	57	2	6	149	0	36	179	39	3,476	1,567	1,287	106	10	29
11	1,483	606	110	175	77	36	728	40	6,889	1,907	32,058	943	51	7
12	4	76	3,852	76	0	28	0	8	74	86	327	1,712	271	84
13	0	57	76	0	0	0	0	0	0	21	172	502	1,418	0
14	0	0	22	5	0	3	245	64	602	356	105	127	2	34

VNIR_CHM_PPC_VI_MNF														
ID	1	2	3	4	5	6	7	8	9	10	11	12	13	14
1	8,310	40	0	2,417	0	5	0	0	6	21	353	371	0	0
2	69	12,246	246	6	2	55	24	7	28	46	609	200	64	5
3	0	5	6,100	0	0	0	0	0	0	17	0	141	928	11
4	14	18	0	7,716	57	1	0	0	94	23	358	140	0	0
5	0	694	0	13	6,601	0	0	0	0	0	614	0	0	0
6	1	193	0	0	0	11,725	0	0	4,073	543	8	0	0	0
7	0	0	0	0	0	0	2,445	50	0	0	0	0	0	0
8	0	0	0	0	0	0	7	3,769	1,030	0	0	8	0	138
9	5	276	26	11	0	208	16	95	11,092	97	4,460	49	19	0
10	0	1	0	0	0	93	35	0	444	4,694	1	12	38	0
11	935	323	2	91	71	127	198	10	5,994	1,015	32,281	239	179	0
12	3	109	3,459	0	0	122	0	7	8	22	223	4,196	0	217
13	0	0	3	0	0	0	0	0	1	1	0	79	1,117	0
14	0	0	31	0	0	0	0	2	0	0	0	428	0	617

MNF_CHM_PPC														
ID	1	2	3	4	5	6	7	8	9	10	11	12	13	14
1	8,130	22	0	1,374	0	0	0	0	0	22	67	334	0	0
2	57	10,906	393	1	0	69	40	10	30	24	583	150	55	0
3	0	3	4,731	0	0	0	0	0	0	29	0	0	1,735	5
4	6	25	0	8,476	297	3	0	0	108	38	514	280	0	0
5	0	829	0	129	6,328	0	0	0	0	0	568	0	0	0
6	0	324	0	0	0	11,206	0	0	5,404	1,288	6	0	0	0
7	0	0	0	0	0	0	2,477	85	3	0	0	0	0	0
8	0	0	0	0	0	0	2	3,725	957	0	0	0	0	96
9	1	301	151	92	1	594	1	98	10,926	121	12,311	0	12	3
10	0	6	0	0	0	119	32	0	17	3,956	0	18	62	0
11	1,143	1,334	6	182	105	141	173	1	5,316	1,000	24,842	112	424	0
12	0	155	4,562	0	0	204	0	4	0	1	16	4,602	0	244
13	0	0	0	0	0	0	0	0	9	0	0	0	57	1
14	0	0	24	0	0	0	0	17	0	0	0	367	0	639

MNF_CHM_PPC_VI														
ID	1	2	3	4	5	6	7	8	9	10	11	12	13	14
1	8,273	34	0	1,731	0	3	0	0	0	26	43	336	0	0
2	46	11,547	294	1	0	85	28	7	22	34	519	153	62	1
3	0	3	5,038	0	0	0	0	0	2	13	0	1	1,314	12
4	6	5	0	8,254	179	1	0	0	91	43	304	274	0	0
5	3	901	0	76	6,457	0	0	0	0	0	595	0	0	0
6	0	322	0	0	0	11,486	0	0	5,105	1,095	8	0	1	0
7	0	0	0	0	0	0	2,484	87	1	0	0	0	1	0
8	0	0	0	0	0	0	2	3,737	863	0	0	0	0	116
9	1	194	131	56	7	353	4	90	14,057	107	11,025	15	28	3
10	0	8	0	0	0	118	34	0	91	4,265	0	16	61	0
11	1,008	759	7	136	88	131	173	10	2,534	888	26,365	148	254	0
12	0	132	4,366	0	0	159	0	5	0	8	48	4,563	0	214
13	0	0	11	0	0	0	0	0	4	0	0	0	624	0
14	0	0	20	0	0	0	0	4	0	0	0	357	0	642
<i>full</i>														
ID	1	2	3	4	5	6	7	8	9	10	11	12	13	14
1	7,944	22	0	5,554	0	27	0	0	13	45	422	501	0	0
2	130	11,827	283	14	5	81	9	0	27	124	537	198	64	13
3	0	0	7,093	0	0	0	0	0	0	11	0	345	561	1
4	92	0	0	4,616	33	2	0	0	98	41	159	72	0	0
5	7	1,171	0	32	6,659	0	0	0	0	0	865	0	0	0
6	14	311	0	0	0	11,772	0	7	2,592	496	28	1	0	0
7	0	0	0	0	0	0	2,332	9	77	12	0	0	0	0
8	0	0	0	0	0	0	19	3,813	1,383	1	0	11	0	336
9	10	48	55	3	0	133	41	91	8,576	77	4,775	238	2	0
10	0	3	0	0	0	158	44	0	745	4,075	3	13	14	0
11	1,140	429	0	35	34	45	280	1	9,257	1,489	32,022	203	85	0
12	0	94	2,342	0	0	118	0	6	2	100	96	3,595	70	203
13	0	0	31	0	0	0	0	0	0	8	0	249	1,549	0
14	0	0	63	0	0	0	0	13	0	0	0	437	0	435

FSJM														
ID	1	2	3	4	5	6	7	8	9	10	11	12	13	14
1	8,045	30	0	2,799	0	11	0	0	5	26	388	403	0	0
2	84	11,992	232	8	7	80	15	3	36	75	575	192	65	9
3	0	4	6,544	0	0	0	0	0	0	11	0	273	720	2
4	32	2	0	7,289	30	0	0	0	119	23	193	132	0	0
5	2	1,031	0	11	6,609	0	0	0	0	0	788	0	0	0
6	10	224	0	0	0	11,673	0	0	3,163	486	18	2	0	0
7	0	0	0	0	0	0	2,399	20	4	1	0	0	0	0
8	0	0	0	0	0	0	7	3,749	1,041	0	0	10	0	195
9	14	206	32	31	0	192	25	146	8,895	59	4,966	163	4	0
10	0	4	0	0	0	154	34	0	915	4,549	1	10	30	0
11	1,149	319	13	116	85	114	245	6	8,582	1,202	31,829	251	143	0
12	1	93	3,005	0	0	112	0	10	6	47	149	3,854	21	207
13	0	0	2	0	0	0	0	0	4	0	0	153	1,362	0
14	0	0	39	0	0	0	0	6	0	0	0	420	0	575

MV (VNIR_CHM_PPC_VI)														
ID	1	2	3	4	5	6	7	8	9	10	11	12	13	14
1	8,918	0	0	2,557	0	0	0	0	0	0	66	650	0	0
2	0	13,486	0	51	0	207	13	0	72	2	714	296	52	0
3	0	0	5,936	0	0	0	2	0	0	1	0	125	1,319	9
4	0	16	0	7,575	0	0	0	0	101	64	203	29	0	0
5	0	117	0	6	6,671	0	0	0	0	0	349	0	0	0
6	0	40	0	0	0	11,837	0	0	5,556	327	0	0	44	0
7	0	0	0	0	0	0	2,680	0	0	0	0	0	0	0
8	0	0	0	0	0	0	0	3,909	954	0	0	0	0	0
9	0	0	0	0	0	201	0	0	13,755	0	3,183	0	0	0
10	0	0	0	0	0	0	0	0	0	5,399	0	20	40	0
11	419	164	0	63	21	0	30	0	2,187	630	34,392	0	120	0
12	0	82	3,931	0	0	91	0	0	0	0	0	4,418	0	101
13	0	0	0	0	0	0	0	0	0	0	0	0	765	0
14	0	0	0	0	0	0	0	0	0	0	0	325	0	878



OBIA (VNIR_CHM_PPC_VI)														
ID	1	2	3	4	5	6	7	8	9	10	11	12	13	14
1	5,943	80	0	62	0	0	0	0	504	414	943	403	0	0
2	674	9,396	9	219	0	70	22	0	19	31	812	460	0	0
3	0	62	9,007	0	0	0	0	0	0	6	0	704	470	12
4	0	0	0	9,531	0	0	0	0	1	0	336	196	0	0
5	0	3,645	0	355	6,669	0	0	0	0	0	1,583	0	0	0
6	0	0	45	0	0	12,082	0	0	593	168	0	0	35	0
7	0	0	0	0	0	0	2,079	0	158	0	0	0	0	0
8	0	0	0	0	0	0	91	3,816	511	0	0	27	0	962
9	11	2	6	0	0	4	273	11	6,099	803	372	420	8	0
10	0	0	0	0	0	0	14	0	0	3,822	0	0	0	0
11	2,709	720	0	87	62	151	246	23	14,885	1,235	34,861	48	37	0
12	0	0	585	0	0	29	0	0	0	0	0	2,721	174	0
13	0	0	0	0	0	0	0	0	0	0	0	172	1,621	0
14	0	0	215	0	0	0	0	90	0	0	0	712	0	14

Table B.2- Confusion matrices using the wSVM algorithm in Area 1.

VNIR														
ID	1	2	3	4	5	6	7	8	9	10	11	12	13	14
1	5,450	223	0	4,096	87	1,064	1	425	250	170	55	178	0	80
2	392	11,440	328	78	234	26	9	8	234	89	1,194	336	15	19
3	2	1,130	4,109	0	0	0	1	0	0	12	195	239	303	0
4	283	43	0	3,601	0	1,055	0	11	50	63	109	14	0	0
5	886	337	0	375	6,386	15	0	14	13	0	1,180	10	0	1
6	487	198	1	1,171	2	9,986	63	1,159	895	646	648	304	0	58
7	0	0	8	10	0	0	1,496	36	2,440	617	454	88	2	1
8	668	203	120	101	20	73	20	1,868	969	303	661	565	0	507
9	29	121	50	310	0	27	251	186	6,375	572	2,234	399	8	35
10	85	1	28	365	0	42	313	84	7,118	2,613	4,722	264	27	45
11	1,051	81	18	31	2	29	161	46	2,397	402	25,722	347	20	2
12	1	47	4,891	100	0	18	13	13	299	126	456	1,856	274	209
13	0	79	199	0	0	0	0	0	0	16	285	812	1,689	0
14	3	2	115	16	0	1	397	90	1,730	850	992	451	7	31

VNIR_CHM_PPC														
ID	1	2	3	4	5	6	7	8	9	10	11	12	13	14
1	8,198	7	0	1,918	0	6	0	0	4	14	369	424	0	0
2	153	11,932	211	5	0	103	20	13	25	66	744	217	100	0
3	0	0	5,276	0	0	0	0	0	0	10	2	140	1,037	2
4	47	45	0	8,008	283	0	0	0	69	25	253	111	0	0
5	0	505	0	21	6,425	0	0	0	0	0	926	0	0	0
6	0	262	0	0	0	11,935	0	0	3,869	539	4	0	0	0
7	0	0	0	0	0	0	2,517	43	12	0	0	0	0	0
8	0	0	0	0	0	0	13	3,747	1,324	0	0	11	0	143
9	1	142	86	203	0	44	22	108	14,345	81	10,700	6	11	8
10	0	2	0	0	0	9	48	0	872	4,886	0	15	80	0
11	933	887	4	99	23	50	105	1	2,244	856	25,665	78	126	0
12	5	123	4,229	0	0	189	0	6	2	1	244	4,355	1	195
13	0	0	22	0	0	0	0	0	4	1	0	5	990	0
14	0	0	39	0	0	0	0	22	0	0	0	501	0	640

VNIR_CHM_PPC_VI														
ID	1	2	3	4	5	6	7	8	9	10	11	12	13	14
1	8,220	14	0	2,196	0	8	0	0	4	21	585	356	0	0
2	138	11,996	266	8	0	115	19	13	35	76	729	227	82	0
3	0	0	5,302	0	0	0	0	0	0	6	0	153	686	1
4	77	13	0	7,688	155	4	0	0	49	25	215	76	0	0
5	0	479	0	7	6,539	0	0	0	0	0	919	0	0	0
6	1	289	0	0	0	11,913	0	0	3,726	548	3	0	0	0
7	0	0	0	0	0	0	2,489	40	14	1	0	0	0	0
8	0	0	0	0	0	0	13	3,750	1,309	0	0	22	0	174
9	0	117	96	156	0	57	29	115	14,027	126	9,427	11	10	2
10	0	1	0	0	0	34	47	0	888	4,761	0	13	66	0
11	896	879	25	199	37	47	128	8	2,713	899	26,850	85	147	0
12	5	117	4,097	0	0	158	0	6	5	15	179	4,384	2	207
13	0	0	17	0	0	0	0	0	0	1	0	9	1,352	0
14	0	0	64	0	0	0	0	8	0	0	0	527	0	604

Table B.3- Confusion matrices using the RF algorithm in Area 1.

VNIR														
ID	1	2	3	4	5	6	7	8	9	10	11	12	13	14
1	5,662	372	1	5,496	30	1,926	2	404	247	208	75	148	0	46
2	345	10,904	596	80	228	37	9	7	231	73	847	555	41	53
3	0	1,312	4,946	0	0	1	0	0	0	4	134	500	413	0
4	79	2	0	2,116	0	1,392	0	10	19	138	29	5	0	0
5	658	200	0	335	6,333	23	0	21	19	0	562	8	0	0
6	243	174	0	1,212	0	8,708	54	1,228	448	469	300	187	0	65
7	0	0	0	0	0	0	125	2	354	30	8	13	0	0
8	376	246	77	182	4	62	29	1,578	762	320	212	669	0	408
9	25	120	40	405	0	39	1,071	488	9,179	1,716	2,186	505	0	248
10	23	0	3	28	0	5	17	9	221	250	39	16	0	10
11	1,926	516	282	376	136	134	1,306	170	10,916	3,017	34,015	1,712	69	54
12	0	14	3,852	24	0	9	2	6	56	44	267	1,289	183	90
13	0	45	39	0	0	0	0	0	0	5	229	181	1,637	0
14	0	0	31	0	0	0	110	17	318	205	4	75	2	14

VNIR_CHM														
ID	1	2	3	4	5	6	7	8	9	10	11	12	13	14
1	6,803	228	10	7,734	431	523	0	90	7	264	40	599	0	338
2	128	11,841	46	20	95	56	10	11	93	61	1,105	491	77	64
3	2	47	9,243	43	0	0	0	0	0	39	17	1,041	1	16
4	35	0	0	1,700	1	223	0	2	6	33	31	6	0	2
5	105	284	33	88	5,991	3	0	8	0	9	349	5	0	3
6	562	147	0	7	1	10,737	61	536	1,508	230	321	5	0	0
7	0	0	0	0	0	0	184	1	946	68	24	0	0	0
8	26	296	0	104	12	318	39	2,647	600	423	319	464	0	312
9	111	210	13	13	0	49	1,040	347	9,955	1,072	2,222	224	16	39
10	0	0	0	0	0	243	79	38	129	613	98	5	0	0
11	1,564	815	65	523	200	159	1,288	169	9,271	3,328	34,090	1,427	78	105
12	1	37	449	22	0	25	0	10	18	24	161	1,203	446	89
13	0	0	0	0	0	0	0	0	0	0	93	251	1,721	0
14	0	0	8	0	0	0	24	81	237	315	37	142	6	20

VNIR_CHM_PPC														
ID	1	2	3	4	5	6	7	8	9	10	11	12	13	14
1	7,342	6	0	40	0	0	0	0	633	28	1,480	319	0	0
2	18	9,557	228	0	0	387	99	44	122	1	2,826	352	0	9
3	0	0	3,623	0	0	0	0	0	0	21	0	16	2,060	0
4	12	22	0	5,735	577	0	0	0	130	6	263	388	0	0
5	0	72	0	1,481	5,524	0	0	0	24	0	652	0	0	0
6	1	828	0	0	0	11,413	0	0	2,842	367	0	86	0	0
7	0	0	0	0	0	0	2,202	12	438	0	0	0	0	0
8	0	0	74	0	0	0	2	3,461	1,347	0	0	0	0	436
9	0	0	291	2,321	0	439	334	350	8,214	834	13,331	0	0	89
10	38	0	0	0	0	17	0	1	2,050	3,641	4	1	10	0
11	1,837	3,273	133	677	630	22	88	61	6,965	1,581	16,834	157	275	0
12	89	147	5,314	0	0	58	0	2	0	0	3,517	3,949	0	76
13	0	0	95	0	0	0	0	0	5	0	0	0	0	0
14	0	0	109	0	0	0	0	9	0	0	0	595	0	378

VNIR_PPC_CHM_MNF														
ID	1	2	3	4	5	6	7	8	9	10	11	12	13	14
1	7,458	1	0	8	0	0	0	0	1	3	517	387	0	0
2	101	10,104	321	0	0	250	73	27	42	6	1,984	316	2	2
3	0	0	3,537	0	0	0	0	0	0	9	0	7	2,162	0
4	28	18	0	5,900	339	0	0	0	61	6	204	328	0	0
5	0	14	0	1,450	5,885	0	0	0	13	0	575	0	0	0
6	26	812	0	0	0	11,861	0	0	4,119	607	0	55	5	0
7	0	0	0	0	0	0	2,231	23	598	0	0	0	0	0
8	0	0	62	0	0	0	14	3,591	1,082	0	0	0	0	445
9	0	0	317	2,409	0	152	332	220	8,266	207	13,533	0	0	22
10	37	7	0	0	0	3	0	0	1,249	3,937	56	1	10	0
11	1,629	2,858	49	487	507	6	75	74	7,339	1,704	17,508	107	166	0
12	58	91	5,238	0	0	64	0	3	0	0	4,530	3,572	0	110
13	0	0	225	0	0	0	0	0	0	0	0	0	0	0
14	0	0	118	0	0	0	0	2	0	0	0	1,090	0	409

VNIR_PPC_CHM_GLCM														
ID	1	2	3	4	5	6	7	8	9	10	11	12	13	14
1	7,184	0	0	51	0	2	0	0	357	35	1,064	403	0	0
2	125	9,941	361	0	0	392	68	33	266	14	3,474	346	15	5
3	0	0	3,650	0	0	0	0	0	0	2	0	15	2,157	0
4	12	14	0	6,060	173	0	0	0	121	27	145	201	0	0
5	0	259	0	850	5,974	0	0	0	7	0	569	0	0	0
6	9	870	0	0	0	11,715	0	0	2,858	264	0	54	4	0
7	0	0	0	0	0	0	2,180	12	557	0	0	0	0	0
8	0	0	192	0	0	0	10	3,539	1,354	0	0	1	0	732
9	0	0	103	2,552	0	152	364	247	7,965	950	13,396	5	0	27
10	62	0	1	0	0	3	0	4	1,797	3,298	1	0	32	0
11	1,931	2,717	37	741	584	15	103	96	7,488	1,889	17,183	237	137	0
12	14	104	5,186	0	0	57	0	4	0	0	3,075	4,027	0	46
13	0	0	295	0	0	0	0	0	0	0	0	0	0	0
14	0	0	42	0	0	0	0	5	0	0	0	574	0	178

VNIR_PPC_CHM_VI														
ID	1	2	3	4	5	6	7	8	9	10	11	12	13	14
1	7,282	6	0	3	0	0	0	0	515	15	1,440	270	0	0
2	24	8,899	288	0	0	387	111	52	189	0	2,787	343	0	18
3	0	0	3,477	0	0	0	0	0	0	23	0	0	1,607	0
4	8	22	0	5,989	647	0	0	0	372	21	394	362	0	0
5	0	52	0	1,675	5,500	0	0	0	16	0	785	0	0	0
6	2	812	0	0	0	11,369	0	0	2,483	345	0	81	1	0
7	0	0	0	0	0	0	2,198	15	462	0	0	0	0	0
8	0	0	107	0	0	0	2	3,456	1,369	0	0	1	0	403
9	0	0	427	1,988	0	473	328	349	8,338	973	13,286	0	0	51
10	38	1	0	0	0	21	0	0	2,343	3,607	0	0	1	0
11	1,777	3,979	66	599	584	31	86	55	6,683	1,495	16,748	219	736	0
12	206	134	5,166	0	0	55	0	2	0	0	3,467	4,097	0	72
13	0	0	195	0	0	0	0	0	0	0	0	0	0	0
14	0	0	141	0	0	0	0	11	0	0	0	490	0	444

VNIR_PPC_CHM_VI_MNF														
ID	1	2	3	4	5	6	7	8	9	10	11	12	13	14
1	7,238	2	0	8	0	0	0	0	0	16	522	424	0	0
2	113	9,253	321	0	0	262	74	20	51	7	2,224	307	3	2
3	0	0	3,505	0	0	0	0	0	1	4	0	4	2,162	0
4	38	11	0	5,968	270	0	0	0	62	11	179	216	0	0
5	0	276	0	1,301	5,970	0	0	0	11	0	621	0	0	0
6	1	801	0	0	0	11,875	0	0	4,333	565	0	58	0	0
7	0	0	0	0	0	0	2,203	20	675	0	0	0	0	0
8	0	0	129	0	0	0	27	3,574	1,078	1	0	2	0	513
9	0	0	270	2,556	0	130	335	235	8,202	234	13,616	2	0	18
10	25	2	0	0	0	1	0	0	1,083	3,716	10	0	5	0
11	1,688	3,459	45	421	491	4	86	85	7,274	1,925	17,548	190	175	0
12	234	101	5,160	0	0	64	0	2	0	0	4,187	3,642	0	93
13	0	0	288	0	0	0	0	0	0	0	0	0	0	0
14	0	0	149	0	0	0	0	4	0	0	0	1,018	0	362

VNIR_VI_MNF_GLCM														
ID	1	2	3	4	5	6	7	8	9	10	11	12	13	14
1	5,853	345	1	5,679	14	2,403	0	397	151	247	77	226	0	52
2	435	10,235	481	193	191	37	3	2	95	48	687	510	26	49
3	0	1,118	4,750	0	0	0	0	0	0	0	85	474	388	0
4	128	0	0	2,117	1	1,699	0	2	18	91	31	6	0	0
5	364	932	0	198	6,438	1	0	0	0	0	695	0	0	0
6	161	206	0	1,084	1	7,972	39	1,323	407	427	125	167	0	67
7	0	0	0	0	0	0	209	0	310	90	1	13	0	0
8	385	238	88	236	10	77	24	1,644	634	400	269	758	0	542
9	41	56	17	383	0	38	1,167	458	9,430	1,692	1,737	396	2	148
10	9	0	1	21	0	3	16	17	304	294	35	31	0	13
11	1,961	735	310	320	76	96	1,174	69	10,561	2,933	34,791	1,757	57	20
12	0	9	4,170	23	0	10	1	9	16	47	182	1,217	185	86
13	0	31	24	0	0	0	0	0	0	11	183	253	1,685	0
14	0	0	25	0	0	0	92	19	844	199	9	55	2	11

MNF_PPC_CHM														
ID	1	2	3	4	5	6	7	8	9	10	11	12	13	14
1	7,499	4	0	87	0	1	0	0	0	4	84	89	0	0
2	85	7,108	498	0	0	349	48	53	39	1	1,482	372	1	0
3	0	0	3,431	0	0	0	0	0	0	35	0	0	1,673	0
4	11	65	0	3,129	605	0	0	0	296	0	580	634	0	0
5	0	16	0	2,011	5,548	0	0	0	25	0	573	0	0	0
6	5	656	0	0	0	10,608	0	0	4,043	914	0	76	18	0
7	0	0	0	0	0	0	2,273	43	532	0	0	0	0	0
8	0	0	58	0	0	0	2	3,573	903	0	0	0	0	349
9	0	1	227	1,458	0	1,291	331	237	7,846	184	12,740	0	0	28
10	9	35	0	0	0	29	0	0	1,525	4,018	16	0	19	0
11	1,454	5,647	98	3,569	578	7	71	28	7,548	1,323	18,374	88	634	0
12	274	373	5,148	0	0	51	0	0	0	0	5,058	3,306	0	121
13	0	0	30	0	0	0	0	0	13	0	0	0	0	0
14	0	0	377	0	0	0	0	6	0	0	0	1,298	0	490

MNF_PPC_CHM_VI														
ID	1	2	3	4	5	6	7	8	9	10	11	12	13	14
1	7,787	6	0	1	0	0	0	0	0	0	118	134	0	0
2	29	7,333	482	0	0	310	55	36	36	0	1,501	422	0	2
3	0	0	3,490	0	0	0	0	0	0	33	0	0	1,991	0
4	20	68	0	3,589	616	0	0	0	72	0	495	522	0	0
5	0	122	0	1,991	5,593	0	0	0	14	0	636	0	0	0
6	0	688	0	0	0	10,577	0	0	3,690	824	0	74	1	0
7	0	0	0	0	0	0	2,259	47	528	0	0	0	0	0
8	0	0	102	0	0	0	3	3,581	898	0	0	0	0	370
9	0	70	197	1,376	0	1,359	334	215	7,947	184	12,611	0	0	30
10	6	58	0	0	0	31	0	0	1,683	4,112	0	0	8	0
11	1,494	5,239	43	3,297	522	11	74	50	7,902	1,326	18,527	104	345	0
12	1	321	5,319	0	0	48	0	2	0	0	5,019	3,563	0	122
13	0	0	45	0	0	0	0	0	0	0	0	0	0	0
14	0	0	189	0	0	0	0	9	0	0	0	1,044	0	464

<i>full</i>														
ID	1	2	3	4	5	6	7	8	9	10	11	12	13	14
1	7,316	0	0	13	0	0	0	0	6	23	465	466	0	0
2	144	9,819	395	0	0	257	56	0	146	11	2,641	317	22	3
3	0	0	3,522	0	0	0	0	0	0	1	0	0	2,193	0
4	39	8	0	6,380	101	0	0	0	69	11	158	187	0	0
5	0	348	0	1,245	6,211	0	0	0	7	0	718	0	0	0
6	4	853	2	0	0	11,921	0	0	3,856	502	0	45	2	0
7	0	0	0	0	0	0	2,190	20	599	0	0	0	0	0
8	0	0	146	0	0	0	27	3,614	1,252	3	0	4	0	619
9	0	0	84	2,116	0	93	364	188	8,042	251	13,341	4	0	20
10	45	0	0	0	0	0	0	3	1,118	3,623	4	0	18	0
11	1,697	2,794	23	500	419	5	88	101	7,675	2,054	17,848	168	110	0
12	92	83	5,183	0	0	60	0	5	0	0	3,732	3,798	0	69
13	0	0	441	0	0	0	0	0	0	0	0	0	0	0
14	0	0	71	0	0	0	0	9	0	0	0	874	0	277

<i>FSJM</i>														
ID	1	2	3	4	5	6	7	8	9	10	11	12	13	14
1	6,804	0	0	10	0	0	0	0	8	13	1,085	388	0	0
2	90	9,932	334	0	0	262	73	9	65	15	2,075	320	3	3
3	0	0	3,492	0	0	0	0	0	0	4	0	10	2,136	0
4	49	7	0	6,096	168	0	0	0	86	26	203	169	0	0
5	0	54	0	1,511	6,029	0	0	0	12	0	749	0	0	0
6	7	846	0	0	0	11,837	0	0	4,093	453	0	47	0	0
7	0	0	0	0	0	0	2,205	12	598	0	0	0	0	0
8	0	0	166	0	0	0	10	3,510	1,212	4	0	4	0	667
9	0	0	305	2,105	0	175	345	309	8,066	257	13,408	3	0	44
10	31	0	0	0	0	2	1	1	964	3,677	0	3	1	0
11	2,324	2,958	53	532	534	1	91	90	7,666	2,030	16,942	277	205	0
12	32	108	5,158	0	0	59	0	2	0	0	4,445	3,693	0	85
13	0	0	260	0	0	0	0	0	0	0	0	0	0	0
14	0	0	99	0	0	0	0	7	0	0	0	949	0	189



OBIA (VNIR_CHM_PPC_VI_MNF)														
ID	1	2	3	4	5	6	7	8	9	10	11	12	13	14
1	6,115	80	0	4,881	0	58	0	0	0	79	328	1,165	0	0
2	745	9,671	8	273	0	588	14	37	349	84	683	1,227	74	21
3	0	0	4,530	0	0	0	0	0	0	0	0	492	2,256	0
4	0	0	0	3,420	0	0	0	0	1	335	211	0	0	0
5	332	3,180	0	442	6,713	0	0	0	0	0	989	0	0	0
6	0	763	42	0	0	11,685	19	0	304	790	0	0	0	0
7	0	0	0	0	0	0	1,182	0	519	0	0	0	0	0
8	0	0	5	0	0	0	24	3,824	100	0	0	49	0	922
9	0	2	345	979	0	4	1,414	56	15,205	1,271	3,515	0	0	0
10	0	0	0	0	0	0	12	0	282	1,573	0	0	0	0
11	2,145	209	0	259	18	1	60	23	6,010	2,347	33,181	129	15	0
12	0	0	4,936	0	0	0	0	0	0	0	0	2,395	0	0
13	0	0	0	0	0	0	0	0	0	0	0	105	0	0
14	0	0	1	0	0	0	0	0	0	0	0	301	0	45

Table B.4- Confusion matrices using the CNN algorithm in Area 1.

VNIR														
ID	1	2	3	4	5	6	7	8	9	10	11	12	13	14
1	8,528	19	0	2,791	0	99	0	0	35	0	0	0	0	0
2	180	13,511	0	98	0	0	0	0	0	35	479	11	0	0
3	0	22	5,009	0	0	0	0	0	39	0	0	902	3	0
4	35	0	0	6,317	0	0	0	0	97	0	61	67	0	0
5	11	295	0	4	6,753	0	0	0	5	0	681	0	0	0
6	0	69	0	0	0	12,110	0	0	241	1,583	0	0	0	0
7	0	0	0	0	0	0	2,601	0	0	0	0	0	0	0
8	0	0	0	0	0	0	1	3,966	10	1	0	7	0	781
9	0	0	0	1,034	0	124	0	0	18,521	29	2,191	3	0	0
10	60	0	0	24	0	0	0	0	980	4,709	2	0	152	0
11	474	12	0	6	0	0	0	0	2,848	171	35,525	986	0	0
12	0	0	4,892	0	0	0	0	0	20	0	0	3,917	40	53
13	0	0	0	12	0	0	0	0	0	0	0	0	2,146	0
14	0	0	0	4	0	0	138	0	2	11	0	6	0	167

VNIR_CHM														
ID	1	2	3	4	5	6	7	8	9	10	11	12	13	14
1	8,077	265	0	3,116	0	231	34	11	366	50	4	165	0	0
2	45	11,833	0	174	0	25	0	110	0	195	422	43	0	1
3	0	1,514	6,152	0	0	0	0	0	258	1	22	627	53	29
4	0	3	0	5,372	0	0	0	0	213	0	96	110	0	0
5	72	310	0	80	6,749	0	0	0	0	0	1,302	0	0	0
6	0	3	0	0	0	11,922	4	10	735	919	169	1	0	0
7	0	0	0	0	0	0	2,574	0	0	0	0	0	0	16
8	0	0	40	0	0	0	13	3,739	103	125	0	0	0	302
9	0	0	0	1,330	0	111	27	6	14,253	598	1,359	73	0	0
10	21	0	0	18	0	44	0	0	1,596	4,044	1	0	630	0
11	1,073	0	0	184	4	0	0	0	3,497	363	35,564	1,106	256	0
12	0	0	3,331	0	0	0	9	0	350	244	0	3,649	0	0
13	0	0	164	16	0	0	0	66	1,427	0	0	40	1,402	0
14	0	0	214	0	0	0	79	24	0	0	0	0	0	653

VNIR_CHM_PPC														
ID	1	2	3	4	5	6	7	8	9	10	11	12	13	14
1	6,974	347	5	2,989	0	181	0	0	94	57	0	9	0	0
2	51	12,570	0	103	0	3	0	2	0	12	382	18	3	0
3	23	238	5,968	0	0	0	0	1	896	7	5	725	162	0
4	0	15	0	2,230	0	5	0	0	239	0	87	256	0	0
5	0	442	0	301	6,730	0	0	0	0	0	1,685	0	0	0
6	2	134	2	189	0	12,022	3	0	714	1,614	15	16	0	0
7	0	133	0	0	0	0	2,531	0	1	0	0	0	0	4
8	0	0	12	0	0	0	61	3,881	387	105	0	11	0	540
9	7	0	0	4,068	0	118	0	40	16,469	327	1,647	0	0	0
10	210	7	0	0	0	4	0	0	138	3,632	0	0	550	0
11	2,021	31	0	354	23	0	0	0	3,610	715	35,118	1,672	22	0
12	0	2	3,914	0	0	0	0	0	175	63	0	3,100	65	0
13	0	9	0	56	0	0	0	0	11	0	0	92	1,539	0
14	0	0	0	0	0	0	145	42	64	7	0	0	0	457

Table B.5- Confusion matrices using the SVM algorithm in Area 2

VNIR											
ID	1	2	4	5	6	15	10	11	12	13	16
1	2,876	81	100	882	11	483	7	39	24	15	9
2	219	10,505	385	25	103	77	200	9	1,037	23	35
4	307	32	4,443	726	140	47	34	118	84	1	11
5	340	103	99	80	300	480	264	197	1,136	26	393
6	149	96	255	46	2,562	262	106	656	2,213	14	62
15	54	3	3	2	3	502	14	31	74	2	1
10	308	49	75	27	26	192	244	107	254	6	21
11	1,571	177	103	20	529	321	311	968	1,185	54	68
12	3,104	491	576	268	321	423	195	184	1,203	370	730
13	52	12	1	0	1	0	0	2	270	508	372
16	24	0	20	4	4	11	23	19	120	24	686

VNIR_CHM											
ID	1	2	4	5	6	15	10	11	12	13	16
1	4,784	28	710	480	0	0	2	137	25	29	0
2	125	10,902	289	0	136	89	277	24	1,004	0	8
4	539	0	4,455	765	0	0	158	113	5	9	26
5	415	0	2	834	0	41	44	154	35	139	473
6	1	194	61	0	2,607	321	372	52	400	0	0
15	1	0	0	0	8	827	1	2	92	0	0
10	181	1	4	0	13	332	459	77	62	0	0
11	1,552	162	199	0	515	480	1	1,209	1,945	0	0
12	858	262	129	0	721	708	9	525	3,977	0	0
13	489	0	22	1	0	0	16	9	0	800	707
16	59	0	189	0	0	0	59	28	55	66	1,174

VNIR_PPC											
ID	1	2	4	5	6	15	10	11	12	13	16
1	2,763	80	103	889	12	483	8	37	26	16	9
2	204	10,540	377	26	105	77	198	9	1,046	23	31
4	260	33	4,448	714	135	48	36	120	86	1	14
5	345	64	95	83	289	476	259	213	1,152	26	410
6	122	95	254	44	2,576	260	106	640	2,223	18	65
15	54	3	3	2	3	501	14	30	74	1	0
10	269	50	74	28	26	195	241	107	256	4	17
11	1,735	179	104	22	530	322	310	965	1,161	94	74
12	3,028	492	577	269	320	424	201	188	1,203	351	738
13	90	13	1	0	1	0	0	2	282	499	425
16	134	0	24	3	3	12	25	19	91	10	605

VNIR_CHM_PPC											
ID	1	2	4	5	6	15	10	11	12	13	16
1	4,642	28	714	479	0	0	4	139	26	27	2
2	126	10,905	285	0	136	90	279	21	1,010	0	8
4	486	0	4,447	766	0	0	149	110	4	7	27
5	357	0	3	835	0	42	26	167	36	147	490
6	1	192	61	0	2,604	321	370	51	404	0	0
15	1	0	0	0	8	832	1	2	91	0	0
10	179	1	3	0	12	332	460	79	64	0	0
11	1,572	161	201	0	518	476	2	1,191	1,930	31	3
12	856	262	123	0	722	705	9	527	3,974	0	0
13	544	0	23	0	0	0	16	14	0	784	825
16	240	0	200	0	0	0	82	29	61	47	1,033

VNIR_CHM_PPC_MNF											
ID	1	2	4	5	6	15	10	11	12	13	16
1	4,561	20	529	474	0	0	7	127	30	30	2
2	88	10,918	341	0	153	89	271	28	1,088	0	4
4	453	0	4,575	874	0	0	100	97	4	7	37
5	356	0	7	729	0	35	48	173	64	144	522
6	7	207	109	0	2,666	387	345	55	444	0	0
15	0	1	0	0	5	696	0	13	74	0	0
10	193	5	5	0	15	335	490	46	51	0	0
11	1,651	193	166	0	552	572	17	1,191	2,061	30	3
12	967	205	131	0	609	684	8	577	3,721	0	0
13	539	0	29	3	0	0	16	5	0	774	811
16	189	0	168	0	0	0	96	18	63	58	1,009

VNIR_CHM_PPC_GLCM											
ID	1	2	4	5	6	15	10	11	12	13	16
1	4,434	29	719	443	0	0	43	202	76	35	17
2	42	10,925	134	0	167	87	194	8	873	0	0
4	485	0	4,517	938	0	0	72	155	0	5	51
5	580	0	38	682	0	191	15	79	34	97	536
6	8	149	75	0	2,520	228	360	53	457	0	0
15	0	9	0	0	28	796	0	0	78	0	0
10	361	23	11	0	8	224	528	24	24	0	0
11	1,313	128	167	0	700	427	36	1,195	1,948	114	22
12	946	286	184	0	577	845	16	580	4,086	0	12
13	467	0	41	13	0	0	29	9	0	752	1,040
16	368	0	174	4	0	0	105	25	24	40	710

VNIR_CHM_PPC_VI											
ID	1	2	4	5	6	15	10	11	12	13	16
1	4,731	11	786	525	0	0	6	130	51	38	11
2	90	10,862	233	0	140	82	250	21	972	0	0
4	481	0	4,382	860	0	0	127	116	10	6	49
5	471	0	9	690	0	51	31	171	44	143	490
6	8	202	81	0	2,653	342	377	51	417	0	0
15	0	1	0	0	5	830	1	2	68	0	0
10	162	3	11	0	11	338	494	56	60	1	0
11	1,412	243	211	4	493	446	17	1,169	1,893	42	5
12	897	227	129	0	696	709	6	572	4,037	0	2
13	468	0	28	1	0	0	17	11	0	742	792
16	284	0	190	0	2	0	72	31	48	71	1,039

VNIR_CHM_PPC_VI_MNF											
ID	1	2	4	5	6	15	10	11	12	13	16
1	4,630	16	575	502	0	0	5	116	38	38	3
2	65	10,901	300	0	157	82	248	25	1,063	0	3
4	464	0	4,504	955	0	0	85	101	10	4	38
5	487	0	10	619	0	42	47	189	65	136	499
6	6	186	123	0	2,655	391	331	60	518	0	0
15	0	1	0	0	4	712	1	9	69	0	0
10	178	4	21	0	17	334	539	34	50	0	0
11	1,462	265	193	2	534	548	19	1,171	1,955	36	3
12	1,016	176	136	0	633	688	10	609	3,778	0	2
13	485	0	22	0	0	0	17	3	0	751	817
16	211	0	176	2	0	1	96	13	54	78	1,023

VNIR_VI_MNF_GLCM											
ID	1	2	4	5	6	15	10	11	12	13	16
1	2,533	69	118	765	27	613	13	44	46	12	0
2	297	10,736	292	39	123	74	175	1	1,097	28	26
4	416	2	4,256	899	190	31	56	111	84	10	7
5	499	49	107	44	300	545	195	250	1,158	29	345
6	136	76	331	45	2,425	125	145	495	1,965	15	60
15	53	2	3	6	6	358	5	37	38	3	1
10	514	40	64	44	21	198	213	109	305	7	22
11	1,453	160	211	1	593	209	391	1,021	1,006	130	84
12	3,035	399	674	236	315	644	162	250	1,563	425	839
13	53	15	1	0	0	0	0	0	252	342	352
16	15	1	3	1	0	1	43	12	86	42	652

MNF_CHM_PPC											
ID	1	2	4	5	6	15	10	11	12	13	16
1	4,369	27	958	642	7	0	48	280	52	11	9
2	231	10,450	212	0	168	65	263	32	1,253	0	0
4	1,257	1	4,159	650	0	0	102	166	5	36	62
5	249	0	8	778	0	14	13	173	11	272	292
6	7	456	175	0	1,700	500	658	54	416	0	0
15	0	0	0	0	170	391	0	1	53	0	0
10	136	4	3	0	101	415	198	339	193	0	0
11	1,468	321	294	0	871	847	5	591	1,437	0	0
12	945	290	113	0	983	566	24	676	4,172	0	0
13	178	0	9	9	0	0	7	0	0	655	1,110
16	164	0	129	1	0	0	80	18	8	69	915

MNF_CHM_PPC_VI											
ID	1	2	4	5	6	15	10	11	12	13	16
1	4,627	12	946	630	2	0	25	161	55	26	1
2	248	10,790	177	0	176	65	287	28	1,190	5	10
4	960	0	4,170	782	0	0	108	153	13	13	50
5	446	0	17	653	0	19	18	175	32	193	278
6	20	304	183	0	2,208	469	562	66	544	0	0
15	0	3	0	0	48	516	0	2	41	0	0
10	130	10	14	0	57	469	278	118	103	0	0
11	1,266	244	219	6	678	579	7	917	1,697	49	8
12	920	186	134	0	831	681	18	681	3,910	0	0
13	267	0	9	1	0	0	12	11	0	663	1,095
16	120	0	191	8	0	0	83	18	15	94	946

FSJM											
ID	1	2	4	5	6	15	10	11	12	13	16
1	5,375	0	61	261	0	0	3	0	0	46	2
2	0	9,729	399	0	17	90	78	6	1,701	0	0
4	1,024	0	2,134	961	0	0	0	0	0	12	131
5	126	0	54	858	2	399	37	252	64	29	0
6	29	2,584	300	0	3,087	25	160	0	282	1	3
15	0	0	304	0	0	1,726	0	1	28	0	0
10	89	59	28	0	0	0	868	0	0	0	0
11	37	156	2,396	0	1	556	127	2,000	3,483	29	6
12	1,911	391	91	0	893	0	0	0	2,138	4	0
13	364	0	2	0	0	0	0	0	0	879	730
16	49	0	868	0	0	2	125	71	272	41	1,516

full											
ID	1	2	4	5	6	15	10	11	12	13	16
1	4,511	17	573	461	0	5	29	158	61	40	14
2	35	11,011	197	0	196	99	194	2	950	0	2
4	496	0	4,524	1,051	1	0	46	136	0	9	50
5	664	0	30	563	0	178	25	107	39	93	489
6	7	156	118	0	2,555	283	286	62	524	0	0
15	0	12	0	0	30	742	2	9	85	0	0
10	308	18	9	0	1	214	566	14	27	0	0
11	1,260	146	220	0	690	481	84	1,294	2,071	88	19
12	1,030	189	234	0	527	796	19	519	3,801	0	5
13	425	0	37	5	0	0	27	4	0	757	1,027
16	268	0	118	0	0	0	120	25	42	56	782

MV (VNIR_CHM)											
ID	1	2	4	5	6	15	10	11	12	13	16
1	5,200	0	4	0	94	0	0	0	0	0	2
2	2	11,546	382	0	0	1	196	0	257	0	63
4	274	0	5,621	691	0	0	222	158	0	0	0
5	317	0	0	1,389	0	27	0	115	0	61	25
6	0	3	0	0	2,473	0	0	0	64	0	0
15	0	0	0	0	0	578	0	0	0	0	0
10	0	0	0	0	0	0	962	0	0	0	0
11	1,713	0	0	0	557	1,413	0	1,531	0	0	0
12	1,084	0	53	0	876	779	18	526	7,279	0	0
13	302	0	0	0	0	0	0	0	0	982	2,029
16	0	0	0	0	0	0	0	0	0	0	269

Table B.6- Confusion matrices using the wSVM algorithm in Area 2

VNIR											
ID	1	2	4	5	6	15	10	11	12	13	16
1	3,052	269	146	879	15	640	9	44	33	10	7
2	291	10,574	302	20	43	63	153	0	786	19	28
4	317	41	4,882	830	178	29	30	139	74	0	15
5	376	523	128	87	356	432	277	290	1,422	16	414
6	112	310	475	60	2,845	214	139	570	2,284	14	27
15	177	35	6	8	6	641	32	46	120	2	1
10	628	217	108	43	33	241	320	143	443	6	29
11	1,483	376	146	14	413	238	278	914	1,186	42	61
12	2,362	527	404	130	104	291	122	175	905	269	348
13	143	24	1	0	1	0	2	0	507	632	563
16	63	23	39	9	6	9	36	9	208	31	895

VNIR_CHM											
ID	1	2	4	5	6	15	10	11	12	13	16
1	4,845	40	681	494	0	0	6	103	16	30	1
2	9	10,554	66	0	45	54	182	0	477	0	0
4	424	0	4,743	790	0	0	141	125	2	9	23
5	326	0	10	795	0	36	28	133	23	114	457
6	2	380	87	0	2,989	376	360	67	374	0	0
15	0	0	0	0	20	945	0	3	103	0	0
10	284	1	7	0	16	419	500	60	38	0	0
11	1,509	194	91	0	441	407	65	1,224	2,182	12	0
12	962	380	172	0	488	559	8	585	4,343	0	0
13	562	0	28	0	0	0	19	3	1	820	699
16	81	0	175	1	1	2	89	27	41	58	1,208

VNIR_CHM_PPC											
ID	1	2	4	5	6	15	10	11	12	13	16
1	4,769	38	724	422	0	0	6	113	25	26	5
2	18	10,612	58	0	47	60	183	0	523	0	1
4	343	0	4,698	796	0	0	129	133	2	4	27
5	299	0	13	862	0	40	21	131	27	125	456
6	0	332	68	0	2,952	344	364	54	343	0	0
15	0	0	0	0	21	946	0	4	80	0	0
10	275	0	4	0	16	417	503	60	33	0	0
11	1,507	210	104	0	433	423	49	1,242	2,224	37	3
12	906	357	165	0	531	568	20	552	4,289	0	0
13	591	0	29	0	0	0	19	14	0	792	825
16	296	0	197	0	0	0	104	27	54	59	1,071



Table B.7- Confusion matrices using the RF algorithm in Area 2.

VNIR											
ID	1	2	4	5	6	15	10	11	12	13	16
1	2,311	5	100	557	19	703	11	57	15	1	1
2	643	11,172	425	98	134	63	240	0	991	59	159
4	391	1	4,385	854	232	40	22	155	25	3	10
5	189	4	66	48	116	153	106	234	427	16	85
6	175	54	344	113	2,228	332	190	586	2,376	16	60
15	3	0	0	0	0	136	1	10	2	0	0
10	349	1	12	10	2	59	41	28	20	0	1
11	1,024	86	166	54	851	617	462	924	915	12	57
12	3,909	225	560	346	418	695	325	328	2,790	800	1,632
13	4	1	1	0	0	0	0	0	31	132	126
16	6	0	1	0	0	0	0	8	8	4	257

VNIR_CHM											
ID	1	2	4	5	6	15	10	11	12	13	16
1	4,828	2	690	427	0	0	19	399	43	0	1
2	54	11,010	155	1	118	68	157	0	457	0	9
4	682	0	4,910	495	0	0	205	142	2	5	109
5	283	0	1	1,154	0	0	4	159	0	304	272
6	0	186	40	0	2,045	292	125	18	246	0	0
15	0	0	0	0	10	481	0	0	0	0	0
10	77	0	0	0	22	124	786	44	10	0	0
11	1,843	88	89	0	741	849	22	977	1,141	3	3
12	898	263	103	1	1,064	984	24	575	5,695	0	52
13	326	0	46	0	0	0	34	14	0	652	1,307
16	13	0	26	2	0	0	22	2	6	79	635

VNIR_PPC											
ID	1	2	4	5	6	15	10	11	12	13	16
1	4,309	8	1,618	242	54	0	4	778	212	1	0
2	17	10,820	109	0	20	50	119	2	553	0	0
4	1,410	24	3,930	340	0	0	265	137	15	0	16
5	574	0	1	1,493	0	1	0	120	0	594	534
6	18	251	35	0	1,687	305	0	11	177	0	0
15	0	0	0	0	34	564	0	0	0	0	0
10	121	0	0	0	44	92	984	92	143	0	0
11	1,373	221	78	0	868	1,332	0	843	341	0	0
12	1,047	225	122	0	1,288	454	0	344	6,145	0	4
13	120	0	42	0	0	0	26	0	0	376	1,111
16	15	0	125	5	5	0	0	3	14	72	723

VNIR_CHM_PPC											
ID	1	2	4	5	6	15	10	11	12	13	16
1	4,323	0	1,659	300	15	0	14	678	166	4	0
2	14	11,000	84	0	40	52	122	4	342	0	0
4	1,559	10	4,010	229	0	0	271	142	1	0	26
5	493	0	1	1,551	0	1	0	133	0	359	326
6	4	251	0	0	1,620	93	0	0	197	0	0
15	0	0	0	0	40	803	0	0	4	0	0
10	99	0	1	0	12	107	981	69	113	0	0
11	1,692	219	47	0	778	1,040	0	866	467	0	0
12	675	69	98	0	1,495	702	0	433	6,309	0	0
13	127	0	47	0	0	0	10	5	0	677	1,289
16	18	0	113	0	0	0	0	0	1	3	747

VNIR_CHM_PPC_MNF											
ID	1	2	4	5	6	15	10	11	12	13	16
1	4,500	0	1,477	310	6	0	5	686	152	12	0
2	20	11,022	65	0	36	50	127	3	409	0	0
4	1,532	11	4,248	233	0	0	285	119	0	0	34
5	334	0	1	1,537	0	0	0	120	0	353	239
6	2	260	2	0	1,725	178	0	4	281	0	0
15	0	0	0	0	53	785	0	0	5	0	0
10	91	0	5	0	13	133	976	84	98	0	0
11	1,545	184	16	0	743	1,044	0	679	454	0	0
12	837	72	104	0	1,424	608	0	631	6,199	0	0
13	125	0	45	0	0	0	5	3	0	673	1,324
16	18	0	97	0	0	0	0	1	2	5	791

VNIR_CHM_PPC_GLCM											
ID	1	2	4	5	6	15	10	11	12	13	16
1	4,584	0	1,604	286	15	0	40	692	124	3	0
2	24	11,207	92	0	36	41	124	1	292	0	0
4	1,379	7	4,089	214	0	0	203	108	0	6	21
5	345	0	1	1,580	0	0	0	99	0	358	300
6	3	194	2	0	1,708	119	0	6	184	0	0
15	0	0	0	0	84	713	0	0	1	0	0
10	110	0	1	0	8	58	979	55	100	0	0
11	1,534	94	27	0	860	1,061	0	854	431	0	0
12	858	47	129	0	1,289	806	0	512	6,467	0	0
13	154	0	56	0	0	0	52	3	0	645	1,470
16	13	0	59	0	0	0	0	0	1	31	597

VNIR_CHM_PPC_VI											
ID	1	2	4	5	6	15	10	11	12	13	16
1	4,342	0	1,667	305	11	0	7	623	134	9	0
2	27	10,997	81	0	33	47	123	2	345	0	0
4	1,532	9	4,051	219	0	0	263	137	0	0	54
5	441	0	4	1,550	0	2	0	123	0	352	264
6	7	230	0	0	1,692	150	1	0	169	0	0
15	0	0	0	0	35	754	0	0	6	0	0
10	113	0	0	0	9	129	979	73	125	0	0
11	1,650	225	40	0	727	946	0	879	498	0	0
12	736	88	118	0	1,493	770	0	489	6,323	0	0
13	140	0	18	0	0	0	25	3	0	673	1,340
16	16	0	81	6	0	0	0	1	0	9	730

VNIR_CHM_PPC_VI_MNF											
ID	1	2	4	5	6	15	10	11	12	13	16
1	4,446	0	1,458	328	7	0	7	698	132	8	0
2	16	11,043	52	0	35	42	125	2	371	0	0
4	1,562	11	4,334	236	0	0	284	122	0	1	46
5	336	0	1	1,516	0	1	0	132	0	353	237
6	15	251	4	0	1,782	195	1	0	252	0	0
15	0	0	0	0	43	758	0	0	5	0	0
10	78	0	0	0	11	114	977	78	63	0	0
11	1,456	170	20	0	728	990	0	670	486	0	0
12	950	74	114	0	1,394	698	0	622	6,290	0	0
13	139	0	21	0	0	0	4	4	0	667	1,318
16	6	0	56	0	0	0	0	2	1	14	787

VNIR_VI_MNF_GLCM											
ID	1	2	4	5	6	15	10	11	12	13	16
1	2,272	6	82	522	58	859	25	133	27	1	0
2	614	11,157	395	95	149	37	231	0	840	57	55
4	432	8	4,297	889	241	27	23	133	36	12	10
5	236	3	74	44	116	116	73	185	388	22	69
6	345	63	335	127	1,912	273	246	517	2,018	25	45
15	7	0	0	1	0	68	1	24	3	0	0
10	275	12	18	4	1	62	26	24	32	3	1
11	1,320	89	146	40	928	581	485	888	889	22	82
12	3,480	211	711	354	595	775	278	426	3,292	629	1,580
13	1	0	0	0	0	0	2	0	65	251	148
16	22	0	2	4	0	0	8	0	10	21	398

<b>MNF_CHM_PPC</b>											
<b>ID</b>	<b>1</b>	<b>2</b>	<b>4</b>	<b>5</b>	<b>6</b>	<b>15</b>	<b>10</b>	<b>11</b>	<b>12</b>	<b>13</b>	<b>16</b>
1	4,099	11	1,763	376	14	0	0	789	192	4	0
2	2	10,339	33	0	56	37	135	1	372	0	0
4	2,168	33	3,887	185	0	0	293	171	0	1	39
5	560	0	6	1,519	0	1	0	94	0	353	257
6	4	432	0	0	1,600	195	0	13	142	0	0
15	0	0	0	0	114	775	0	0	0	0	0
10	96	0	65	0	9	63	968	119	167	0	0
11	1,067	534	47	0	721	991	0	562	1,054	0	0
12	776	199	72	0	1,486	736	0	559	5,673	0	0
13	187	1	122	0	0	0	2	18	0	682	1,183
16	45	0	65	0	0	0	0	4	0	3	909

<b>MNF_CHM_PPC_VI</b>											
<b>ID</b>	<b>1</b>	<b>2</b>	<b>4</b>	<b>5</b>	<b>6</b>	<b>15</b>	<b>10</b>	<b>11</b>	<b>12</b>	<b>13</b>	<b>16</b>
1	4,363	10	1,678	326	10	0	0	776	179	7	0
2	3	10,478	30	0	37	32	137	2	386	0	0
4	1,955	22	4,048	223	0	0	294	177	0	0	69
5	378	0	20	1,531	0	1	0	100	0	354	242
6	6	334	0	0	1,588	197	0	11	165	0	0
15	0	0	0	0	127	765	0	0	1	0	0
10	86	0	47	0	6	83	966	117	98	0	0
11	1,106	532	57	0	680	894	0	545	777	0	0
12	858	172	74	0	1,552	826	0	579	5,993	0	0
13	225	1	42	0	0	0	1	17	0	673	1,231
16	24	0	64	0	0	0	0	6	1	9	846

<b>FSJM</b>											
<b>ID</b>	<b>1</b>	<b>2</b>	<b>4</b>	<b>5</b>	<b>6</b>	<b>15</b>	<b>10</b>	<b>11</b>	<b>12</b>	<b>13</b>	<b>16</b>
1	5,872	0	0	761	0	0	0	0	0	115	0
2	0	5,819	887	0	5	26	274	0	3,966	0	0
4	1,625	0	2,187	1	0	0	0	0	0	13	2,167
5	19	0	4	1,314	0	108	1	126	4	31	0
6	16	1,237	417	0	3,608	98	3	0	367	0	0
15	0	0	0	0	0	2,374	0	0	0	0	0
10	0	5,849	77	0	0	0	1,083	0	0	0	0
11	0	14	2,875	0	0	192	37	2,203	1,599	0	0
12	1,322	0	0	4	387	0	0	0	2,032	31	1
13	150	0	0	0	0	0	0	0	0	851	190
16	0	0	190	0	0	0	0	1	0	0	30

<i>full</i>											
ID	1	2	4	5	6	15	10	11	12	13	16
1	4,655	0	1,335	297	8	0	23	691	85	13	0
2	25	11,216	64	0	30	42	129	4	311	0	0
4	1,318	3	4,411	236	0	0	243	103	0	1	11
5	317	0	0	1,547	0	1	0	156	0	345	242
6	8	220	14	0	1,805	261	0	4	275	0	0
15	0	0	0	0	75	689	0	0	2	0	0
10	112	0	0	0	7	65	974	55	66	0	0
11	1,414	58	28	0	700	1,019	0	763	382	0	0
12	997	52	139	0	1,375	721	0	551	6,478	0	0
13	149	0	33	0	0	0	29	2	0	659	1,477
16	9	0	36	0	0	0	0	1	1	25	658

Table B.8- Confusion matrices using the CNN algorithm in Area 2.

VNIR											
ID	1	2	4	5	6	15	10	11	12	13	16
1	4,878	0	0	1,693	0	0	0	0	0	5	0
2	0	12,762	174	0	0	0	43	2	2,754	0	0
4	725	0	5,522	384	0	0	0	0	0	0	0
5	64	0	0	0	0	152	182	286	24	0	0
6	0	0	110	0	3,951	0	0	0	1,258	0	0
15	0	0	0	0	0	2,638	29	0	10	0	0
10	1	0	1	0	0	0	1,083	0	4	0	0
11	0	0	13	0	0	0	62	2,057	1,189	0	0
12	3,345	0	238	14	46	0	0	0	2,367	0	86
13	0	0	0	0	0	0	0	0	6	1,041	0
16	0	0	0	0	0	0	0	0	0	0	2,308

VNIR_CHM											
ID	1	2	4	5	6	15	10	11	12	13	16
1	4,765	0	0	1,494	0	0	0	0	0	0	0
2	0	12,762	93	0	0	0	272	0	2,540	0	0
4	743	0	5,627	597	0	0	0	0	0	0	6
5	160	0	2	0	0	516	0	0	326	0	0
6	0	0	146	0	3,955	0	0	0	339	0	0
15	0	0	0	0	0	2,274	0	0	9	0	0
10	82	0	0	0	0	0	1,033	0	85	0	0
11	0	0	142	0	0	0	94	2,345	2,647	0	0
12	3,247	0	28	0	42	0	0	0	1,536	0	0
13	16	0	0	0	0	0	0	0	49	1,046	68
16	0	0	20	0	0	0	0	0	81	0	2,320

VNIR_CHM_PPC											
ID	1	2	4	5	6	15	10	11	12	13	16
1	3,575	0	0	1,601	0	0	0	0	0	0	0
2	0	12,762	212	0	0	0	416	0	1,479	0	0
4	376	0	5,006	320	0	0	0	0	0	0	0
5	340	0	2	0	0	394	0	0	428	0	0
6	0	0	35	0	3,990	0	0	0	1,554	0	0
15	0	0	0	0	0	2,396	24	0	3	0	0
10	0	0	1	0	0	0	921	0	42	0	0
11	0	0	327	0	0	0	1	2,345	2,136	0	0
12	4,722	0	141	170	7	0	37	0	1,897	0	76
13	0	0	0	0	0	0	0	0	73	1,046	15
16	0	0	334	0	0	0	0	0	0	0	2,303